LAKE RECORDS OF HOLOCENE CLIMATE CHANGE, CORDILLERA DE MÉRIDA, VENEZUELA

A Dissertation Presented

by

PRATIGYA J. POLISSAR

Submitted to the Graduate School of the
University of Massachusetts Amherst in partial fulfillment
of the requirements for the degree of

DOCTOR OF PHILOSOPHY

September 2005

Geosciences

UMI Number: 3193933

INFORMATION TO USERS

The quality of this reproduction is dependent upon the quality of the copy submitted. Broken or indistinct print, colored or poor quality illustrations and photographs, print bleed-through, substandard margins, and improper alignment can adversely affect reproduction.

In the unlikely event that the author did not send a complete manuscript and there are missing pages, these will be noted. Also, if unauthorized copyright material had to be removed, a note will indicate the deletion.

UMI®

UMI Microform 3193933

Copyright 2006 by ProQuest Information and Learning Company.

All rights reserved. This microform edition is protected against unauthorized copying under Title 17, United States Code.

ProQuest Information and Learning Company
300 North Zeeb Road
P.O. Box 1346
Ann Arbor, MI 48106-1346

© Copyright by Pratigya J. Polissar 2005

All Rights Reserved

LAKE RECORDS OF HOLOCENE CLIMATE CHANGE, CORDILLERA DE MÉRIDA, VENEZUELA

A Dissertation Presented

by

PRATIGYA J. POLISSAR

Approved as to style and content by:

Raymond S. Bradley, Chair

Stephen J. Burns, Member

Mark B. Abbott, Member

John Machta, Member

Michael Williams, Department Head
Department of Geosciences

DEDICATION

In memory of John Barlow Reid Jr.
1940 – 2003

ACKNOWLEDGMENTS

I would like to thank my wife, Heather for her support throughout my Ph.D. Funding for this research was primarily from an N.S.F. grant to Dr. Abbott. Fieldwork was also funded in part by a grant from the Geological Society of America. An N.S.F. graduate research fellowship provided two years of salary. I would also like to thank Dr. Aldo Shemesh, Dr. Ruth Yam, and the dedicated staff at the Weizmann Institute of Science, Isreal for the analysis of the oxygen isotope composition of diatoms. Travel and expenses for laboratory work in Israel was funded by an N.S.F. International Programs grant to Dr. Bradley and myself.

ABSTRACT

LAKE RECORDS OF HOLOCENE CLIMATE CHANGE, CORDILLERA DE MÉRIDA, VENEZUELA

SEPTEMBER 2005

PRATIGYA J. POLISSAR, B.A., HAMPSHIRE COLLEGE

M.S., UNIVERSITY OF MASSACHUSETTS AMHERST

Ph.D., UNIVERSITY OF MASSACHUSETTS AMHERST

Directed by: Professor Raymond S. Bradley

Multi-proxy sediment records from four lakes in the Venezuelan Andes document changes in tropical climate over timescales of decades to millennia. The results are grouped into three topics: the Little Ice Age, the Holocene climate history, and atmospheric moisture balance of South America from oxygen isotopes.

A 1500-year reconstruction of climate history and glaciation indicates four glacial advances occurred between 1250 and 1810 A.D. These advances are coincident with solar activity minima. Temperature declines of 2.3 to 3.4° C and precipitation increases of 25 to 70% are required to produce the observed glacial responses. These results highlight the sensitivity of high-altitude tropical regions to relatively small changes in radiative forcing, implying even greater responses to future anthropogenic forcing.

On longer timescales, the Venezuelan Andes were generally wetter during the early Holocene. The middle Holocene was a time of low lake levels and reduced moisture balance whereas the late Holocene was wetter, with the wettest period occurring during the Little Ice Age. The pattern of millennial climate variability in

Venezuela appears to be either a wet-dry-wet (Andes) or dry-wet-dry (lowlands) sequence. Comparison with climate records from North, Central and South America suggests this pattern is widespread near the northern and southern edges of the tropical monsoon climate regime and along the Andes near the equatorial Pacific.

The isotopic composition of Andean precipitation reflects evaporation conditions over the Atlantic Ocean, moisture recycling over the South American lowlands and uplift to the Andes. The isotopic composition of precipitation in the Venezuelan Andes, reconstructed from lake sediment diatom oxygen isotope records, show a 2.4 ‰ decrease during the Holocene. This decrease reflects a reduction in the moisture entering South America which reaches the Andes. Ice cores from Peru and Bolivia exhibit similar isotopic trends.

Direct orbital changes in solar insolation cannot explain the synchronous trends in both climatic and isotopic histories throughout the neotropics. However, sea surface temperature variation in the tropical Pacific may explain these trends because modern interannual variability in this region has similar effects in both hemispheres.

TABLE OF CONTENTS

Page

LIST OF TABLES

LIST OF FIGURES

CHAPTER 1

INTRODUCTION AND BACKGROUND

Introduction

The tropics are an important component of the global climate system. Defined as the area between 23.5° north and south latitude, they cover 40% of the globe, receive 47% of the earth's potential solar insolation and contain 35% of the earth's population (Fig. 1.1). More energy is gained than lost in the tropics, thus there is a net surplus of heat which is exported to higher latitudes in both the atmosphere and oceans. In the atmosphere this energy is transported to the mid-latitudes by the Hadley circulation, much of it as latent heat derived from evaporation over the tropical oceans. The oceans are responsible for the remainder of the heat transported to high latitudes. Through the export of heat and moisture the tropics have a direct link to the climates of mid- and high-latitude regions. In turn, high-latitude processes such as deep-water production, sea-ice formation and ice-sheet growth can affect the sinks for exported tropical heat and change global and tropical climates.

Despite their importance in the global climate system, significant gaps exist in our understanding of the causes and consequences of tropical climate variability at different timescales. At periods of 10^4 to 10^5 years, significant tropical cooling and regional changes in the precipitation/evaporation balance (P/E) have accompanied the growth and decay of high-latitude ice sheets (e.g. Haberle and Maslin, 1999; Peterson et al., 2000). In contrast, interannual to decadal climate variability such as the El Niño-Southern Oscillation has a large effect on extratropical climate (Ropelewski and Halpert, 1987). At intermediate periods of 10^2 to 10^3 years, the cause of tropical climate

variability and the extratropical influences are less clear. These timescales encompass changes in solar irradiance and insolation forcing which might directly affect tropical climate. However, the extra-tropical response to the same forcing may also impact tropical climate. Variation at these (and greater) timescales extends beyond the period of instrumental measurement. Thus, proxy records of climate are essential to understand the variables which control tropical climate and the interaction of the tropics with higher latitudes.

In this dissertation I address the nature and regional patterns of climate change in the tropics by focusing on climate variability in the Venezuelan Andes during the past 10,000 y. Two facets of this dissertation represent a contribution to our understanding of tropical and global climate variability. First, by adding to the global collection of paleoclimate data this research furthers our understanding of the timing and spatial variability of climate change. Second, I try to understand the regional pattern of climate change and the possible mechanisms responsible for these changes by comparing the records from the Venezuelan Andes with other tropical records. Three broad questions are addressed in this dissertation:

1. How has climate in northern South America varied during the past 10,000 years?
2. How does climate variability in northern S. America correlate with records from other tropical locations?
3. What are the important causes of past climate variability in northern S. America at different timescales?

I concentrate on the past 10,000 years because the boundary conditions are similar to the present, thus drastic changes such as the growth and decay of continental ice sheets are not a confounding factor.

The dissertation is written as a series of manuscripts. This chapter serves as an introduction to the study region. In chapter two, glacier advances, temperature and moisture variability during the past 1,500 y are reconstructed at decade to century resolution. Chapter three documents the nature of climate variations during the Holocene (10,000 y-present) and examines regional correlations and potential forcing mechanisms. This chapter also puts the higher resolution record of chapter two into the context of variability during the last 10,000 y. The fourth chapter discusses how variations in the isotopic composition of precipitation in the Andes (reconstructed from lake sediment records) can be used to understand the evolution of low elevation atmospheric moisture during the Holocene. The final chapter summarizes the findings of the earlier chapters and attempts to put them into a broader context.

Modern Climate in Venezuela

Significant seasonal changes in precipitation are characteristic of Venezuela and the subtropical Andes (7-11°N), with wet season precipitation (April-October or November) accounting for 80-85% of the annual precipitation in the Cordillera de Mérida (Bradley et al., 1991). The pronounced seasonality in precipitation is caused by the annual cycle of solar declination; maximum solar insolation occurs in April and August and minimum insolation in November-February (Fig. 1.2. Berger and Loutre, 1991). Maximum insolation in the northern hemisphere summer causes a trough of low pressure to develop ~10°N (the intertropical convergence zone or ITCZ), leading to

wind convergence and atmospheric instability. Daily solar heating of the earth's surface then drives deep atmospheric convection and intense precipitation (Fig. 1.3). During minimum northern hemisphere solar insolation, the ITCZ moves into the southern hemisphere and the northern hemisphere tropics are under the influence of the northeast trade winds. Strong vertical wind shear and lower insolation suppress convection and lead to an annual minimum in precipitation.

It should be noted that the ITCZ is generally considered a marine phenomenon and the organized convection that represents the rainy season in Venezuela is located in a relatively narrow latitude band which forms an extension of the Atlantic ITCZ proper (Fig. 1.3). Likewise, the southern hemisphere wet season corresponds to the development of the south American summer monsoon (SASM, Zhou and Lau, 1998). Thus, variables which control the development, strength and dissipation of precipitation over the continents may be different from the controls on the ITCZ. This distinction should be kept in mind when discussing the effects of changes in ITCZ migration on continental climate (c.f. Bush and Silman, 2004).

Interannual Variability

There is considerable spatial and temporal variability in precipitation throughout the Venezuelan Andes. These variations result from both the large-scale circulation and local circulation effects due to topography (Pulwarty et al., 1998). Shown in Fig. 1.4 is precipitation (1967-76) and pan evaporation (1970-76) recorded at Laguna Mucubají. This station is located near several of the study lakes and should provide information on regional climate. The annual precipitation regime at Mucubají is generally unimodal, with a maximum in June-July and a minimum in Dec-Mar (Fig. 1.2). However, some

years show a bimodal regime with a mid-summer minimum occurring sometime between June and August (Fig. 1.4). The mid-summer minimum is common in several regions of Venezuela and is the principle factor in interannual precipitation variability (Pulwarty et al., 1992; Pulwarty et al., 1998). Evaporation is generally constant throughout the year, with slightly higher values in Feb-April (Fig. 1.2). The P/E balance is positive (>1) April-November and negative December-March.

During the period 1967-76, interannual changes in both precipitation and evaporation occurred at L. Mucubají (Fig. 1.4). Annual evaporation was higher in 1970 and 1973 while precipitation was lower in 1971 and 1973-1975. Positive evaporation anomalies tended to occur during spring (February-May) while negative anomalies were less intense and more likely to occur during the rainy season. Interannual variability in evaporation is principally associated with variability in February-May. Correlation between monthly evaporation and precipitation is high and negative during these months, indicating lower precipitation in any of these months is generally associated with higher evaporation in the same month. Precipitation variability in Venezuela is primarily associated with changes in the mid-summer drought (Pulwarty et al., 1998). This is apparent in the Mucubají data when principle components analysis is used to group months with similar variability. Annual precipitation variations are closely associated with June-July precipitation anomalies (Fig. 1.5). Interestingly, precipitation anomalies in the transition months of March-April and August-September are anticorrelated, and both are uncorrelated with annual precipitation.

Precipitation variability in Venezuela is affected by conditions in the tropical Pacific, Atlantic and Caribbean regions. Pulwarty (1992) found that conditions leading

to a wetter than average rainy season in Venezuela are: a positive Southern Oscillation Index (La Niña conditions), below normal sea-surface temperatures (SSTs) in the east Pacific and tropical south Atlantic, above normal SSTs in the Caribbean and deep easterlies (850-250mb) 10°-20° N. The precipitation record from L. Mucubají shows similar correlations with the climate variables investigated in Pulwarty (1992). Correlation of L. Mucubají precipitation with tropical SSTs shows that more June-August precipitation is associated with negative SST anomalies (SSTa) in the tropical south Atlantic and positive SSTa in the tropical north Atlantic and Caribbean (Fig. 1.6). In contrast, precipitation in March-May is positively associated with a pattern of SSTa in the equatorial Pacific which resemble a warm El Niño-Southern Oscillation (ENSO) event. Evaporation anomalies at L. Mucubají are also strongly associated with ENSO. The El Niño events in 1969 and 1972 led to greatly increased evaporation in the spring following El Niño onset (Fig. 1.4).

Previous Research

Paleoclimate research in Venezuela indicates there have been significant changes in hydrology and climate on glacial-interglacial timescales. Late Pleistocene glaciers were extensive in the Cordillera de Mérida, occupying ~200 km^2 (Schubert, 1984) compared with 3 km^2 today (Schubert and Fritz, 1985). Radiocarbon dates indicate that the Mérida Glaciation ended approximately 15,500 calendar y BP (Salgado-Labouriau et al., 1977). Palynologic evidence from Lake Valencia (situated at a low elevation east of the Cordillera de Mérida) suggests conditions were drier than present 15.6-12.0 ky BP (Bradbury et al., 1981; Curtis et al., 1999). Rapid filling of Lake Valencia 12.0-11.7 ky BP, indicating an increase in effective moisture, was

followed by relatively saline lake conditions until 9.7ky BP. Evidence from Lake Los Lirios in the Venezuelan Andes indicates very cold conditions 13.3-10.5 ky BP suggesting the increased moisture may have been associated with lower temperatures (Weingarten et al., 1991). In Lake Valencia, overflowing conditions with low salinity were established between 9.7-7.9 ky BP, but by 7.9-6.8ky BP low lake levels had returned. Lake Los Lirios shows warmer conditions during this interval (10.5-8.0 ky BP). In contrast, the pollen record from Laguna Mucubají, located at 3,500m a.s.l. in the Cordillera de Mérida, shows establishment of modern páramo vegetation occurring by 9.2 ky BP and relatively little change in the vegetation up to modern times (Salgado-Labouriau et al., 1992). Between 6.8-3.5ky BP Lake Valencia was overflowing and decreasingly saline. During this period peat deposits began to grow in the Guayana highlands (Schubert and Fritz, 1985) suggesting that this was a period of higher moisture balance throughout Venezuela. Lake Los Lirios indicates generally cooler conditions throughout this interval (8.0-2.8 ky BP). Between 3.5-0.5ky BP, Lake Valencia was still overflowing, but with increasing salinity. Warmer conditions prevailed in Lake Los Lirios between 2.8-2.0 ky BP with the establishment of modern conditions 2.0 ky BP. Rapid glacial retreat has occurred during the last 100 years, with three glaciers disappearing since 1972 (Abbott and Stafford, 1996).

Previous work on lake sediment records in the Venezuelan Andes (Weingarten et al., 1991; Salgado-Labouriau et al., 1992; Rull and Vegas-Vilarrúbia, 1993) has relied on palynology, clay mineralogy and the sedimentary geochemistry of iron and manganese from several locations to reconstruct climate. However these sites and/or proxies may not be sensitive to climate fluctuations during the Holocene. For example,

the only continuous Holocene pollen record comes from L. Mucubají and shows little regional changes in vegetation during the Holocene. However, the lake is currently located near the middle of the Páramo vegetation zone, thus relatively large fluctuations in the elevation of ecological zones may have occurred without any significant change in the pollen assemblage at L. Mucubají. Likewise, clay mineralogy and iron geochemistry may not be sensitive to climate fluctuation on shorter timescales such as the Holocene. As an additional note, the chronology for the previous research has relied on radiocarbon dating of bulk sediments. The organic carbon in sediments can represent a mixture of various sources and ages (Abbott and Stafford, 1996), thus bulk radiocarbon dates add an element of uncertainty to the reconstruction of past climate changes. In some of the lakes studied as part of this dissertation research, there are significant and variable differences between bulk and terrestrial macrofossil radiocarbon ages of up to several thousand years. These differences could lead to reconstruction of climate events with significant offsets from their true calendar age. Previous work in the Venezuelan Andes has provided a valuable contribution to our understanding of the regional climate history however there is a need for additional paleoclimate studies.

Figures

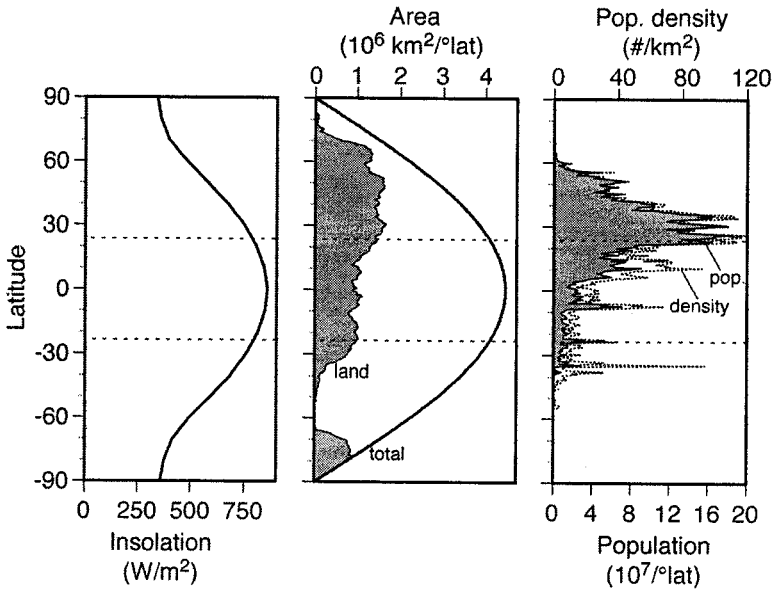

Figure 1.1 – Global distribution of annual average solar insolation, surface area and population by latitude. Population data is for 1995 (CIESIN et al., 2000). Horizontal dashed lines delimit the tropics.

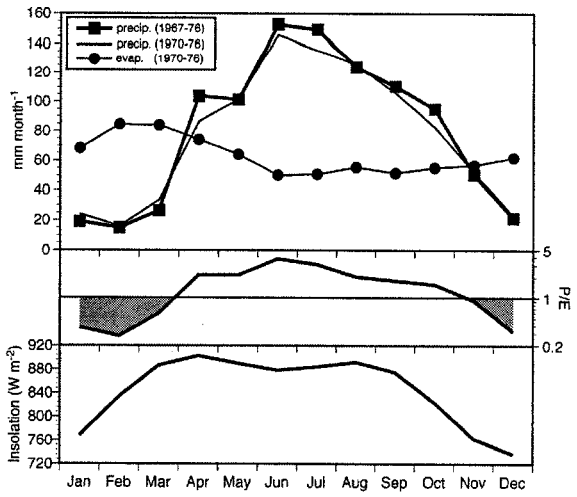

Figure 1.2 – Average monthly climatology of precipitation, evaporation, P/E balance and insolation for L. Mucubají. The precipitation climatology is calculated for the full record (1967-76) and for the period 1970-76 for comparison with the evaporation and P/E data. P/E (1970-76) is plotted on a log scale so that the magnitude of anomalies is linear above and below 1. Shown in the bottom panel are monthly values of potential insolation at 10°N (Berger and Loutre, 1991).

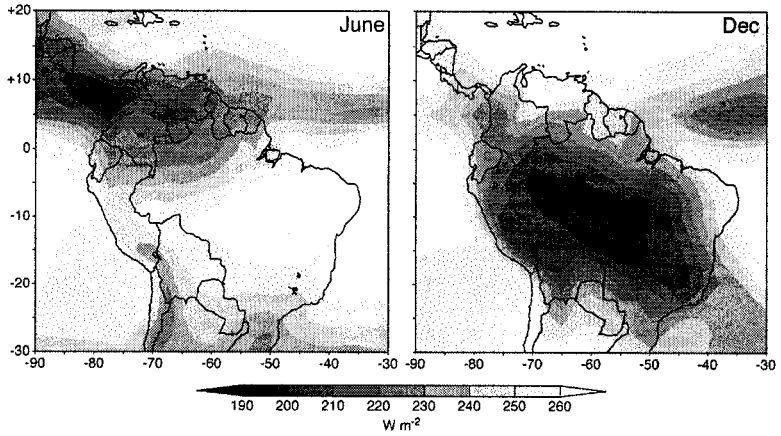

Figure 1.3 – Average monthly values of outgoing longwave radiation (OLR) over South America in June and December. Data is averaged from the period 1970 to 1995 (Liebmann and Smith, 1996). Regions of low OLR (dark) are indicative of cold cloud tops and deep convection. Image provided by the NOAA-CIRES Climate Diagnostics Center, Boulder Colorado from their web site at http://www.cdc.noaa.gov/.

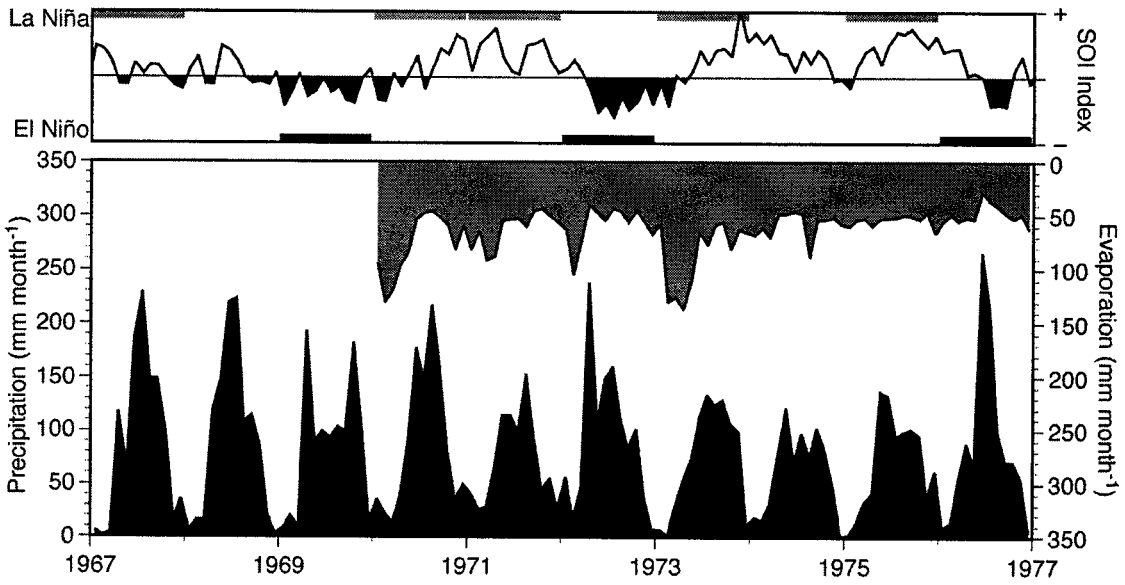

Figure 1.4 – Precipitation and evaporation at Laguna Mucubají, 1967 to 1976. Precipitation is shown in black and pan evaporation in gray (Azocar and Monasterio, 1980). Monthly southern oscillation index (SOI) values are plotted in the top panel along with El Niño and La Niña events.

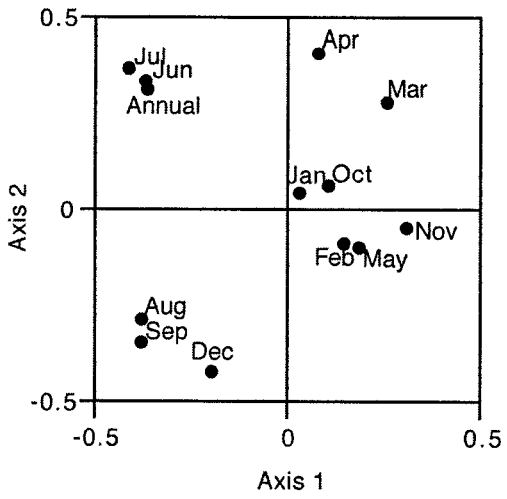

Figure 1.5 – Principle components analysis of monthly precipitation at Laguna Mucubají. Precipitation z-scores were calculated relative to monthly means for 1967-76. Axis 1 and 2 explain 25 and 21% of the total variance, respectively.

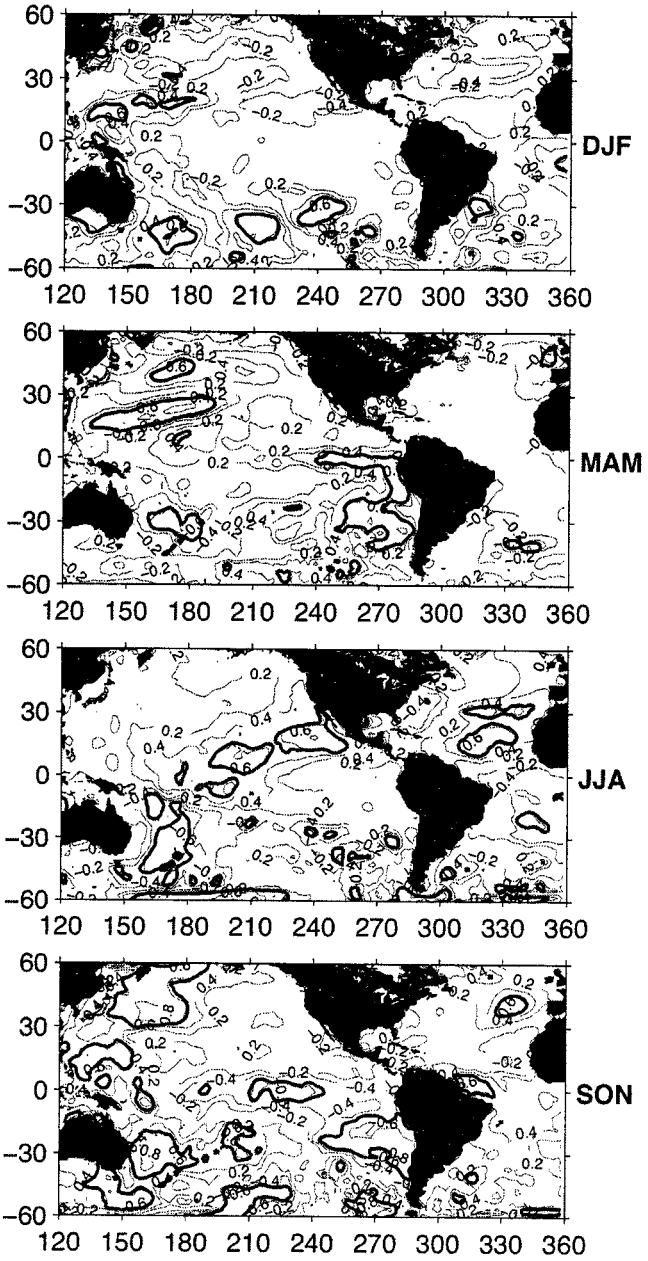

Figure 1.6 – Seasonal correlation between L. Mucubají precipitation and gridded SST for the period 1967-1976. Solid and dashed lines indicate positive and negative correlation, respectively. Heavy lines indicate areas of correlation above the 95 % confidence level (degrees of freedom are uncorrected for both spatial and temporal correlation). (Data provided by the NOAA-CIRES Climate Diagnostics Center, Boulder Colorado from their web site at http://www.cdc.noaa.gov/.

CHAPTER 2

SOLAR MODULATION OF LITTLE ICE AGE CLIMATE IN THE TROPICAL ANDES

Introduction

During the past millennium, significant climate fluctuations have occurred. Prominent among these is the Little Ice Age (LIA), recognized in historical records (e.g. Pfister, 1992) and documented in proxy climate records from many locations (Jones and Mann, 2004). Although the LIA was a significant global event (Mann et al., 1999), its causes and regional differences in the timing and climate response remain unclear (Crowley, 2000; Jones and Mann, 2004). This is particularly true in the tropics where well dated records with sufficient temporal resolution to resolve decadal changes in climate are sparse (Jones and Mann, 2004). Better knowledge of tropical climate during the LIA will help determine its causes and aid in the prediction of future climate change.

It is hypothesized that variations in the sun's energy output played a role in climate change during the LIA (Crowley, 2000). However, although the tropics receive 47% of the planetary insolation, their response to solar irradiance variability is uncertain. Here we present evidence that climate change in the Venezuelan Andes is linked to changes in solar activity during the LIA. Venezuela is situated near the northern limit of the annual migration of the intertropical convergence zone (ITCZ, Fig. 2.1). The annual displacement of the ITCZ between hemispheres leads to pronounced seasonality in rainfall at the latitudinal extremes of this migration. Thus, Venezuela is particularly sensitive to changes in the position and strength of the ITCZ (Enfield,

1996), which are expressed as changes in the amplitude of the annual cycle (Hastenrath, 1984). The annual cycle is a function of the intensity and zonal migration of maximum insolation receipts at the earth's surface. Therefore, variations in solar energy can be expected to cause changes in the strength of the ITCZ, leading to precipitation and temperature anomalies in Venezuela.

Tropical glaciers respond rapidly to precipitation and temperature variations, and hence are useful recorders of climate variability (Thompson et al., 1985; Kaser, 2001; Seltzer et al., 2002). In this study we use glacier fluctuations and paleoclimate records of precipitation and moisture balance to reconstruct Venezuelan climate during the past 1,500 y. Previous glacial geologic study in the Cordillera de Mérida, Venezuela indicates that glaciers were widespread during the Last Glacial Maximum and rapidly retreated at the beginning of the Holocene (Schubert, 1984; Stansell, 2005). During most of the past 10,000 years, glaciers were absent from all but the highest peaks in the Cordillera de Mérida (Stansell, 2005). Evidence for recent glacier advances comes from unweathered moraines and other glacial landforms. These features have been correlated with the LIA (Schubert, 1992), however, they have not been dated and thus the timing of recent advances remains unknown.

Here, we present continuous, decadal-scale, lake-sediment records of glacier activity and moisture balance in the Venezuelan Andes during the past 1,500 years. The continuous nature of the glacial record allows us to resolve multiple advances and determine the timing of these events. This represents a significant development over previous studies that have relied upon dating glacial landforms which represent a single point in the glaciers time-position map. Additionally, because glaciers are sensitive to

both temperature and precipitation changes, we have developed independent proxy records of precipitation and moisture balance that allow a more accurate determination of the climate during the LIA. Mapping of the paleoglacier and modeling of the glacier response to precipitation and temperature variations provides a quantitative estimate of the climate change during the LIA. Comparison of these glacier and climate records from Venezuela with regional and global proxy data as well as probable forcing variables allows us to infer potential causes for the glacier advances.

Materials and Methods

Study Sites

Sediment records from two watersheds were analyzed to reconstruct the timing of glacial advances and regional changes in precipitation/evaporation (P/E) balance for the past 1,500 years. Laguna Mucubají (Fig. 2.1) is situated in a north facing catchment with a maximum elevation of 4616 m. By comparison, the only four remaining glaciated peaks in Venezuela have elevations of 4979 m (Pico Bolívar), 4922 m (Pico La Concha), 4942 m (Pico Humboldt) and 4883 m (Pico Bonpland). Establishment of glaciers in the L. Mucubají watershed increased the flux of inorganic sediment to the lake, producing a continuous record of glacier activity. We corroborate climate changes during glacial advances with sediments from Laguna Blanca (Fig. 2.1), a small, closed-basin lake at 1620 m in unglaciated terrain. During wet periods the transport of inorganic material to the lake is increased, leading to higher concentrations in the sediments compared with drier periods. The records of glacier activity and climate change are also compared with nearby pollen records of floristic changes which document greater moisture and lowering of tree line during the LIA (Rull et al., 1987).

Sediment Chronology

In 1999 we recovered sediment cores from Lagunas Mucubají and Blanca using percussion and square-rod coring systems (Wright et al., 1984). Duplicate cores and undisturbed sediment/water interface cores were retrieved from L. Mucubají and the interface core was extruded at 0.5 cm interval in the field. A composite sediment record for L. Mucubají was constructed from the two long cores and the interface core by matching visual stratigraphy and variations in volume magnetic susceptibility, total organic carbon (TOC), total nitrogen (TN), $\delta^{13}C_{TOC}$, $\delta^{15}N_{TN}$ and C/N ratios. A composite sediment record for L. Blanca was developed by matching visual stratigraphy and variations of TOC, magnetic susceptibility and bulk density between sediment sections.

Accelerator mass-spectrometry radiocarbon dates and excess ^{210}Pb profiles constrain the age-depth relationship for the cores. Excess ^{210}Pb profiles were converted to calendar ages using the constant rate of supply model (Appleby and Oldfield, 1978) and the 1964 ^{137}Cs nuclear testing peak. Radiocarbon ages were converted to calendar ages using the CALIB 4.2 dataset (Table 2.1, Stuiver et al., 1998a; Stuiver et al., 1998b). Age models (Fig. 2.2) were constructed with polynomial spline curves to interpolate ages between radiocarbon dates. A single radiocarbon date at 72.5 cm in L. Mucubají was excluded from the age-depth model because it produced sedimentation rates which were anomalous in the context of the complete 8000 y record.

Sediment Geochemistry

Clastic material represents the non-biogenic component of sediments and can be used as an indicator of sediment supply from the catchment. In Laguna Mucubají,

clastic sediment content was calculated as the total minus the sum of biogenic silica and organic matter content (no carbonates were present in these sediments). Biogenic silica was analyzed by time-dissolution experiments (DeMaster, 1979; DeMaster, 1981) following the recommendations of (Conley, 1998). Dissolved silica from the dissolution experiments was determined by ICP-AES (Carter and Colman, 1994). Total organic carbon (TOC) was measured with a Carlo-Erba CHNS elemental analyzer connected via a ConFlo-II interface to a Finnegan MAT 252 mass-spectrometer. Total organic matter (TOM) was calculated as 2.05*TOC based upon 8 samples where TOM was measured by loss-on-ignition (Dean Jr., 1974; Heiri et al., 2001) and compared with TOC values. In cores from both Lagunas Blanca and Mucubají, magnetic susceptibility (MS) was measured on sediment immediately after splitting the cores using a Tamiscan automated sediment track and a Bartington high resolution surface scanning sensor connected to a Bartington susceptibility meter.

Glacier Reconstruction

We use the equilibrium line altitude (ELA, the elevation of the dividing line between the glacier accumulation and ablation areas) as a climatically-sensitive measure to document variations in glacier extent. The Mucubají valley paleoglacier ELA was calculated by reconstructing the glacier topography and applying the accumulation area ratio (AAR) method (Meirding, 1982). Glacier topography was reconstructed by defining the glacial limits, calculating ice thickness along the glacier centerline and contouring the glacier surface. Glacier limits were drawn from field data, visual observations of aerial photographs and 1:24,000 topographic maps. The glacier centerline was then defined by connecting the lowest points in topographic cross-

sections of the glacier area. The surface slope along the glacier centerline was reconstructed assuming a basal shear stress (τ_b) of 100 kPa (Paterson, 1981). (Alternate constructions with τ_b=50 and 150 kPa did not alter the contours significantly.) The surface slope was then integrated along the glacier centerline, starting at the glacier terminus, to give the ice elevation. The glacier surface was contoured by connecting reconstructed centerline elevations and bedrock contour lines at the glacier margin. A hypsometric curve of glacier area vs. elevation was then developed from the contour plot and used to construct a normalized cumulative area versus elevation profile. If the glacier accumulation area ratio (AAR, the ratio of accumulation area to total glacier area) is known, these profiles can be used to determine the ELA. For comparison with the Mucubají paleo-ELA, the ELA of modern glaciers in the Cordillera de Mérida was determined by constructing cumulative elevation profiles from the maps of (Schubert, 1972).

Results and Discussion

Chronology of Glacial Advances

Increased catchment glacierization enhances clastic sedimentation in proglacial lakes, leading to higher concentrations of fine-grained magnetic minerals that can be identified visually by color changes and quantified by MS measurements (Rosqvist, 1995; Seltzer et al., 2002). In L. Mucubají, the clastic sediment concentration is significantly correlated with the MS of the sediment throughout the past 6000 years (r=0.74 p<0.0001) and yields a high-resolution record of clastic sediment concentration (continuous 0.25 cm samples representing 2 to 6 years per sample). The MS record has low values prior to 1150 A.D., followed by four peaks (1180 to 1350, 1450 to 1590,

1640 to 1730 and 1800 to 1820 A.D.) and decreasing values from 1820 A.D. to the present (Fig. 2.3A). The onset and cessation of recent glacial activity in L. Mucubají (1180 and 1820 A.D., respectively) occurs at a similar time to other late Neoglacial advances and retreats throughout the South American Andes (Seltzer, 1990; Rosqvist, 1995; Glasser et al., 2002) and corresponds to the Andean expression of the LIA. The peaks and troughs in the susceptibility records match fluctuations of solar irradiance reconstructed from ^{10}Be (Bard et al., 2000) and Δ^{14}C (Stuiver et al., 1998a) measurements (Fig. 2.3E). Spectral analysis shows significant peaks at 227 and 125 years in both the irradiance and MS records, closely matching the de Vreis and Gleissberg oscillations identified from solar irradiance reconstructions. The LIA period in Mucubají occurs during an extended interval of low solar activity (Bond et al., 2001; Solanki et al., 2004) which likely promoted the growth of permanent ice in the watershed. Based upon the L. Mucubají sediment record, the establishment of an active glacier occurred around 1150 A.D. The lack of sediment MS response to the irradiance minima at 750 and 1050 A.D. is likely attributed to the absence of an active glacier in the watershed.

Although the shielding effect of volcanic aerosols may have contributed to glacier growth, it is difficult to differentiate the effects of solar and volcanic forcing because they are correlated during the past 1000 y (Crowley, 2000). However solar and volcanic forcing are uncorrelated between 1500 and 1650 A.D. and the magnetic susceptibility record follows the solar irradiance reconstruction during this interval (Fig. 2.3F). This suggests solar forcing is the principal cause of variations in glacier activity during the LIA.

Climatic Inferences from Glaciers

The response of glaciers to both temperature and precipitation changes must be assessed to fully interpret the glacial record (Kaser, 2001). This is accomplished by reconstructing changes in glacial extent and then calculating the temperature and precipitation changes needed to support the new glacier size. Figure 2.4 shows the modern and reconstructed LIA glacier extent. From these maps, cumulative area-elevation curves for the LIA and modern glaciers were developed (Fig. 2.5A). The vertical difference between these curves, a measure of the LIA-modern ELA depression (ΔELA), is shown in Fig. 2.5B. Theoretical AAR values for tropical glaciers are ~0.82 (Kaser and Osmaston, 2002) while an average AAR from 78 modern tropical glaciers is 0.69 (Klein et al., 1999). The ΔELA does not change significantly with the AAR, thus values of 0.69 to 0.82 give an estimated ΔELA of around -300 m. However, modern glaciers on Pico Bolívar have been rapidly retreating since at least 1870 A.D. (Schubert, 1992), thus -300 m represents a minimum estimate of the ΔELA. Accelerated melting since 1972 A.D. has caused two glaciers to disappear completely (Schubert, 1992) suggesting late 20th century ELAs are actually nearer to the elevation of Pico Bolívar (4979 m) and the ΔELA may be as much as –500 m.

The temperature and precipitation changes associated with this ELA lowering can be calculated by combining equations for the mass and heat balances of a glacier. This method is more accurate than simply multiplying the atmospheric lapse rate by the change in ELA because the elevation gradients of precipitation and humidity cause changes in the sensible and latent heat transfers at the glacier surface and affect the magnitude of the estimated temperature depression. The relationship between

temperature depression, precipitation and ELA lowering was calculated using the combined energy-balance and mass-balance model of (Kuhn, 1989) after (Seltzer, 1992). Vertical gradients in temperature, atmospheric humidity and precipitation were calculated from data in Bradley et al. (1991), Kalnay et al. (1996) and Pulwarty (1998) respectively. Transfer coefficients for sensible and latent heat are from Kuhn (1989). The uncertainty in the temperature estimate is largely related to uncertainty in the estimated ELA depression. This method suggests that an ELA lowering of -300 to -500 m is equivalent to a temperature depression of 2.6 to 4.3° C using the modern annual precipitation of 950 mm (Fig. 2.6).

Pollen evidence from two nearby sites (Fig. 2.1) documents the expansion of the superpáramo (alpine tundra) ecotone and a lowering of tree-line by 200 m during the glacial advances in L. Mucubají (Fig. 2.3C, Rull et al., 1987). The temperature and precipitation change associated with tree-line movement is calculated from the climatology at the modern forest/sub-páramo ecological boundary and the vertical gradients of temperature and precipitation. The effect of precipitation on the forest/sub-páramo ecological boundary can be estimated from modern climate data. Compared to the NW slopes of the Venezuelan Andes the modern forest/sub-páramo ecological boundary is higher on SE-facing slopes, with a mean annual temperature that is 2.9 °C lower. This is primarily a function of the precipitation difference between the slopes (+1225 mm y^{-1}) and provides an estimate of the effect precipitation has on the temperature of the forest/sub-páramo boundary ($k = -0.0024$ °C y mm^{-1}). Thus, the temperature (T) and precipitation (P) combinations which define the modern and LIA forest/sub-páramo boundary are:

Eq. 2.1 $$T_m - k \cdot P_m = T_{LIA} - k \cdot P_{LIA}$$

The temperature depression during the LIA can then be written as:

Eq. 2.2 $$T_{LIA} - T_m = k \cdot (P_{LIA} - P_m)$$

This equation can be re-written to include a change in the elevation of the forest/sub-páramo boundary (Δz) using the vertical gradients in P and T and solved for the temperature change (ΔT):

Eq. 2.3 $$\Delta T_{LIA-M} = k\Delta P_{LIA-M} + \Delta z\left(k\frac{\partial P}{\partial z} - \frac{\partial T}{\partial z}\right)$$

Eq. 2.3 gives the relationship between precipitation and temperature change when the elevation shift of the forest/sub-páramo boundary is known. Vertical gradients in temperature and precipitation were calculated from data in (Bradley et al., 1991) and (Pulwarty et al., 1998) respectively and used to determine the climate changes associated with the 200 m lowering of the forest/sub-páramo boundary during the LIA. The intersection of the ELA and pollen estimates indicate that during the Little Ice Age the Venezuelan Andes were both cooler (-2.3 to –3.4° C) and wetter (+230 to +680 mm y^{-1}, +25 to +73 %) than present (Fig. 2.6).

Our reconstructed LIA temperature depression in the high altitudes of the Venezuelan Andes is greater than that inferred for Caribbean sea-surface temperatures (~2° C, Winter et al., 2000; Watanabe et al., 2001; Nyberg et al., 2002). This is likely a consequence of changes in adiabatic lapse rates due to cooling. Cooler tropical SST's would reduce the absolute humidity of the lower troposphere and steepen the slope of the moist adiabat above the condensation level. This would lead to cooling at 4500 m a.s.l. which was ~1.5 times that at sea-level, in agreement with our glacier and pollen temperature estimates (Fig. 2.7).

Sediment Record of Moisture Balance

Laguna Blanca (Fig. 2.1) contains a non-glacial record of catchment erosion associated with increased precipitation. The MS of the sediments reveals a low concentration of clastic sediment prior to 1250 followed by high values 1300 to 1550, 1640 to1710, 1730 to 1750, 1780 to 1790, and 1795 to 1820 A.D (Fig 2B). These peaks indicate greater precipitation and erosion during the glacial advances identified in L. Mucubají. The wetter conditions during the LIA inferred from the sediment record at the non-glacial L. Blanca site verifies that the change in climate that caused renewed glacial activity in the Mucubají valley was not only a response to lower temperatures. This conclusion is also supported by higher abundances of Cyperaceae (sedge) pollen in a nearby peat bog (Fig. 2.1) during the glacial period. Maxima of Cyperaceae occur during glacial advances (Fig. 2.3D, Rull et al., 1987) indicating a marshy environment, corroborating the L. Blanca MS record and supporting the moisture changes inferred from the ELA reconstruction.

Intuitively it would seem that cooler temperatures and lower absolute humidity would lead to less precipitation in the Venezuelan Andes during the LIA. However, this view may be reconciled with the paleoclimate data for increased precipitation in the Venezuelan Andes by recognizing that it is the transport of moisture to high elevations, which most likely controls the precipitation amount as has been clearly documented for the Bolivian/Peruvian Andes (Garreaud, 2000). During the LIA, a steeper latitudinal temperature gradient induced stronger easterly trade-winds (Black et al., 1999) which may have actually enhanced the transport of moisture to the Venezuelan Andes. Thus,

greater moisture flux may have more than compensated for the reduced atmospheric water vapor concentration.

Paleoclimate records from other tropical sites support our interpretation of the glacier and sedimentary records in Venezuela. P/E changes on the Yucatan Peninsula, Mexico are coherent with solar irradiance over the past two millennia (Fig. 2.3G, Hodell et al., 2001). Trade-wind strength off the Venezuelan coast was also higher during solar minima (Fig. 2.3H, Black et al., 1999). These changes are in phase with the Venezuelan records indicating the P/E shifts were geographically extensive, involving both the ITCZ and subtropical high pressure.

A notable exception to the regional picture of wetter LIA conditions in northern South America is the record of terrigenous sediment input to the Cariaco Basin (Haug et al., 2001). Lower concentrations of titanium were found in Cariaco sediments during the LIA, suggesting decreased terrestrial sediment delivery to the basin. One possible explanation for this difference is an antiphasing of precipitation between the coastal Venezuela (near the Cariaco Basin) and the Venezuelan Andes. For example, 20th century Venezuelan climate records show that rainy-season precipitation anomalies have opposite signs in coastal and Andean regions (Pulwarty et al., 1992). This suggests the possibility that, during the LIA, positive rainfall anomalies in the Andes were accompanied by negative anomalies in coastal drainages entering the Cariaco Basin. Alternately, catchments draining the Venezuelan Andes may not directly influence the sedimentology of the Cariaco Basin, as they are either filtered by Laguna Maracaibo, or drain to the Orinoco River.

Conclusions

The data presented here suggest that solar activity has exerted a dominant control on century-scale tropical climate variability, modulating both precipitation and temperature. Surface cooling is enhanced at high altitudes by feedbacks involving water vapor, ultimately depressing temperatures in the Venezuelan Andes by 2.3° to 3.4° C during the LIA. It is likely that this mechanism may also serve to amplify the effects of warming trends, irrespective of their origin, which raises concern that global warming will adversely affect high-altitude tropical montane regions (Bradley et al., 2004). Supporting this concern, 20th century temperature increases have raised the ELAs of tropical glaciers leading to accelerated ablation and disappearance in many cases (Hastenrath and Kruss, 1992; Schubert, 1992; Kaser, 1999; Ramirez et al., 2001). We have demonstrated considerable sensitivity of tropical climate to small changes in globally averaged radiative forcing from solar irradiance variability. Conservative estimates of net anthropogenic greenhouse-gas radiative forcing during the next 50 y are equal or greater than the solar forcing in previous centuries (Hansen et al., 2000), implying that profound climate impacts can be predicted for tropical montane regions.

Tables

Table 2.1 – Accelerator mass spectrometry radiocarbon ages on L. Mucubají and L. Blanca sediments.

Lab Code*	Lake	Core	Material	Composite Depth (cm)	^{14}C Age (y A.D.)	1σ calibrated age ranges (y A.D.)
CAMS-96809	L. Mucubají	99A	wood	44.5	1620±40	1495 to 1500, 1508 to 1532, 1541 to 1600, 1614 to 1636
AA-35204	L. Mucubají	99C	aq macro†	54.2	1315±45	1299 to 1325, 1349 to 1391
CURL-4959	L. Mucubají	99C	aq macro	66.2	770±30	782 to 791, 809 to 845, 846 to 891
CAMS-96810	L. Mucubají	99A	aq macro	72.5	585±30	645 to 685‡
CURL-4960	L. Mucubají	99C	aq macro	85.8	-160±35	-194 to -193, -172 to -89, -74 to -59
CURL-4973	L. Blanca	99A	wood	64.5	1820±35	1679 to 1708, 1719 to 1739, 1805 to 1822, 1827 to 1885, 1912 to 1935
CURL-4974	L. Blanca	99A	leaf	103.5	1290±35	1290 to 1312, 1354 to 1387
CAMS-73134	L. Blanca	99A	wood	123.5	970±40	1002 to 1012, 1016 to 1045, 1088 to 1121
CAMS-96802	L. Blanca	99A	wood	188.6	-170±35	-197 to -187, -180 to -91

* CAMS, Center for Accelerator Mass Spectrometry, Lawrence Livermore National Labs;
AA, Accelerator Mass Spectrometry Lab, University of Arizona;
CURL, National Ocean Sciences Accelerator Mass Spectrometry Facility, Woods Hole Oceanographic Institute

† aquatic macrophyte

‡ not included in age model

Figures

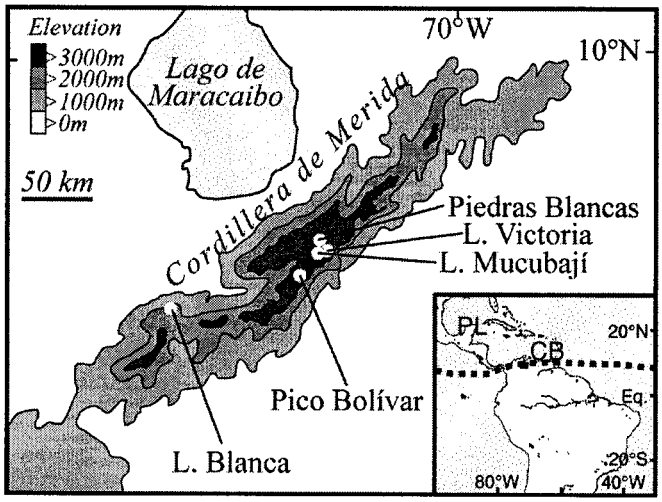

Figure 2.1- Map showing the location of L. Mucubají, L. Blanca and other locations mentioned in the text. L. Mucubají (8° 47'N, 70° 50'W, 3570 m a.s.l.); L. Blanca (8° 20'N, 71° 47'W, 1620 m a.s.l.); Punta Laguna, Mexico (PL); Cariaco Basin (CB). Pollen records are from the Piedras Blancas peat bog and L. Victoria (15 and 1 km from L. Mucubají respectively). The dashed line on the inset map shows the approximate position of the intertropical convergence zone during the northern hemisphere summer.

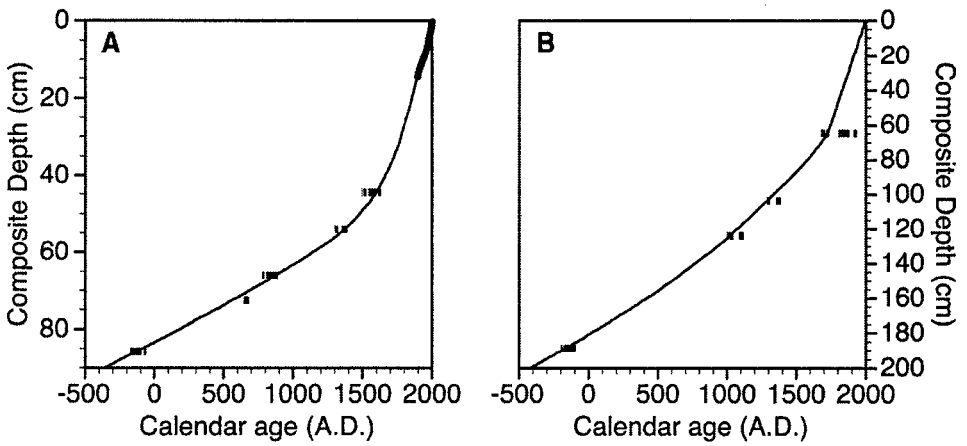

Figure 2.2- Age-depth curves for Laguna Mucubají and Laguna Blanca. Laguna Mucubají is shown in (A) and Laguna Blanca in (B). Calibrated 1 σ radiocarbon age ranges are indicated by the horizontal bars. The thick black line in (A) represents ^{210}Pb ages.

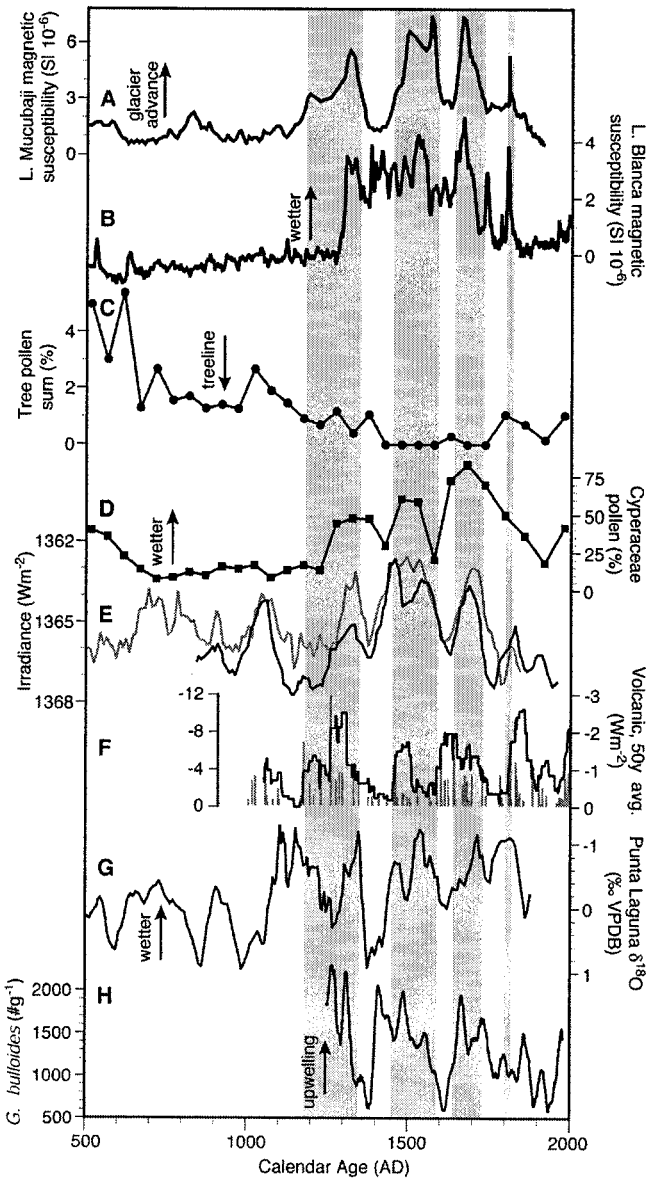

Figure 2.3 – Lake sediment records from the Venezuelan Andes compared with indices of solar activity and additional tropical paleoclimate proxies. Glacial advances, indicated by increases of sediment magnetic susceptibility in L. Mucubají (A, vertical gray shading) coincide with an increase in precipitation, shown by higher magnetic susceptibility in L. Blanca (B) and higher abundances of Cyperaceae (sedge) pollen in the Piedras Blancas peat bog located near to L. Mucubají (D, Rull et al., 1987). Decreased abundance of tree pollen (C, sum of *Podocarpus* and *Hedyosmum*, the best indicators of tree-line in the Venezuelan Andes) indicate lowering of ecological zones and colder/wetter climate during glacial advances. The tree pollen decrease lags the onset of glacial activity in L. Mucubají and does not increase between glacial advances because tree-line position involves plant community changes which occur on timescales longer than individual glacial advances. (E) Minima in reconstructed solar irradiance (black line, Bard et al., 2000) using the scaling of (Lean et al., 1995) or maxima in $\Delta^{14}C$ (gray line, inverted scale, Stuiver et al., 1998a) are coeval with glacier advances. The

$\Delta^{14}C$ record reflects solar modulation of the ^{14}C production rate and is scaled to the reconstructed irradiance curve of Bard (2000). (F) Annual record of latitude weighted volcanic aerosol forcing (gray bars and left scale, Crowley, 2000) and 50 y averages (line and right scale, multiplied by four to scale with the reconstructed solar irradiance and plotted at youngest age of the 50 y window). Wetter conditions are supported by the Punta Laguna, Mexico $\delta^{18}O$ record of higher P/E during Mucubají glacial advances (G, Hodell et al., 2001). Abundances of the foraminifer *G. bulloides* in Cariaco basin sediments (H) are higher during glacial advances indicating stronger trade winds (Black et al., 1999).

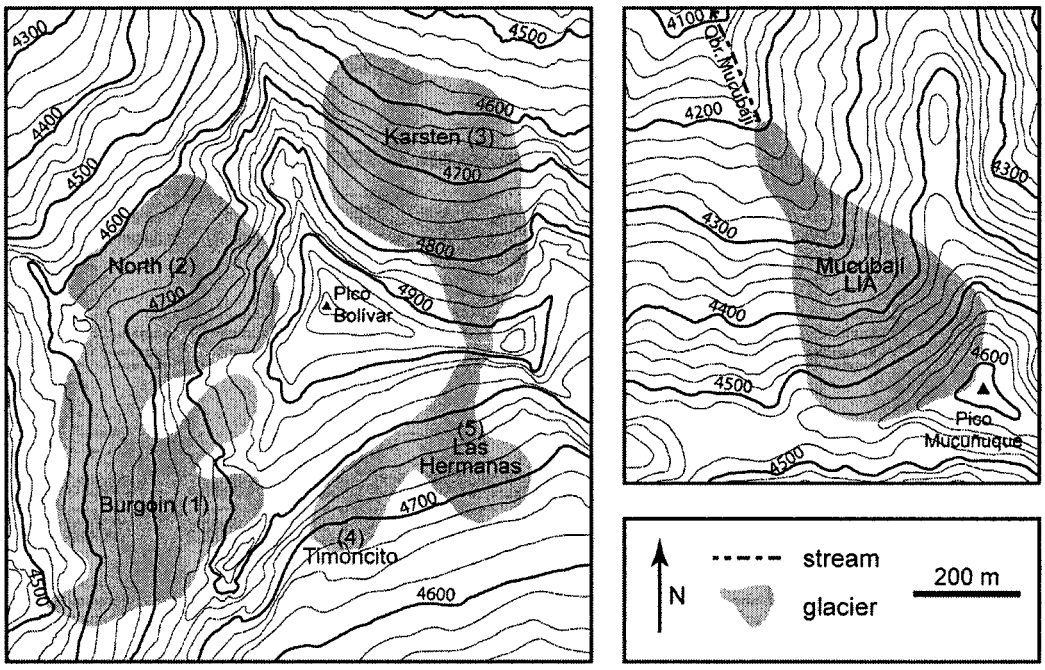

Figure 2.4 – Maps of modern glaciers on Pico Bolívar and the reconstructed LIA glacier in the Mucubají watershed. The modern glaciers are from mapping by (Schubert, 1972) and represent the glacier extent *circa* 1972 A.D. Accelerated melting since 1972 have caused Las Hermanas and Timoncito glaciers to disappear completely (Schubert, 1992).

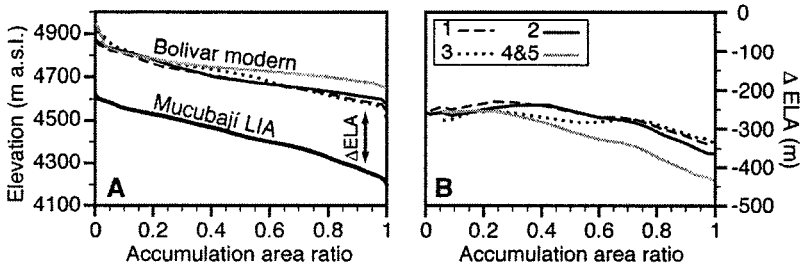

Figure 2.5 – Altitude profiles of normalized cumulative glacier area (accumulation area ratio, AAR) for the Mucubají LIA glacier and modern glaciers on Pico Bolívar. Numbers refer to different glaciers on Pico Bolívar, glaciers 2 and 3 are the best comparison with the Mucubají glacier because these cirques have aspects and morphologies similar to the Mucubají cirque. The ELA depression (ΔELA) of the LIA glacier from the modern glaciers on Pico Bolívar(B) is the difference between the AAR profiles of the Mucubají and modern glaciers in (A).

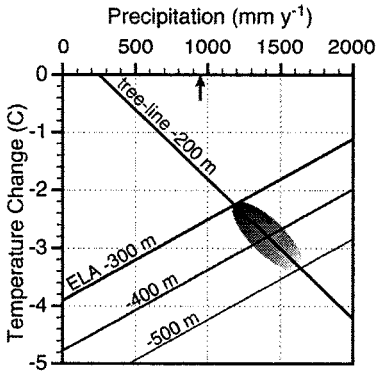

Figure 2.6 - Relationship between temperature change and precipitation in the Venezuelan Andes during the LIA from glacier ELA and pollen data. The small arrow indicates the modern precipitation amount. The intersection of ELA and tree-line estimates (gray ellipse) indicate the LIA was at least –2.3° C (-300 m) and more probably –2.8 to –3.4° C cooler (-400 to –500 m) and wetter by 230 mm y^{-1} to 680 mm y^{-1} precipitation.

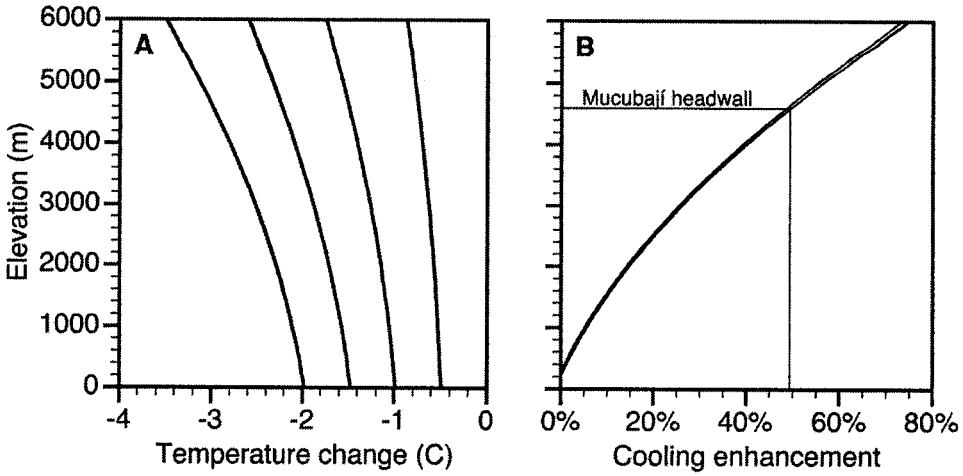

Figure 2.7 - Vertical profiles of temperature change and enhancement of surface cooling at high elevations. Vertical temperature profiles were calculated using standard meteorological formulae and a surface relative humidity of 80%. Temperature change (A) is the difference from the 26° C surface temperature vertical profile. Average tropical Atlantic surface temperature and humidity are 26° C, 80% (Kalnay et al., 1996). The cooling enhancement is the magnitude of the temperature change at a given altitude divided by the temperature change at sea level. Cooling enhancement is independent of the magnitude of the temperature change (overlapping curves in B are for the -0.5 to -2.0° C temperatures changes plotted in A).

CHAPTER 3

LAKE RECORDS OF HOLOCENE CLIMATE IN THE TROPICAL ANDES, VENEZUELA

Introduction

The tropics are an important component of the climate system. They cover 40% of the earth, receive 48% of the earth's potential insolation and export heat and moisture to the extratropics. Despite their importance, we still do not fully understand all the variables which control tropical climate at different timescales. At periods of 10^4 to 10^5 years, significant tropical cooling and regional changes in the precipitation/evaporation balance (P/E) have accompanied the growth and decay of high-latitude ice sheets. In contrast, interannual to decadal climate variability such as the El Niño-Southern Oscillation has a large effect on extratropical climate (Ropelewski and Halpert, 1987). At intermediate periods of 10^2 to 10^3 years, the cause of tropical climate variability and the extratropical influences are less clear. These timescales encompass changes in solar irradiance and insolation forcing which might directly affect tropical climate. However, the extra-tropical response to the same forcings may also impact tropical climate. Variation at these (and greater) timescales extends beyond the period of instrumental measurement. Thus, proxy records of climate are essential to understand the variables which control tropical climate and the interaction of the tropics with higher latitudes.

Atmospheric circulation in the tropics is driven by the annual cycle of solar insolation. Maximum heating of the earth surface at the latitude of solar declination leads to wind convergence, uplift, low pressure and precipitation. Annual migration of this band of low pressure (the intertropical convergence zone or ITCZ) leads to

pronounced wet and dry cycles which define the tropical seasons. Because solar heating drives tropical circulation, it is a logical step to hypothesize that variations in the amount and seasonality of solar insolation could change tropical climate. Extensive work in the southern hemisphere tropical Andes has documented a pattern of humid and arid intervals during the past 10 ka. The timing of these wet and dry periods matches predictions based upon orbitally driven variations of solar insolation (e.g. Abbott et al., 1997; Thompson et al., 1998; Seltzer et al., 2000; Baker et al., 2001a; Abbott et al., 2003), and bolsters the idea that direct insolation forcing of tropical climate is the dominant factor on millennial timescales.

Direct insolation forcing should produce climate changes in the northern and southern hemispheres which are opposite in sign but occur at similar times. Thus, comparison between records north and south of the equator provides a natural test of the direct insolation hypothesis. Climate reconstructions from the northern neotropics are equivocal in their support of direct insolation forcing. Some records agree with insolation predictions (Hodell et al., 1991; Hodell et al., 1995; Haug et al., 2001), while others do not show the expected pattern (Bush et al., 1992; Hughen et al., 1996; Curtis et al., 1999; Vélez et al., 2003). These differences could result from uncertainties in the chronology of different records (unlikely), changes in the proxy-climate relationship through time (possibly), and/or regional complexity in the patterns of climate change (likely).

The goal of this paper is to add to our knowledge of the tropics by reconstructing climate variability in northern South America. Multiproxy climate records from lakes in the Venezuelan Andes were developed to better understand the

spatial pattern of climate change in the northern neotropics. The wet season in Venezuela occurs during boreal summer when the ITCZ is at the northern limit of its annual migration. Thus, the study location is particularly sensitive to changes in the position and strength of the ITCZ (Enfield, 1996), and inter-annual climate variability is related to the strength of the annual cycle (Hastenrath, 1984). In turn, the annual cycle is a function of the intensity and zonal migration of maximum insolation receipts at the earth's surface. Therefore, variations in solar energy are expected to cause changes in the strength of the ITCZ, leading to precipitation and temperature anomalies at the study location. The sites chosen for study are high-altitude and have similar atmospheric circulation and physiographic settings to locations in the southern hemisphere Andes, allowing comparison with these records. Focusing upon the past 10 ka removes the effects of the large continental ice sheets and sea-level changes on the climate record. Thus, orbitally-induced insolation changes are the largest external factor affecting climate during the study interval.

Study Sites

Laguna Blanca is a small shallow lake in Venezuelan Andes (Table 3.1, Fig. 3.1). The lake water is acidic, moderately conductive and anoxic within 0.5 m of the sediment/water interface. The lake has no surface inflow and lake level is currently greater than 5 m below a dry outflow channel. The watershed is forested and contains a dry lake which would drain into L. Blanca during very wet intervals. The stable oxygen and hydrogen isotopes of the lake water are significantly enriched relative to modern precipitation and groundwater, and lie on an evaporation trend distinct from the local and global meteoric water line (Table 3.1). The low watershed/lake area ratio, lack of

surface outflow and enriched lakewater isotopes indicate the lake is hydrologically closed and loses most inflow waters via evaporation.

Lagunas Verdes Alta (LVA) and Baja (LVB) are small lateral-moraine dammed lakes in the Venezuelan Andes (Table 3.1, Fig. 3.1). The watersheds of both lakes are steep, small and covered by bare rock, wet soil and dry Páramo vegetation. Both lakes are currently fed by groundwater although during exceptionally wet periods LVB may receive some water from L. Verdes Medio (located between LVA and LVB; Fig. 3.1). LVA has a small outflow stream while LVB has no surface outflow and the watershed/lake area ratio is higher in LVA than LVB (Table 3.1). Isotopic analyses of modern lake waters show that both lakes fall along an evaporative trend distinct from the meteoric water line with LVB significantly more enriched than LVA. This indicates that LVA is hydrologically open with minimal evaporative water loss while LVB is hydrologically closed and evaporation is a significant component of the water balance. The proximity of LVA to LVB (<500m) means that they have similar input waters, climates (humidity, temperature, wind speed) and thermal regimes and differ only in their hydrologic balance.

Methods

Coring and Chronology

In 1999 we recovered sediment cores from Laguna Blanca, LVA and LVB using a square-rod coring system (Wright et al., 1984). Duplicate cores or a single core with overlapping drives were retrieved from each lake to prevent gaps in core recovery. Undisturbed sediment/water interface cores were retrieved from LVA and LVB and extruded and sectioned in the field due to their unconsolidated consistency. Composite

sediment records for each lake were constructed from the long cores and interface cores by matching the visual stratigraphy and variations in volume magnetic susceptibility, bulk density, total organic carbon (TOC), total nitrogen (TN), $\delta^{13}C_{TOC}$, $\delta^{15}N_{TN}$ and C/N ratios.

Accelerator mass-spectrometry (AMS) radiocarbon dates (all lakes) and excess ^{210}Pb profiles (LVA) constrain the age-depth relationship for the cores. Excess ^{210}Pb profiles were converted to calendar ages using the constant rate of supply model (CRS) and the 1964 ^{137}Cs nuclear testing peak. Radiocarbon ages were converted to calendar ages using the CALIB 4.2 dataset (Table 3.2, Stuiver et al., 1998a; Stuiver et al., 1998b). All ages in the text are in calendar years BP unless specifically noted. Age models (Fig. 3.2) were constructed using a polynomial spline between the midpoint of the ^{14}C calibration age ranges with the largest relative area under the probability distribution. Because LVB lacked macrofossil material for ^{14}C dating at most sediment levels, ages were calculated using the sediment mass accumulation rate and tie points to the LVA record as additional constraints. Plotting accumulated sediment mass versus calendar age yields a linear relationship for the past 10,000 years which gives a better estimate of sediment age for LVB than simple interpolation by depth.

Sediment properties and geochemistry

Immediately after opening cores, 1 cm^3 samples for sediment density were removed and stored at 4° C. Density samples were dried at 60° C for 24 h and weighed to determine dry density. Volume magnetic susceptibility (MS) was measured at 0.25 cm intervals on split cores using a Tamiscan automated sediment track and a Bartington high resolution surface scanning sensor connected to a Bartington susceptibility meter

(reported in 10^{-6} SI units). Total organic matter (TOM) and carbonate content were measured by loss-on-ignition at 550° C and 1000° C (Dean Jr., 1974; Heiri et al., 2001). Calculated carbonate contents were very low (maximum 5 wt. % with average values below 2 wt. %) and thus LOI_{1000} represent water loss from clay minerals rather than CO_2 loss from carbonate minerals. This inference is supported by the absence of CO_2 evolution when sediments were treated with concentrated nitric acid during preparation of diatom slides.

Total organic carbon (TOC), total nitrogen (TN) and $\delta^{13}C_{TOC}$ and $\delta^{15}N_{TN}$ were measured with a Carlo-Erba CHNS elemental analyzer connected via a ConFlo-II interface to a Finnegan MAT 252 mass-spectrometer. Sediments were acid treated to remove carbonates prior to analysis. Total organic matter was calculated from TOC measurements based on the ratio of TOM/TOC. This ratio was calculated using a subset of samples from each core where TOM and TOC were measured on aliquots of the same sample. The TOM/TOC ratios were generally ~2.

Diatoms

Species abundance

Sediment samples for diatom species analysis (10-100 mg dry weight) were freeze dried and organic matter was removed by reaction with hot concentrated nitric acid and 40% hydrogen peroxide. Diluted aliquots of the digested sediments were dried onto glass coverslips and mounted to slides with Naphrax©. Diatoms were counted at 1000x magnification using oil immersion lenses on an Olympus research microscope equipped with differential interference contrast optics. At least 400 valves were counted on transects which started at the N, S, E or W edge and ended at the center of

the coverslip. Diatom counts were tallied using the program MacCount v2.42 (Johnson, 1998).

Species identification was based upon examination of valves at 1000x magnification and was supplemented by scanning electron microscopy of selected samples. The taxonomy of South American diatoms is not particularly well-described although several recent publications have begun to fill the void (Lange-Bertalot, 1998). The primary texts used for taxonomic identification were descriptions of the North American (Patrick and Reimer, 1966; Patrick and Reimer, 1975) and European flora (Krammer and Lange-Bertalot, 1986; Krammer and Lange-Bertalot, 1988; Krammer and Lange-Bertalot, 1991a; Krammer and Lange-Bertalot, 1991b). These works were supplemented by descriptions of the diatom flora of lowland tropical south America (Lange-Bertalot, 1998). Appendix A lists all species identified in modern and core sediments.

The relative frequencies of diatoms from modern and fossil sediments of Laguna Verdes Alta, Verdes Baja and five other high altitude Venezuelan lakes were analyzed by direct ordination methods to determine species-environment relationships. Canonical correspondence analysis (CCA, Ter Braak and Prentice, 1988) was used to relate the physical and chemical characteristics of modern sample locations with the diatom abundances. Fossil assemblages were treated as passive samples in the CCA, allowing their projection into the modern species/sample/environment space. Only taxa with relative abundances greater than 1% in at least two samples were included in the analysis. The effects of square-root transformation of diatom frequencies and down-weighting of rare species on CCA analyses were examined and found to be

insignificant. Likewise log transformation of environmental variables with concentration units (*e.g.* total phosphorus) in the CCA analyses had no significant effect on the results. Based upon these observations untransformed species relative abundances and environmental variables were used for CCA. Analyses were run under the CANOCO computer program.

Diatom $\delta^{18}O$

Organic matter was removed from sediments with perchloric/nitric acid and diatoms were separated from other oxygen bearing phases by sieving, heavy-liquid density separation and differential settling (Shemesh et al., 1995). Controlled isotope exchange (Juillet-Leclerc and Labeyrie, 1987) followed by high temperature recrystallization was used to minimize the isotopic effect of opal-bound water. Oxygen was liberated by reaction with BrF_5, and quantitatively converted to CO_2. The oxygen isotopic composition analyzed via dual-inlet by an upgraded Finnegan MAT 250. The results are calibrated versus NBS-28 quartz international standard and are reported on the VSMOW scale using the notation: $\delta^{18}O_{sample} = (R_{sample}/R_{VSMOW}-1)*1000$, where R is the ratio $^{18}O/^{16}O$. Each sample $\delta^{18}O$ value represents the average of two to four analyses. The median standard deviation of replicate measurements was 0.13‰ (n=80) with a range of 0.01-0.53‰. The long-term reproducibility is 0.14‰. Although the diatom $\delta^{18}O$ ($\delta^{18}O_d$) measurements could include contributions of opal from other sources (*e.g.* phytoliths, chrysophyte cysts or sponge spicules) visual inspection of all cleaned samples indicated negligible contributions. Variations of $\delta^{18}O_d$ in Laguna Verdes Alta and Baja do not directly coincide with floristic changes in the diatom community indicating minimal species effects on the $\delta^{18}O$ values.

Reconstructing moisture balance from diatom $\delta^{18}O$

The oxygen isotopic composition of lake water reflects the composition of input water (in this case groundwater) and its modification by evaporative enrichment and atmospheric exchange (governed by the hydrologic balance of the lake). The lakewater $\delta^{18}O$ is then recorded in the opal frustules of diatoms growing in the lake (modified by a fractionation factor which depends on temperature). Typically, reconstructing the precipitation/evaporation balance (P/E) from a single lake requires assumptions about how lake input water $\delta^{18}O$ and temperature have changed through time. However, the uncertainty of the P/E reconstruction can be greatly reduced when isotope records from two lakes with end-member hydrologic balances are compared. In this study, the record from LVA (open-basin) is sensitive to input water $\delta^{18}O$ and temperature whereas the LVB record (closed-basin) is also influenced by humidity and P/E. Similar features in the LVA and LVB $\delta^{18}O_d$ records indicate changes in the input water $\delta^{18}O$ or temperature. The difference between the $\delta^{18}O_d$ records from LVA and LVB ($\Delta\delta^{18}O_d$) is primarily controlled by the regional P/E balance. The $\Delta\delta^{18}O_d$ was calculated by linearly interpolating LVA $\delta^{18}O_d$ at the sample ages of LVB and then subtracting the LVB $\delta^{18}O_d$ from the interpolated LVA $\delta^{18}O_d$.

Results & Holocene Climate History

Laguna Blanca

The age-depth model for Laguna Blanca is shown in Fig. 3.2. All radiocarbon ages are in stratigraphic order except the samples at 172 and 175 cm. The sediment composition does not change near these samples thus the sedimentation rate likely remained constant across this interval. The 172 cm age produces sedimentation rates

more consistent with nearby samples and was retained in the age-model. The deepest radiocarbon sample in the age model was on bulk sediment rather than terrestrial macrofossils and thus is a maximum limiting age (Abbott and Stafford, 1996). The sedimentation rate derived from this age represents a minimum estimate.

In Laguna Blanca, sediments from the past 10,000 y vary between organic poor, clay rich lake sediments and rooty aquatic and terrestrial macrophyte rich shallow lake/bog sediments. Six sediment units can be delineated based upon the visual appearance, magnetic stratigraphy, bulk density, TOM and sediment accumulation rates (Fig. 3.3). These units are primarily the result of different lake levels (LL). During periods of high (probably overflowing) LL, dense, organic poor, high MS, mineral rich sediments were deposited. In contrast, low lake levels were associated with low-density, low MS and high TOM sediments with abundant macrophyte remains.

The lowest unit (I) is characterized by high MS, high dry density and low TOM. Faint color banding is visible in the sediments of Unit I and reveals disturbances such as intermittent micro-faulting, cm scale folds and vertical boundaries between sediment colors. The disturbance in these bands as well as their indurate texture indicates they have been reworked. The sediment accumulation rate is moderately high in this unit (Fig. 3.3). The sediment composition and evidence of re-working in Unit I suggest a lake highstand followed by a period of lake desiccation and possibly deflation. The radiocarbon date on bulk sediments from the top of Unit I suggests that desiccation started after 9470 y BP. Extrapolation of the sedimentation rate in Unit II indicates 8550 y BP as the end of the desiccation event.

Unit II (423-185 cm, 8220-2050 y BP) has low MS, dry density and high TOM. The sediment in Unit II is a dark black color composed of fine sediment, twigs, leaves and aquatic plant remains. Within Unit II are many 0.5 to 2.0 cm tan layers of dense, high MS and low TOM sediment. A subset of these layers were sampled for dry density and TOM analysis, the rest were identified visually. The frequency of these events is greatest between 8250 to 7000 y BP and 4000 to 1000 y BP (Fig. 3.3). Both organic and inorganic sediment accumulation rates are ~10% those in Unit I and increase slightly towards the top of the unit. Unit II represents a period of shallow lake conditions extending from 8550 to 2000 y BP. The abundance of leaves and woody macrofossils suggests that LL was low enough to allow terrestrial vegetation to grow near the coring site (5.5 m water depth today). The intercalated tan layers in this unit probably represent short periods of high LL. The frequency of these layers imply an early wet period (8550 to 8000 y BP), an extended dry interval 8000 to 4000 y BP (driest 7000 to 4000 y BP) and increasingly wet conditions 4000 to 2000 y BP.

There is an abrupt transition from Unit II to Unit III (185-103 cm, 2050-700 y BP) where the dry density increases, TOM decreases, the MS slightly increases and organic and inorganic sediment accumulation rates rise. This transition occurs within a single coring drive (as do all other major lithologic transitions) and is thus not an artifact of the coring method. In Unit III the macrophyte content is much lower compared with Unit II and sediment accumulation rates are similar to Unit I. The sediment composition and sediment accumulation rates suggest an increase of LL around 2000 y BP and high LL 2000 to 700 y BP.

The Unit III/IV boundary represents another abrupt transition. Visually there is a sharp change from black to laminated tan/gray sediments and macrofossils become very sparse. In Unit IV (103-40 cm, 700-45 y BP) the MS dramatically increases, bulk density nearly doubles and TOM decreases to the lowest values in the core. Unit IV sediments represent the highest LL in the record (700 to 45 y BP) and probably include fluvial sediment transported by the currently dry inflow stream. The LL was probably high enough to allow water to overflow through the currently dry outlet valley. Unit V (40-0 cm, 45 y BP to present) has a composition intermediate between Unit III and IV with more TOM, lower dry density and MS than Unit IV. The sediments in Unit V are similar to Unit III and indicate a return to lower lake conditions 45 y BP to the present.

Laguna Verdes Alta and Baja

The sediments of LVA and LVB are nearly uniform in composition during the Holocene. They contain 25-35 % TOC, have low MS and dry density. The age-depth relationships for LVA and LVB are shown in Fig. 3.2. In LVA, the uppermost radiocarbon age was not used in the age model because it is inconsistent with the excess ^{210}Pb chronology. The LVB age model is not well constrained during the Holocene, however the similarity of LVA and LVB sedimentation rates lends support to the LVB ages.

Diatoms

The diatom flora of the modern and fossil assemblages examined from Venezuela total 81 identified taxa (Appendix A). Raphid and araphid pennate taxa are well represented while the only centric diatom present is *Aulacoseira alpigena*. Canonical correspondence analysis (CCA) of 28 surface sediments from seven lakes in

the Venezuelan Andes exposes two dominant ecological gradients (Fig. 3.4). The strongest gradient (Axis 1) captures variability associated with lake conductivity. Specific conductivity (SpC), total alkalinity (Alk_{tot}) and silicon are all positively correlated with Axis 1. Lake depth and total phosphorus are negatively correlated with Axis 1, reflecting the tendency for deeper lakes to have higher total P and lower conductivities. The second axis captures the variability associated with lake elevation. High altitude lakes are colder, more acidic and transparent (allowing benthic macrophyte growth).

The CCA results show that SpC and/or correlated variables are the most important control on diatom taxa abundance. A measure of the SpC optima for individual diatom species, or estimated specific conductivity of a sample (SpC score) can be determined by calculating the orthogonal projection of species or site scores onto the specific conductivity vector in Fig. 3.4 (Ter Braak and Prentice, 1988). When sample scores are calculated from species abundances, the SpC scores of these samples are proportional to a weighted-averaging estimate of the specific conductivity of the sampling site (Ter Braak and Prentice, 1988). The SpC scores for modern sites increase with the measured water conductivity indicating a good relationship between these variables in the modern samples (Fig. 3.4). This relationship is supported by comparison of species' SpC scores with conductivity optima determined in the NAWQA calibration project. Species in the NAWQA dataset (Potapova and Charles, 2003) which also occur in the Venezuelan samples (n=27) have specific conductivity optima that are significantly correlated with the SpC scores calculated from the CCA analysis (r=0.60, p<0.002). Figure 3.5 shows the modern distribution of the 15 diatom

species which are dominant in the fossil data. The species are arranged by their SpC scores (optima) while the samples are arranged by specific conductivity and water depth. It is apparent from this diagram that species with low (high) SpC scores are much more likely to occur in low (high) conductivity lakes. Again, this underscores the impact of SpC on diatom distributions and provides a framework for interpreting variations in fossil diatom species abundances.

Fig. 3.6 shows the stratigraphic variation of diatom relative abundances in LVB during the past 12,000 y. In diatom zone A (12,000 to 10,500 y BP) the flora is primarily composed of moderately low SpC species such as *Encyonema sp. #3* and *Achnanthes minutissima* (all var.). The zone A/B transition marks the introduction of several higher SpC species (*Sellaphora pupula* var. *capitata*, *Nitzschia gracilis* and *Navicula laevissima* var. *perhibita*). During zone B (10,500 to 8,000 y BP) abundances of *Encyonema sp. #3* decline and the higher SpC taxa *Navicula podzorskii* increases and then decreases. At the beginning of Zone C (8,000 to 3,800 y BP) the lower SpC species *Aulacoseira alpigena*, *Encyonema lunatum* and *Nitzschia perminuta* have peaks in their abundance. These species are then replaced by the higher SpC *Encyonema sp. #4* which has greater abundances throughout zone C. Zone D (4,000 to 750 y BP) has higher abundances of low SpC species such as *Aulacoseira alpigena*, *Gomphonema gracile* and declining amounts of *Encyonema sp. #4*. The youngest diatom zone (E, 750 y BP to present) contains decreasing followed by increasing amounts of *Achnanthes minutissima* (all var.) and the opposite pattern for *Sellaphora sp. #1*, *Navicula minima* and *Nitzschia gracilis*. It is important to note that the only obligate planktonic diatom

(*Aulacoseira alpigena*) does not appear until ~8,500 y BP and has abundance maxima 8,500 to 7,500 and 3,000 y. B.P. to the present.

Evaporation will concentrate the dissolved material in a lake leading to higher specific conductivities. Thus, periods of higher conductivity inferred from LVB SpC scores can be interpreted as low P/E and dry conditions (and *vice versa*). Higher inferred SpC 10,000 to 8800, 6500 to 4000, 1500 to 800 and ~100 y BP to present indicate lower P/E and dry conditions (Fig. 3.6). Lower SpC 8800 to 6500, 4000 to 1500 and 800 to 100 y BP indicate wet conditions. The LVB SpC scores are also low prior to 10,000 y BP which would indicate wet conditions. However, the diatom assemblage in this interval does not have an analogue in the modern surface sediments and these SpC scores should be interpreted with caution.

Diatom isotopes

Further evidence for Holocene changes in the P/E balance comes from the $\delta^{18}O_d$ records in LVA and LVB. The primary difference between LVA and LVB is their hydrologic balance (Table 3.1), therefore changes in the regional P/E balance or atmospheric relative humidity will cause unequal $\delta^{18}O_d$ changes in the two lakes. The identical long-term Holocene trend in the $\delta^{18}O_d$ records from LVA and LVB primarily reflects changes in the isotopic composition of precipitation and/or temperature (Fig. 3.7A). Changes in the $\delta^{18}O$ of the ocean due to melting of continental ice sheets accounts for a small part of the trend (Fig. 3.7B). The remainder is caused by precipitation $\delta^{18}O$ changes due to a decrease in the efficiency of water vapor transport from the Atlantic Ocean to the Venezuelan Andes (see Chapter 4). Removal of the ocean $\delta^{18}O$ change and the linear trend due to precipitation $\delta^{18}O$ highlights millennial-

scale variations present in both records (Fig. 3.7C). Although these variations could reflect both changes in the regional P/E balance and precipitation $\delta^{18}O$, the scaling of isotope shifts between the records argues for P/E as the primary factor. Changes in P/E balance have a larger impact on lakes such as LVB which lose more of their water through evaporation. Thus larger magnitude shifts in the LVB vs. LVA record agrees with predictions from the modern hydrology. This feature is highlighted when the difference between the isotopic records from LVB and LVA ($\Delta\delta^{18}O_d$, Fig. 3.7D) is examined. The $\Delta\delta^{18}O$ record is unaffected by changes in precipitation $\delta^{18}O$, thus the coincidence of changes in both $\delta^{18}O_d$ and $\Delta\delta^{18}O_d$ is strong evidence that P/E variability is driving the isotope changes.

An exception to this interpretation is the jump in $\delta^{18}O_d$ in LVA at ~2200 y BP. Several observations suggest this jump is not caused by regional climatic variability and results from processes endemic to LVA. First, the similarity of $\delta^{18}O_d$ variations in LVA and LVB prior to 2200 y BP and the correspondence between $\delta^{18}O_d$ and $\Delta\delta^{18}O_d$ changes indicate the two records are responding to the same forcing factors. In this context the shift appears anomalous. Second, the shift would imply a $\Delta\delta^{18}O_d$ <3.5 ‰, the lowest values in the Holocene and significantly lower than the modern $\Delta\delta^{18}O_d$ of 4.1 to 4.9 ‰. The modern $\Delta\delta^{18}O_d$ was calculated using the modern lakewater $\delta^{18}O$, temperature, and the water-opal fractionation factors from (Shemesh et al., 1992; Brandriss et al., 1998). Evidence from other lakes in the region does not support a large shift towards drier climate at 2200 y BP or such a large difference between the present climate and the past 2000 y. Third, the similarity between the long-term $\delta^{18}O_d$ trends in LVA above and below the shift suggests that the lake is still responding to precipitation $\delta^{18}O$ changes

and the offset is the result of a within-lake change in the hydrologic balance. Although the cause of the shift in LVA is not known, the preceding arguments suggest it is unrelated to climate. We have tentatively corrected the data by adjusting the youngest three points in LVA so they continue the trend defined prior to 2200 y BP. This correction is not completely satisfactory and these data points are not emphasized in our reconstruction.

The $\delta^{18}O_d$ and $\Delta\delta^{18}O_d$ records suggest wettest conditions 10,000 to 6500 y BP, drier average conditions 6500 to 3000 y BP, wet periods 2,000 to 1,000 and 600 to 200 y BP and modern conditions slightly drier than the Holocene average. Between 10,000 and 2,000 y BP the timing of these wet and dry periods is similar to the diatom inferred specific conductivity changes in LVB indicating the $\Delta\delta^{18}O_d$ and diatoms are both responding to evaporative enrichment of the lake water due to moisture balance changes. After ~2,000 y BP the diatom conductivity continues to vary with the LVB $\delta^{18}O_d$ curve however the absolute value of the SpC scores increases. The difference in scaling between the SpC and LVB $\delta^{18}O_d$ records after 2,000 y BP may reflect the influence of nutrient availability on the SpC scores. Lower nutrient availability and nitrogen limitation, indicated by higher sedimentary $\delta^{15}N$ values after 2,000 y BP (see data tables in Appendix), would force a secular shift in the SpC scores towards higher values with specific conductivity variations superimposed (Fig. 3.4). Periods of higher P/E inferred from the $\delta^{18}O_d$ records also coincide with greater abundances of the only obligate planktonic diatom found in LVB (*Aulacoseira alpigena*) indicating higher lake levels and supporting the isotope record.

Discussion

Comparison of the L. Blanca, LVA and LVB records with climate reconstructions from Lake Valencia (10° 10' N, 67° 45' W) and the Cariaco Basin (10° 42' N, 65° 10' W, Fig. 3.8) reveals a strong correspondence. The period of high lake-level (LL) in L. Blanca at ~10,000 to 9,500 y BP corresponds to the onset of early Holocene high P/E in LVA and LVB (Fig. 3.9). At the same time, L. Valencia LL was lower, and hydrographic changes in the Cariaco Basin suggest a seasonality skewed towards the summer wet season. This period also corresponds with a second phase of deglaciation identified in the Venezuelan Andes (Stansell *et al.*, in prep). Very low or dry LL in L. Blanca between 9,500 and 8,500 y BP corresponds with a period of reduced P/E in LVB-LVA and higher L. Valencia LL. Between 8,500 and 8,000 LL was high in L. Blanca, P/E was at its highest early-Holocene values in LVB-LVA and L. Valencia experienced a pronounced lowstand. There is also evidence for dry conditions in Costa Rica at this time (Lachniet et al., 2004).

Between ~8,000 and 6,000 y BP, L. Blanca LL and LVB-LVA moisture balance decreased to mid-Holocene values, Cariaco Basin hydrology became dominated by dry-season upwelling and L. Valencia LL increased to its high mid-Holocene levels. Also, basal ages for peat deposits on the table mountains (*tepuis*) in the Guayanas highlands of Venezuela cluster in this interval (Fig 8, Schubert and Fritz, 1985). During the middle Holocene (~6,000 to 4,000 y BP) low moisture balance and LL occurred in the Venezuelan Andes, dry-season upwelling continued to dominate annual conditions in the Cariaco Basin, and LL was high in L. Valencia. Between 4,000 to 2,000 y BP LVB-LVA moisture balance was variable but increased over low mid-Holocene values, L.

Blanca experienced more wet episodes, wet-season conditions became more important in the Cariaco Basin and LL in L. Valencia started to decrease. At 2,000 y BP there is an abrupt increase in L. Blanca LL and a transition to consistently higher P/E in LVB-LVA. These conditions are maintained between 2,000 and 1,000 y BP and correspond with decreasing LL in L. Valencia. A sharp drop in LVB P/E occurs after 1000 y BP, with a small corresponding drop in L. Blanca LL. During the last 700 y BP, L. Blanca LL reaches the highest levels since the early Holocene and LVB-LVA moisture balance is high. This wet interval corresponds with Little Ice Age glacier advances in the Venezuelan Andes (see Chapter 2). Modern conditions are established by approximately 100 y BP.

A significant exception to the pattern of climate change discussed above has been documented in geochemical records from the Cariaco Basin. Decreasing titanium concentration in Cariaco Basin sediments during the Holocene have been interpreted to indicate a southward shift in the ITCZ and reduction in coastal rainfall in response to decreasing insolation seasonality (Haug et al., 2001). In contrast, sediment grayscale reflectance (a proxy for the relative amounts of dark colored terrigenous vs. light biogenic material) suggests an increase in the terrigenous sediment concentration and increasingly humid conditions during the Holocene (Hughen et al., 1996). The glacial-interglacial interpretation of these records agree (Hughen et al., 1996; Peterson et al., 2000; Haug et al., 2001). However, the Holocene shifts in these proxies require opposing climate trends: decreasing terrigenous sediment and increasing biogenic sediment (Haug et al., 2001) vs. increasing terrigenous sediment and decreasing biogenic sediment (Hughen et al., 1996). In fact, the titanium and grayscale records are

inversely correlated during the Holocene (r^2=0.43, p<0.0001). Several alternative explanations for the titanium and grayscale trends are possible. For example, rising sea-level has increased the area of submerged coastal shelf available to trap terrigenous sediment which could decrease the titanium contribution to the sediment. Alteration of the chemistry of terrigenous sediment such that the titanium/terrigenous sediment ratio decreases during the Holocene could also explain the titanium trend. Changes in the relative contribution of different organisms (zooplankton, diatoms, dinoflagellates, coccolithophorids) to biogenic sedimentation (Werne et al., 2000) could alter the relationship between grayscale reflectance and terrigenous vs. upwelling sediment composition. An important constraint on any explanation is that sedimentation rates are reasonably constant through the Holocene. As noted by (Haug et al., 2001) this constraint favors mechanisms such as ITCZ migration which inversely alter the terrigenous and biogenic flux. At this time it is not possible to resolve the differences between these records. Here we rely upon the isotope records of water column structure and upwelling (Lin et al., 1997) with the caveat that additional research my show them to be incomplete recorders of Cariaco Basin climate variability.

The preceding comparison between climate records in Venezuela indicates that the sign of climate changes in L. Valencia and the Guayanas highlands is reversed from the Venezuelan Andes and Cariaco Basin. An explanation for this regionally complex pattern of Holocene climate change may be found in studies of modern Venezuelan rainfall variability. Pulwarty (1998) noted that precipitation in the Andes is correlated with other parts of Venezuela except during the July-August period, when higher rainfall amounts in the Andes are accompanied by drier conditions in the central

lowlands. This finding suggests that the opposite sign of climate records from L. Valencia and the Andes represents a fundamental feature of Venezuelan climate. Supporting this conclusion, several climate model simulations for the mid-Holocene also exhibit a pattern of wet/dry anomalies similar to the paleoclimate data (Valdes, 2000; Ruter et al., 2004). Pulwarty (1992) could not determine the cause of this pattern and further research is needed.

Despite the heterogeneous sign of climate shifts in Venezuela the similar timing of these shifts implies a common cause. One possibility is that changing solar insolation had a direct effect on atmospheric circulation and moisture balance in Venezuela. Calculation of changes in solar insolation at the latitude of Venezuela (10° N) indicate that seasonality was at a maximum during the early Holocene and decreased to the present (Fig. 3.10, Berger and Loutre, 1991). Thus, direct insolation forcing would indicate wettest conditions during the early Holocene and increasingly drier conditions to the present. This pattern is not observed in the climate records from the Venezuelan Andes, Venezuelan lowlands or Cariaco Basin hydrography. However ,it is possible that insolation during the transition months is responsible for the observed changes in Venezuela. Reduced March-May insolation during the middle Holocene (Fig. 3.10) may have delayed the onset of the wet season. This change would resemble a modern El Niño event, where March-May precipitation is reduced, evaporation greatly enhanced and P/E strongly negative. This explanation also requires that the climate effects of reduced March-May insolation outweigh those from increased September-November insolation. This could be possible if greater cloudiness during the wet-dry transition reduces the impact of increased September-November insolation.

Thus, unlike climate records from the equatorial neotropics (Lago Junin, Amazon River discharge, see Chapter 5), it appears that decreasing insolation seasonality during the Holocene did not directly affect Venezuelan climate. However, the timing of climate shifts in Venezuela is similar to records located near the southernmost edge of tropical monsoon circulation in the southern hemisphere neotropics (e.g. Bolivian *altiplano*) and may indicate an effect from insolation forcing during transition months.

Another explanation for Holocene P/E change is found in the spatial correlation pattern of tropical SST and modern Venezuelan precipitation timeseries. The correlation pattern of modern rainfall anomalies in Venezuela with Atlantic and Caribbean SSTs is generally positive or negative throughout the country. In contrast, the correlation pattern with ENSO or eastern tropical Pacific SSTs exhibits a longitudinal pattern of positive and negative associations (Pulwarty et al., 1992) which generally correspond to the Andes/Valencia/Cariaco regions. This correlation pattern makes tropical Pacific SST change an attractive explanation for Holocene P/E variability in Venezuela. During the middle Holocene, lower SSTs in the eastern tropical Pacific would lead to drier conditions in the Andes and coastal regions while central and southeastern Venezuela were wetter. Conditions during the early and late Holocene would be reversed. A lake-level record from Bainbridge Crater lake in the Galápagos archipelago (-1° N, 90° W) shows a pattern of Holocene P/E change which is similar to the records in the Venezuelan Andes (Fig. 3.9). High lake levels during the early Holocene gave way to an extended period of low lake level between 7,000 and 3,300 y BP, followed by high lake levels to the present (Colinvaux and Schofield, 1976a). Seasonal precipitation in the Galápagos is closely tied to regional SST

variations (warm SSTs during the wet austral summer), thus this lake-level record indicates cooler SSTs during the middle compared to the early or late Holocene. Three different climate modeling studies also exhibit cooler SSTs in the eastern Pacific during the middle Holocene (Bush, 1999; Clement et al., 2000; Kitoh and Murakami, 2002), consistent with the record from Brainbridge Crater lake. These data suggest that millennial scale P/E change in Venezuela may be a response to eastern equatorial Pacific SST variability. The changes are independent of ENSO variability, which generally shows increasing amplitude during the past 5,000 y (Sandweiss et al., 2001; Tudhope et al., 2001; Andrus et al., 2002; Moy et al., 2002; Riedinger et al., 2002)and is consistent with the observation that Pacific SSTs affect Venezuelan rainfall independent of the SOI sign (Pulwarty et al., 1992).

Climate records from Panama, and Columbia also exhibit a pattern of Holocene moisture balance change similar to Venezuela and the Galápagos (Fig. 3.8). A record from Lake La Yeguado, Panama (8° 27' N, 80° 51' W, 650 m) documents a period of reduced lake level between 6,600 and 3,200 y BP (Bush et al., 1992). A similar pattern is also present in Lake Fúquene, Columbia (5° 27' N, 73° 46' W, 2580 m) (Vélez et al., 2003). In contrast, a pollen record from Laguna Las Margaritas, Columbia (3° 23' N, 73° 26' W, 290 m) indicates forest expansion and wetter lake conditions 7,300 to ~3,000 y BP (Wille et al., 2003). The similarity between the high-elevation sites in Columbia and Venezuela with the records from Panama and the Cariaco basin suggests moisture balance changes in the high elevation Andes correspond with changes of opposite sign in low elevation foothills (Laguna Las Margaritas and Lake Valencia).

Although insolation forcing or eastern Pacific SST changes are attractive explanations for Holocene P/E change in Venezuela, other factors may have been important during specific intervals. As noted above, the period of low LL in L. Valencia and high LL in L. Blanca between ~8,500 to 8,000 y BP corresponds with the '8,200 y' cold event identified in climate records from the North Atlantic, and increasingly from tropical sites (Stager and Mayewski, 1997; Gasse, 2000; Lachniet et al., 2004). This event has also been identified in Cariaco sediments as a time of enhanced upwelling and stronger trade winds (Hughen et al., 1996). The association of stronger trade winds over the Cariaco basin and wet conditions in the Venezuelan Andes is also proposed for Little Ice Age glacial advances (see Chapter 2), and thus may be a stable pattern of Venezuelan climate. The opposite sign of moisture balance changes in L. Valencia vs. the Andes and Cariaco Basin is maintained during this wet interval suggesting that this feature is present regardless of the cause of climate change.

Conclusions

Multi-proxy climate records from three lakes in the Venezuelan Andes document regional changes in moisture balance during the Holocene. During the early Holocene, the Andes were generally wetter although there were short periods of aridity and a distinct wet interval which probably corresponds to the 8,200 y BP cooling event in the N. Atlantic. The middle Holocene was a time of low lake levels and reduced P/E balance while the late Holocene was wetter, with the wettest period occurring during the Little Ice Age. The timing of moisture balance changes in the Venezuelan Andes is similar to Lake Valencia and some records from the Cariaco Basin. However, the sign of P/E changes in L. Valencia is opposite to the Andes and Cariaco Basin. This pattern

of positive and negative anomalies is similar to modern rainfall anomalies, suggesting it represents a stable feature of Venezuelan climate. The cause of P/E change in the Andes does not appear to be insolation forcing during the peak of the wet and dry seasons. However, lower insolation during the March-May transition from dry to wet season may explain the mid-Holocene aridity. Alternatively, changes in eastern tropical Pacific SSTs could produce both the spatial and temporal pattern of P/E change in Venezuela. Evidence for cooler SSTs in the eastern tropical Pacific during the middle Holocene are consistent with this theory.

Tables

Table 3.1 – Study site characteristics.

Lake	Location	Lake area (10^3 m^2)	Watershed area (10^3 m^2)	Watershed/ lake area	Z_{max} (m)	$d^{18}O_w$ (‰ VSMOW)*
L. Blanca	8° 20'N, 71° 47'W, 1620 m	50.8	857	16.9	5.5	-1.7
L. Verdes Alta	8° 51'N, 70° 52'W, 4220 m	10.0	139	13.9	3.1	-9.3
L. Verdes Baja	8° 51'N, 70° 52'W, 4200 m	17.4	116	6.7	5.5	-3.9

*Oxygen isotope composition of lake water relative to VSMOW, expressed as $\delta^{18}O = (R_{sample}/R_{VSMOW}-1)*10^3$ where R is the $^{18}O/^{16}O$ ratio. Average modern precipitation near L. Verdes Alta and Baja is –12.5‰, near L. Blanca ~ -7‰.

Table 3.2 - Radiocarbon ages (AMS) from sediment cores.

Lab #	Lake-Core	Depth (cm)	Material	14C yr B.P.	cal yr B.P. (median)
CAMS-73090	LVA GL-99A	33.50	terr. macrofossil	820 ±40	715
CAMS-73091	LVA GL-99A	46.50	terr. macrofossil	1780 ±40	1640
AA-35201	LVA 99A	110.50	terr. macrofossil	4170 ±110	4700
CAMS-96816	LVA 99A	256.25	terr. macrofossil	9720 ±180	10890
AA-35203	LVA 99A	316.50	terr. macrofossil	12270 ±150	14240
CAMS-73203	LVB 99A	45.20	terr. macrofossil	750 ±50	685
CAMS-73092	LVB 99A	302.20	terr. macrofossil	12740 ±130	15400
OS-CURL-4973	Blanca 99A	64.50	terr. macrofossil	130 ±35	104
OS-CURL-4974	Blanca 99A	103.50	terr. macrofossil	660 ±35	580
CAMS-73134	Blanca 99A	123.50	wood	980 ±40	924
CAMS-96801	Blanca 99A	175.00	wood	2700 ±60	2780
CAMS-96802	Blanca 99A	188.58	wood	2120 ±35	2120
CAMS-96803	Blanca 99A	271.74	wood	3480 ±40	3800
CAMS-96804	Blanca 99A	310.70	wood	4200 ±35	4830
CAMS-96805	Blanca 99A	388.30	wood	7055 ±40	7900
OS-CURL-4975	Blanca 99A	419.88	terr. macrofossil	7370 ±45	8180
CAMS-96806	Blanca 99A	431.27	terr. macrofossil	7550 ±45	8370
CAMS-96807	Blanca 99A	445.62	bulk sed.	8430 ±50	9470

Figures

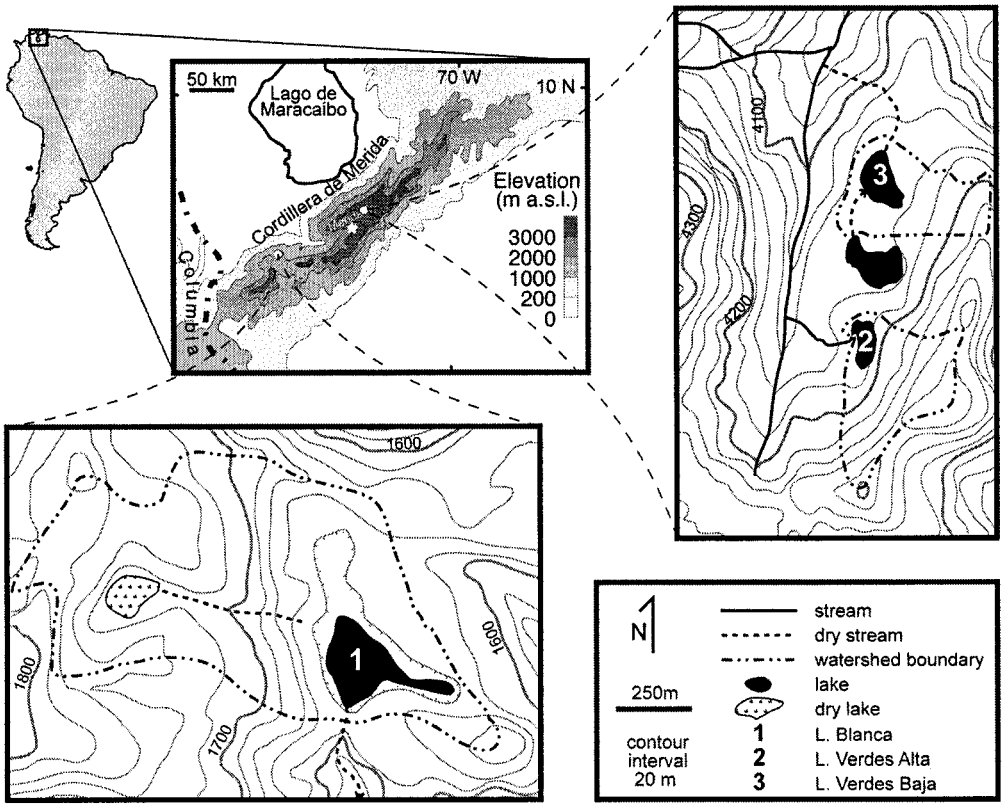

Figure 3.1 – Map showing study location and watersheds of Lagunas Blanca, Verdes Alta and Verdes Baja.

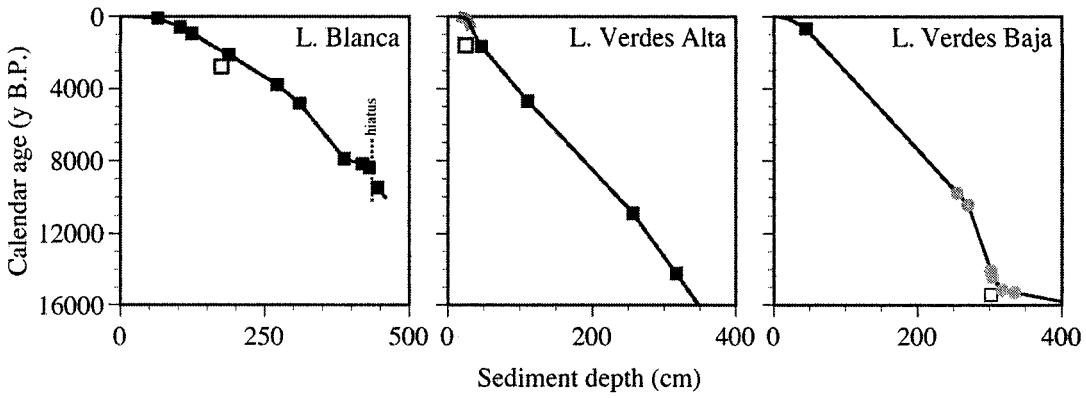

Figure 3.2 – Age-depth relationships for Lagunas Blanca, Verdes Alta and Verdes Baja. Age-depth models (thin black line) are derived from calibrated radiocarbon ages (solid squares) and ^{210}Pb ages (thick gray line). Open squares indicate radiocarbon ages not used in age models. The model for L. Verdes Baja is also based upon tie-points (gray circles) with L. Verdes Alta (see text).

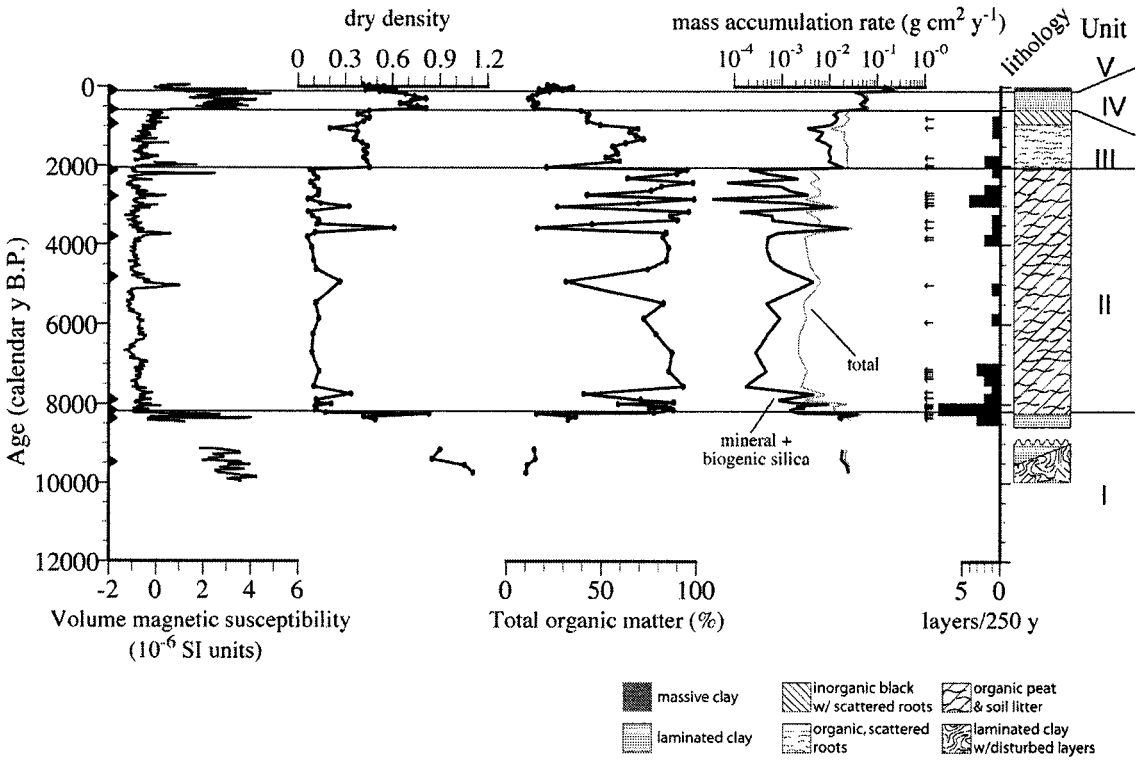

Figure 3.3 – Laguna Blanca sediment properties and magnetic susceptibility. The total mass accumulation rate (MAR) was calculated by multiplying the linear sedimentation rates (cm y^{-1}, derivative of Fig. 3.2) and dry density (g cm^{-3}). The mineral+biogenic silica MAR was calculated by subtracting the organic sediment MAR (TOM*total MAR) from the total MAR. Triangles along the left axis denote the location of radiocarbon ages used in the age model. Arrows on the right indicate sediment layers discussed in the text and the histogram shows the frequency of these layers.

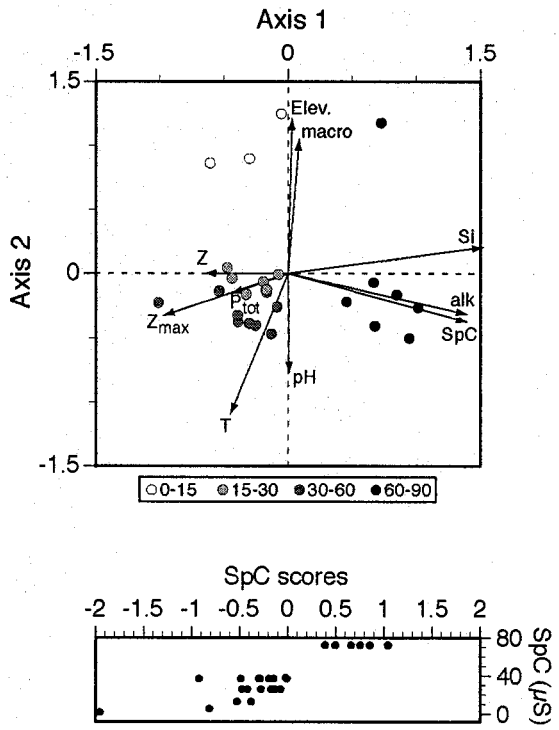

Figure 3.4 – Results from CCA analysis of Laguna Verdes Baja and modern lake sediment diatom assemblages. (Top) Biplot of the environmental variable and modern sample scores for the first two CCA axes. The modern sample scores are calculated from species abundance data and shaded by the sample site conductivity (µS). Environmental vectors are shown at 3x scaling (clockwise from top the variables are elevation, presence of macrophytes, silicon concentration, total alkalinity, specific conductivity, pH, temperature, lake depth, total phosphorus and water depth). The eigenvalues of the first and second canonical axes are 0.253 and 0.181 while the total inertia is 1.636 and the sum of all canonical eigenvectors is 0.738. (Bottom) SpC scores for modern sample sites plotted against the measured conductivity.

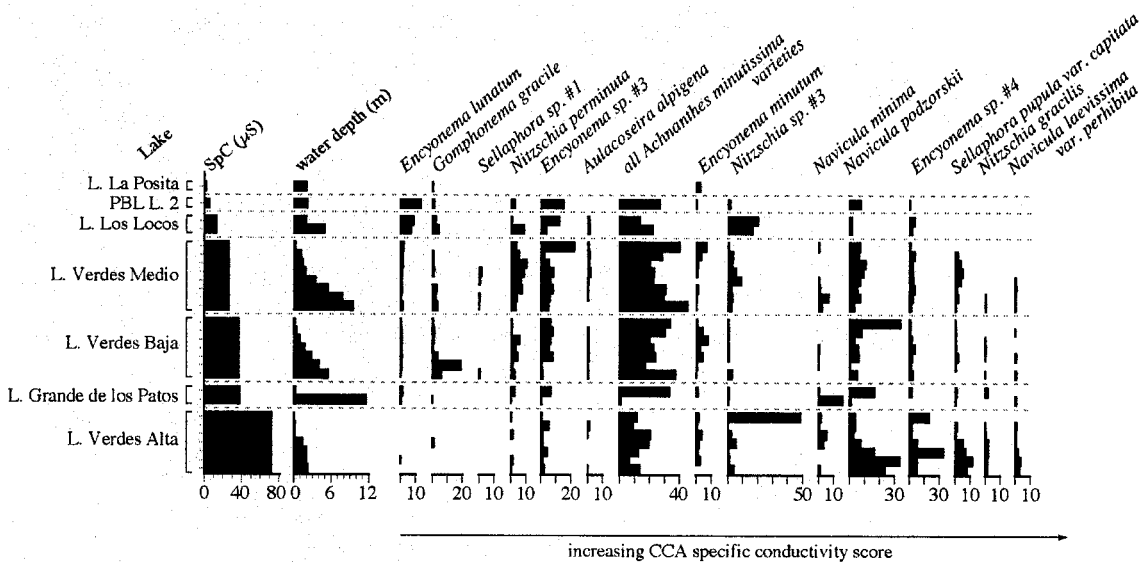

Figure 3.5 – The relative frequencies of the dominant diatom taxa in surface sediments of seven Venezuelan lakes. The specific conductivity and water depth of samples are shown in the two histograms. The taxa are arranged by increasing specific conductivity maxima determined from CCA (see text).

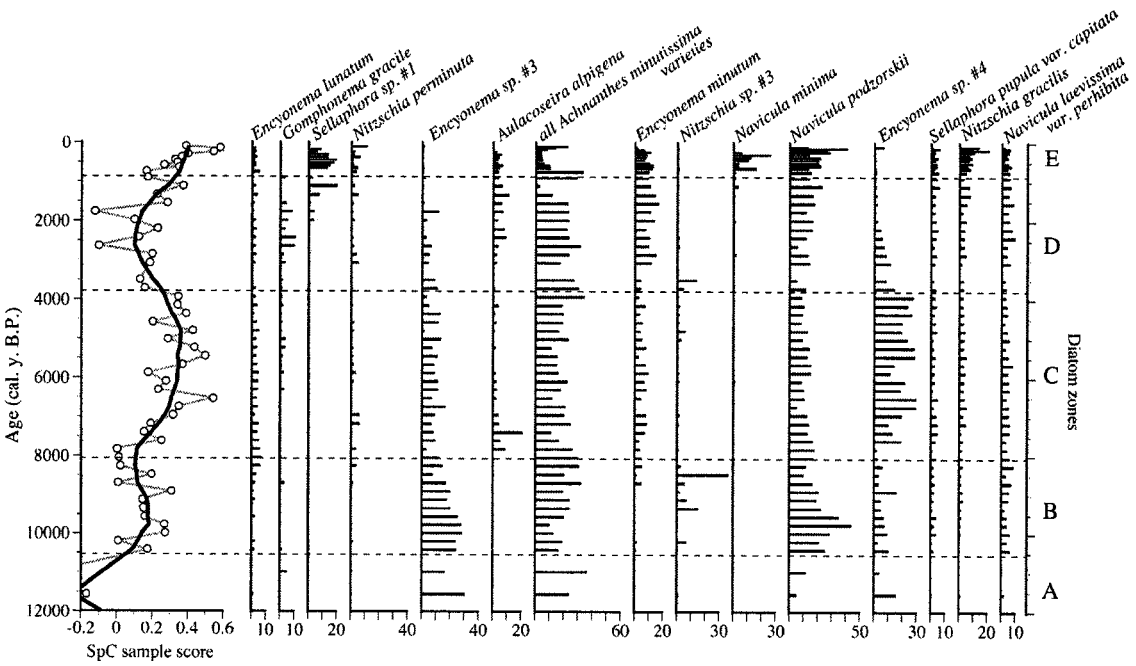

Figure 3.6 – Stratigraphic variations of the relative frequencies of the 15 most abundant diatom taxa in the Laguna Verdes Baja core. The SpC sample scores are calculated from the fossil data using the modern species-environment relationships from CCA (thick line is 500 y running average). Diatom zones discussed in the text are defined to the right.

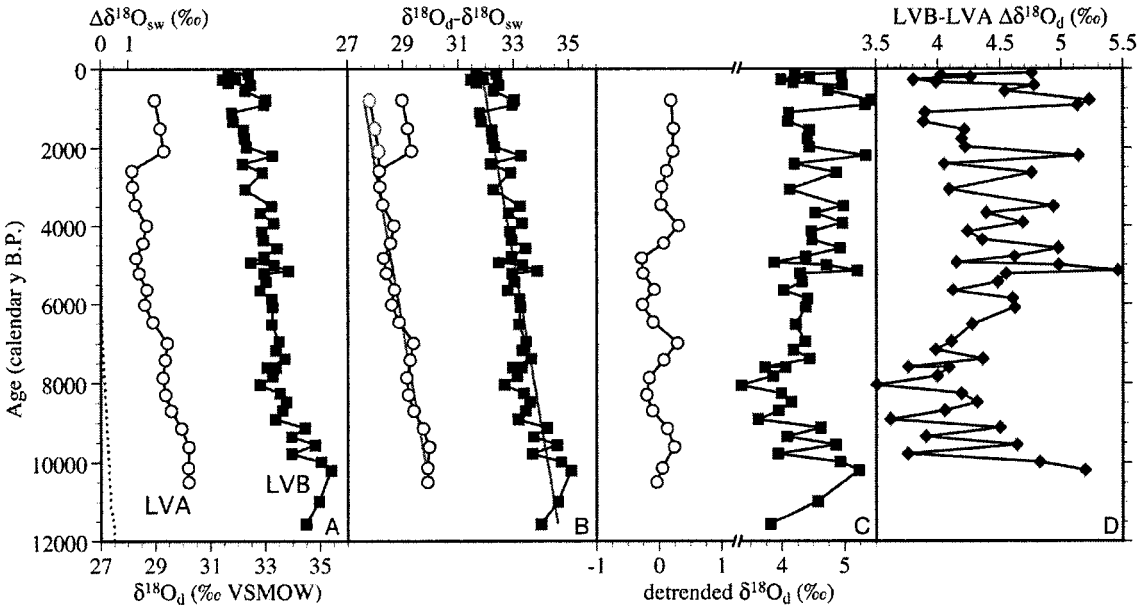

Figure 3.7 – Diatom $\delta^{18}O$ records from Laguna Verdes Alta and Baja. The dotted line shows the isotopic change in the oceanic reservoir due to melting Pleistocene ice sheets (Adkins et al., 2002; Peltier, 2002). Subtraction of the oceanic reservoir trend yields climate related diatom $\delta^{18}O$ changes (B). Detrending the ocean corrected diatom $\delta^{18}O$ records in (B) highlights the similar millennial scale variability (C). The difference between the records in A ($\Delta\delta^{18}O$) is primarily a measure of the regional hydrologic balance (D).

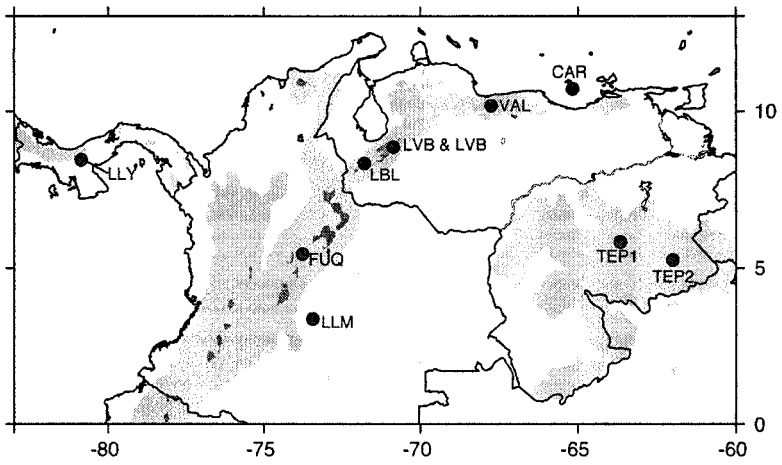

Figure 3.8 – Location of sites near the Venezuelan Andes with Holocene climate records. (Site codes are: LLY, Lake La Yeguada; CAR, Cariaco Basin; VAL, Lake Valencia; LVA & LVB, Lagunas Verdes Alta and Baja; LBL, Laguna Blanca; FUQ, Lake Fúquene; LLM, Lake Las Margaritas; TEP1, Guaiquinima Massif-Tepui; TEP2, Churi-Tepui.) Light shading indicates elevations above 500 m and dark shading above 3000 m.

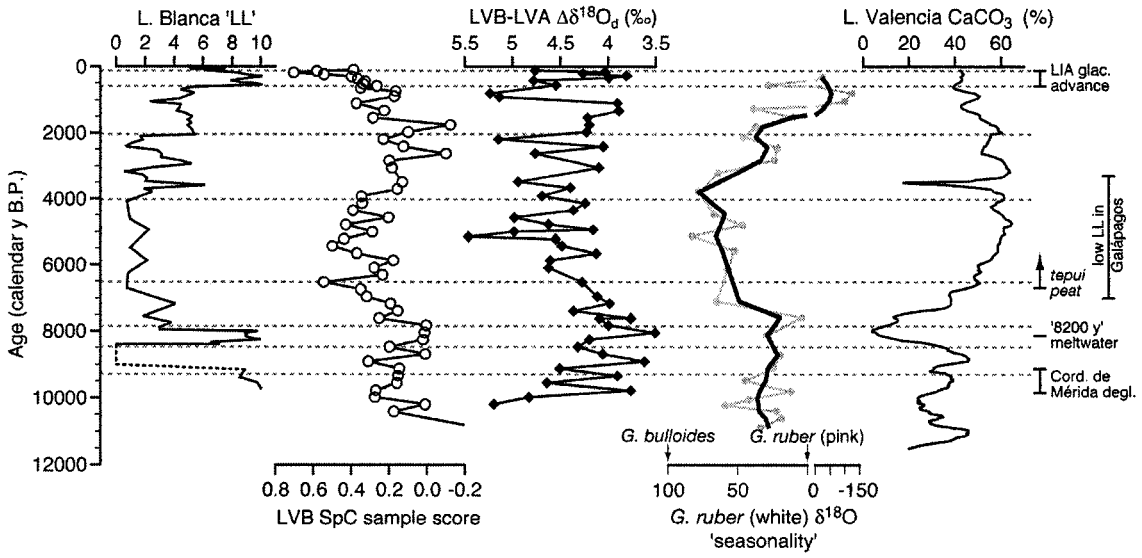

Figure 3.9 – Comparison of Holocene climate change in the Venezuelan Andes with nearby sites. Laguna Blanca 'LL' is a qualitative record of lake-level, constructed using sediment dry density, magnetic susceptibility, frequency of wet events and the elevation of the lake bottom, modern lake level and outlet sill. The *G. ruber* (white) $\delta^{18}O$ 'seasonality' is the isotopic difference between *G. ruber* (white) – *G. ruber* (pink) normalized to the difference *G. bulloides* – *G. ruber* (pink) (calculated from data in Lin et al., 1997). *G. ruber* (white) grows year-round while the pink variety primarily grows during the summer wet season and *G. bulloides* is most abundant during the winter upwelling season (Lin et al., 1997). Thus, 'seasonality' indicates whether annual average conditions are more similar to the winter (100) or summer (0). (Note the x-axis break for samples above ~1500 y.) L. Valencia $CaCO_3$ concentrations (Curtis et al., 1999) track Holocene lake-level changes (Bradbury et al., 1981; Leyden, 1985) with low carbonate corresponding to low lake levels. See text for description of climate events at right.

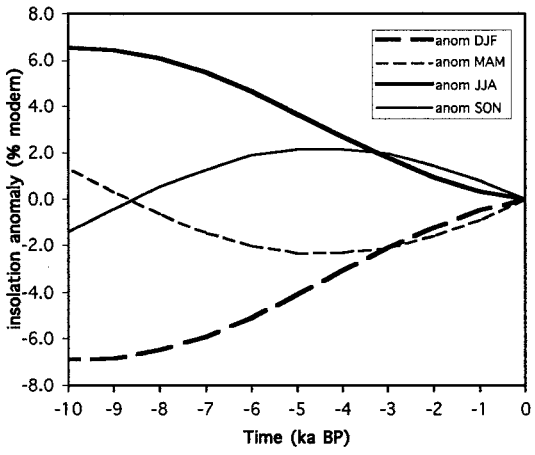

Figure 3.10 – Insolation anomalies at 10° N during the peak wet season (JJA), dry season (DJF), and transition months.

CHAPTER 4

HOLOCENE HYDROLOGIC BALANCE OF TROPICAL SOUTH AMERICA FROM OXYGEN ISOTOPES OF LAKE SEDIMENT OPAL, VENEZUELAN ANDES

Introduction

The tropical rainforests of South America flourish because of the abundant precipitation they receive. Water balance calculations indicate that approximately 40-50% of the annual precipitation is lost as runoff and the remaining moisture returned to the atmosphere by evaporation and transpiration (Salati, 1985; Costa and Foley, 1999). Transpiration accounts for most of the recycled water vapor (Gat and Matsui, 1991), thus the hydrologic balance of lowland South America is intimately linked to the vegetation. This interplay between vegetation and climate creates an internal feedback that makes it difficult to predict the impact of external perturbations such as orbital insolation cycles, solar variability and increasing carbon dioxide on the climate of the region. Indeed, the Quaternary evolution of the lowlands and their susceptibility to land-use changes and global warming are topics of considerable interest and debate (Curtis and Hastenrath, 1999; Colinvaux et al., 2001; Bush et al., 2002; Henderson-Sellers et al., 2002). Thus proxy records of past changes in the hydrologic balance of lowland South America are valuable for understanding the ecological and climatic sensitivity of the region.

The isotopic composition of precipitation and atmospheric water vapor is a sensitive indicator of moisture recycling and the atmospheric water balance (Gat, 2000). Unfortunately no long proxy records exist of the isotopic composition of precipitation in

lowland tropical South America. However the east-to-west atmospheric flow (Fig. 4.1) transports water vapor from the low elevation tropics to the high Andes where it falls as precipitation, leading to the potential for reconstructing the lowland water balance from proxy records in the Andes. The composition of Andean precipitation integrates the isotopic effects of oceanic evaporation, lowland moisture recycling and orographic uplift. If the impacts of oceanic evaporation and orographic uplift can be constrained, it is then possible to solve for the lowland moisture balance. We exploit this potential by reconstructing the isotopic composition of precipitation in the Venezuelan Andes from the oxygen isotope composition of diatom opal in lake sediments. The water balance of northern South America is then reconstructed for the past 10,000 years through modeling the isotopic evolution of water vapor as it is transported from the Atlantic Ocean to the high Andes. The reconstruction is then compared to ice core and marine isotope records from tropical South America.

Methods and Data

Study Site

Laguna Verdes Alta (LVA, 8° 51.17' N, 70° 52.45' W, 4215 m) and Baja (LVB, 8° 51.49' N, 70° 52.42' W, 4170 m) are small lateral-moraine dammed lakes in the Venezuelan Andes (Fig. 4.1). Both lakes are groundwater fed with overland flow contributing water only during heavy precipitation events. LVA has a small outflow stream while LVB has no surface outflow suggesting LVA is hydrologically open while LVB is hydrologically closed. This inference is supported by isotopic analyses of modern surface water samples from the region. On a plot of δD_{lw} vs. $\delta^{18}O_{lw}$, both lakes fall along an evaporative trend below the meteoric water line, however LVB is

significantly more enriched than LVA (Fig. 4.2). The proximity of the lakes means that they have similar climates (humidity, temperature and wind speed) and thermal regimes, only differing significantly in their hydrologic balance.

Sediment cores were retrieved from the deepest location in LVA (3 m water depth) and LVB (5 m water depth) using a modified square-rod Livingstone corer (Wright et al., 1984). Sequential drives were overlapped 10 cm to ensure a complete sediment record. Undisturbed sediment/water interface cores were retrieved from both lakes, extruded and sectioned in the field. Variations of total organic carbon (TOC), total nitrogen (TN), $\delta^{13}C_{TOC}$, $\delta^{15}N_{TN}$, C/N ratios and bulk density were used to match sediment depths between the Livingstone and surface cores. Composite sediment records for LVA and LVB were then developed using both the surface and Livingstone cores. The composite core lengths for LVA and LVB are 348 cm and 373 cm respectively.

Sediment Chronology

Accelerator mass-spectrometry (AMS) radiocarbon dates from both lakes and an excess ^{210}Pb profile from LVA constrain the age-depth relationship for the cores (Fig. 4.3, see also Chapter 3). Radiocarbon ages were converted to calendar ages using the CALIB 4.2 dataset (Stuiver et al., 1998a; Stuiver et al., 1998b). Age models were constructed using the midpoint of the ^{14}C calibration age range with the largest relative area under the probability distribution. Polynomial spline curves were used to interpolate ages between radiocarbon dates. Because LVB lacked macrofossil material for ^{14}C dating at most sediment levels, ages were calculated using the sediment mass accumulation rate and tie points to the LVA record as additional constraints. The

transition from inorganic glacial material to organic sedimentation occurs at ~15.5 ka BP in both lakes.

Diatom Isotope Analyses

Organic matter was removed from sediments with perchloric/nitric acid and diatoms were separated from other oxygen bearing phases by sieving, heavy-liquid density separation and differential settling (Shemesh et al., 1995). Controlled isotope exchange (Juillet-Leclerc and Labeyrie, 1987) followed by high temperature recrystallization was used to minimize the isotopic effect of opal-bound water. Oxygen was liberated by reaction with BrF_5, released O_2 quantitatively converted to CO_2 and the isotopic composition analyzed via dual-inlet by an upgraded Finnegan MAT 250. The results are calibrated versus NBS-28 quartz international standard and are reported on the VSMOW scale using the standard delta notation:

$$\text{Eq. 4.1} \qquad \delta^{18}O_{sample} = \left(\frac{R_{sample}}{R_{VSMOW}} - 1 \right) \cdot 10^3$$

where R is the ratio of $^{18}O/^{16}O$. Each sample measurement represents the average of two to four analyses. The median standard deviation of replicate measurements is 0.13 ‰ (n=80) with a range of 0.01-0.53 ‰. The long term reproducibility is 0.14 ‰.

Reconstructing precipitation $\delta^{18}O$ from lake sediments

The isotopic composition of lake water reflects the composition of input water (in this case groundwater) and its modification by evaporative enrichment and atmospheric exchange (governed by the hydrologic balance of the lake). The approach in this paper is to reconstruct the oxygen isotope composition of input water from sediment opal using two lakes with different hydrologic balances to remove the effect of individual lake hydrology. Modern water samples from the study area show that

groundwater and non-evaporated surface waters are identical in composition and reflect precipitation without significant modification, thus reconstructed input water is used as a proxy for precipitation composition through time.

The steady-state isotopic composition of a lake is described by:

$$\text{Eq. 4.2} \qquad \delta_{lake} = \frac{\delta_a - \delta_{in} + \frac{\varepsilon^*}{h} + (\frac{1-h}{h})C_k}{1 + \frac{P}{E}k(\frac{1-h}{h})} - \delta_{in}$$

where δ_{lake}, δ_a and δ_{in} are the isotopic composition of lake, atmospheric and inflow waters, h is the relative humidity $\varepsilon*$ is the equilibrium liquid-vapor fractionation factor (Horita and Wesolowski, 1994), C_k the kinetic fractionation factor (Gat, 1995), P/E is the regional precipitation/evaporation ratio and k a constant relating P/E to the input/evaporation ratio (F_{in}/E) of a specific lake ($F_{in}/E = k\ P/E$, modified from Gat, 1995). Assuming atmospheric water vapor is in isotopic equilibrium with precipitation ($\delta_a = \delta_{in}-\varepsilon^*$, a reasonable assumption in tropical South America as shown by Matsui et al., 1983), Eq. 4.2 simplifies to:

$$\text{Eq. 4.3} \qquad \delta_{lake} = \frac{(1-h)(\varepsilon^* + C_k)}{h + (1-h)\frac{P}{E}k} - \delta_{in}$$

It can be seen from Eq. 4.3 that diatom $\delta^{18}O$ ($\delta^{18}O_d$) records from two lakes will vary in a 1:1 relationship if they both experience the same input water variations (δ_{in}), *regardless* of the hydrologic balances of the lakes ($\frac{P}{E}k$). Variations of P/E or h will affect hydrologically closed lakes more than open lakes ($k_{closed} << k_{open}$) and result in unequal $\delta^{18}O_d$ variations. The only other mechanism for a 1:1 variation of $\delta^{18}O_d$ records from two lakes is when the denominator term $(1-h)\frac{P}{E}$ in Eq. 4.3 remains constant. The evaporation rate from a water surface is approximately proportional to the gradient in relative humidity between the saturated boundary layer directly above the water surface

(humidity = 1) and the free atmosphere (h) which is (1-h) (Craig and Gordon, 1965). Thus, the evaporation term in $\frac{P}{E}$ is approximately proportional to (1-h), and the term $(1-h)\frac{P}{E}$ can remain constant only if precipitation does not change. Thus variations in evaporation alone (driven by changes in relative humidity) could potentially cause a 1:1 change in $\delta^{18}O_d$ records from two lakes. However it is highly likely that such a change would be accompanied by changes in precipitation and result in unequal shifts in the $\delta^{18}O_d$ of the two records (Shemesh and Peteet, 1998).

The diatom opal used to reconstruct lake water $\delta^{18}O$ is subject to a temperature dependent fractionation during formation. Estimates for the magnitude of the temperature fractionation range from -0.2 to -0.5 ‰/°C (Shemesh et al., 1992; Brandriss et al., 1998; Moschen et al., 2005). Regardless of the correct value, if two lakes have similar temperature regimes and experience similar temperature variations then changes in $\delta^{18}O_d$ will be identical in both lakes. LVA and LVB are shallow, unstratified and are located 500 m from each other, suggesting they have comparable temperature regimes. Thus, $\delta^{18}O_d$ changes due to temperature change should be equal in both lakes. The Holocene trend in the $\delta^{18}O_d$ record from both lakes could be explained by a +5 to +14 °C increase in temperature. However, a pollen record from LVA suggests that temperatures were relatively stable during the Holocene with a possibility for slightly cooler temperatures 8000 to 4500 y BP (Rull et al., 2005). Thus, the $\delta^{18}O_d$ would be slightly higher during the middle Holocene due to temperature changes but the long-term trend during the Holocene is probably not due to temperature changes.

The preceding discussion shows that 1:1 variations of the $\delta^{18}O_d$ records from LVA and LVB will occur with input water (δ_{in}) and lake water temperature changes.

However, lake water temperature changes were likely minimal during the Holocene. Thus, the component of the $\delta^{18}O_d$ variations shared by the two lake records is primarily due to changes in the $\delta^{18}O$ of precipitation ($\delta^{18}O_p$) feeding the lakes.

Modeling $\delta^{18}O$ of Precipitation in the Andes

In the tropics, solar heating of the land and ocean leads to a surface low pressure trough, moisture convergence and abundant precipitation. This inter-tropical convergence zone (ITCZ) migrates north and south of the equator following the annual cycle of solar declination and controls the atmospheric circulation and tropical seasons. Moisture is fed to the ITCZ by nearly zonal (easterly) trade-wind flow close to the trough and more meridional flow at higher latitudes. The easterly trade winds transport air and moisture from the Atlantic Ocean across tropical South America (Fig. 4.1, see also Fig. 3 in Trenberth, 1999). The water vapor content and isotopic composition of this air is modified by precipitation, re-evaporation and runoff during transport across the continent and is further modified during orographic uplift into the Andes (Fig. 4.4). Predicting the isotopic composition of precipitation in the high Andes thus involves understanding the processes which occur during evaporation over the Atlantic Ocean, transport across the South American continent and uplift to the high Andes (Grootes and Stuiver, 1989; Pierrehumbert, 1999). These three steps will be discussed in the following sections.

Oceanic Evaporation

At steady state, the isotopic composition of atmospheric water vapor over the ocean is described by:

Eq. 4.4 $$\delta_{atm} = \delta_{ocean} - (\varepsilon^* + (1-h)C_k)$$

where ε^* and C_k are the equilibrium and kinetic isotope effects (Craig and Gordon, 1965) and *h* is the boundary layer relative humidity normalized to the ocean water temperature. The key parameters needed to predict δ_{atm} are thus the ocean water isotopic composition, relative humidity and temperature (which controls ε^*). Values for the oceanic mixed layer $\delta^{18}O$ are available from the NASA/GISS Global Seawater Isotope Database (Schmidt et al., 1999). In the region near tropical South America (30-60° W, 15° S-20° N) the average ocean $\delta^{18}O$ is +1.00±0.15 ‰ (average of data in 5°x5° bins). Average oceanic boundary layer temperature and humidity are constrained by data from the NCEP/NCAR reanalysis project (Kalnay et al., 1996). Oceanic sea-surface temperatures from the NODC (Levitus) World Ocean Atlas (NODC, 1998) can be used to normalize boundary layer relative humidity to ocean temperature. Figure 4.4 illustrates the effect that large changes in relative humidity have on the $\delta^{18}O$ of marine precipitation.

Lowland Recycling

Several authors have described the isotopic evolution of water vapor as it is transported across lowland South America (Salati et al., 1979; Matsui et al., 1983; Martinelli et al., 1996; Gat, 2000). In its simplest form this process can be described by a Rayleigh equation:

Eq. 4.5 $$\delta_{out} = (\delta_{in} + 1000) f^{(\alpha^* - 1)} - 1000$$

where δ_{in} and δ_{out} are the isotopic composition of water vapor entering and leaving the basin, *f* is the fraction of incoming moisture that leaves the basin (export fraction, $f = F_{out}/F_{in}$) and α^* is the equilibrium vapor-liquid fractionation factor. In a true Rayleigh process all vapor lost from the atmosphere as precipitation would be removed from the

system as runoff. However in a real-world model some of the precipitation must be added back to the atmosphere through evapotranspiration from the land surface. The parameter *f* in Eq. 4.5 thus describes the effect of moisture export on the isotopic composition of atmospheric water vapor. The effect of less efficient moisture recycling and export (lower *f*) is to decrease the ^{18}O content of water vapor leaving the lowlands (Fig. 4.4) and increase the amount of incoming moisture (F_{in}) leaving the continent as runoff.

The recycled water is a mixture of transpired and evaporated waters which differ in their isotopic composition: transpiration is non-fractionating ($\delta_T=\delta_p$) while water vapor derived from evaporation is isotopically lighter than the precipitation ($\delta_E<\delta_p$). Because transpired water is isotopically equivalent to the atmospheric moisture from which it is derived, it has no isotopic effect in the Rayleigh formulation above and can be ignored. Isotopic studies indicate that transpiration accounts for 60-80 % of the total evapotranspiration in the lowlands (Gat and Matsui, 1991; Victoria et al., 1991). In this work we make the assumption that all return flux to the atmosphere is via transpiration (non-fractionating). This assumption simplifies the calculation to a modified Rayleigh equation but leads to a small systematic underestimate of the export fraction from isotopic data. This bias (discussed below) is small compared to the uncertainty of the evaporation/ transpiration ratio in the past and other aspects of the isotope model.

A hidden variable in Eq. 4.5 is temperature, through its effect on the fractionation factor (α^*). We assume that the fractionation occurs at a temperature of 20°C, which roughly corresponds to the average lifting condensation level in lowland

Venezuela (1200-1500 m). The incoming water vapor (δ_{in}) is assumed to have an isotopic composition equal to the steady-state ocean evaporation $\delta^{18}O$ from Eq. 4.4.

Orographic Uplift and Precipitation

Uplift of the airmass to the high Andes is an extension of the Rayleigh distillation process with a variable, temperature dependent fractionation factor. We use the formulation proposed by Pierrehumbert (1999) and detailed in Rowley et al. (2001), where altitude gradients in temperature and specific humidity are derived from standard meteorological formulae. The isotopic gradient with altitude is then calculated from these values and numerically integrated with height to yield the altitude-isotope relationship. Following Pierrehumbert (1999), the liquid-vapor isotopic fractionation factor (Horita and Wesolowski, 1994) and saturation vapor pressure relative to water was used for temperatures above 273K. The ice-vapor fractionation factor and saturation vapor pressure relative to ice were used for temperatures below 253K. Between 253-273K, values for the saturation vapor pressure and isotopic fractionation factor were linearly interpolated from the values at 253 and 273K. This formulation accounts for the coexistence of ice and supercooled water at these temperatures in the deep convective systems typical of tropical precipitation. Kinetic effects during snow formation were ignored but are likely insignificant because most precipitation at the elevation of the lakes in this study falls as rain. Figure 4.5 illustrates the vertical gradient of $\delta^{18}O_p$ for different values of the boundary layer water vapor $\delta^{18}O$ (a function of the lowland recycling ratio and oceanic evaporation).

The boundary conditions which must be known to calculate the altitude-water vapor $\delta^{18}O$ relationship are: the lowland boundary layer temperature, humidity and

water vapor $\delta^{18}O$. The boundary layer $\delta^{18}O$ is taken as the output from the Rayleigh fractionation in the lowlands (Eq. 4.5). Temperature and humidity are constrained by modern climate data. For past climates we assume that the boundary layer temperature and humidity are determined in the oceanic boundary layer (consistent with the modern data). The effect of variations in temperature and humidity on precipitation $\delta^{18}O$ were investigated in a series of sensitivity experiments detailed below.

Predicting the precipitation $\delta^{18}O$ from the vertical gradient in vapor $\delta^{18}O$ involves and additional variable: precipitation height (Pierrehumbert, 1999; Thompson et al., 2000). Precipitation reaching the ground surface does not form at the ground elevation, rather it originates at some elevation range above that surface. Following Rowley et al. (2001) we calculated precipitation weighted averages of $\delta^{18}O_p$ for several elevation ranges above the ground surface (0-1000, 500-1500, 1000-2000 and 1500-2500 m). We tested these different precipitation height ranges against modern precipitation, surface and groundwater $\delta^{18}O$ data from tropical mountains in Cameroon, Bolivia, Peru (Gonfiantini et al., 2001) and Venezuela (Seiler, 2000; IAEA/WMO, 2001). The optimal fit for the vertical precipitation $\delta^{18}O$ gradient was for precipitation elevations 0-1000 m above the land surface, independent of the absolute $\delta^{18}O_p$ values. When the lowland boundary layer $\delta^{18}O$ is calculated from Eqs. 5-6 using modern climate data, precipitation elevations greater than 0-1000 m give precipitation $\delta^{18}O$ values which are too depleted for the modern precipitation data. We chose therefore to use an integrated precipitation elevation 0-1000 m above the ground surface. The conclusions we draw in this paper are insensitive to the choice of precipitation height if the height has remained constant through time. This is because the isotope shifts we

discuss are very similar for all precipitation heights even though the absolute isotope values are different.

Discussion

The isotopic records from LVA and LVB have nearly identical long-term trends towards more negative $\delta^{18}O_d$ values during the Holocene (Fig.4.6). The absolute difference in $\delta^{18}O_d$ between LVA and LVB is the result of greater evaporative enrichment of LVB and can be used to infer past variations in the regional moisture balance (see Chapter 3) Here, we concentrate on the long-term trend shared by both isotope records. This pattern is the result of a change in the composition of input water (not P/E) and suggests a shift of -2.4 ‰ in the $\delta^{18}O$ composition of precipitation during the last 10,000 years. Changes in the oceanic $\delta^{18}O$, evaporation conditions, the lowland recycling ratio and orographic uplift conditions could all contribute to this shift. It is important to note the jump in isotope value for the upper three data points in LVA. Given the similarity between the LVA and LVB records prior to these points, this shift appears anomalous and it is difficult to hypothesize a climatic process which would cause such a change in LVA and not LVB. At this point we do not have a good explanation for the shift and do not use these data points in this paper. As a final note, both the short-term shifts and long-term trends in the $\delta^{18}O_d$ records do not correspond to floristic changes in the diatom assemblage. This observation is in accord with previous work showing no inter-species effects on $\delta^{18}O_d$ (Brandriss et al., 1998; Moschen et al., 2005).

Ocean Evaporation and $\delta^{18}O$

The oceanic $\delta^{18}O$ has decreased by 0.3 ‰ during the Holocene due to addition of ^{18}O-depleted water from melting Pleistocene ice sheets (Fig. 4.6). Correcting the diatom $\delta^{18}O$ records for the change in the oceanic reservoir decreases the isotopic shift during the Holocene, however it does not account for the majority of the observed $\delta^{18}O$ decrease (Fig. 4.6). Changes in the oceanic surface temperature and/or relative humidity could also affect the $\delta^{18}O$ of moisture advected to South America, and ultimately the $\delta^{18}O_p$ in the Andes. However, an increase in temperature of several tens of degrees would be required to cause a 2.4 ‰ decrease in the water vapor entering South America (Fig. 4.7), making temperature an unlikely cause of the shift. Corroborating this, sea-surface temperature (SST) records from a number of tropical Atlantic and Caribbean sites show only small changes during the Holocene (Rühlemann et al., 1999; Lea et al., 2003; Schmidt et al., 2004). Alternatively, a decrease of ~16 % in the relative humidity of the atmospheric boundary layer would also be sufficient to cause a 2.4 ‰ decrease in the precipitation $\delta^{18}O$ (Fig. 4.7). However, the tight clustering of relative humidity and temperature values in the oceanic source region for S. American water vapor (Fig. 4.7) suggests that this is at most a minor cause of isotopic changes over S. America. Given the homogeneity of modern relative humidity and temperature values over the tropical Atlantic even large displacements in atmospheric circulation patterns over the ocean would not have a significant effect.

The inference that changes in oceanic conditions did not cause the isotope shift in the Andes is supported by a speleothem record from coastal Venezuela. The $\delta^{18}O$ of speleothem calcite from Cuevo Zárraga (11° 10.51' N, 69° 37.68' W, 960 m; Fig. 4.1),

indicates that the $\delta^{18}O$ of coastal precipitation has been relatively constant during the Holocene (Fig. 4.10, González and Gómez, 2002)). This provides empirical support for little or no change in the isotopic composition of water advected into Venezuela during the Holocene (except for the $\delta^{18}O_p$ change due to melting ice-sheets).

Changing lowland export and precipitation height

Changes in the water balance of the lowlands can have a significant impact on the isotopic composition of moisture reaching the tropical Andes. We can estimate the modern *f* ratio (the lowland export fraction) using surface water, ground water and precipitation data from Venezuela (gray diamonds in Fig. 4.5). These data cluster around the altitude-$\delta^{18}O_p$ line for f=0.8 suggesting the *f* ratio in lowland Venezuela is in this range today. Figure 4.8 shows the range of precipitation $\delta^{18}O$ values at the elevation of LVA and LVB calculated with different precipitation heights and *f* ratios. As discussed above, the best fit to modern data puts the precipitation height at 0-1000 m above the ground surface. Using this range and the modern precipitation $\delta^{18}O$ at LVA-LVB (-10.6 to -11.4 ‰), the modern *f* ratio is between 0.76 and 0.82. The same calculation for the *f* ratio 10,000 years ago (when precipitation was +2.4 ‰ from modern) yields a range of 0.97 to 1. Thus, a modern *f* ratio that is ~78 % that of the *f* ratio 10,000 years ago is needed to account for a –2.4 ‰ shift in precipitation at the elevation of LVA-LVB. This is further illustrated in Fig. 4.9, which shows the change in the *f* ratio required to cause a given isotope shift.

Changes in precipitation height have been invoked to explain shifts in the isotopic composition of high-altitude tropical precipitation (Thompson et al., 2000). Thus, it is possible that changes in the precipitation height were responsible for the

isotope shift observed in LVA-LVB. An increase in the precipitation height of 945 m would be necessary to cause an isotope change of –2.4 ‰ during the Holocene. However, the modern precipitation height appears to be just above the surface, thus the early Holocene precipitation height would need to lie below the ground surface. Additionally, it is difficult to justify large changes in precipitation height for the orographically driven upslope precipitation which characterizes the region. Thus, although precipitation height changes cannot be ruled out, the available data suggests they were not the cause of the precipitation $\delta^{18}O$ changes.

Evapotranspiration and Seasonality

In addition to a change in the runoff ratio (*f*), the decrease of $\delta^{18}O_p$ observed in the Venezuelan Andes could be caused by an increase in the amount of evaporation relative to transpiration in the lowlands. Evaporation returns water to the atmosphere which is depleted in ^{18}O compared to transpired water. Increasing the ratio of evaporation to transpiration would thus cause a decrease of the $\delta^{18}O_p$ in the Andes. However, two lines of evidence suggest this was not a significant factor in the decrease. First, a –2.4 ‰ shift in the $\delta^{18}O$ of atmospheric water vapor leaving the lowlands would require that evaporation change from approximately 0 % to almost 100 % of the lowland evapotranspiration (Fig. 8 in Gat and Matsui, 1991). Clearly this is an unrealistically large change. Second, the type of vegetation cover (grasslands vs. forest) has a marked impact on the ratio of evaporation to transpiration (Moreira et al., 1997). However a lowland pollen record from Lake Valencia, Venezuela (Fig. 4.1) shows minimal changes in the vegetation cover during the Holocene (Bradbury et al., 1981). Absent the vegetation changes, it is difficult to explain a large change in the

evaporation/transpiration ratio. These arguments suggest that an increase of the evaporation/transpiration ratio was not a significant cause of the isotopic shift.

The seasonality of precipitation is another factor which may change the average $\delta^{18}O_p$. In inland tropical locations, precipitation $\delta^{18}O$ during the wet season is more negative relative to the dry season. Thus, an increase in the contribution of wet-season precipitation to the total precipitation would result in more negative annual averages. The limited data in Venezuela suggests that the range of monthly average $\delta^{18}O_p$ is ~8 ‰ (IAEA/WMO, 2001) and that the wet season accounts for 80-95 % of the annual precipitation near the study site (Azocar and Monasterio, 1980). If the average dry season minus average wet season difference is 8 ‰, isotopic mass-balance calculations indicate a +2.4 ‰ change of the average $\delta^{18}O_p$ (to give the early Holocene value) requires that the wet season contribution to the total precipitation decrease from 80-95 % to 50-65 %. A more realistic scenario, where the difference in the seasonal averages is ~4 ‰ yields a decrease to 20-35 %. (The smaller wet/dry $\delta^{18}O$ difference better represents the average dry and wet season values compared to the total range of $\delta^{18}O$.)

Are such changes in the seasonality of precipitation realistic? In order to produce the isotope shift, dry-season precipitation would have to become a dominant source of moisture during the early Holocene. An increase in the duration of the wet season cannot be invoked because the isotopic composition of this precipitation is more negative. Thus, a significant enhancement of dry-season precipitation would have to occur without the ITCZ circulation which provides most precipitation at present. It is difficult to suggest any mechanism which could explain such a shift, and pollen

histories from both low- and high-elevation sites in Venezuela do not support this scenario (Bradbury et al., 1981; Rull et al., 2005).

Reconstructing the Continental Hydrologic Balance

The preceding discussion indicates that a likely cause for the decreasing $\delta^{18}O_p$ in the Venezuelan Andes lake isotope records is a decreasing export ratio ($f=F_{out}/F_{in}$) of northern South America. The implication is that the fraction of water vapor entering the continent (F_{in}) which is lost as runoff ($R=F_{in}(1-f)$) has increased during the Holocene. This conclusion indicates changes in the partitioning of moisture between the lowlands and Andes, independent of the absolute intensity of the hydrologic cycle (proportional to F_{in}). In this section we address three questions which arise from this conclusion. First, is the LVA-LVB isotope record a local signal, or does it capture large-scale variations in S. American hydrology? Second, how has the intensity of the hydrologic cycle changed in conjunction with the lowland export ratio? Third, what factor(s) could be responsible for the change in lowland moisture export?

Isotope histories from three high-altitude ice cores in the tropical Andes are available to compare with the LVA-LVB record (Fig. 4.1). These isotope records primarily reflect changes in the composition of precipitation, similar to the LVA-LVB data. The data from Huascarán, Peru (Thompson et al., 1995; Thompson, 2001) and Illimani, Bolivia (Ramirez et al., 2003) bear a striking resemblance to the LVA-LVB record (Fig. 4.10). Both histories are dominated by trends which are nearly identical to the LVA-LVB data. In contrast, the isotope record from Sajama, Bolivia (not shown, Thompson et al., 1998) shows little trend during the Holocene and is dominated by century-scale variability. Contributions from locally derived water vapor (Ramirez et

al., 2003) combined with variable wind ablation of surface snow (Hardy et al., 2003) may explain why the Sajama history is so different from the Illimani and Huascarán records. Given the greater proximity of Illimani and Huascarán to the Amazon basin, we concentrate on the histories from these sites as more faithful records of the isotopic composition of water vapor exported from the lowlands.

The changes of the f ratio during the Holocene inferred from the lake isotope records in the Venezuelan Andes could also explain the isotope shifts observed at Nevados Illimani and Huascarán. To illustrate this we modeled the isotope shifts expected at Illimani and Huascarán if the LVA-LVB record is assumed to be a faithful recorder of changes in the export of lowland moisture to the high Andes. First, the Holocene evolution of the f/f_o ratio was constrained by the $\delta^{18}O_p$-f/f_o relationship in Fig. 4.9 and a linear fit to the isotope shift in LVA and LVB (Fig. 4.6). Next, the isotope shift at the elevation of each record was calculated using these f/f_o ratios and the f_o value which provides the best fit to the absolute values of Holocene isotope history (the choice of f_o affects the absolute value, not the shape of the modeled curve). Finally, the $\Delta\delta^{18}O_{sw}$ was added to the modeled isotope values. The results from this modeling exercise fit the ice core isotope records very well (dashed lines, Fig. 4.10). This fit suggests that the LVA-LVB data is capturing variations in the lowland hydrology which occurred throughout tropical S. America.

As an additional exercise, the isotopic composition of Amazon River water was calculated using the f/f_o history inferred from the LVA-LVB record and compared to an isotope record of Amazon River discharge during the Holocene. The calculation used a value for f_o (0.45) which provides the correct isotope signature for the modern Amazon

River (-5 ‰ VSMOW, Maslin and Burns, 2000). This calculated runoff record was then corrected for the $\Delta\delta^{18}O_{sw}$ and the amount of runoff was assumed proportional to (1-*f*) (from mass balance). Finally, the isotopic composition of a mixture of Amazon River and ocean water ($\Delta\delta^{18}O$) was calculated for comparison to the $\Delta\delta^{18}O$ record from the Amazon Fan (Maslin and Burns, 2000). This mixing calculation was scaled to the modern ratio of ocean to river water at the coring site (5:1) by using the equation:

Eq. 4.6 $$\Delta\delta_{mix} = \left(5\delta_{ocean} + \frac{1-f(t)}{1-f_o}\delta_{river}\right)\Big/\left(5 + \frac{1-f(t)}{1-f_o}\right)$$

where *f(t)* is the *f* ratio at time *t* (derived from the LVA-LVB record). Comparison of the modeled and measured isotope shifts shows a strong correspondence(Fig. 4.10). This exercise suggests that the increase in Amazon River discharge inferred from the Amazon Fan record (Maslin and Burns, 2000) could be the result of a shift in the partitioning of moisture between the Andes and the Amazon Basin. Additionally, the $\Delta\delta^{18}O$ shift observed in the Amazon Fan record is consistent with the Andean records of $\delta^{18}O_p$, without invoking any change in the intensity of the hydrologic cycle.

The similarities between the Holocene $\delta^{18}O_p$ records from both hemispheres of tropical S. America intimate that there might be a single underlying cause. Possibilities include changes in the oceanic source regions, continental temperature changes, vegetation changes in the lowlands (moisture recycling), circulation shifts driven directly by orbital variations of solar insolation or indirectly through teleconnections with other regions. As discussed previously for the LVA-LVB record, there is no evidence for Holocene changes in the oceanic source regions which could explain the isotope shifts observed in the Andes. Additionally, although continental temperatures could affect the isotope records by altering the vapor/liquid fractionation during

precipitation, the required temperature changes are quite large and no paleoclimate evidence supports such changes. A shift from forest to savanna in the tropical lowlands during the Holocene would decrease transpiration and increase evaporation and runoff, possibly decreasing the export ratio (*f*) and the $\delta^{18}O_p$ in the Andes. However pollen records from lowland tropical S. America do not support the large change in vegetation coverage which would be required to cause the isotope shifts (Haberle and Maslin, 1999; Mayle and Beerling, 2004). Finally, insolation changes due to orbital variations could be invoked to directly explain either the northern or southern hemisphere isotope records. However the effects of this insolation forcing are opposite in the northern and southern hemispheres which suggests that direct insolation forcing of climate changes are not a likely source of the isotope trend in the Andes.

Shifts in the atmospheric circulation of tropical S. America driven by changes in the equatorial Pacific may provide a unifying explanation for the isotope trends observed in the Andean records. Interannual variations of sea-surface temperatures (SSTs) in the eastern equatorial Pacific (EEP) have a significant effect on the moisture transport and the amount and isotopic composition of precipitation in tropical S. America (based upon instrumental records). Warmer SSTs and stronger latitudinal temperature gradients in the EEP cause westerly anomalies in upper tropospheric winds over S. America leading to decreased precipitation during the austral summer in the southern hemisphere Andes (Aceituno, 1988; Vuille, 1999; Garreaud et al., 2003). Precipitation in the lowlands also decreases (Aceituno, 1988; Lyon, 2004) leading to less rainout, higher *f* ratios and a higher $\delta^{18}O$ of precipitation in the Andes (Gonfiantini et al., 2001; Bradley et al., 2003; Hoffmann et al., 2003; Vuille et al., 2003; Hastenrath

et al., 2004). In Venezuela and northern S. America, higher SSTs in the EEP also lead to reduced precipitation during the boreal summer (Aceituno, 1988; Pulwarty et al., 1992; Enfield, 1996). Climate model experiments suggest the relationship between EEP SST variability and $\delta^{18}O_p$ in northern S. America is similar to the southern hemisphere tropics (Vuille et al., 2001) making EEP variability an attractive explanation for the synchronous changes in both hemispheres.

Applying the relationship between modern interannual variability of Pacific SSTs and the $\delta^{18}O$ of Andean precipitation to the observed changes in the Holocene isotope stratigraphies from the tropical Andes suggests that higher isotope values during the early Holocene resulted from warmer temperatures in the EEP. However, this suggestion does not agree with paleoclimate data and global climate model (GCM) experiments which suggests that the EEP was generally cooler during the early Holocene (Bush, 1999; Kitoh and Murakami, 2002; Liu et al., 2003; Carré et al., 2005). The relationship of interannual variability and the mean conditions of EEP SSTs to the S. American water cycle on millennial timescales is probably not straightforward. The interannual variability which dominates SSTs in the EEP today may not be a good model for millennial-scale shifts in the mean state of the tropical Pacific. Additionally, asymmetric response of the continental water cycle to warm and cold events (c.f. Poveda and Mesa, 1997) could cause a directional response to increased variability, even if the mean remains unchanged. Although paleoclimate data and climate models suggest that interannual SST variability in the EEP was lower during the early Holocene (e.g. Clement et al., 2000; Sandweiss et al., 2001; Tudhope et al., 2001; Moy et al., 2002; Koutavas and Lynch-Stieglitz, 2003), there is some evidence to the contrary

(Carré et al., 2005). It should also be noted that some records from the EEP do indicate warmer conditions during the early Holocene (Lea et al., 2000; Loubere et al., 2003), consistent with the Andean isotope histories.

While acknowledging the complexities which link SST variations in the equatorial Pacific to the hydrologic cycle of tropical S. America, we suggest that it is difficult to explain the similarity of precipitation isotope records north and south of the equator by another mechanism. Better understanding of how changes in the Pacific Ocean affect S. American climate on millennial timescales may strengthen or weaken this interpretation of the Andean isotope records. Additional records of the isotopic composition of precipitation in S. America during the Holocene may also shed light by revealing regional differences which are not apparent in the available data.

Summary & Conclusions

Diatom isotope records from two lakes in the Venezuelan Andes indicate a +2.4 ‰ shift in the $\delta^{18}O$ of Andean precipitation during the Holocene. This shift could be caused by changes in ocean evaporation conditions, transport across lowland S. America or orographic uplift to the Andes. However, several lines of evidence suggest that a change in the efficiency of water vapor transport across the lowlands is responsible for the shift. Ice cores from Nevados Huascarán, Peru and Illimani, Bolivia exhibit isotope trends which are very similar to the Venezuelan record suggesting the changes occurred in both hemispheres of tropical S. America. The interhemispheric similarity of the isotope records makes orbitally driven trends in solar insolation an unlikely primary cause for the shifts. Modern interannual variability in the equatorial Pacific Ocean has similar climate effects in both hemispheres of tropical S. America

making variability in this region an attractive explanation for the isotope trends. However, the interpretation of the millennial scale isotope histories based upon the modern teleconnections between the tropical Pacific and S. America does not agree with available paleoclimate evidence from the tropical Pacific. This may reflect additional complexity in the relationship between tropical Pacific interannual and millennial scale variability and its effects on the hydrologic cycle of S. America. At this time, a tropical Pacific source for the isotope trends is still favored but better understanding of the teleconnection between the Pacific and S. America are needed to test this theory.

Figures

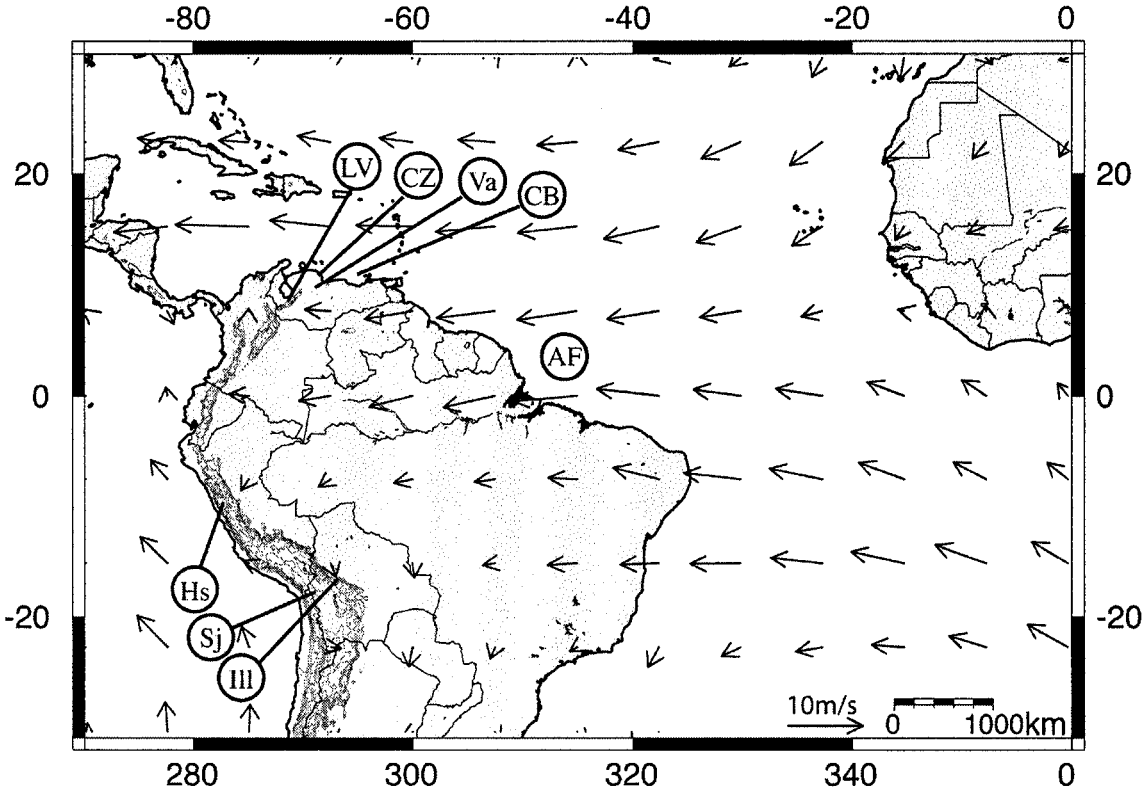

Figure 4.1 – Location of Laguna Verdes Alta, Baja and other South American isotope histories. Sites are: Laguna Verdes Alta and Baja (LV), Cuevo Zarraga (CZ), Lake Valencia (Va), the Cariaco Basin (CB), Navados Huascarán (Hs), Sajama (Sj) and Illimani (Ill), and the Amazon Fan (AF). Arrows indicate the direction and magnitude of surface winds (annual average, 1000-850mb Kalnay et al., 1996).

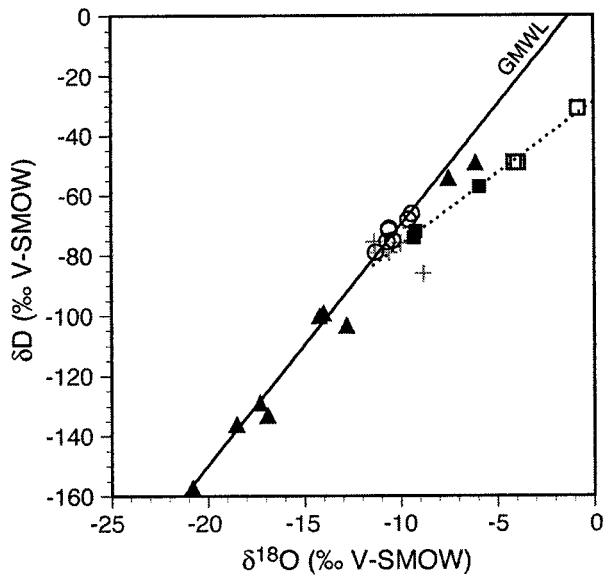

Figure 4.2 - Oxygen-18 vs. deuterium content of surface waters and precipitation from the Cordillera de Mérida, Venezuela. Precipitation samples (triangles, collected June, 2002), springs (crosses) and hydrologically open lakes (circles) fall along the global meteoric water line (GMWL). Water samples from LVA (filled squares) and LVB (open squares, collected 1999-2002) lie along an evaporative trend below the meteoric water line (dashed line).

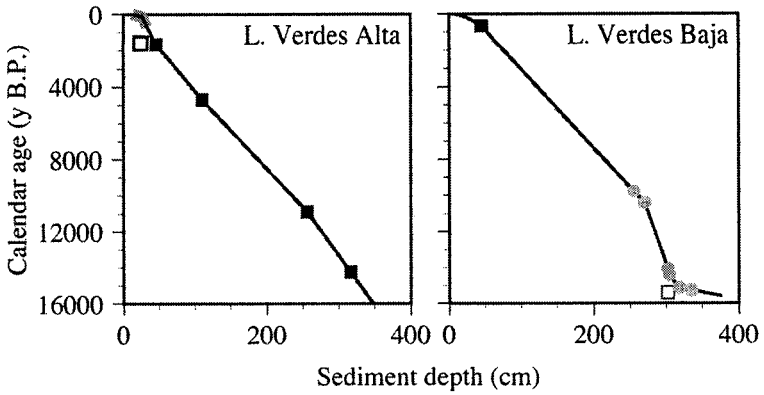

Figure 4.3 – Age-depth models for LVA and LVB derived from calibrated AMS radiocarbon ages and ^{210}Pb ages. Thin black line denotes age-depth model while solid squares are radiocarbon ages and the thick gray line represents ^{210}Pb ages. Open squares indicate radiocarbon ages not used in age models. The model for LVB is also based upon tie-points (gray circles) with LVA (see text).

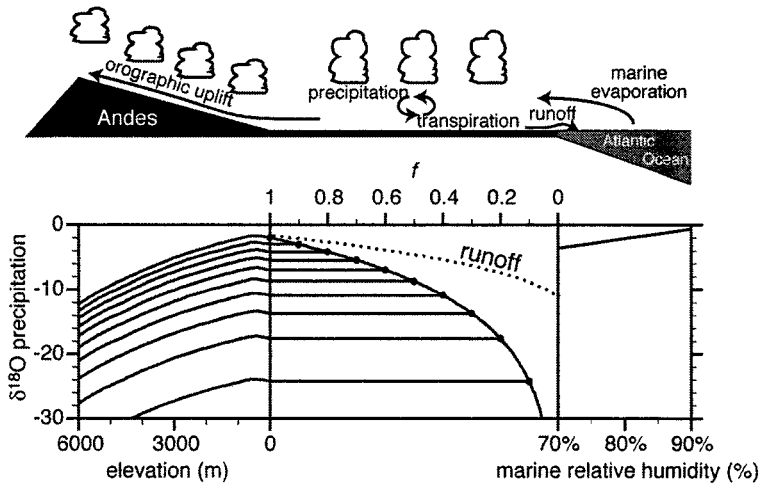

Figure 4.4 – Schematic of the evaporation, transport and uplift of water vapor from the Atlantic Ocean to the South American Andes. The lower panel illustrates variations in the isotopic composition of precipitation expected from changes in the marine boundary layer humidity (right), the fraction of evaporated moisture exported to the Andes (*f*, center) and the uplift elevation (left). Also shown is the isotopic composition of water lost as runoff.

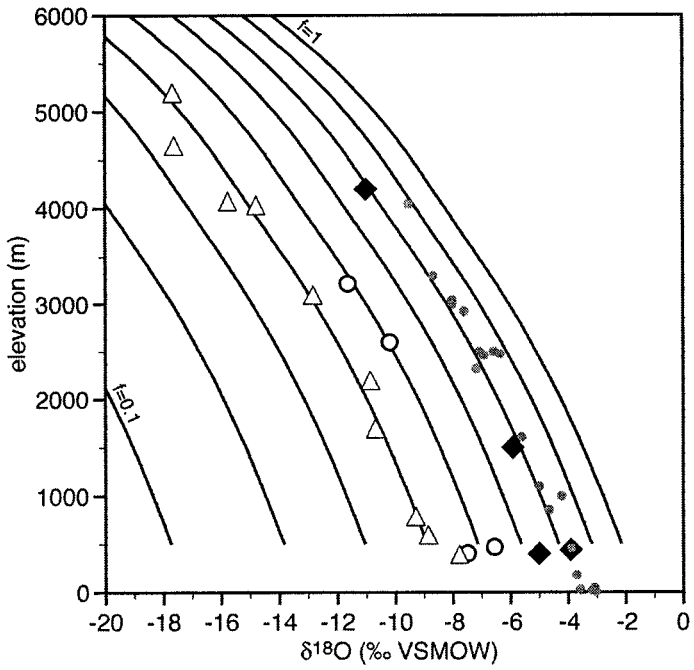

Figure 4.5 – Altitude-$\delta^{18}O$ gradients for a precipitation integration height 0-1000m above the ground surface. Each line represents a different lowland recycling ratio (*f*). Precipitation data from two altitude transects of the eastern slope of the Bolivian Andes (open triangles and circles) and Mt. Camaroon (gray circles) are plotted for comparison (Gonfiantini et al., 2001). The black diamonds are groundwater (400 m a.s.l. near Lake Valencia, Seiler, 2000)), precipitation (Maracay, 442 m and Bocono, 1500 m, IAEA/WMO, 2001) and surface water (4200 m a.s.l., data from this study) samples in Venezuela. Gradients were calculated using initial temperature and relative humidity values (24.5 °C, 79 %) which provide the best match to surface temperatures in the Venezuela Andes (Bradley et al., 1991).

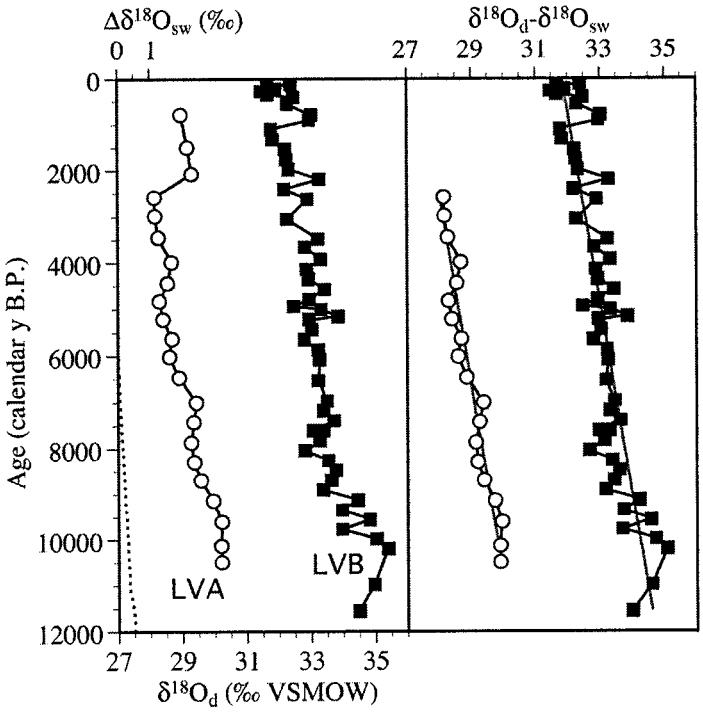

Figure 4.6 – Diatom $\delta^{18}O$ records from LVA and LVB illustrating the trend towards depleted values through the Holocene. Square data points are from LVB and circles are from LVA. The dashed line shows how the melting of Pleistocene ice sheets and resulting change in the whole ocean $\delta^{18}O$ would affect the lake isotope records (Adkins et al., 2002; Peltier, 2002). Subtracting the ocean $\delta^{18}O$ change from the $\delta^{18}O_d$ (B) provides an estimate of the Holocene shift in precipitation $\delta^{18}O$ ($2.39*10^{-4}$ ‰/y). The upper three data points from LVA are omitted in (B) because they probably do not represent precipitation $\delta^{18}O$ precipitation changes (see text).

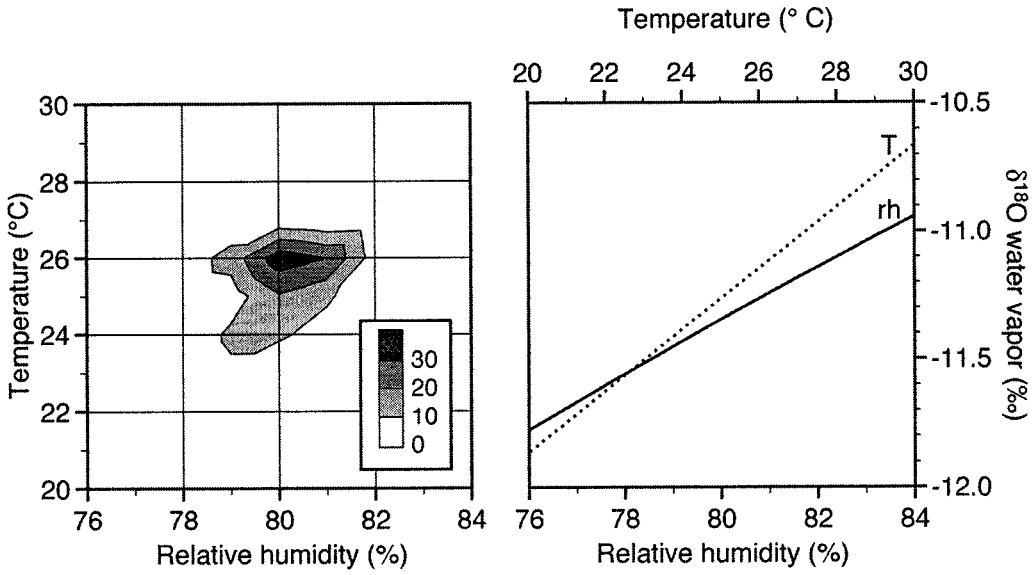

Figure 4.7 – Frequency distribution of oceanic relative humidity and temperature, and the effect of these variables on the $\delta^{18}O$ of marine atmospheric water vapor. The frequency distribution (n=199) was calculated from annual average Atlantic surface air temperature and relative humidity in the region 20S-20N, 285-340E, excluding land areas (Kalnay et al., 1996).

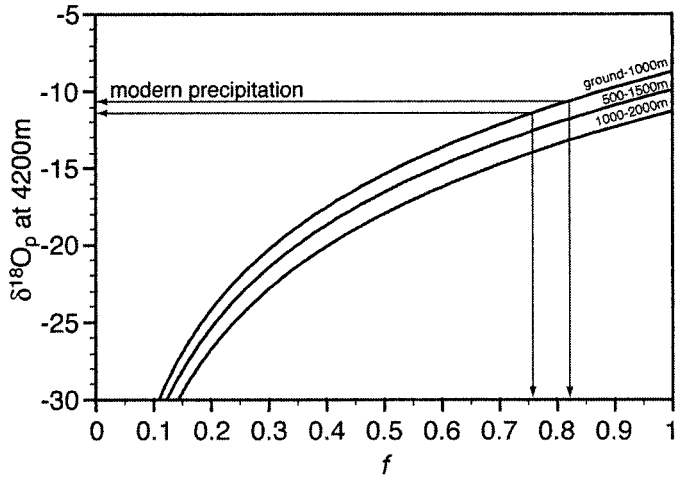

Figure 4.8 – Oxygen isotopic composition of precipitation at the elevation of LVA and LVB as a function of the elevation above the land surface where the precipitation is derived. The modern precipitation $\delta^{18}O$ indicates a lowland *f* ratio between 0.76 and 0.82.

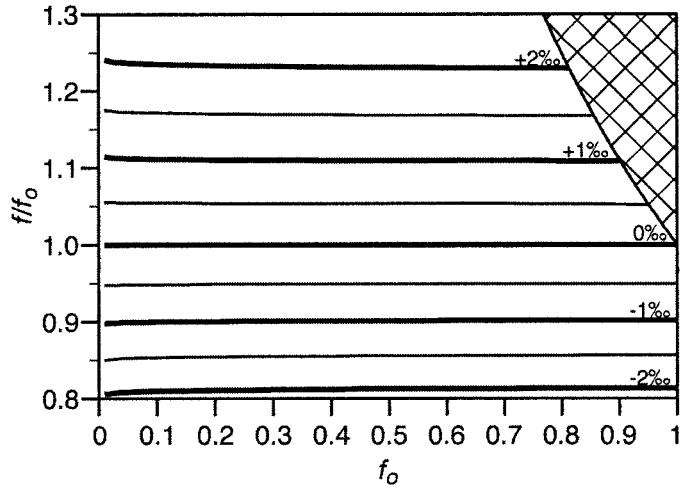

Figure 4.9 – Changes in the $\delta^{18}O$ of precipitation at the altitude of LVA and LVB expressed as a function if the initial export fraction (f_o) and the fractional change in the export fraction (f/f_o). Although an integration height of 0-1000 m was used for this plot, other integration heights yield nearly identical results. Cross-hatching encompasses f_o – f/f_o pairs which will result in f>1.

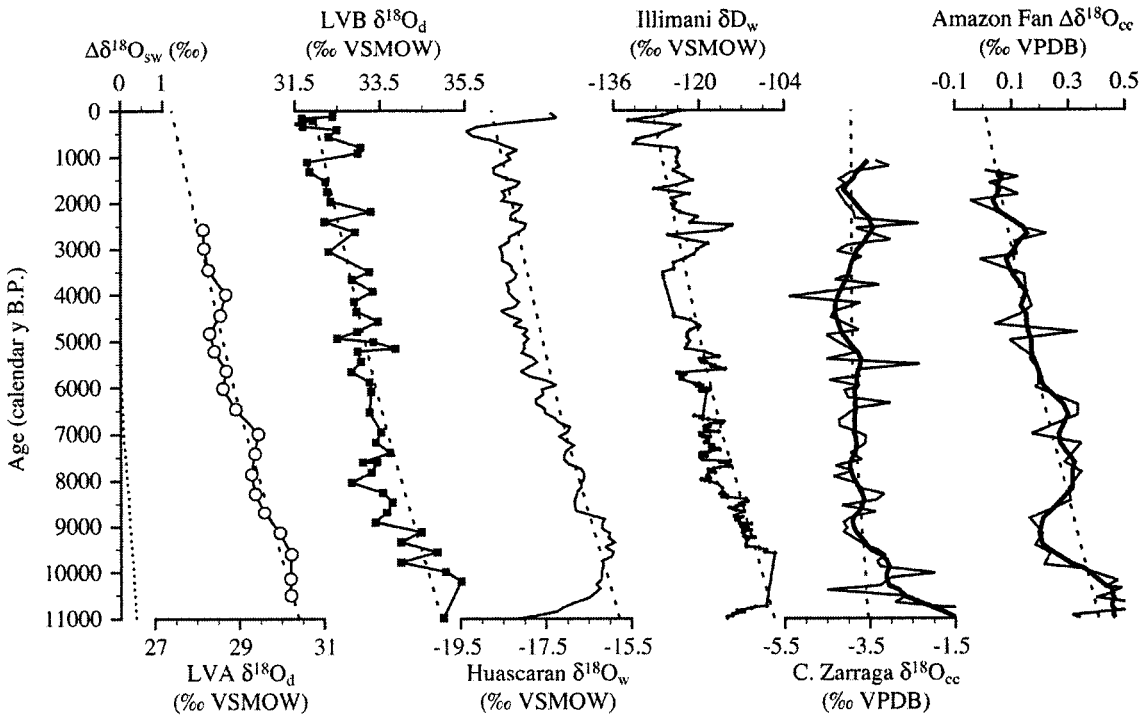

Figure 4.10 – Isotope records from tropical South America. Materials analyzed include diatom (d) water (w) and calcite (cc) which are reported on either the VSMOW or VPDB international isotope scales. Isotopic shifts are nearly equal on the two scales. The δD record from Illimani was scaled using the ratio of the $\delta^{18}O/\delta D$ equilibrium fractionation factors for vapor-liquid transition (~8). This scaling is validated by measurements of the $\delta^{18}O$ and δD of precipitation and surface waters near Illimani (Gonfiantini et al., 2001; Abbott et al., 2003). The isotopic shift expected due to changing seawater isotopic composition ($\Delta\delta^{18}O_{sw}$) is shown on the left. Dashed line overlay on each record (except Cuevo Zarraga) indicates an isotopic shift modeled from the LVA and LVB records (see text). The dashed line over the Cuevo Zarraga record shows the expected $\delta^{18}O_p$ trend from the ocean $\Delta\delta^{18}O_{sw}$ for this coastal location.

CHAPTER 5

SUMMARY AND CONCLUSIONS

The significant findings of this dissertation are summarized in the following chapter. Unresolved questions and directions for further research are also discussed.

Decadal Climate Variability 1,000 A.D. to Present

During the past 1,000 years significant changes in climate occurred in the Venezuelan Andes. The record of clastic sedimentation in Laguna Blanca (Fig. 5.1) indicates a period of wetter climate between 1300 to 1820 A.D. This wet period is corroborated by increased abundance of Cyperaceae (sedge) pollen in a nearby peat core from the Páramo de Las Piedras Blancas (Fig. 5.1, Rull et al., 1987). Decreased abundance of tree pollen during this interval indicates a lowering of tree line by approximately 200 m. Associated with the wet period identified in L. Blanca, four glacier advances occurred in the Laguna Mucubají watershed (Fig. 5.1). The combination of lower tree line and glacier advances indicates cooler climatic conditions. The permutations of precipitation and temperature change which explain the glacier advances is obtained by calculating the equilibrium line altitude (ELA) depression and modeling the heat and mass-balance changes necessary to sustain the glacier at the lower ELA. The precipitation and temperature changes which could explain the lower tree-line are calculated from the modern relationship between tree line and these variables. The intersection of the glacier and tree-line temperature-precipitation relationships indicates a temperature depression of –2.3 to –3.4° C and 25 to 73% increase of precipitation during the glacial advances.

The glacier advances and climate change during the past millennium documented in the Venezuelan Andes correspond with climate variability in nearby tropical locations. The onset and cessation of recent glacial activity in L. Mucubají occurs at a similar time to late Neoglacial advances and retreat throughout the South American Andes (Seltzer, 1990; Rosqvist, 1995; Glasser et al., 2002). Higher P/E values on the Yucatan Peninsula (Punta Laguna, Curtis et al., 1996) and stronger trade winds over the Cariaco Basin (Black et al., 1999) correspond with the moisture fluctuations identified in L. Blanca and the glacier advances documented in L. Mucubají. Cooler sea surface temperatures in the Caribbean (Winter et al., 2000; Watanabe et al., 2001; Haase-Schramm et al., 2003) have also been documented during the period of glacial advances in L. Mucubají.

Variations in solar irradiance provide one possible explanation for the glacier advances in the Venezuelan Andes. Each glacier advance identified in L. Mucubají corresponds with a minima in reconstructed solar irradiance. However, prior to the late-Holocene advances there is no evidence of glacier activity or higher P/E associated with irradiance minima suggesting that irradiance variations may provide a second-order control on climate fluctuations. It is possible that global cooling during the Little Ice Age provided the primary control by decreasing evaporation (higher P/E balance) and allowing glaciers to grow in the Mucubají watershed. Within this period of global cooling, variations in solar irradiance were able to cause changes in the P/E balance and possibly temperature which led to the variations around the mean state. This theory could be tested with sediment records from proglacial lakes on the Pico Bolívar massif in the Cordillera de Mérida. These peaks are currently glaciated and thus more likely to

have supported glaciers prior to the LIA. Reconstruction of glacier activity prior to the LIA would shed light on both cause of climate fluctuations within the LIA and the circumstances which led to the establishment of glaciers during the LIA.

Millennial Climate Variability, 10,000 y B.P. to Present

Proxy data from sediments in Lagunas Verdes Alta, Baja and Laguna Blanca (Fig. 5.1) indicate large changes in the climate of the Venezuelan Andes during the last 10,000 years. The sediment record from L. Blanca shows a wet interval during the early Holocene followed by significantly drier conditions during the middle Holocene. Increased P/E during the late Holocene culminated in maximum wetness during the LIA. Diatom species and isotope composition of sediments in L. Verdes Alta and Baja suggest a similar patter of P/E change. During the early Holocene, lower diatom inferred salinity and a more negative isotopic composition of lake water indicates a higher P/E balance and wetter climate. The middle Holocene situation was essentially the reverse: higher salinity and more positive isotope composition point to lower P/E conditions and a drier climate. During the late Holocene, slightly more negative isotopes along with generally lower salinity signify wetter conditions.

Comparison of the sequence of wet early-, dry middle- and wet late-Holocene climate in the Venezuelan Andes with other locations in Venezuela reveals an interesting correspondence. The timing of changes in the paleoclimate records from L. Valencia (Fig. 5.2) is very similar to the Andean records. However, the sign of the changes is reversed such that L. Valencia is drier when the Venezuelan Andes is wet and *vice versa*. The antiphasing of climate in the Andes and L. Valencia region is also present in anomalies of modern rainfall (Fig. 5.2, Pulwarty et al., 1992) implying this is

fundamental feature of Venezuelan climate. The limited paleoclimate records from the *tepuis* tablelands of eastern Venezuela (Fig. 5.2) suggest this region behaves similarly to the L. Valencia region (Schubert and Fritz, 1985). An indication of the spatial extent of mid-Holocene aridity in the Andes comes from the record in marine core M35003-1 (Fig. 5.2) of terrigenous sediment flux from the Orinoco River (Vink et al., 2001). Although the flow in the Orinoco River is derived from both eastern and western Venezuela, nearly all of the suspended sediment in the river is supplied by the Venezuelan and Columbian Andes (Edmond et al., 1996). Thus, reduced terrigenous sediment in M35003-1 during the middle Holocene may indicate widespread aridity in the northern hemisphere Andes.

Another important comparison is to paleoclimate studies of the Cariaco Basin (Fig. 5.2). This site provides a high-resolution record of both terrestrial and marine changes during the Holocene. During the dry season, strong easterly trade winds cause upwelling and deposition of a light colored layer rich in biogenic calcite. During the wet season, terrigenous input leaves a dark layer of inorganic sediment. A number of studies have produced records of sediment properties during the Holocene which are thought to record variations in the dry *versus* wet season sediment contribution (Hughen et al., 1996; Hughen et al., 1998; Peterson et al., 2000; Haug et al., 2001; Piper and Dean Jr., 2002). However, these records do not agree with each other and it is not obvious which sediment property is the best proxy for climate. Perhaps the most detailed study of the sediment geochemistry is that of Piper and Dean (2002). Their work indicates minimum terrigenous sediment flux during the middle Holocene relative to the early and late Holocene. Although this could indicate a local reduction of

terrigenous sediment, the terrigenous fraction in Cariaco Basin sediments is a combination of local sources and long-distance transport from the Orinoco and Amazon rivers (Clayton et al., 1999). Thus, reduced siliciclastic flux during the middle Holocene could reflect greater aridity in the coastal region near the basin or less sediment from the Orinoco or Amazon Rivers. An aridity signal from local sources is supported by records of Cariaco Basin hydrology. The oxygen isotopic composition of foraminifera tests (Lin et al., 1997) and sea-surface temperatures inferred from foraminifer calcite Mg/Ca ratios (Lea et al., 2003) indicate annual average conditions during the middle Holocene were more similar to the dry upwelling period. In contrast, early- and late-Holocene conditions were more similar to the wet season. These data are consistent with a shorter wet season and coastal aridity during the middle Holocene. Although there is disagreement between different proxy records from the Cariaco Basin, the work of Piper and Dean (2002) is generally consistent with the sediment reflectance records of Peterson et al. (2000) and Hughen et al. (1996; 1998). Further work is necessary to evaluate whether these records are the best indicators of terrestrial climate.

The pattern of millennial climate variability in Venezuela appears to be either a wet-dry-wet or dry-wet-dry sequence during the Holocene, the sign depending upon location. Comparison with climate records from North, Central and South America suggests that this pattern is widespread in the neotropics (Fig. 5.3). Records from Haiti, Panama, Venezuela, Columbia, the Galápagos Islands (eastern equatorial Pacific), Bolivian/Peruvian *altiplano* and northern Argentina (Fig. 5.3, Table 5.1) contain this pattern while a few locations show the same pattern but the sign is reversed (dry-wet-dry). The locations which exhibit these patterns group either near the northern and

southern edges of the tropical monsoon climate regime or along the Andes near the equatorial Pacific. In contrast, sites in equatorial Amazonia and the central Peruvian Andes exhibit monotonic trends of decreasing aridity during the Holocene (Fig. 5.3).

The similar timing and sign of Holocene climate anomalies north and south of the equator makes direct insolation forcing a doubtful cause of the changes. During the last 10,000 years, precession of the equinoxes was the primary reason for changes in the seasonality and latitudinal distribution of solar radiation. The sign of precessional changes is reversed in the two hemispheres, thus climate shifts in the northern and southern hemispheres should be opposite in sign if direct insolation forcing were the cause.

An alternative explanation for the similar climate change in both the northern and southern hemisphere of S. America may be from the effects of the tropical Pacific. Although precipitation in most of tropical S. America is derived from water vapor over the Atlantic Ocean, conditions in the tropical Pacific exert a substantial control on the transport of moisture across lowland South America to the Andes. At least in the southern Andes it is actually the transport of water vapor from the adjacent lowlands which controls precipitation variability (Garreaud, 2000). In the Venezuelan Andes, there is a negative correlation between wet season precipitation and equatorial Pacific SSTs (Pulwarty et al., 1992). Thus, variations of SSTs in the tropical Pacific Ocean may be able to explain synchronous changes in both hemispheres.

Evolution of H and O Isotopes in Andean Precipitation 10,000 y B.P. to Present

The similarity of precipitation isotope records from both hemispheres of the tropical Andes is intriguing. The trend towards more negative isotope values during the

Holocene may indicate a gradual decrease in the fraction of water vapor entering lowland S. America which is exported to the Andes (the export fraction). Intuitively this might suggest that the lowlands became wetter during the Holocene while the Andes became drier. However, it is difficult to relate the changing export fraction directly to lowland and Andean climate variability. It seems likely that the isotope signal reflects the moisture balance of the tropical lowlands and is decoupled from local climate effects. This is a logical hypothesis because, at least on the Bolivian *altiplano*, precipitation variability is controlled by the atmospheric circulation which brings moisture to the Andes. Thus, the local climate signal is decoupled from the lowlands and will only agree with the isotope signal to the degree that the local (Andean) moisture balance is correlated with the lowland moisture balance. Consistent with this idea, the monotonic isotope trend is recorded in locations where the regional climate signal is actually wet-dry-wet during the Holocene (Venezuela, Bolivia). This indicates that the isotope signal reflects the moisture balance history of the airmass which precipitated at the proxy site rather than local climate. The trend towards negative isotope values during the Holocene would thus be construed as an indicator of wetter conditions in the lowlands.

Directions for Further Research

1. The Little Ice Age stands out as a unique climate event in Venezuela during the last several thousand years. Solar irradiance changes may have caused variations in glacier activity during this interval, however, solar variations similar to those during the LIA have occurred during the Holocene and did not lead to glacier advances. Perhaps the local response to solar irradiance variation is P/E change while global cooling is

necessary to establish glaciers. Sediment records from watersheds which are currently glaciated (and which presently receive glacial meltwater) would improve our understanding of the timing and cause of glacier fluctuations and climate. These sites are more likely to contain a record of pre-LIA glacier fluctuations which would extend the results from this work.

2. Antiphasing of climate change in the Andes and Lake Valencia appears to occur at interannual to millennial timescales. This was an unexpected finding which highlights the complexity of regional climate. Additional paleoclimate records distributed in different climate zones of Venezuela would provide a valuable contribution to understanding this pattern.

3. Proxy records from the lowland tropics of South America could improve our understanding of the spatial variability associated with Holocene climate trends. A majority of the paleoclimate records from the Amazon Basin have used pollen analysis as their primary tool. Although palynology can provide significant information about changes in terrestrial and aquatic ecosystems, the relationship between vegetation and climate is not always straightforward. It would be a valuable contribution to develop paleoclimate records from lowland tropical sites which use proxies which may be more easily interpreted in terms of climate.

4. The reconstructions of Holocene climate from different proxy records in the Cariaco Basin need to be reconciled. Better understanding of the source of terrigenous material deposited in the basin, the changes in terrigenous flux during the Holocene and its climate interpretation would be a valuable addition to regional and global climate records.

Tables

Table 5.1 – Paleoclimate records in the neotropics which were compared to climate records in Venezuela.

#	Site	Country	Lon.	Lat.	Elev. (m)	Reference
1	Laguna Taypi Chaka Kkota	Bolivia	291° 39'	-16° 12'		(Abbott et al., 1997)
2	Laguna Potosi	Bolivia	294° 19'	-19° 38'		(Abbott et al., 2003)
2	Laguna Paco Cocha	Peru	288° 8'	-13° 54'		(Abbott et al., 2003)
3	Lake Titicaca	Bolivia/ Peru	290° 30'	-15° 45'	3800	(Baker et al., 2001b)
4	Lago Calado	Brazil	299° 25'	-3° 16'	23	(Behling et al., 2001)
5	Lake Valencia	Venezuela	292° 15'	10° 10'	400	(Bradbury et al., 1981)
6	Cuenca de México	Mexico	261° 0'	19° 30'	2240	(Bradbury, 1989)
7	Lake La Yeguado	Panama	279° 9'	8° 27'	650	(Bush et al., 1992)
8	Cuenca de Mexico, Lake Chalco	Mexico	261° 0'	19° 30'	2240	(Caballero and Guerrero, 1998)
9	El Junco Lake	Galapagos Islands	270° 15'	-1° 0'	500	(Colinvaux and Schofield, 1976b)
10	Lake Yaguarcocha	Ecuador	281° 55'	0° 23'	2201	(Colinvaux et al., 1988)
11	Lake Titicaca	Bolivia/ Peru	290° 30'	-15° 45'	3800	(Cross et al., 2000)
12	Botuverá Cave	Brazil	310° 50.7'	-27° 13.4'	230	(Cruz Jr. et al., 2005)

continued on following page

Table 5.1 – Continued.

#	Site	Country	Lon.	Lat.	Elev. (m)	Reference
13	Lake Valencia	Venezuela	292° 15'	10° 10'	400	(Curtis et al., 1999)
14	BR 319 (highway, soil samples)	Brazil	296° 29'	-8° 10.5'		(de Freitas et al., 2001)
15	São Francisco River peat bog	Brazil	316° 47'	-10° 24'	480	(De Oliveira et al., 1999)
16	Laguna Pallcacocha	Ecuador	280° 46'	-2° 46'	4060	(Hansen et al., 2003)
16	Laguna Chorreras	Ecuador	280° 50.5'	-2° 45.5'	3700	(Hansen et al., 2003)
17	Cariaco Basin		294° 49.9'	10° 42.7'	-893	(Haug et al., 2001)
18	Lake Chichancanab	Mexico	271° 15'	19° 50'	15	(Hodell et al., 1995)
19	Lake Miragoane	Haiti	286° 0'	18° 0'		(Hodell et al., 1991)
20	Lago de las Morrenas	Costa Rica	276° 31'	9° 29'	3480	(Horn, 1993)
21	Cariaco Basin	Venezuela	294° 49.9'	10° 42.7'	-893	(Hughen et al., 1998)
22	Argentine Basin		315° 0'	-42° 30'		(Jones, 1994)
23	Lagoa do Caçó	Brazil	316° 45'	-2° 50'	120	(Ledru et al., 2002)
24	Lake Valencia	Venezuela	292° 15'	10° 10'	400	(Leyden, 1985)

continued on following page

Table 5.1 – Continued.

#	Site	Country	Lon.	Lat.	Elev. (m)	Reference
25	Cuenca de México	Mexico	261° 0'	19° 30'	2240	(Lozano-García and Ortega-Guerrero, 1994)
26	Amazon Fan		310° 54'	5° 45'	-3346	(Maslin and Burns, 2000)
27	Laguna Chaplin	Bolivia	298° 56'	-13° 28'	~750	(Mayle et al., 2000)
28	Rondonia State	Brazil	293° 53'	-12° 42'		(Pessenda et al., 1998)
29	Maranhao State	Brazil	315° 30'	-3° 0'	110	(Pessenda et al., 2004)
30	Cariaco Basin		294° 49.8'	10° 42.7'		(Piper and Dean Jr., 2002)
31	Lake Aricota	Peru	289° 6'	-16° 54'	2800	(Placzek et al., 2001)
32	Laguna Blanca	Venezuela	288° 12.9'	8° 20.1'	1500	This study
32	Lagunas Las Verdes	Venezuela	289° 7.6'	8° 51.2'	4200	This study
33	Gulf of Mexico		264° 28.2'	23° 0'		(Poore et al., 2003)
34	Gulf of Mexico		269° 0'	28° 0'		(Poore et al., 2005)
35	Nevado Illimani	Bolivia	292° 14'	-16° 37'	6350	(Ramirez et al., 2003)
36	Lake Titicaca	Bolivia/ Peru	290° 30'	-15° 45'	3800	(Rowe et al., 2003)

continued on following page

Table 5.1 – Continued.

#	Site	Country	Lon.	Lat.	Elev. (m)	Reference
37	Laguna Junín	Peru	285° 0'	-11° 0'	4250	(Seltzer et al., 2000)
38	Nevado Huascaran	Peru	282° 30'	-9° 0'	6050	(Thompson et al., 1995)
39	Nevado Sajama	Bolivia	291° 7'	-18° 6'	6542	(Thompson et al., 1998)
40	Lake Fúquene	Columbia	286° 14'	5° 27'	2580	(Vélez et al., 2003)
41	Atlantic Ocean (M35003-4)		298° 45'	12° 5'		(Vink et al., 2001)
42	Lake Tulane	U.S.A. (Florida)	279° 0'	27° 0'	36	(Watts and Hansen, 1994)
43	Laguna Las Margaritas	Columbia	286° 34'	3° 23'	290	(Wille et al., 2003)

Figures

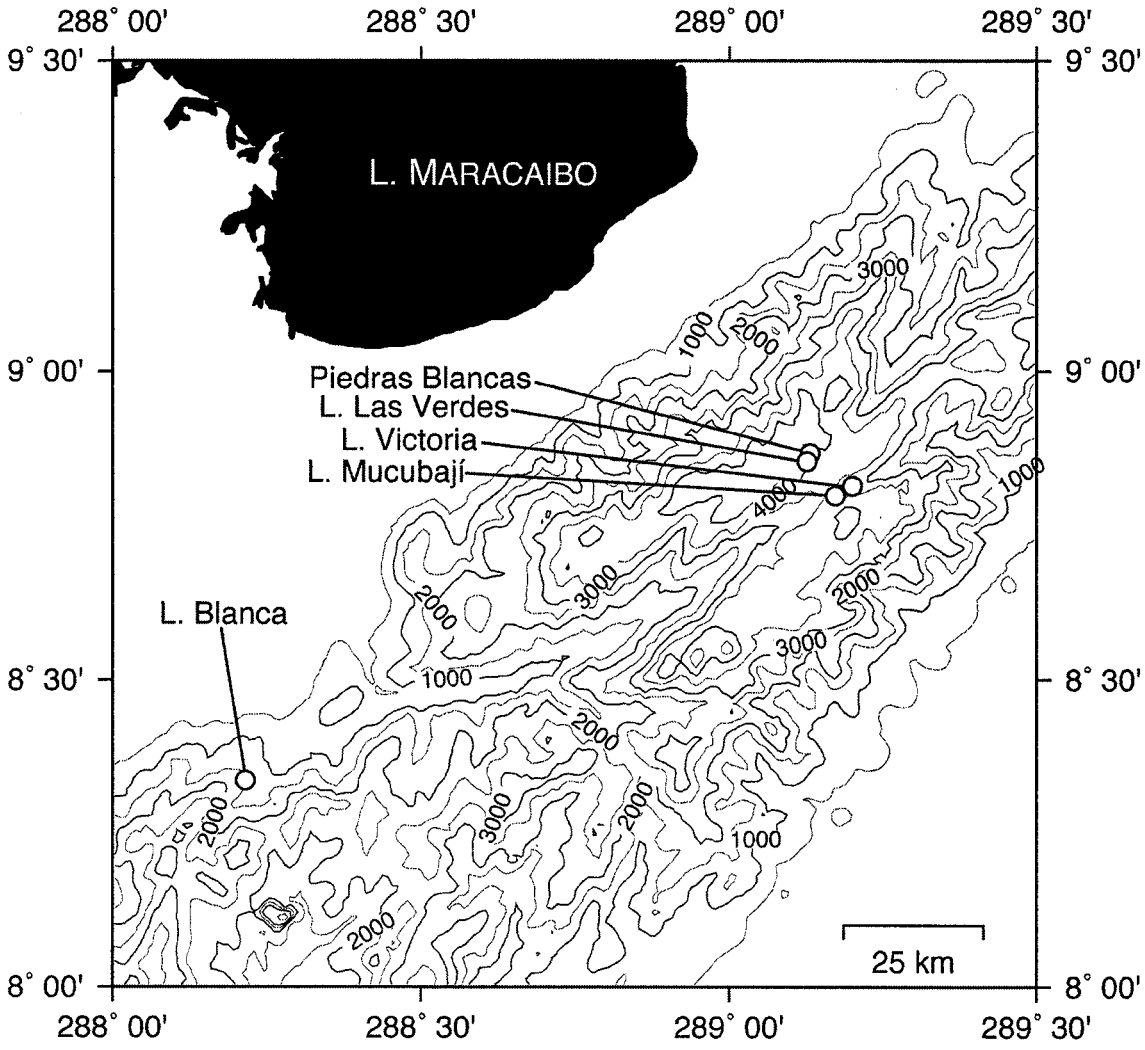

Figure 5.1 – Study locations in the Cordillera de Mérida, Venezuela.

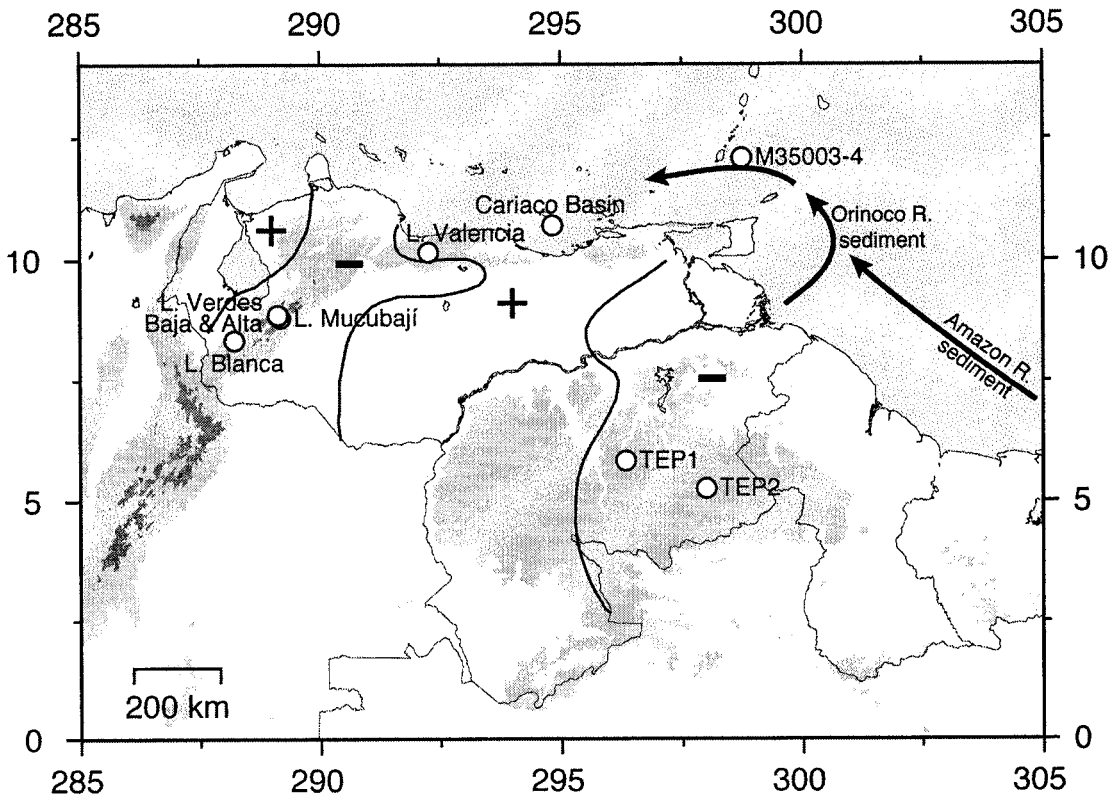

Figure 5.2 – Location of Holocene paleoclimate records in Venezuela. TEP1 and TEP2 refer to the Guaiquinima Massif-*tepui* and Churi-*tepui*. Dark lines and plus or minus signs indicate the longitudinal pattern of precipitation anomalies identified by Pulwarty (1992). The location of boundaries between zones is approximate and varies in location and extent between years. Light and dark shading indicates elevations above 500 and 3000 m respectively.

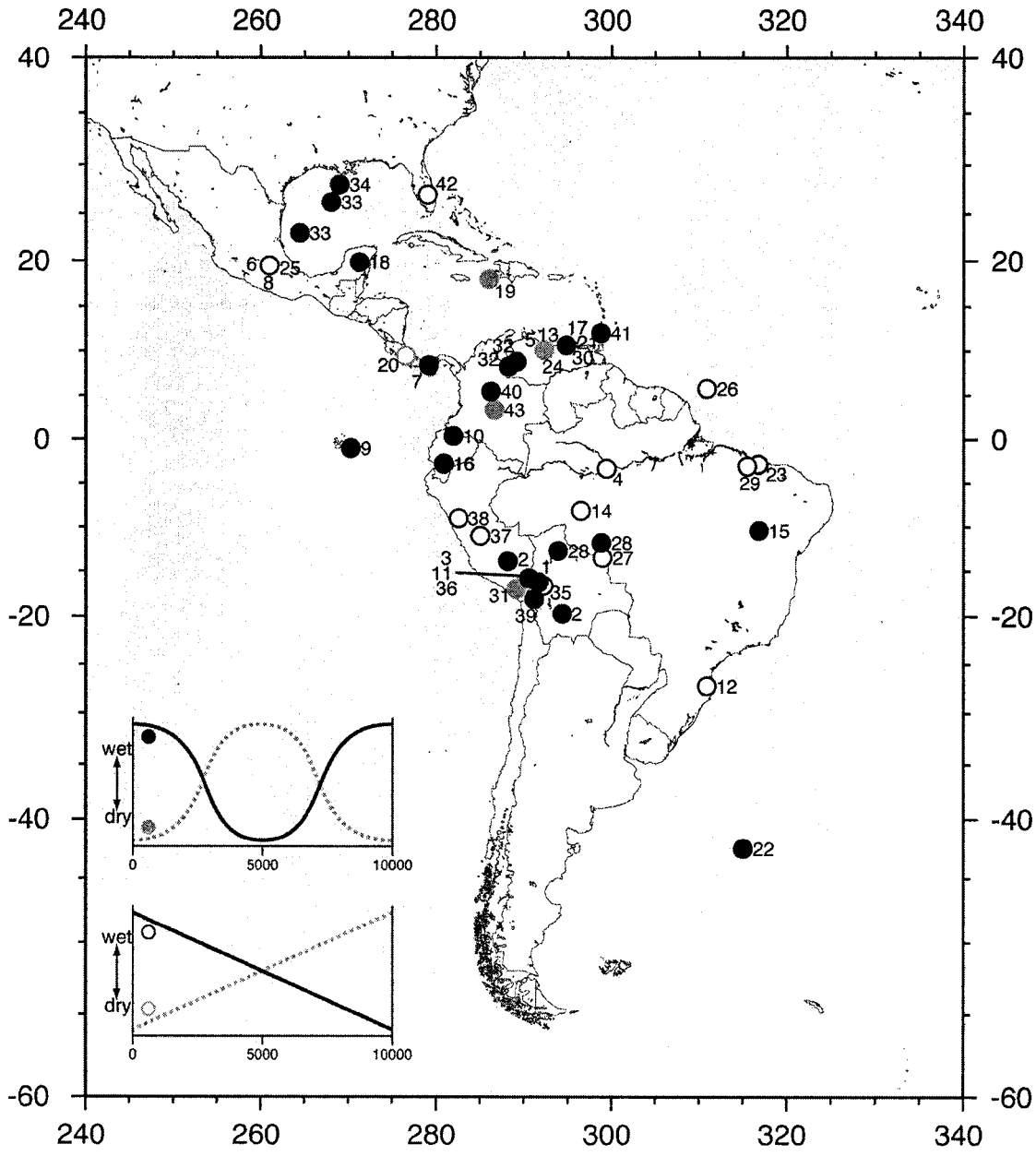

Figure 5.3 – Map of Holocene climate records from the tropical and subtropical Americas. Black and gray filled circles indicate a dry-wet-dry or wet-dry-wet sequence of moisture balance change respectively while black and gray open circles indicate a dry-to-wet or wet-to-dry trend during the Holocene (inset). Numbers correspond to the entries is Table 5.1.

APPENDIX A

DIATOMS IDENTIFIED IN MODERN AND FOSSIL SEDIMENTS FROM THE VENEZUELAN ANDES.

Achnanthes chlidanos Hohn & Hellerman
Achnanthes minutissima Kütz
Achnanthes minutissima var. *jackii* (Rabenhorst) Lange-Bertalot
Achnanthes spp.
Achnanthes ventralis (Krasske) Lange-Bertalot
Aulacoseira alpigena (Grunow) Krammer
Brachysira arcoborealis REF
Brachysira brebissonii R. Ross in Hartley
Brachysira vitrea (Grun.) R. Ross in Hartley
Caloneis silicula (Ehrenb.) Cleve
Cavinula pseudoscutiformis (Hust.) Mann & Stickle
Cocconeis placentula var. *lineata* (Ehrenb.) Van Heurck
Craticula cuspidata (Kutz.) Mann
Cymbella amphicephala Naegeli ex Kutz.
Cymbella aspera (Ehrenb.) H. Perag. in Pell.
Cymbella cymbiformis Ag.
Cymbella muellerii Hustedt 1938
Cymbella naviculiformis Auersw. ex Heib.
Denticula keutzingii Grunow
Encyonema lunatum (W. Sm. in Grun.) V.H.
Encyonema minutum (Hilse in Rabenhorst) Mann
Encyonema neogracile Krammer
Encyonema perpusillum (Cleve) Mann
Encyonema silesiacum (Bleisch in Rabenhorst) Mann
Encyonema sp. #3 (aff. *Cymbella cesatii*)
Encyonema sp. #4 (aff. *Cymbella falaisensis*)
Encyonema sp. #4a (aff. *Cymbella microcephala*)
Encyonema sp. #6 (aff. *Encyonema sublanceolatum*)
Eunotia incisa Gregory 1854
Eunotia intermedia (Hust) Norpel, Lange-Bertalot & Alles
Fragilaria angustissima-Sippen (*S. ulna* complex in K.&L.-B.)
Fragilaria construens var. *exigua* (W. Sm.) Schulz
Fragilaria oldenburgiana Hust.
Fragilaria pseudoconstruens Marciniak
Gomphonema angustatum ssp. #1
Gomphonema angustatum var. *aequalis* Greg.
Gomphonema gracile Ehrenb.
Gomphonema pumilum (Grunow) Reichardt & Lange-Bertalot
Gomphonema sp. #1 (aff. *Gomphonema bohemicum*)
Gomphonema sp. #5
Gomphonema sp. #6
Gomphonema variostriatum Cambern & Charles 2000
Hantzschia amphioxys (Ehrenb.) Grun.
Hantzschia elongata (Hantzsch) Grun.
Navicula absoluta Hust.
Navicula jaagii Meister
Navicula laevissima var. *perhibita* (Hustedt)Lange-Bertalot
Navicula minima Grun. in Van Heurck
Navicula podzorskii Lange-Bertalot

Navicula pseudoventralis Hust.
Navicula schoenfeldii Hust.
Navicula seminuloides var. *sumatrana* Hustedt
Navicula sp. #1 (aff. *Navicula minima*)
Navicula sp. #6
Navicula sp. #9
Navicula subrotundata Hust.
Neidium ampliatum (Ehrenberg) Krammer 1985
Neidium hercynicum A. Mayer
Neidium sacoense Reim.
Neidium sp. #2
Nitzschia bryophila (Hust.) Hust.
Nitzschia gracilis Hantzsch
Nitzschia perminuta (Grun. in Van Heurck) M. Perag.
Nitzschia sp. #2
Nitzschia sp. #3
Nupela lesothensis (Schoeman) Lange-Bertalot
Pinnularia aestuarii Cleve
Pinnularia brebissonii var. *diminuta* (Grun. in Van Heurck) Cleve
Pinnularia microstauron (Ehrenb.) Cleve
Pinnularia sp. #1
Pinnularia sp. #6
Pinnularia subcapitata Greg.
Pinnularia viridis (Nitzsch) Ehrenb.
Sellaphora pupula var. *capitata* Hust.
Sellaphora sp. #1
Stauroneis anceps f. *gracilis* Rabenh.
Stauroneis phoenicenteron (Nitzsch) Ehrenb.
Staurosirella leptostauron (Ehrenb.) Williams & Round
Staurosirella pinnata (Ehrenb.) Williams & Round
Stenopterobia curvula (W. Smith)Krammer 1987
Tabellaria flocculosa (Roth) Kutz.

APPENDIX B

EVOLUTION OF $\delta^{18}O_{SW}$ SINCE THE LAST GLACIAL MAXIMUM

Introduction

The large volume of ice present during the Last Glacial Maximum (LGM, ~21,000 y BP) represents a substantial transfer of water from the oceans to land. This transfer had several effects on the global ocean: sea level was lower during the LGM, average ocean salinity was higher, and the average ocean $^{18}O/^{16}O$ ratio ($\delta^{18}O_{sw}$) was greater relative to the present. Of particular interest to paleoclimatologists is the ocean $^{18}O/^{16}O$ change. The $\delta^{18}O$ composition of marine carbonates are a function of both the precipitation temperature and the local seawater $\delta^{18}O$ composition. Local sea water $\delta^{18}O$ reflects the average seawater $\delta^{18}O$ modified by local processes. Thus, understanding local $\delta^{18}O_{sw}$ and temperature changes requires knowing the global $\delta^{18}O_{sw}$ through time. In addition, water which falls out of the atmosphere as rain or snow is ultimately derived from the surface ocean. Thus the isotopic composition of precipitation will reflect secular shifts of $\delta^{18}O_{sw}$ (in addition to other isotope effects).

Constraining shifts in the average $\delta^{18}O_{sw}$ requires knowing the amount and isotopic composition of water stored outside the ocean. Methods for determining these values will be discussed in the following sections and an LGM to modern $\delta^{18}O_{sw}$ record presented.

Volume of water removed from the oceans

The volume of water removed from the oceans which should be used to calculate the isotopic composition of sea water is the sum of any water that does not physically mix with global sea water. This sum includes ice (both grounded and

floating), groundwater and surface water. This sum has been reconstructed by two different methods.

The first method involves modeling the volume of ice sheets from geomorphic and geophysical methods. These ice sheet models rely on the fact that loading of the lithosphere by ice sheets results in deformation of the solid earth. The magnitude of this deformation can be related to the mass (volume x density) of ice present at a give location through time. Thus by measuring the magnitude of the deformation at many locations once covered by ice, the mass of past ice sheets can be estimated. Glacial geologic features help these estimates by providing constraints on the spatial coverage of the ice sheets through time. Floating ice does not load the lithosphere and is not included in these calculations. In theory this method is also sensitive to changes in surface and groundwater storage. However, the volume change of these reservoirs through time is considered small relative to the ice sheets and is ignored. This method generally provides a single estimate of ice volume at the LGM.

The second method attempts to determine the volume of water removed from the ocean basins by reconstructing sea-level through time. This method provides a continuous estimate of ice volume and is more useful for calculating $\delta^{18}O_{sw}$ variations through time. The relative sea-level change recorded at a given location on the earth reflects both the removal of water from the ocean basins (eustatic sea level) and associated deformation of the lithosphere. The lithospheric deformation includes the effects of crustal loading by ice sheets, the corresponding unloading of the ocean basins and continental margins, and deformation of the geoid due to changes in the rotation of the earth caused by the redistribution of mass (Fleming et al., 1998; Milne et al., 2002;

Peltier, 2002). The effect of ice sheet loading dominates relative sea-level changes at sites located near to ice sheets. These near-field sites are not good recorders of eustatic sea-level but have been used to constrain ice sheet mass. Sites located away from the local effects of ice sheets (far-field sites) are better recorders of eustatic sea level (ice volume). However, there are significant non-eustatic sea-level changes which still affect these locations. Several authors have modeled the effects of eustatic and non-eustatic sea-level changes on relative sea-level curves at far-field sites (Fleming et al., 1998; Milne et al., 2002; Peltier, 2002). These models indicate that the relative sea-level changes at Barbados (13.2°N, 59.5°W) are quite close to the global eustatic sea-level curve for the period LGM to present (Peltier, 2002). The similarity between relative and eustatic sea-level at this location results from cancellation between the different non-eustatic effects. This situation is not true for other far-field sites such as Tahiti (18.0°S, 149.5°W) and Huon Peninsula, Papau New Guinea (6.0°S, 147.5°E) which have been used to reconstruct eustatic sea-level. Thus, based upon these modeling studies, the relative sea-level variations at Barbados are a better approximation of the eustatic sea-level curve (ice-volume) than other far-field sites (Peltier, 2002).

Fig. B.B.1 shows relative sea-level data from the far-field sites of Barbados, Huon Peninsula and Tahiti. A continuous LGM-Holocene record is obtained by splicing the Holocene record from Tahiti into the Barbados curve. Using the Holocene Tahiti data is justified because the non-eustatic effects are quite small in this interval (Peltier, 2002). As a final constraint, it is assumed that melting of ice sheets had ceased

by 4,000 calendar years BP (Peltier, 2002). Together, these data provide a continuous record of eustatic sea level during the past 19,000 years.

Ocean $\delta^{18}O_{sw}$ at the LGM

The isotopic composition of water removed from the oceans during the LGM has been estimated by several methods. The first method uses estimates of the excess volume and isotopic composition of the different ice-sheets present during the LGM to calculate an average $\delta^{18}O$ for the removed water. A simple mass-balance equation then relates this value to the $\delta^{18}O_{sw}$ change. There is significant uncertainty in both the volume and isotopic composition of LGM ice sheets resulting in a wide range of estimates from this method. The available data suggests a $\delta^{18}O$ shift of +0.84 to +1.47‰ between the present and LGM (Duplessy et al., 2002).

The second method uses measurements of the $\delta^{18}O$ composition of benthic foraminifera to constrain the magnitude of $\delta^{18}O_{sw}$ changes. The LGM-modern difference in benthic $\delta^{18}O$ records ($\Delta\delta^{18}O$) reflects both $\delta^{18}O_{sw}$ and bottom water temperature changes. However, bottom water temperatures cannot be lower than the freezing point of seawater (corrected for adiabatic warming as water descends from the surface to the ocean bottom). Thus, the difference between the modern and freezing point temperature at benthic sites is an estimate of the maximum temperature change possible. Subtracting this effect from the $\Delta\delta^{18}O$ value results in a minimum estimate of the $\delta^{18}O_{sw}$ change. It is important to note that the estimated $\delta^{18}O_{sw}$ change is only valid for the water over a particular site. Bottom waters in the modern ocean have different isotopic compositions, thus a number of sites from different locations are needed to reconstruct the global change in $\delta^{18}O_{sw}$. Using this method, the best estimate of the

minimum global $\delta^{18}O_{sw}$ change between the present and LGM is +0.85‰ (Duplessy et al., 2002).

The third method uses measurements of pore-water isotopic composition from deep-ocean sediment cores to calculate the $\delta^{18}O_{sw}$ of the LGM ocean. Changes in the isotopic composition of sea water bathing a particular site propagate down into the sediment pore water by diffusion. Thus by measuring pore-water isotope profiles and modeling the effects of diffusion on these profiles it is possible to determine changes in $\delta^{18}O_{sw}$ during the LGM. (This process is quite similar to the propagation and attenuation of surface temperature variations into the subsurface and the inversion of borehole temperature profiles to determine past temperature change.) Measurements from a number of locations which are bathed by different bottom waters suggest the LGM to modern $\delta^{18}O$ shift was +1.0±0.1‰ (Adkins et al., 2002; Schrag et al., 2002).

Summary and Conclusions

The pore-water method appears to provide the best constraint for LGM to modern $\delta^{18}O_{sw}$ change and is consistent with the benthic foraminifera $\Delta\delta^{18}O$ calculations and ice-sheet models. Combining the +1.0±0.1‰ shift calculated by this method with an estimated +120 m eustatic sea-level change over the same interval yields a slope of –0.0083±0.0008 ‰/m of eustatic sea-level rise (Fig. B.2). This value provides the best estimate given available data. Applying these slopes to the Barbados sea-level curve discussed above yields a record of global ocean $\delta^{18}O_{sw}$ variations during the past 20,000 y (Fig. B.3). There are several caveats which must be noted:

1. Recent studies have suggested that LGM eustatic sea-level could have been below –120 m at the LGM and –120 m at 19,000 calendar years BP (Clark et

al., 2004). Using a range of –115 to -135 m (Yokoyama et al., 2000) and +1.0±0.1‰ yields a slope of 0.008±0.001 ‰/m. This would change the reconstructed $\Delta\delta^{18}O_{sw}$ curve in Fig. B.3 but, at this time, the data are insufficient to adopt these values.

2. The curve in Fig. B.3 assumes that the isotopic composition of melting ice sheets is invariant with time. However, melting of different ice sheets at different rates undoubtedly violated this assumption. It is difficult to assess the impact this effect would have on the reconstructed $\delta^{18}O_{sw}$.
3. New sea-level records may show that the relative sea-level curve from Barbados is not a good estimate of eustatic sea-level. If this occurs, the shape of the curve in Fig. B.3 will change, although the absolute magnitude of the LGM-modern $\Delta\delta^{18}O_{sw}$ would not change.

Figures

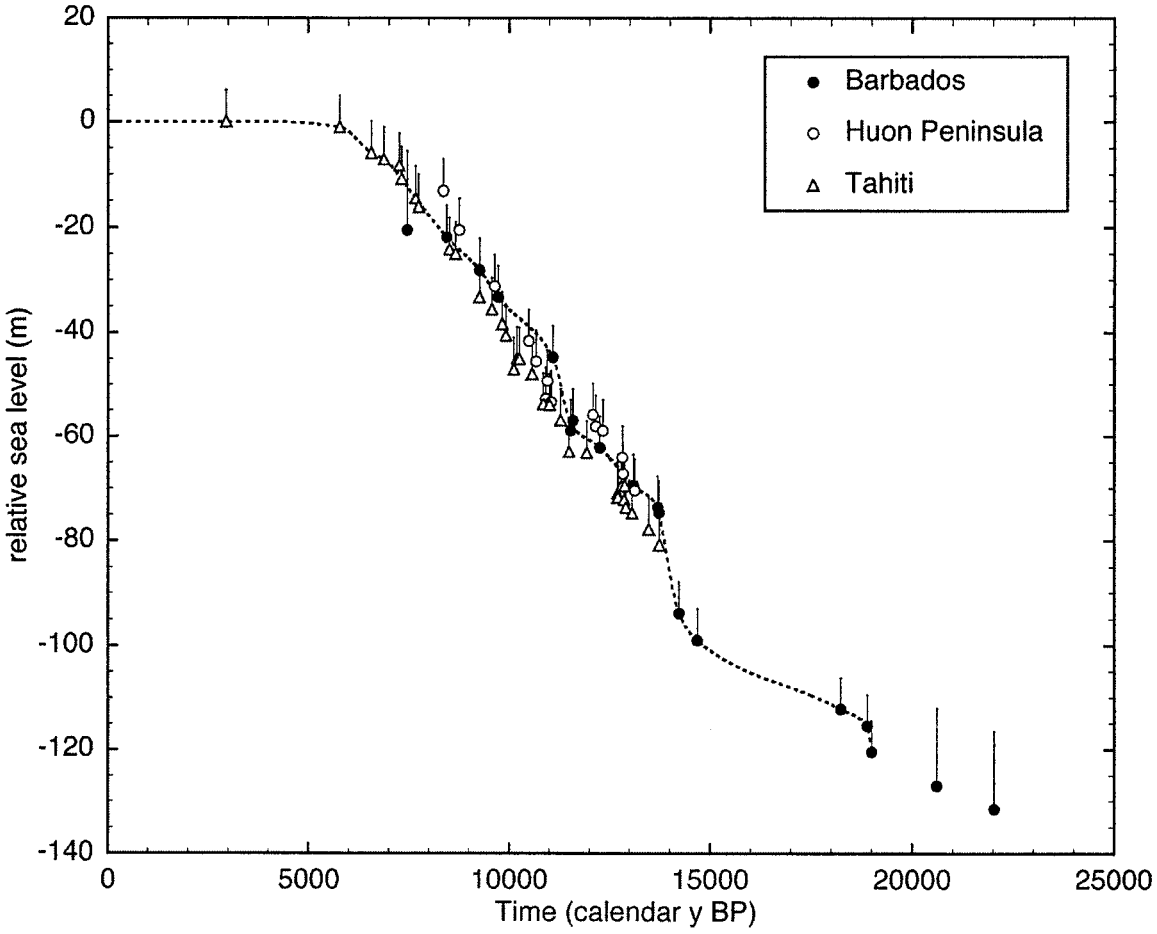

Figure B.1 – Relative sea-level and inferred eustatic sea-level changes. Relative sea-level histories from Barbados (Fairbanks, 1989; Bard et al., 1990a; Bard et al., 1990b; Bard et al., 1990c; Bard et al., 1993), Huon Peninsula (Papau New Guinea) (Edwards et al., 1993) and Tahiti (Bard et al., 1996). All dates are U/Th (and thus calendar) ages except the Holocene samples from Tahiti. Radiocarbon AMS ages on these samples were corrected for the ocean reservoir effect and converted to calendar ages using the Calib4.4 data set (Stuiver et al., 1998a; Stuiver et al., 1998b). Replicate ages on the same sample have been averaged and plotted as a single data point. The records have been corrected for tectonic uplift or subsidence (+0.34 mm/y, +1.9mm/y, -0.2 mm/y for Barbados, Huon Peninsula and Tahiti respectively). Error bars represent the depth range of the sampled coral species. The dashed line is a cubic spline curve through the Barbados and Tahiti (Holocene) splice discussed in the text.

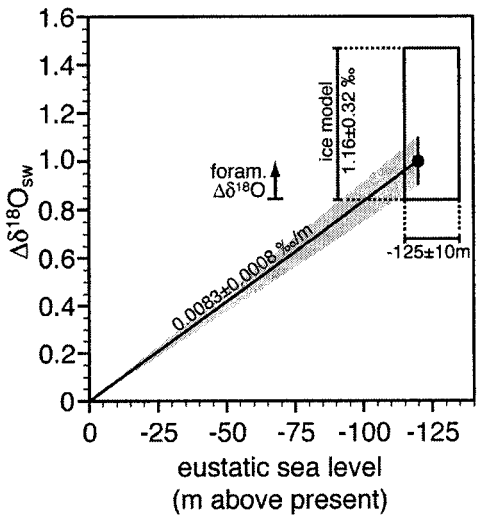

Figure B.2 – Constraints on the modern-LGM change in eustatic sea-level and $\delta^{18}O_{sw}$. The filled circle with vertical line is the best estimate from pore-water $\Delta\delta^{18}O$ constraints (Schrag et al., 2002) and the various sea-level records (Peltier, 2002). The box represents the range of estimates from ice models and relative sea-level curves (Duplessy et al., 2002; Milne et al., 2002).

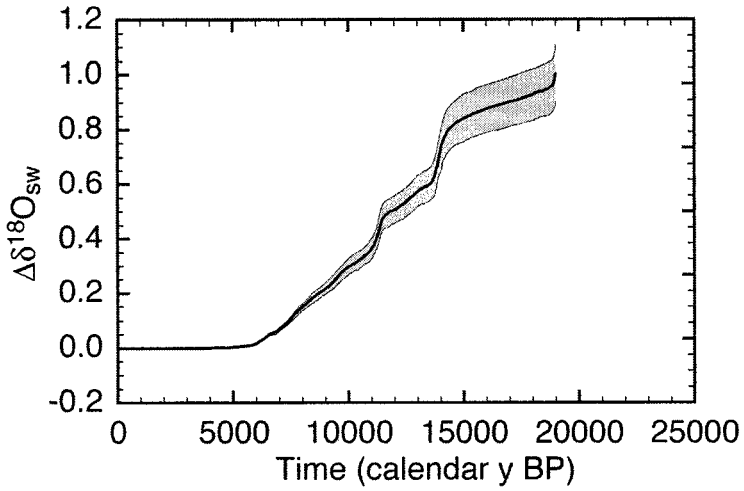

Figure B.3 – Inferred changes of $\delta^{18}O_{sw}$ since the Last Glacial Maximum calculated from the Barbados-Tahiti (Holocene) spliced sea-level curve and a slope of 0.0083±0.0008 ‰/m. Thin lines indicate the range of uncertainty due to this slope.

APPENDIX C

ANALYTICAL METHODS

Modern Lake Water Chemistry

Physical and Chemical Limnologic Measurements

Water depth profiles of each lake (simultaneous GPS position and acoustic water depth measurements) were acquired with a Garmin GPS-Fishfinder Model 168 every 10 horizontal meters. Hydrocasts of pH, temperature, dissolved oxygen and conductivity were measured in the deepest part of the lake using a Hydrolab Minisonde and Surveyor 4a. Measurements were taken at 0.1m, 0.2m, 0.3m, 0.4m, 0.5m, 1.0m and every subsequent meter to the lake bottom. Water clarity was measured by recording the depth at which the Ekman bottom sampler disappeared from view when lowered.

Water Sample Collection and Storage

Plastic sample bottles were rinsed three times with sample water, filled and capped 30-40cm below the water surface. Alkalinity samples were refrigerated at 3°C and analyzed within 36 hours. Dissolved nitrogen/phosphorus samples were frozen after sampling and thawed for 12 hours before filtering. Cation samples (125ml) were stored at room temperature and acidified with three drops of concentrated nitric acid within one week of sampling. Water isotope samples were stored at room temperature in the field. Once returned to the University of Massachusetts, all samples were refrigerated at 2°C until analysis.

Chemical Analysis of Water Samples

Alkalinity

Alkalinity was determined using the GRAN titration method. Samples were titrated with 0.16N sulfuric acid using a Hach digital titrator. If the initial sample pH was above 8.3, the sample was titrated to a pH of 8.3 and the amount of acid added was recorded (phenolphthalein alkalinity). Samples were then titrated to a pH of 4.9, recording the pH and volume of acid added at several points along the way. At this point, acid was added 2-3 units at a time and the pH recorded after each addition until a pH of ~4.3 was reached. Total alkalinity was determined using a plot of the amount of acid added vs. hydrogen ion concentration (x- and y-axis respectively). The total alkalinity was calculated from the x-intercept of a regression line fit to the linear portion of the data with a hydrogen ion concentration greater than pH 4.9. Bicarbonate, carbonate and hydroxide alkalinity were calculated from the phenolphthalein and total alkalinity using the procedure outlined in Standard Methods for the Examination of Water and Wastewater (APHA, 1992).

Cations

Cations were analyzed at the University of Massachusetts using a Perkins Elmer Spectroflame E inductively coupled plasma-atomic emission spectrophotometer (ICP-AES). A working stock standard was prepared from ICP primary standards. Working standards were diluted from the working stock solution using 18MΩ deionized water. Table I lists the elements analyzed for, along with the standard concentrations, emission lines and approximate analytical detection limits. Prior to each days run, a check solution (near the Std. 3 concentration) was used to scan all the analytical emission

lines, ensuring that the predefined peak and background wavelengths were correct. The same check solution was run every eight samples to ensure the continued validity of the instrument calibration. The analytical detection limits were calculated by averaging the standard deviations of the three measurements made for each sample and multiplying by three. The distribution of the standard deviations of the replicate samples with sample concentration was used to determine which subset of the samples would give the best estimate of the detection limit (check standard & samples, samples only, low concentration samples only).

Total and Dissolved Phosphorus and Nitrogen

Samples for dissolved phosphorus and nitrogen were frozen after sampling. Before shipping to the University of Massachusetts, the samples were thawed and filtered into new sample bottles through 0.45μm nitrocellulose filters (Fisherbrand) using a 60ml syringe and filter holder attachment. Following filtration of the dissolved samples, both dissolved and total samples were treated identically. Potassium persulfate digestion of phosphorus and nitrogen compounds yields orthophosphate and nitrate as products. The digested product was then analyzed using the automated molybdate blue colorimetric method (phosphate) and the sulfanilamide colorometric method (nitrate) on a LACHAT instruments Quik-Chem 8000 flow injection analyzer at Hampshire College, Amherst Massachusetts. Standards run through the digestion were used for calibration. Samples were corrected for reagent blank. Dissolved P samples were corrected for contribution of cellulose phosphate filters (less than a ppb).

Diatom Species Analysis

Sediment samples (10-100mg dry weight) for diatom species analysis were freeze dried to disagregate them. Concentrated nitric acid (4-5ml) was added to the dry sediment and heated in a waterbath for 3 hours at 65°C. Forty percent hydrogen peroxide (4-5ml) was then added to the nitric acid/sediment mixture and heated until vigorous bubbling ceased (a minimum of 1 hour, typically 2-3 hours). The nitric acid, hydrogen peroxide, sediment mixture was centrifuged, the supernatant decanted and de-ionized water added. Sediments were rinsed 4-5 times in de-ionized water until neutral. After the final washing, de-ionized water was added to the 10ml mark on the 15ml polypropylene centrifuge tubes and the tubes labeled with the sample name and "primary slurry."

Aliquots of the primary slurry (100-1000µl) were transferred to a second 15ml centrifuge tube using an Eppendorf variable volume calibrated syringe. The transferred slurry was diluted to 5 ml and 0.4 ml of this secondary slurry pipetted onto a glass coverslip. The secondary slurry was then diluted to 10ml and 0.4 ml of this solution pipetted onto a second coverslip. Coverslips were dried overnight in a closed chamber using a 15 watt light bulb as a gentle heat source. Dried coverslips were cemented to glass slides using Naphrax.

Diatom coverslips were counted at 1000x magnification using an oil immersion lens under differential interference illumination on an Olympus BH-2 microscope. Valves were counted along transects which started at either the north, south, east or west edge and ended at the center of the coverslip. At least 400 valves per slide were counted and only full transects were counted. Counting full transects minimizes

counting biases due to uneven distribution of diatoms between the edge and center of the coverslip and any species specific sorting which occurs during the drying process. Diatom counts were tallied using the freeware program MacCount (http://www.bgsu.edu).

Sediment diatom concentration was calculated using pollen marker grains and Battarbee trays. A solution of eucalyptus pollen (1.0 g pollen in 100ml de-ionized water) was calibrated by pipetting aliquots of the solution onto a hematocytometer slide and counting the pollen deposited on the slide. Two-hundred microliters of the eucalyptus solution were added to the secondary diatom slurry prior to the addition of de-ionized water. When the diatom coverslips were counted, eucalyptus pollen grains were enumerated along with the diatom species. The concentration of diatoms in the sediment was then calculated as:

$$\text{diatoms}(\#/g) = \frac{\frac{\#\text{valves}}{\#\text{pollen}} V_{\text{pollen}} \frac{\text{pollen}}{\text{ml}} \frac{10\text{ml}}{V_{\text{primary}}}}{\text{sediment}(g)}$$

where # valves and # pollen are the counted diatom frustules and pollen grains, V_{pollen} is the volume of the pollen solution added to the secondary slurry, pollen/ml is the concentration of pollen in the slurry (#/ml) and $V_{primary}$ is the volume of the primary slurry diluted in the secondary slurry. A subset of samples were analyzed using Battarbee trays (Battarbee, 1973) to determine the diatom concentration. For these samples, the diatom concentration determined by eucalyptus pollen and Battarbee trays were linearly correlated indicating the robust nature of the diatom concentration measurements.

Appendix A lists all the species identified in the Venezuelan lakes along with the authority and reference (where applicable). Several undescribed species were found and have been given temporary designation as sp. #1, #2 etc.

Tables

Table C.1 – Standard concentrations, emission lines and detection limits for cation analyses by ICP-AES.

Element	emission line (nm)	detection limit	Standard Concentration (mg/L) Blnk	Std1	Std2	Std3	Std4	Std5	Std6
Ca	315	0.017[a,d]	0.0	0.5	1.0	2.0	4.0	10.0	20.0
	317	0.019[a,d]							
K	766	0.005[a,d]	0.0	0.3	0.5	1.0	2.0	5.0	10.0
Mg	280	0.004[a,d]	0.0	0.3	0.5	1.0	2.0	5.0	10.0
	285	0.005[a,d]							
Na	589	0.008[a,d]	0.0	0.3	0.5	1.0	2.0	5.0	10.0
Si	251	0.017[a,d]	0.0	0.3	0.5	1.0	2.0	5.0	10.0
	288	0.026[a,d]							
Al	167	0.4[a,e]	0.000	0.025	0.050	0.100	0.200	0.500	1.000
B	182	3.1[c,e]	0.000	0.025	0.050	0.100	0.200	0.500	1.000
Ba	455	0.1[b,e]	0.000	0.025	0.050	0.100	0.200	0.500	1.000
Cr	267	2.6[c,e]	0.000	0.025	0.050	0.100	0.200	0.500	1.000
Cu	324	2.7[c,e]	0.000	0.025	0.050	0.100	0.200	0.500	1.000
	327	5.4[c,e]							
Fe	259	2.2[a,e]	0.000	0.025	0.050	0.100	0.200	0.500	1.000
Li	670	0.1[b,e]	0.000	0.025	0.050	0.100	0.200	0.500	1.000
Mn	259	0.5[a,e]	0.000	0.025	0.050	0.100	0.200	0.500	1.000
Pb	168	14.5[c,e]	0.000	0.025	0.050	0.100	0.200	0.500	1.000
	182	17.5[c,e]							
Sr	407	0.2[a,e]	0.000	0.025	0.050	0.100	0.200	0.500	1.000
Ti	334	1.1[b,e]	0.000	0.025	0.050	0.100	0.200	0.500	1.000
Zn	213	0.6[b,e]	0.000	0.025	0.050	0.100	0.200	0.500	1.000

(a)- determined from average of the standard deviations of three replicate measurements on low concentration samples (lower 50%);
(b)- determined from average of the standard deviation of three replicate measurements on all samples;
(c)- determined from average of the standard deviation of three replicate measurements on all samples and higher concentration check standard;
(d)- parts per million
(e)- parts per billion

APPENDIX D

DATA TABLES

Modern Lake Samples

The depth, water chemistry and H and O isotopic composition were determined for 24 modern lakes in the Venezuelan Andes. These lakes are listed in Table D.1 their locations shown if Fig. D.1. The water chemistry and isotopic composition of lake water are listed in Table D.2.

Precipitation and Surface Water H and O Isotopes

Oxygen and hydrogen isotope analyses were carried out on precipitation, lake, stream and groundwater samples from the Venezuelan Andes. These data are tabulated in Table D.3 and the sample locations shown in Fig. D.2.

Sediment Dating

Table D.4 lists all of the radiocarbon age determination on lake sediment cores from the Venezuelan Andes. The calibrated ages were determined using the CALIB 4.2 dataset (Stuiver et al., 1998a; Stuiver et al., 1998b). Tables D.5 and D.6 contain ^{210}Pb and ^{137}Cs analyses on surface sediment core GL-99A from Laguna Mucubají. Table D.7 tabulates ^{210}Pb results for the surface sediment core GL-99A from Laguna Verdes Alta.

Sediment Geochemistry

Table D.8 lists the geochemistry of modern sediments, plants and soils from Lagunas Verdes Alta, Baja and Laguna Mucubají. Tables D.9 through D.17 tabulate the geochemistry of sediment cores from Laguna Blanca, Laguna Mucubají, Laguna

Verdes Alta and Laguna Verdes Baja. Diatom $\delta^{18}O$ measurements on Laguna Verdes Alta and Baja sediments are listed in Table D.18 and D.19.

Tables

Table D.1 – Lakes in the Venezuelan Andes sampled for water chemistry.

#	Lake Name	Code	Latitude	Longitude	Elev. (m)
1	Laguna Blanca (nr. Tovar)	LBLA01	N8 20.105	W71 47.072	1620
2	Laguna Brava	LBRA01	N8 18.355	W71 50.356	2399
3	Laguna de La Pata (nr. Gavidia)	LPAT02	N8 39.200	W70 56.041	3982
4	Laguna Grande de los Patos (Páramo El Banco)	LBAN10	N8 48.820	W70 56.926	4190
5	Laguna La Cura	LBAN24	N8 48.776	W70 57.175	4220
6	Laguna La Posita	LBAN23	N8 48.757	W70 57.069	4225
7	Laguna Los Lirios	LLIR01	N8 18.452	W71 49.594	2305
8	Laguna Los Locos (Piedras Blancas Lake 1)	LPBL01	N8 51.772	W70 53.845	4371
9	Laguna Michurao Alto	LMIC02	N8 43.823	W70 51.766	3738
10	Laguna Michurao Bajo	LMIC09	N8 44.156	W70 52.000	3718
11	Laguna Misteque	LMIS03	N8 43.345	W70 53.128	3803
12	Laguna Mucubají	LMUC01	N8 47.795	W70 49.701	3573
13	Laguna Negra (nr. Mucubají)	LNEG03	N8 47.175	W70 48.301	3462
14	Laguna Negra (Páramo El Banco)	LBAN03	N8 48.655	W70 56.940	4205
15	Laguna Parche	LPAR02	N8 38.814	W70 55.682	3894
16	Laguna Royal "A"	LROY01	N8 42.979	W70 52.302	3827
17	Laguna Royal "C"	LROY07	N8 43.308	W70 52.227	3824
18	Laguna Royal "D"	LROY13	N8 43.696	W70 52.361	3763
19	Laguna Verdes Alta	LVES05	N8 51.165	W70 52.449	4215
20	Laguna Verdes Baja	LVES24	N8 51.488	W70 52.420	4170
21	Laguna Verdes Medio	LVES09	N8 51.337	W70 52.412	4193
22	Laguna Victoria	LVIC01	N8 48.782	W70 47.997	3223
23	Piedras Blancas Lake 2	LPBL05	N8 51.656	W70 54.281	4403
24	small pond nr. L Misteque	LMIS08	N8 43.481	W70 53.062	3817

Table D.2 – Temperature, conductivity, dissolved oxygen and pH of modern lakes.

	Lake #	1	2	3	4	5	6
	Lake Name	Laguna Blanca (nr. Tovar)	Laguna Brava	Laguna de La Pata (nr. Gavidia)	Laguna Grande de los Patos (Paramo El Banco)	Laguna La Cura	Laguna La Posita
	Sample Date	6/12/02	6/12/02	6/14/02	6/6/02	6/7/02	6/7/02
	Z_{max} (m)	6	14	13	10	6	2
	Temp. 0-50cm (°C)	20.1	19.5	9.8	11.7	10.9	11.1
	Temp. Z_{max} (°C)	17.5	16.4	9.9	11.1	10.6	10.9
	SpC 0-50cm (µS)	57.94	37.26	2.10	38.00	11.28	1.64
	SpC Z_{max} (µs)	321.30	55.20	2.10	37.80	11.30	1.60
	DO (ppm) 0-50cm	2.87	7.67	5.81	6.07	6.04	5.66
	DO (ppm) Z_{max}	0.12	0.14	5.63	5.91	5.84	5.63
	DO (% sat) 0-50cm	38.4%	111.4%	82.8%	93.0%	91.0%	85.7%
	DO (% sat) Z_{max}	1.5%	1.9%	80.3%	89.2%	87.3%	84.9%
	pH 0-50cm	5.89	8.76	6.65	7.52	6.47	5.82
	pH Z_{max}	5.56	5.79	6.54	7.55	6.57	5.58
alk. 0-50cm ($CaCO_3$ mg/l)	phenolphthalein	0	1.8	0	0	0	0
	hydroxide	0	0	0	0	0	0
	carbonate	0	3.6	0	0	0	0
	bicarbonate	26.6	10.0	2.6	19.5	6.7	0.9
	total	26.6	13.6	2.6	19.5	6.7	0.9
	Al (µg/l)	4.26	18.37	11.42	6.14	15.17	64.40
	B (µg/l)	9.10	18.96	below det.	below det.	below det.	below det.
	Ba (µg/l)	12.00	1.44	0.92	0.57	0.26	1.37
	Ca (mg/l)	4.51	1.62	0.57	6.15	1.68	0.35
	Fe (µg/l)	629.00	33.16	29.40	10.78	76.10	10.68
	K (mg/l)	2.45	1.74	0.13	0.04	0.23	0.10
	Li (µg/l)	0.406	0.879	0.349	1.216	0.387	0.360
	Mg (mg/l)	2.45	1.35	0.15	0.19	0.32	0.11
	Mn (µg/l)	132.200	5.260	3.482	1.580	37.280	3.073
	Na (mg/l)	3.21	3.19	0.30	2.76	0.92	0.44
	Si (mg/l)	3.820	5.041	0.356	0.037	0.938	0.096
	Sr (µg/l)	33.56	15.72	2.76	21.39	15.08	4.00
	Zn (µg/l)	12.37	below det.	below det.	below det.	below det.	0.93
	total P (µg/l)	23.6	18.8	5.4	7.3	5.5	8.7
	dissolved P (µg/l)	10.3	9.7	4.2	5.3	4.5	3.9
	particulate P (µg/l)	13.3	9.1	1.0	2.0	1.0	4.8
	$\delta^{18}O$ 0-50cm (‰ VSMOW)	-1.69	-0.50	-6.63	-1.23	-7.05	-1.56
	δD 0-50cm (‰ VSMOW)	-15.8	-12.8	-55.1	-34.1	-62.0	-38.5
	d-excess (‰)	-2.3	-8.8	-2.0	-24.3	-5.6	-26.0

Table continued on next page

Table D.2 – Continued

	Lake #	7	8	9	10	11	12
	Lake Name	Laguna Los Lirios	Laguna Los Locos (Piedras Blancas Lake 1)	Laguna Michurao Alto	Laguna Michurao Bajo	Laguna Misteque	Laguna Mucubaji
	Sample Date	6/12/02	6/9/02	6/4/02	6/4/02	6/5/02	6/18/02
	Z_{max} (m)	7	4	45	12	20	14
	Temp. 0-50cm (°C)	20.0	9.7	12.1	12.5	13.2	12.1
	Temp. Z_{max} (°C)	17.5	9.5	10.7	12.0	11.6	11.5
	SpC 0-50cm (µS)	23.50	12.90	22.94	24.14	22.16	8.70
	SpC Z_{max} (µs)	27.10	13.10	27.10	23.80	22.30	8.60
	DO (ppm) 0-50cm	7.19	6.33	6.17	6.16	5.78	6.09
	DO (ppm) Z_{max}	0.32	6.15	0.51	5.71	4.78	5.33
	DO (% sat) 0-50cm	104.4%	94.5%	90.0%	90.5%	87.2%	87.1%
	DO (% sat) Z_{max}	4.4%	91.4%	7.2%	83.0%	69.5%	75.2%
	pH 0-50cm	8.70	6.94	7.06	7.15	7.00	6.35
	pH Z_{max}	5.64	6.91	6.05	7.15	6.70	6.12
alk. 0-50cm ($CaCO_3$ mg/l)	phenolphthalein	0.8	0	0	0	0	0
	hydroxide	0	0	0	0	0	0
	carbonate	1.6	0	0	0	0	0
	bicarbonate	8.5	7.3	11.1	11.4	9.9	5.1
	total	10.1	7.3	11.1	11.4	9.9	5.1
	Al (µg/l)	35.77	11.01	6.25	8.99	6.34	34.70
	B (µg/l)	6.30	below det.	7.39	8.11	9.12	5.95
	Ba (µg/l)	0.97	0.25	1.12	1.16	4.11	1.27
	Ca (mg/l)	0.54	1.41	3.43	3.48	2.51	1.04
	Fe (µg/l)	42.69	178.60	10.65	17.31	19.07	69.50
	K (mg/l)	1.51	0.64	0.45	0.49	0.82	0.35
	Li (µg/l)	0.321	0.897	0.375	0.352	0.353	0.393
	Mg (mg/l)	0.73	0.57	0.36	0.37	0.47	0.29
	Mn (µg/l)	1.368	96.100	3.519	3.231	4.456	9.250
	Na (mg/l)	2.82	0.93	1.22	1.27	1.43	0.80
	Si (mg/l)	3.412	0.734	2.383	2.187	2.425	1.755
	Sr (µg/l)	3.89	5.43	8.00	8.28	19.32	4.72
	Zn (µg/l)	2.45	0.94	below det.	below det.	below det.	1.07
	total P (µg/l)	23.0	9.5	3.4	3.9	4.5	4.7
	dissolved P (µg/l)	13.7	5.4	4.2	3.4	3.8	3.9
	particulate P (µg/l)	9.3	4.0	0.0	0.5	0.7	0.6
	$\delta^{18}O$ 0-50cm (‰ VSMOW)	-1.01	-4.20	-8.66	-7.86	-8.27	-9.65
	δD 0-50cm (‰ VSMOW)	-16.6	-47.4	-66.3	-62.4	-64.4	-68.1
	d-excess (‰)	-8.6	-13.8	3.0	0.5	1.7	9.1

Table continued on next page

Table D.2 – Continued

	Lake #	13	14	15	16	17	18
	Lake Name	Laguna Negra (nr. Mucubaji)	Laguna Negra (Paramo El Banco)	Laguna Parche	Laguna Royal "A"	Laguna Royal "C"	Laguna Royal "D"
	Sample Date	6/17/02	6/6/02	6/14/02	6/3/02	6/3/02	6/3/02
	Z_{max} (m)	17	1.5	5	6.4	12	12
	Temp. 0-50cm (°C)	10.2	11.5	9.0	12.0	12.8	14.9
	Temp. Z_{max} (°C)	9.6	11.3	9.0	10.5	11.4	11.5
	SpC 0-50cm (µS)	8.26	15.64	11.40	14.06	19.08	27.60
	SpC Z_{max} (µs)	9.30	16.20	11.50	13.40	19.40	30.90
	DO (ppm) 0-50cm	6.68	5.67	6.00	6.21	6.28	6.18
	DO (ppm) Z_{max}	5.42	5.31	5.70	5.88	5.66	5.44
	DO (% sat) 0-50cm	90.0%	86.4%	82.9%	91.4%	94.2%	96.4%
	DO (% sat) Z_{max}	72.1%	80.6%	78.7%	83.4%	82.1%	78.5%
	pH 0-50cm	6.09	6.78	6.72	6.80	6.93	7.20
	pH Z_{max}	5.82	6.75	6.74	6.77	6.88	6.85
alk. 0-50cm ($CaCO_3$ mg/l)	phenolphthalein	0	0	0	0	0	0
	hydroxide	0	0	0	0	0	0
	carbonate	0	0	0	0	0	0
	bicarbonate	4.0	8.0	5.4	6.9	9.5	11.5
	total	4.0	8.0	5.4	6.9	9.5	11.5
	Al (µg/l)	35.47	92.00	23.67	32.01	11.03	22.06
	B (µg/l)	6.30	below det.	7.10	below det.	8.16	13.09
	Ba (µg/l)	0.98	0.68	1.06	0.87	0.87	1.83
	Ca (mg/l)	1.14	1.58	1.83	1.78	2.60	3.38
	Fe (µg/l)	46.01	42.89	53.20	47.22	39.23	33.58
	K (mg/l)	0.31	0.78	0.29	0.39	0.45	0.77
	Li (µg/l)	0.451	0.395	0.411	0.334	0.377	0.345
	Mg (mg/l)	0.26	0.31	0.30	0.31	0.40	0.56
	Mn (µg/l)	4.544	11.360	3.396	4.840	2.755	4.381
	Na (mg/l)	0.67	1.77	0.63	0.98	1.21	1.65
	Si (mg/l)	1.773	0.933	1.687	1.888	2.035	2.953
	Sr (µg/l)	3.97	13.04	5.29	5.86	8.71	14.37
	Zn (µg/l)	below det.	below det.	below det.	1.32	below det.	below det.
	total P (µg/l)	5.0	9.3	6.1	5.2	3.8	5.1
	dissolved P (µg/l)	3.7	5.9	4.5	4.7	4.1	5.7
	particulate P (µg/l)	1.3	3.4	1.4	0.5	0.0	0.0
	$\delta^{18}O$ 0-50cm (‰ VSMOW)	-11.34	-7.89	-9.95	-9.56	-8.59	-9.54
	δD 0-50cm (‰ VSMOW)	-78.6	-71.1	-73.7	-72.1	-66.0	-72.3
	d-excess (‰)	12.1	-7.9	5.9	4.4	2.7	4.0

Table continued on next page

Table D.2 – Continued

	Lake #	19	20	21	22	23	24
	Lake Name	Laguna Verdes Alta	Laguna Verdes Baja	Laguna Verdes Medio	Laguna Victoria	Piedras Blancas Lake 2	small pond near L Misteque
	Sample Date	6/8/02	6/8/02	6/8/02	6/2/02	6/9/02	6/5/02
	Z_{max} (m)	2.5	5.5	9	2	3	0.5
	Temp. 0-50cm (°C)	11.5	13.4	11.7	13.8	9.9	16.0
	Temp. Z_{max} (°C)	11.5	12.3	9.8	10.6	9.5	15.9
	SpC 0-50cm (µS)	72.18	37.00	26.12	10.78	5.50	17.74
	SpC Z_{max} (µs)	72.00	36.90	28.70	11.20	5.50	17.80
	DO (ppm) 0-50cm	6.00	6.06	6.55	6.67	6.27	5.52
	DO (ppm) Z_{max}	5.96	6.08	0.18	6.81	6.23	5.44
	DO (% sat) 0-50cm	91.7%	96.3%	100.2%	94.9%	94.3%	89.0%
	DO (% sat) Z_{max}	91.2%	94.2%	2.7%	90.0%	92.9%	87.6%
	pH 0-50cm	7.98	7.87	8.62	7.36	6.86	7.57
	pH Z_{max}	7.99	8.12	6.11	6.92	6.81	7.57
alk. 0-50cm ($CaCO_3$ mg/l)	phenolphthalein	0	0	0	0	0	0
	hydroxide	0	0	0	0	0	0
	carbonate	0	0	0	0	0	0
	bicarbonate	36.3	18.3	10.9	8.1	3.7	8.3
	total	36.3	18.3	10.9	8.1	3.7	8.3
	Al (µg/l)	19.84	11.23	9.11	29.90	13.31	51.30
	B (µg/l)	4.68	below det.	below det.	8.27	below det.	below det.
	Ba (µg/l)	55.00	1.93	5.36	1.02	0.29	8.17
	Ca (mg/l)	13.81	7.12	5.08	1.31	0.89	1.94
	Fe (µg/l)	25.63	35.49	137.00	47.18	462.20	11.83
	K (mg/l)	0.58	0.16	0.60	0.36	0.45	0.84
	Li (µg/l)	1.338	0.547	0.466	0.480	0.382	0.328
	Mg (mg/l)	0.96	0.32	0.31	0.30	0.23	0.41
	Mn (µg/l)	3.501	6.750	82.900	2.257	29.000	0.000
	Na (mg/l)	1.48	1.21	0.87	0.88	0.46	1.52
	Si (mg/l)	2.010	0.176	0.387	2.057	0.086	0.273
	Sr (µg/l)	57.90	27.83	21.08	4.80	2.78	17.16
	Zn (µg/l)	2.26	below det.	below det.	0.61	below det.	below det.
	total P (µg/l)	10.4	9.6	18.2	6.2	9.9	6.6
	dissolved P (µg/l)	6.4	6.0	7.9	6.4	6.0	5.1
	particulate P (µg/l)	4.0	3.6	10.3	1.5	3.9	1.5
	$\delta^{18}O$ 0-50cm (‰ VSMOW)	-5.94	-0.79	-0.83	-10.83	-2.15	-5.73
	δD 0-50cm (‰ VSMOW)	-57.5	-30.8	-30.9	-74.5	-37.8	-56.9
	d-excess (‰)	-10.0	-24.4	-24.2	12.1	-20.6	-11.0

Table D.3 – Isotope composition of water samples from the Venezuelan Andes.

GPS Code	Site	Date	Group	GPS Latitude	GPS Longitude	Altitude (m)	$\delta^{18}O$ (‰ VSMOW)	δD (‰ VSMOW)	d-excess (‰)	notes
LVES07	Laguna Verdes Alta	6/8/02	grnd. water	N8 51.146	W70 52.463	4217	-8.80	-85.6	-15.2	dug 10 cm hole and let fill with water
LVES08	Laguna Verdes Alta	6/8/02	grnd. water	N8 51.146	W70 52.463	4218	-10.63	-79.5	5.6	dug 10 cm hole and let fill with water
LVES06	Laguna Verdes Alta	6/8/02	puddle	N8 51.150	W70 52.462	4216	-10.61	-85.2	-0.4	standing puddle in wet inlet area
LVES23	Laguna Verdes Baja	6/8/02	grnd. water	N8 51.472	W70 52.453	4170	-10.04	-76.1	4.2	dug 10 cm hole and let fill with water
LVES20	Laguna Verdes Medio	6/8/02	grnd. water	N8 51.339	W70 52.475	4194	-9.43	-71.5	4.0	dug 10 cm hole and let fill with water
LMUC	Mucubaji Spring	1/1/97	grnd. water				-11.37	-75.5	15.4	springs
LGON	Springs ~200m above L. Arenales on N. side of valley	1/21/00	grnd. water				-11.30	-79.0	11.4	spring
LMIS01	Laguna Misteque	6/5/02	stream	N8 43.208	W70 53.074	3804	-8.32	-70.4	-3.8	inflow stream
LBAN04	Laguna Negra (Paramo El Banco)	6/6/02	stream	N8 48.637	W70 56.976	4206	-11.65	-87.2	5.9	inflow stream
LCRUC	Las Cruces Stream 1	1/1/99	stream				-7.90	-62.0	1.2	
LCRUC	Las Cruces Stream 2	1/1/99	stream				-11.30	-81.5	8.9	
LBAN27	Paramo El Banco	6/7/02	stream	N8 49.265	W70 56.718	4123	-11.52	-88.3	3.8	stream sample on valley side near pass of Qbr. El Banco
LBAN11	Paramo El Banco Lake 2	6/6/02	stream	N8 48.934	W70 57.066	4196	-7.15	-63.2	-6.0	inflow stream
LBAN28	Stream draining N and W valleys of Paramo el Banco	6/7/02	stream	N8 48.694	W70 55.670	3840	-11.03	-82.3	6.0	stream draining N and W valleys
LBAN29	Stream draining SW valley of Paramo el Banco	6/7/02	stream	N8 48.655	W70 55.453	3801	-11.58	-86.7	5.9	stream from SW valley
LPBL07	Quebrada Mifafi	6/9/02	stream	N8 52.182	W70 53.945	4234	-11.39	-86.1	5.0	

Table continued on next page

Table D.3 – Continued

GPS Code	Site	Date	Group	GPS Latitude	GPS Longitude	Altitude (m)	$\delta^{18}O$ (‰ VSMOW)	δD (‰ VSMOW)	d-excess (‰)	notes
LVES01	Laguna Verdes Alta	6/8/02	stream	N8 51.891	W70 52.156	3961	-11.10	-83.7	5.1	stream draining main valley of L Las Verdes
LBAN12	Paramo El Banco Lake 2	6/6/02	lake	N8 48.940	W70 57.071	4192	-7.42	-66.9	-7.5	
LBAN14	Paramo El Banco Lake 3	6/6/02	lake	N8 48.976	W70 57.034	4195	-13.23	-106.5	-0.7	
LBAN26	Paramo El Banco Lake 4	6/7/02	lake	N8 49.035	W70 57.424	4296	-11.85	-90.3	4.5	
LGON	Lake #1 above Laguna Arenales	1/20/00	lake				-9.60	-70.0	6.8	
LGON	Lake #2 above Laguna Arenales	1/20/00	lake	N8 43.636	W71 11.260	4092	-6.50	-57.0	-5.0	
LGON	Lake #4 above Laguna Arenales	1/21/00	lake				-9.40	-66.0	9.2	
LGON	Lake #5 above Laguna Arenales	1/21/00	lake				-10.50	-73.0	11.0	
LGON	Lago Encierro Alto	1/24/00	lake				-8.20	-63.0	2.6	
LGON	Lago Encierro Bajo	1/24/00	lake				-7.60	-60.0	0.8	
LURAO	Lago Urao	1/1/99	lake	N8 31.000	W71 23.000	1100	-1.30	-18.5	-8.1	
LGON	Laguna Arenales Alta	1/22/00	lake				-9.60	-70.0	6.8	
LGON01	Laguna Arenales Baja	1/19/00	lake	N8 43.470	W71 11.754	4005	-10.00	-72.0	8.0	
LBLA	Laguna Blanca	1/1/99	lake	N8 20.105	W71 47.072	1620	-1.60	-21.5	-8.7	
LBLA01	Laguna Blanca	6/12/02	lake	N8 20.105	W71 47.072	1620	-1.69	-15.8	-2.3	
LGON	Laguna Bolsa Azul	1/23/00	lake				-5.90	-54.0	-6.8	
LBRA	Laguna Brava	1/1/97	lake	N8 18.355	W71 50.356	2399	0.44	-4.5	-8.0	

Table continued on next page

Table D.3 – Continued

GPS Code	Site	Date	Group	GPS Latitude	GPS Longitude	Altitude (m)	$\delta^{18}O$ (‰ VSMOW)	δD (‰ VSMOW)	d-excess (‰)	notes
LBRA	Laguna Brava	1/1/99	lake	N8 18.355	W71 50.356	2399	0.80	-12.0	-18.4	
LBRA01	Laguna Brava	6/12/02	lake	N8 18.355	W71 50.356	2399	-0.50	-12.8	-8.8	
LPAT02	Laguna de La Pata (nr. Gavidia)	6/14/02	lake	N8 39.200	W70 56.041	3982	-6.63	-55.1	-2.0	
LBAN10	Laguna Grande de Los Patos	6/6/02	lake	N8 48.820	W70 56.926	4190	-1.23	-34.1	-24.3	
LBAN32	Laguna Grande de Los Patos	6/25/02	lake	N8 48.858	W70 56.836	4190	-1.56	-34.7	-22.2	
LBAN24	Laguna La Cura	6/7/02	lake	N8 48.776	W70 57.175	4220	-7.05	-62.0	-5.6	
LBAN18	Laguna La Posita	6/7/02	lake	N8 48.789	W70 57.059	4226	-12.34	-100.0	-1.2	subbasin B
LBAN17	Laguna La Posita	6/7/02	lake	N8 48.801	W70 57.044	4224	-12.09	-96.8	-0.1	subbasin C
LBAN23	Laguna La Posita	6/7/02	lake	N8 48.757	W70 57.069	4226	-1.56	-38.5	-26.0	subbasin A (main basin)
LLIR	Laguna Los Lirios	1/1/97	lake	N8 18.452	W71 49.594	2305	-2.23	-20.1	-2.2	
LLIR	Laguna Los Lirios	1/1/99	lake	N8 18.452	W71 49.594	2305	-3.00	-31.0	-7.0	
LLIR01	Laguna Los Lirios	6/12/02	lake	N8 18.452	W71 49.594	2305	-1.01	-16.6	-8.6	
LPBL01	Laguna Los Locos (Piedras Blancas Lake 1)	6/9/02	lake	N8 51.772	W70 53.845	4371	-4.20	-47.4	-13.8	
LPBL08	Laguna Los Locos (Piedras Blancas Lake 1)	6/24/02	lake	N8 51.803	W70 53.923	4371	-5.74	-57.3	-11.4	resampled after 2 weeks of rain
LMIC02	Laguna Michurao Alto	6/4/02	lake	N8 43.823	W70 51.766	3738	-8.66	-66.3	3.0	

Table continued on next page

Table D.3 – Continued

GPS Code	Site	Date	Group	GPS Latitude	GPS Longitude	Altitude (m)	$\delta^{18}O$ (‰ VSMOW)	δD (‰ VSMOW)	d-excess (‰)	notes
LMIC09	Laguna Michurao Bajo	6/4/02	lake	N8 44.156	W70 52.000	3718	-7.86	-62.4	0.5	
LMIS03	Laguna Misteque	6/5/02	lake	N8 43.345	W70 53.128	3803	-8.27	-64.4	1.7	
LMUC	Laguna Mucubaji	1/1/97	lake	N8 47.795	W70 49.701	3573	-9.41	-66.1	9.2	
LMUC	Laguna Mucubaji	1/1/99	lake	N8 47.795	W70 49.701	3573	-10.70	-75.5	10.1	
LMUC	Laguna Mucubaji	1/27/00	lake	N8 47.795	W70 49.701	3573	-10.40	-75.0	8.2	
LMUC01	Laguna Mucubaji	6/18/02	lake	N8 47.795	W70 49.701	3573	-9.65	-68.1	9.1	
LNEG	Laguna Negra (nr Mucubaji)	1/1/97	lake	N8 47.175	W70 48.301	3462	-10.60	-71.6	13.2	
LNEG	Laguna Negra (nr Mucubaji)	1/1/97	lake	N8 47.175	W70 48.301	3462	-10.59	-71.1	13.7	
LNEG03	Laguna Negra (nr Mucubaji)	6/17/02	lake	N8 47.175	W70 48.301	3462	-11.34	-78.6	12.1	
LBAN03	Laguna Negra (Paramo El Banco)	6/6/02	lake	N8 48.655	W70 56.940	4206	-7.89	-71.1	-7.9	
LPAR02	Laguna Parche	6/14/02	lake	N8 38.814	W70 55.682	3894	-9.95	-73.7	5.9	
LCRUC	Laguna Patos (nr. Las Cruces)	6/21/02	lake				-11.11	-76.5	12.4	
LGON	Laguna Quatrobrasso	1/22/00	lake				-9.50	-68.0	8.0	
LROY01	Laguna Royal "A"	6/3/02	lake	N8 42.979	W70 52.302	3827	-9.56	-72.1	4.4	
LROY07	Laguna Royal "C"	6/3/02	lake	N8 43.308	W70 52.227	3824	-8.59	-66.0	2.7	
LROY13	Laguna Royal "D"	6/3/02	lake	N8 43.696	W70 52.361	3763	-9.54	-72.3	4.0	

Table continued on next page

Table D.3 – Continued

GPS Code	Site	Date	Group	GPS Latitude	GPS Longitude	Altitude (m)	$\delta^{18}O$ (‰ VSMOW)	δD (‰ VSMOW)	d-excess (‰)	notes
LVES	Laguna Verdes Alta	1/1/99	lake	N8 51.165	W70 52.449	4215	-9.20	-72.0	1.6	
LVES	Laguna Verdes Alta	1/28/00	lake	N8 51.165	W70 52.449	4215	-9.30	-74.0	0.4	
LVES05	Laguna Verdes Alta	6/8/02	lake	N8 51.165	W70 52.449	4215	-5.94	-57.5	-10.0	
LVES	Laguna Verdes Baja	1/1/99	lake	N8 51.488	W70 52.420	4170	-4.10	-49.0	-16.2	
LVES	Laguna Verdes Baja	1/28/00	lake	N8 51.488	W70 52.420	4170	-3.90	-49.0	-17.8	
LVES24	Laguna Verdes Baja	6/8/02	lake	N8 51.488	W70 52.420	4170	-0.79	-30.8	-24.4	
LVES	Laguna Verdes Medio	1/1/99	lake	N8 51.337	W70 52.412	4193	-3.00	-42.5	-18.5	
LVES	Laguna Verdes Medio	1/28/00	lake	N8 51.337	W70 52.412	4193	-2.90	-44.0	-20.8	
LVES09	Laguna Verdes Medio	6/8/02	lake	N8 51.337	W70 52.412	4193	-0.83	-30.9	-24.2	
LVIC01	Laguna Victoria	6/2/02	lake	N8 48.782	W70 47.997	3223	-10.83	-74.5	12.1	
LGON	Lagunita nr. Rio Gonzales A	1/22/00	lake				-6.00	-54.0	-6.0	
LCRUC	Las Cruces Laguna 1	1/1/99	lake				-7.00	-62.5	-6.5	
LCRUC	Las Cruces Laguna 3	1/1/99	lake				-8.10	-69.0	-4.2	
LCRUC	Las Curces Laguna 2	1/1/99	lake				-3.80	-49.5	-19.1	
LMUC	Lateral Moraine Bog-Mucubaji	1/1/99	lake				-1.40	-17.0	-5.8	
LPBL05	Piedras Blancas Lake 2	6/9/02	lake	N8 51.656	W70 54.281	4404	-2.15	-37.8	-20.6	
LPBL03	Piedras Blancas small pond 1	6/9/02	lake	N8 51.790	W70 53.959	4381	-12.36	-96.5	2.4	

Table continued on next page

Table D.3 – Continued

GPS Code	Site	Date	Group	GPS Latitude	GPS Longitude	Altitude (m)	$\delta^{18}O$ (‰ VSMOW)	δD (‰ VSMOW)	d-excess (‰)	notes
LPBL06	Piedras Blancas small pond 1	6/9/02	lake	N8 51.678	W70 54.495	4392	-11.45	-86.4	5.2	
LMIS08	small L nxt to L Misteque	6/5/02	lake	N8 43.481	W70 53.062	3813	-5.73	-56.9	-11.0	
APAR01	Apartaderos	6/4/02	rain	N8 48.089	W70 51.460	3407	-17.29	-129.5	8.9	about 0.65cm of precipitation night of 6/3/02
APAR02	Apartaderos	6/19/02	rain	N8 48.089	W70 51.460	3407	-16.89	-132.6	2.5	rained 9:30-12:30pm ~1cm of rain
APAR03	Apartaderos	6/23/02	rain	N8 48.089	W70 51.460	3407	-20.75	-156.7	9.3	2h of hard rain, sampled at end of storm
APAR04	Apartaderos	6/29/02	rain	N8 48.089	W70 51.460	3407	-6.06	-49.0	-0.5	2h light mist and heavier bursts, collected from drainpipe, represents mostly the heaviest rain
LBAN31	Laguna Grande de Los Patos	6/25/02	rain	N8 48.858	W70 56.836	4192	-12.76	-103.1	-1.0	precip sample from rain/sun, on and off hard rain
MERI01	Merida	6/12/02	rain	N8 36.138	W71 08.853	1498	-7.50	-54.5	5.6	rained 5-8pm, about 85ml of rain in bottle
LBAN16	Paramo El Banco	6/6/02	rain	N8 48.778	W70 56.937	4189	-14.00	-99.4	12.6	rained 20min, some hail, hard rain
LBAN25	Paramo el Banco	6/7/02	rain	N8 48.771	W70 57.092	4210	-14.17	-99.7	13.7	45 minute rain storm
LMUC02	Pico Mucuñuque	6/21/02	snow	N8 45.575	W70 48.444	4536	-18.49	-135.6	12.3	snow sample from summit of headwall

Table D.4 – Accelerator mass spectrometry (AMS) radiocarbon ages of sediments.

Laboratory Identifier	Lake	Core type[a]	Core	Drive	Drive depth (cm)	Composite depth (cm)[b]	Material[c]	$\delta^{13}C$ (‰ VPDB)	f. modern	±1σ	^{14}C Age	±1σ	Calib. age (y BP)	age model[d]
OS-CURL-4973	L. Blanca	Liv.	99A	1	64.5	64.5	terr. macro.	-23.2	0.9838	0.0040	130	35	104	yes
OS-CURL-4974	L. Blanca	Liv.	99A	2	13.5	103.5	terr. macro.	-25.1	0.9208	0.0038	660	35	578	yes
CAMS-73134	L. Blanca	Liv.	99A	2	33.0 - 34.0	123.5	wood	-25.0	0.8851	0.0037	980	40	926	yes
CAMS-96801	L. Blanca	Liv.	99A	2	84.5 - 85.5	175.0	wood	-25.0	0.7150	0.0050	2700	60	2780	yes
CAMS-96802	L. Blanca	Liv.	99A	3	11.0	188.6	wood	-25.0	0.7682	0.0033	2120	35	2115	yes
CAMS-96803	L. Blanca	Liv.	99A	3	90.0	271.7	wood	-25.0	0.6483	0.0030	3480	40	3795	yes
CAMS-96804	L. Blanca	Liv.	99A	4	21.5	310.7	wood	-25.0	0.5929	0.0023	4200	35	4825	yes
CAMS-96805	L. Blanca	Liv.	99A	5	30.0 - 30.5	388.3	wood	-25.0	0.4154	0.0018	7055	40	7900	yes
OS-CURL-4975	L. Blanca	Liv.	99A	6	12.0	419.9	terr. macro.	-26.1	0.3995	0.0024	7370	45	8175	yes
CAMS-96806	L. Blanca	Liv.	99A	6	23.5	431.3	terr. macro.	-25.0	0.3908	0.0021	7550	45	8370	yes
CAMS-96807	L. Blanca	Liv.	99A	6	37.5 - 38.5	445.6	bulk sed.	-25.0	0.3501	0.0021	8430	50	9470	yes

Table continued on next page

Table D.4 – Continued

Laboratory Identifier	Lake	Core type[a]	Core	Drive	Drive depth (cm)	Composite depth (cm)[b]	Material[c]	$\delta^{13}C$ (‰ VPDB)	f. modern	±1σ	^{14}C Age	±1σ	Calib. age (y BP)	age model[d]
CAMS-96814	L. Mucubají	Glew	GL-99A	-	23.0 - 24.0	23.5	aq. moss	-25.0	0.9236	0.0141	640	130	606	no
CAMS-96808	L. Mucubají	Perc.	99A	1	18.0 - 20.0	36.7	wood	-25.0	0.9368	0.0041	525	35	533	no
CAMS-96809	L. Mucubají	Perc.	99A	1	24.0 - 26.0	41.1	wood	-25.0	0.9596	0.0043	330	40	380	yes
AA-35204	L. Mucubají	Liv.	99C	1	30.0	48.5	aq. moss	-31.1			635	45	580	yes
OS-CURL-4959	L. Mucubají	Liv.	99C	1	43.0	61.3	aq. moss	-30.5	0.8636	0.0034	1180	30	1082	yes
CAMS-96810	L. Mucubají	Perc.	99A	1	52.0 - 54.0	69.5	aq. moss	-25.0	0.8439	0.0034	1365	35	1285	yes
OS-CURL-4960	L. Mucubají	Liv.	99C	1	71.0	93.1	aq. moss	-31.6	0.7687	0.0034	2110	35	2081	yes
AA-35205	L. Mucubají	Liv.	99C	1	90.0	107.3	aq. moss	-32.6			2640	45	2761	yes
OS-CURL-4961	L. Mucubají	Liv.	99C	2	20.0	111.9	aq. moss	-32.3	0.6798	0.0040	3100	45	3341	yes
AA-35206	L. Mucubají	Liv.	99C	2	41.5	134.3	aq. moss	-33.2			3665	80	3988	yes
OS-CURL-4962	L. Mucubají	Liv.	99C	2	48.0	141.7	aq. moss	-31.5	0.6030	0.0043	4060	60	4542	yes

Table continued on next page

Table D.4 – Continued

Laboratory Identifier	Lake	Core type[a]	Core	Drive	Drive depth (cm)	Composite depth (cm)[b]	Material[c]	$\delta^{13}C$ (‰ VPDB)	f. modern	±1σ	^{14}C Age	±1σ	Calib. age (y BP)	age model[d]
AA-35207	L. Mucubají	Liv.	99C	2	70.0	164.5	aq. moss	-34.1			4640	110	5384	yes
OS-CURL-4963	L. Mucubají	Liv.	99C	2	77.0	171.7	aq. moss	-32.2	0.5445	0.0031	4880	45	5620	yes
CAMS-96811	L. Mucubají	Liv.	02F	3	0.5-1.0	184.6	aq. moss	-25.0	0.5069	0.0024	5455	40	6223	yes
AA-35208	L. Mucubají	Liv.	99C	2	94.0	191.9	aq. moss	-32.0			5360	55	6128	no
CAMS-96812	L. Mucubají	Liv.	02F	3	30.5 - 31.5	214.3	aq. moss	-25.0	0.4386	0.0108	6620	200	7537	yes
CAMS-96813	L. Mucubají	Liv.	02F	3	58.5 - 59.5	243.3	aq. moss	-25.0	0.3991	0.0047	7380	100	8183	yes
CAMS-104913	L. Mucubají	Liv.	02F	6	38.0	533.5	aq. moss	-25.0	0.4144	0.0064	7080	130	7883	no
CAMS-96815	L. Verdes Alta	Liv.	99A	1	18.0 - 21.0	24.5	terr. macro.	-25.0	0.8121	0.0044	1670	45	1570	no
OS-CURL-4970	L. Verdes Alta	Glew	GL-99A	-	32.0 - 33.0	33.5	bulk sed.	-16.0	0.8305	0.0042	1500	40	1373	no
CAMS-73090	L. Verdes Alta	Glew	GL-99A	-	32.0 - 33.0	33.5	terr. macro.	-22.0	0.9031	0.0044	820	40	714	yes
OS-CURL-4971	L. Verdes Alta	Glew	GL-99A	-	45.0 - 46.0	46.5	bulk sed.	-16.6	0.7612	0.0040	2190	40	2270	no

Table continued on next page

Table D.4 – Continued

Laboratory Identifier	Lake	Core type[a]	Core	Drive	Drive depth (cm)	Composite depth (cm)[b]	Material[c]	$\delta^{13}C$ (‰ VPDB)	f. modern	±1σ	^{14}C Age	±1σ	Calib. age (y BP)	age model[d]
CAMS-73091	L. Verdes Alta	Glew	GL-99A	-	45.0 - 46.0	46.5	terr. macro.	-22.0	0.8008	0.0040	1780	40	1643	yes
OS-CURL-4972	L. Verdes Alta	Glew	GL-99A	-	55.0 - 56.0	56.5	bulk sed.	-16.2	0.6522	0.0032	3430	40	3676	no
OS-CURL-4988	L. Verdes Alta	Liv.	99A	1	76.5 - 77.5	82.0	bulk sed.	-16.7	0.5745	0.0027	4450	35	5014	no
OS-CURL-4989	L. Verdes Alta	Liv.	99A	2	15.0 - 16.0	110.5	bulk sed.	-17.2	0.5005	0.0038	5560	60	6327	no
AA-35201	L. Verdes Alta	Liv.	99A	2	15.5	110.5	terr. macro.	-20.7			4170	110	4701	yes
OS-CURL-4990	L. Verdes Alta	Liv.	99A	2	39.0 - 40.0	134.5	bulk sed.	-16.4	0.4313	0.0040	6800	75	7631	no
OS-CURL-4991	L. Verdes Alta	Liv.	99A	2	51.0 - 52.0	146.5	bulk sed.	-17.8	0.3982	0.0024	7400	50	8280	no
OS-CURL-4992	L. Verdes Alta	Liv.	99A	2	75.0 - 76.0	170.5	bulk sed.	-16.4	0.3310	0.0022	8880	55	10041	no
OS-CURL-4993	L. Verdes Alta	Liv.	99A	3	16.0 - 17.0	201.5	bulk sed.	-16.0	0.2974	0.0021	9740	55	11160	no
OS-CURL-4994	L. Verdes Alta	Liv.	99A	3	34.0 - 35.0	219.5	bulk sed.	-15.5	0.2757	0.0020	10400	60	12547	no
CAMS-73202	L. Verdes Alta	Liv.	99A	3	38.0	223.0	bulk sed.	-25.0	0.2817	0.0014	10180	50	11824	no

Table continued on next page

Table D.4 – Continued

Laboratory Identifier	Lake	Core type[a]	Core	Drive	Drive depth (cm)	Composite depth (cm)[b]	Material[c]	$\delta^{13}C$ (‰ VPDB)	f. modern	±1σ	^{14}C Age	±1σ	Calib. age (y BP)	age model[d]
OS-CURL-4995	L. Verdes Alta	Liv.	99A	3	58.0 - 59.0	243.5	bulk sed.	-13.1	0.2574	0.0019	10900	60	12942	no
CAMS-96816	L. Verdes Alta	Liv.	99A	3	70.5 - 72.0	256.3	terr. macro.	-25.0	0.2980	0.0064	9720	180	10887	yes
OS-CURL-4964	L. Verdes Alta	Liv.	99A	3	86.0 - 87.0	271.5	bulk sed.	-11.2	0.2297	0.0019	11800	65	13609	no
OS-CURL-4965	L. Verdes Alta	Liv.	99A	4	12.0 - 13.0	287.5	bulk sed.	-10.9	0.2064	0.0018	12700	70	14569	no
OS-CURL-4966	L. Verdes Alta	Liv.	99A	4	27.0 - 28.0	302.5	bulk sed.	-10.2	0.1909	0.0021	13300	90	15983	no
OS-CURL-4996	L. Verdes Alta	Liv.	99A	4	36.0 - 37.0	311.5	bulk sed.	-9.3	0.1952	0.0017	13100	70	15758	no
OS-CURL-4997	L. Verdes Alta	Liv.	99A	4	41.5	316.5	bulk sed.	-12.8	0.2466	0.0022	11200	70	13109	no
AA-35203	L. Verdes Alta	Liv.	99A	4	41.5	316.5	terr. macro.	-31.1			12270	150	14238	yes
OS-CURL-4967	L. Verdes Alta	Liv.	99A	4	43.0 - 44.0	318.5	bulk sed.	-12.4	0.1591	0.0014	14750	70	17653	no
OS-CURL-4968	L. Verdes Alta	Liv.	99A	4	47.5 - 48.5	323.0	bulk sed.	-10.4	0.1613	0.0016	14650	80	17538	no
OS-CURL-4969	L. Verdes Alta	Liv.	99A	4	57.0 - 58.0	332.5	bulk sed.	-13.8	0.1544	0.0025	15000	130	17940	no

Table continued on next page

Table D.4 – Continued

Laboratory Identifier	Lake	Core type[a]	Core	Drive	Drive depth (cm)	Composite depth (cm)[b]	Material[c]	$\delta^{13}C$ (‰ VPDB)	f. modern	±1σ	^{14}C Age	±1σ	Calib. age (y BP)	age model[d]
CAMS-73272	L. Verdes Baja	Liv.	99A	1	34.5 - 35.5	45.2	bulk sed.	-22.0	0.9130	0.0041	730	40	671	no
CAMS-73203	L. Verdes Baja	Liv.	99A	1	34.5 - 35.5	45.2	terr. macro.	-25.0	0.9106	0.0051	750	50	684	yes
OS-CURL-4979	L. Verdes Baja	Liv.	99A	4	16.5 - 17.0	302.2	bulk sed.	-13.5	0.2091	0.0017	12550	65	14565	no
CAMS-73092	L. Verdes Baja	Liv.	99A	4	16.5 - 17.0	302.2	terr. macro.	-22.0	0.2047	0.0031	12740	130	15398	yes

(a) Livingstone square rod, Nesje percussion or Glew surface sediment corer
(b) Depth below sed. water interface, corrected for overlap between drives and stretching/compression during coring
(c) unidentifed terrestrial macrophyte, aquatic moss
(d) Sample included in age-depth model

Table D.5 – Lead-210 analyses of L. Mucubají surface core GL-99A.

Sample #	Dry wt. (g)	Accum. dry wt. (g/cm^2)	Sample Depth top (cm)	Sample Depth bottom (cm)	^{210}Pb activity (Bq/g)	± 1σ	excess ^{210}Pb activity (Bq/g)	Linear model years/ level	Linear model Median yr of deposition (A.D.)	Constant Rate of Supply model years/ level	Constant Rate of Supply model Median yr of deposition (A.D.)	Rapid Steady State Mixing Model years/ level	Rapid Steady State Mixing Model Median yr of deposition (A.D.)
1	1.089	0.0338	0.0	0.5	0.1224	0.0048	0.1044	1.8	1999.1	0.8	2000.0	1.0	2000.0
2	1.580	0.0829	0.5	1.0	0.1231	0.0053	0.1051	2.6	1997.0	1.2	1998.0	2.0	1997.0
3	1.662	0.1346	1.0	1.5	0.1638	0.0052	0.1458	2.7	1994.3	1.9	1997.0	2.0	1995.0
4	1.488	0.1809	1.5	2.0	0.1736	0.0071	0.1556	2.4	1991.8	1.9	1995.0	2.0	1992.0
5	1.841	0.2381	2.0	2.5	0.1572	0.0050	0.1392	3.0	1989.1	2.3	1992.0	3.0	1989.0
6	1.579	0.2872	2.5	3.0	0.1783	0.0072	0.1603	2.6	1986.3	2.4	1990.0	2.0	1986.0
7	1.653	0.3386	3.0	3.5	0.1874	0.0052	0.1694	2.7	1983.7	2.9	1987.0	2.0	1983.0
8	1.713	0.3918	3.5	4.0	0.1752	0.0062	0.1572	2.8	1981.0	3.1	1984.0	2.0	1981.0
9	1.541	0.4397	4.0	4.5	0.1714	0.0049	0.1534	2.5	1978.4	3.0	1981.0	2.0	1978.0
10	1.741	0.4938	4.5	5.0	0.1390	0.0052	0.1210	2.8	1975.7	2.9	1978.0	3.0	1975.0
11	1.974	0.5552	5.0	5.5	0.1322	0.0047	0.1142	3.2	1972.7	3.4	1975.0	3.0	1972.0
12	1.999	0.6173	5.5	6.0	0.1191	0.0054	0.1011	3.2	1969.5	3.4	1972.0	3.0	1969.0
13	1.993	0.6793	6.0	6.5	0.1209	0.0038	0.1029	3.2	1966.3	3.8	1968.0	3.0	1965.0
14	2.318	0.7513	6.5	7.0	0.1045	0.0038	0.0865	3.7	1962.8	4.3	1964.0	4.0	1962.0
15	2.158	0.8184	7.0	7.5	0.0897	0.0036	0.0717	3.5	1959.2	3.7	1960.0	4.0	1958.0
16	2.423	0.8937	7.5	8.0	0.0681	0.0030	0.0501	3.9	1955.5	3.3	1957.0	4.0	1954.0
17	2.710	0.9779	8.0	8.5	0.0598	0.0021	0.0418	4.4	1951.3	3.4	1954.0	5.0	1950.0
18	2.677	1.0611	8.5	9.0	0.0660	0.0023	0.0480	4.3	1947.0	4.3	1949.0	5.0	1945.0
19	3.086	1.1570	9.0	9.5	0.0619	0.0023	0.0439	5.0	1942.3	5.3	1944.0	5.0	1940.0
20	2.931	1.2481	9.5	10.0	0.0583	0.0021	0.0403	4.7	1937.5	5.4	1939.0	5.0	1935.0
21	4.782	1.3968	10.0	11.0	0.0514	0.0019	0.0334	7.7	1931.2	9.2	1930.0	8.0	1929.0

Table continued on next page

Table D.5 – Continued

Sample #	Dry wt. (g)	Accum. dry wt. (g/cm^2)	Sample Depth top (cm)	Sample Depth bottom (cm)	^{210}Pb activity (Bq/g)	± 1σ	excess ^{210}Pb activity (Bq/g)	Linear model years/ level	Linear model Median yr of deposition (A.D.)	Constant Rate of Supply model years/ level	Constant Rate of Supply model Median yr of deposition (A.D.)	Rapid Steady State Mixing Model years/ level	Rapid Steady State Mixing Model Median yr of deposition (A.D.)
22	5.238	1.5596	11.0	12.0	0.0502	0.0019	0.0322	8.5	1923.1	13.9	1918.0	9.0	1920.0
23	5.429	1.7284	11.8	13.0	0.0329	0.0015	0.0149	8.8	1914.5	9.6	1909.0	9.0	1911.0
24	6.307	1.9244	13.0	14.0	0.0265		0.0085	10.2	1905.0	8.5	1902.0	11.0	1901.0
25	5.984	2.1104	14.0	15.0	0.0202	0.0011	0.0022	9.7	1895.1	2.5		11.0	1891.0
26	6.540	2.3137	15.0	16.0									
27	7.239	2.5388	16.0	17.0	0.0202	0.0009							
28	6.661	2.7459	17.0	18.0									
29	6.272	2.9408	18.0	19.0	0.0224	0.0009							
30	6.820	3.1528	19.0	20.0									
31	6.106	3.3426	20.0	21.0	0.0167	0.0008							
32	6.552	3.5463	21.0	22.0									
33	6.612	3.7518	22.0	23.0	0.0201	0.0009							
34	6.127	3.9423	23.0	24.0									
35	6.891	4.1564	24.0	25.0	0.0193	0.0010							
36	1.915	4.2160	25.0	25.5									

Table D.6 – Cesium-137 analyses of L. Mucubají surface core GL-99A.

Sample #	Dry wt. (g)	Accum. dry wt. (g/cm^2)	Sample Depth (cm) top	bottom	^{137}Cs activity (Bq/g)	± 1σ
1	1.089	0.0338	0.0	0.5		
2	1.580	0.0829	0.5	1.0		
3	1.662	0.1346	1.0	1.5		
4	1.488	0.1809	1.5	2.0	0.0000	
5	1.841	0.2381	2.0	2.5		
6	1.579	0.2872	2.5	3.0	0.0000	
7	1.653	0.3386	3.0	3.5		
8	1.713	0.3918	3.5	4.0	0.0000	
9	1.541	0.4397	4.0	4.5		
10	1.741	0.4938	4.5	5.0		
11	1.974	0.5552	5.0	5.5	0.0000	
12	1.999	0.6173	5.5	6.0		
13	1.993	0.6793	6.0	6.5	0.0127	0.0041
14*	2.318	0.7513	6.5	7.0	0.0265	0.0106
15	2.158	0.8184	7.0	7.5	0.0200	0.0040
16	2.423	0.8937	7.5	8.0	0.0000	0.0000
17	2.710	0.9779	8.0	8.5		
18	2.677	1.0611	8.5	9.0	0.0000	

*^{137}Cs peak

Table D.7 – Lead-210 analyses of L. Verdes Alta surface core GL-99A.

Sample #	Dry wt. (g)	Accum. dry wt. (g/cm^2)	Sample Depth top (cm)	Sample Depth bottom (cm)	^{210}Pb activity (Bq/g)	± 1σ	excess ^{210}Pb activity (Bq/g)	Linear model years/ level	Linear model Median yr of deposition (A.D.)	Constant Rate of Supply model years/ level	Constant Rate of Supply model Median yr of deposition (A.D.)	Rapid Steady State Mixing Model years/ level	Rapid Steady State Mixing Model Median yr of deposition (A.D.)
1	0.099	0.0031	0.0	0.5				0.6	1999.7	0.3	1999.8	0.0	2000.0
2	0.249	0.0108	0.5	1.0	0.4030	0.0180	0.3970	1.6	1998.6	0.8	1999.3	1.0	1999.0
3	0.271	0.0192	1.0	1.5				1.7	1997.0	0.9	1998.4	1.0	1998.0
4	0.321	0.0292	1.5	2.0	0.4326	0.0156	0.4266	2.0	1995.1	1.2	1997.3	1.0	1996.0
5	0.326	0.0394	2.0	2.5				2.0	1993.1	1.2	1996.1	1.0	1994.0
6	0.322	0.0494	2.5	3.0	0.4310	0.0185	0.4250	2.0	1991.1	1.3	1994.9	1.0	1993.0
7	0.349	0.0602	3.0	3.5				2.2	1989.0	1.4	1993.5	2.0	1991.0
8	0.315	0.0700	3.5	4.0	0.4077	0.0194	0.4017	2.0	1986.9	1.3	1992.2	1.0	1989.0
9	0.306	0.0795	4.0	4.5				1.9	1985.0	1.2	1991.0	1.0	1987.0
10	0.258	0.0875	4.5	5.0	0.3561	0.0208	0.3501	1.6	1983.2	1.0	1989.9	1.0	1985.0
11	0.298	0.0968	5.0	5.5				1.9	1981.5	1.2	1988.8	1.0	1984.0
12	0.309	0.1064	5.5	6.0	0.3443	0.0180	0.3383	1.9	1979.6	1.2	1987.6	1.0	1982.0
13	0.322	0.1164	6.0	6.5				2.0	1977.6	1.3	1986.3	1.0	1980.0
14	0.326	0.1265	6.5	7.0	0.3385	0.0182	0.3325	2.0	1975.6	1.4	1985.0	2.0	1979.0
15	0.338	0.1371	7.0	7.5				2.1	1973.5	1.5	1983.6	1.0	1977.0
16	0.308	0.1466	7.5	8.0	0.3622	0.0170	0.3562	1.9	1971.5	1.5	1982.0	1.0	1975.0
17	0.380	0.1584	8.0	8.5				2.4	1969.3	1.9	1980.3	2.0	1973.0
18	0.323	0.1685	8.5	9.0	0.3468	0.0181	0.3408	2.0	1967.1	1.7	1978.5	1.0	1971.0
19	0.328	0.1787	9.0	9.5				2.1	1965.1	1.8	1976.7	2.0	1969.0
20	0.338	0.1892	9.5	10.0	0.3405	0.0175	0.3345	2.1	1963.0	2.0	1974.8	1.0	1967.0
21	0.468	0.2037	10.0	11.0				2.9	1960.5	2.8	1972.4	2.0	1965.0

Table continued on next page

Table D.7 – Continued

Sample #	Dry wt. (g)	Accum. dry wt. (g/cm^2)	Sample Depth top (cm)	Sample Depth bottom (cm)	^{210}Pb activity (Bq/g)	± 1σ	excess ^{210}Pb activity (Bq/g)	Linear model years/ level	Linear model Median yr of deposition (A.D.)	Constant Rate of Supply model years/ level	Constant Rate of Supply model Median yr of deposition (A.D.)	Rapid Steady State Mixing Model years/ level	Rapid Steady State Mixing Model Median yr of deposition (A.D.)
22	0.684	0.2250	11.0	12.0	0.3211	0.0097	0.3151	4.3	1956.9	4.5	1968.7	3.0	1962.0
23	0.497	0.2405	11.8	12.8				3.1	1953.2	3.8	1964.6	2.0	1958.0
24	0.771	0.2644	13.0	14.0	0.3277	0.0092	0.3217	4.8	1949.3	7.0	1959.2	4.0	1955.0
25	0.853	0.2910	14.0	15.0				5.3	1944.2	8.0	1951.7	5.0	1950.0
26	0.705	0.3129	15.0	16.0	0.2102	0.0088	0.2042	4.4	1939.3	6.4	1944.6	4.0	1946.0
27	1.043	0.3453	16.0	17.0				6.5	1933.9	9.7	1936.5	5.0	1941.0
28	1.174	0.3818	17.0	18.0	0.1280	0.0044	0.1220	7.3	1926.9	11.2	1926.1	6.0	1935.0
29	0.862	0.4086	18.0	19.0				5.4	1920.6	8.5	1916.3	5.0	1929.0
30	0.817	0.4340	19.0	20.0	0.0692	0.0031	0.0632	5.1	1915.3	7.0	1908.5	4.0	1924.0
31	0.985	0.4646	20.0	21.0				6.2	1909.7	8.8	1900.7	5.0	1919.0
32	1.066	0.4977	21.0	22.0	0.0470	0.0022	0.0410	6.7	1903.3	10.0	1891.3	6.0	1913.0
33	1.198	0.5350	22.0	23.0				7.5	1896.2	11.8	1880.4	7.0	1907.0
34	1.814	0.5914	23.0	24.0	0.0271	0.0023	0.0211	11.3	1886.8	19.2	1864.9	10.0	1899.0
35	1.917	0.6510	24.0	25.0				12.0	1875.1	27.8	1841.4	11.0	1888.0
36	1.039	0.6833	25.0	26.0	0.0138	0.0022	0.0078	6.5	1865.9	15.1	1819.9	6.0	1880.0
37	1.199	0.7205	26.0	27.0				7.5	1858.9	24.9	1799.9	7.0	1874.0
38	0.812	0.7458	27.0	28.0	0.0107	0.0014	0.0047	5.1	1852.6	26.6	1774.2	5.0	1868.0
39	1.215	0.7835	28.0	29.0				7.6	1846.3			7.0	1862.0
40	1.129	0.8186	29.0	30.0	0.0071	0.0010	0.0011	7.1	1839.0			7.0	1856.0

Table D.8 –Geochemistry of modern plants, sediments and soils.

#	Lake	Sample date	Descrpition	water depth	C_{org} (wt. %)	N_{total} (wt. %)	$\delta^{13}C_{org}$ (‰ VPDB)	$\delta^{15}N_{total}$ (‰ AIR)	C/N (atomic)
1	L. Mucubají	Jan-99	surf. sediment	14.0	12.24	0.962	-25.32	1.78	14.85
2	L. Verdes Alta	Jan-00	surf. sediment	0.1	25.29	2.701	-17.09	5.72	10.93
3	L. Verdes Alta	Jan-00	surf. sediment	0.2	29.12	1.911	-24.04	5.44	17.78
4	L. Verdes Alta	Jan-00	surf. sediment	2.0	34.48	3.198	-16.73	4.29	12.58
5	L. Verdes Alta	Jan-00	surf. sediment	2.2	36.55	3.675	-15.15	3.26	11.60
6	L. Verdes Alta	Jan-00	surf. sediment	2.3	37.34	3.892	-14.61	2.93	11.19
7	L. Verdes Alta	Jan-00	surf. sediment	2.5	34.96	3.753	-15.15	2.71	10.87
8	L. Verdes Alta	Jan-00	surf. sediment	2.6	37.35	3.869	-14.46	3.20	11.26
9	L. Verdes Alta	Jan-00	surf. sediment	2.0	28.73	2.807	-16.23	2.80	11.94
10	L. Verdes Alta	Jan-00	surf. sediment	1.5	31.15	3.168	-17.85	3.71	11.47
11	L. Verdes Alta	Jan-00	surf. sediment	0.2	6.60	0.512	-22.23	8.02	15.03
12	L. Verdes Baja	Jan-99	surf. sediment	5.5	29.45	2.914	-12.74	5.59	11.79
13	L. Verdes Alta	Jan-00	aq. macrophyte	0.2	42.17	2.959	-22.20	3.44	16.63
14	L. Verdes Alta	Jan-00	aq. macrophyte	0.2	46.10	2.659	-25.39	10.25	20.22
15	L. Verdes Alta	Jan-00	aq. macrophyte	0.2	46.47	2.794	-24.54	9.72	19.40
16	L. Verdes Alta	Jan-00	aq. macrophyte	0.2	27.74	1.625	-25.06	9.55	19.92
17	L. Verdes Alta	Jan-00	aq. macrophyte	0.2	49.97	2.974	-25.77	10.93	19.60
18	L. Verdes Baja	Jan-99	aq. macrophyte	0.2	38.33	1.808	-26.92	5.90	24.73
19	L. Verdes Alta	Jan-00	soil	-	14.83	1.055	-24.98	4.84	16.40
20	L. Verdes Alta	Jan-00	soil	-	14.57	0.999	-24.74	6.18	17.02
21	L. Verdes Alta	Jan-00	soil	-	5.06	0.301	-26.14	5.97	19.64

Table D.9 – Sediment geochemistry of L. Mucubají surface core GL-99A.

#	top depth (cm)[a]	bottom depth (cm)[a]	Median age (cal. y AD)	Dry density (g/cm^3)	C_{org} (wt. %)	N_{total} (wt. %)	$\delta^{13}C_{org}$ (‰ VPDB)	$\delta^{15}N_{total}$ (‰ AIR)	C/N (atomic)
1	0.0	0.5	2001	0.0677	8.32	0.773	-25.24	2.36	12.62
2	0.5	1.0	1998	0.0982	8.35	0.725	-25.02	1.86	13.45
3	1.0	1.5	1997	0.1033	9.81	0.841	-25.39	2.00	13.51
4	1.5	2.0	1995	0.0925	10.22	0.883	-25.74	1.81	13.50
5	2.0	2.5	1992	0.1144	9.80	0.848	-25.34	1.98	13.48
6	2.5	3.0	1990	0.0982	10.34	0.906	-25.49	1.98	13.24
7	3.0	3.5	1987	0.1028	10.95	0.956	-25.83	1.84	13.36
8	3.5	4.0	1984	0.1065	11.17	0.965	-25.58	2.18	13.49
9	4.0	4.5	1981	0.0958	11.39	0.983	-25.67	1.75	13.52
10	4.5	5.0	1978	0.1082	10.98	0.917	-25.53	2.03	13.97
11	5.0	5.5	1975	0.1227	10.91	0.911	-25.30	2.16	13.97
12	5.5	6.0	1972	0.1243	10.66	0.871	-25.45	2.39	14.29
13	6.0	6.5	1968	0.1239	10.26	0.860	-25.43	2.45	13.91
14	6.5	7.0	1964	0.1441	9.36	0.770	-25.17	2.55	14.18
15	7.0	7.5	1960	0.1342	8.66	0.711	-25.18	2.72	14.22
16	7.5	8.0	1957	0.1506	7.82	0.622	-25.29	3.25	14.63
17	8.0	8.5	1954	0.1685	8.10	0.655	-25.14	3.25	14.43
18	8.5	9.0	1949	0.1664	7.81	0.635	-25.22	2.97	14.35
19	9.0	9.5	1944	0.1918	7.99	0.653	-25.51	3.19	14.27
20	9.5	10.0	1939	0.1822	6.88	0.546	-25.29	2.89	14.68
21	10.0	11.0	1930	0.1486	7.99	0.643	-25.34	3.11	14.50
22	11.0	12.0	1918	0.1628	8.25	0.622	-25.24	3.39	15.48
23	11.8	12.8	1909	0.1688	7.80	0.598	-25.24	3.60	15.22
24	13.0	14.0	1902	0.1961	7.60	0.565	-25.26	3.42	15.69
25	14.0	15.0	1895	0.1860	7.57	0.567	-25.12	3.48	15.29
26	15.0	16.0	1888	0.2033	7.73	0.570	-25.18	3.42	15.81
27	16.0	17.0	1880	0.2250	7.27	0.535	-25.08	3.22	15.84
28	17.0	18.0	1872	0.2071	7.27	0.542	-25.20	3.84	15.64
29	18.0	19.0	1864	0.1950	7.17	0.527	-25.21	3.16	15.87
30	19.0	20.0	1855	0.2120	9.03	0.665	-25.25	2.93	15.85
31	20.0	21.0	1847	0.1898	7.66	0.575	-25.03	3.73	15.70
32	21.0	22.0	1837	0.2037	7.95	0.582	-25.17	3.67	15.94
33	22.0	23.0	1828	0.2055	8.94	0.662	-25.26	3.83	15.75
34	23.0	24.0	1818	0.1905	8.46	0.615	-25.12	3.76	16.04
35	24.0	25.0	1808	0.2142	9.12	0.675	-25.09	3.69	15.77
36	25.0	25.5	1798	0.1984	9.19	0.676	-25.15	3.14	15.85

(a) Core and composite depths are identical for this core

Table D.10 – Sediment geochemistry of L. Verdes Alta surface core GL-99A.

#	top depth (cm)[a]	bottom depth (cm)[a]	Median age (cal. y BP)	Dry density (g/cm^3)
1	0.0	0.5	-50	0.0062
2	0.5	1.0	-49	0.0155
3	1.0	1.5	-48	0.0168
4	1.5	2.0	-47	0.0200
5	2.0	2.5	-46	0.0203
6	2.5	3.0	-45	0.0200
7	3.0	3.5	-44	0.0217
8	3.5	4.0	-42	0.0196
9	4.0	4.5	-41	0.0190
10	4.5	5.0	-40	0.0160
11	5.0	5.5	-39	0.0185
12	5.5	6.0	-38	0.0192
13	6.0	6.5	-36	0.0200
14	6.5	7.0	-35	0.0203
15	7.0	7.5	-34	0.0210
16	7.5	8.0	-32	0.0191
17	8.0	8.5	-30	0.0236
18	8.5	9.0	-28	0.0201
19	9.0	9.5	-27	0.0204
20	9.5	10.0	-25	0.0210
21	10.0	11.0	-22	0.0145
22	11.0	12.0	-19	0.0213
23	11.8	12.8	-16	0.0155
24	13.0	14.0	-9	0.0240
25	14.0	15.0	-2	0.0265
26	15.0	16.0	5	0.0219
27	16.0	17.0	13	0.0324
28	17.0	18.0	24	0.0365
29	18.0	19.0	34	0.0268
30	19.0	20.0	41	0.0254
31	20.0	21.0	49	0.0306
32	21.0	22.0	59	0.0331
33	22.0	23.0	70	0.0372
34	23.0	24.0	85	0.0564
35	24.0	25.0	109	0.0596
36	25.0	26.0	130	0.0323
37	26.0	27.0	150	0.0373
38	27.0	28.0	176	0.0252
39	28.0	29.0	266	0.0378
40	29.0	30.0	355	0.0351
41	30.0	31.0	445	0.0347
42	31.0	32.0	535	0.0392
43	32.0	33.0	624	0.0358
44	33.0	34.0	714	0.0398

Table continued on next page

Table D.10 – Continued

#	top depth (cm)[a]	bottom depth (cm)[a]	Median age (cal. y BP)	Dry density (g/cm^3)
45	34.0	35.0	785	0.0411
46	35.0	36.0	857	0.0368
47	36.0	37.0	928	0.0353
48	37.0	38.0	1000	0.0395
49	38.0	39.0	1071	0.0484
50	39.0	40.0	1143	0.0376
51	40.0	41.0	1214	0.0410
52	41.0	42.0	1286	0.0435
53	42.0	43.0	1357	0.0432
54	43.0	44.0	1429	0.0405
55	44.0	45.0	1500	0.0524
56	45.0	46.0	1572	0.0386
57	46.0	47.0	1643	0.0540
58	47.0	48.0	1691	0.0534
59	48.0	49.0	1739	0.0614
60	49.0	50.0	1786	0.0508
61	50.0	51.0	1834	0.0664
62	51.0	52.0	1882	0.0518
63	52.0	53.0	1930	0.0392
64	53.0	54.0	1977	0.0556
65	54.0	55.0	2025	0.0621
66	55.0	56.0	2073	0.0548

(a) Core and composite depths are identical for this core

Table D.11 – Sediment geochemistry of L. Verdes Baja surface core GL-99A.

#	top depth (cm)[a]	bottom depth (cm)[a]	Median age (cal. y BP)	Dry density (g/cm^3)	C_{org} (wt. %)	N_{total} (wt. %)	$\delta^{13}C_{org}$ (‰ VPDB)	$\delta^{15}N_{total}$ (‰ AIR)	C/N (atomic)
1	0.0	0.5	-50	0.0012	35.31	6.172	-18.33	-1.42	6.67
2	0.5	1.0	-51		36.42	6.096	-18.87	3.86	6.97
3	1.0	1.5	-50	0.0022	35.88	5.747	-18.66	0.75	7.28
4	1.5	2.0	-49	0.0041	35.02	5.870	-16.69	0.72	6.96
5	2.0	2.5	-47	0.0086	30.39	5.223	-15.44	1.80	6.79
6	2.5	3.0	-44	0.0100	28.48	4.067	-14.84	2.66	8.17
7	3.0	3.5	-41	0.0147	27.76	3.639	-14.34	3.77	8.90
8	3.5	4.0	-38	0.0159	27.40	3.103	-14.02	5.55	10.30
9	4.0	4.5	-34	0.0179	26.73	3.128	-13.87	4.71	9.97
10	4.5	5.0	-30	0.0158	27.45	3.112	-13.71	4.71	10.29
11	5.0	5.5	-26	0.0187	27.29	3.067	-13.50	5.11	10.38
12	5.5	6.0	-21	0.0204	26.65	2.996	-13.48	5.03	10.38
13	6.0	6.5	-17	0.0221	26.04	2.975	-13.38	5.03	10.21
14	6.5	7.0	-12	0.0265	25.68	2.782	-13.29	6.25	10.77
15	7.0	7.5	-8	0.0209	26.46	2.943	-13.33	5.27	10.49
16	7.5	8.0	-3	0.0268	25.72	2.764	-13.31	6.39	10.86
17	8.0	8.5	2	0.0241	25.57	2.817	-13.66	5.85	10.59
18	8.5	9.0	7	0.0305	25.73	2.946	-14.23	6.28	10.19
19	9.0	9.5	11	0.0210	28.44	3.163	-13.41	6.45	10.49
20	9.5	10.0	16	0.0200	30.09	3.059	-11.90	7.60	11.47
21	10.0	10.5	21	0.0205	31.37	2.910	-11.09	8.68	12.58
22	10.5	11.0	26	0.0139					
23	11.0	11.5	30	0.0013	31.65	2.832	-10.58	9.23	12.78
24	11.5	12.0	35	0.0338					
25	12.0	12.5	40	0.0234	30.38	2.790	-10.24	9.00	12.70
26	12.5	13.0	45	0.0082					
27	13.0	13.5	50	0.0270	30.44	2.736	-10.20	9.94	12.98
28	13.5	14.0	55	0.0129					
29	14.0	14.5	60	0.0252	31.67	2.871	-10.40	9.61	12.87
30	14.5	15.0	65	0.0251					
31	15.0	16.0	72	0.0207	30.77	2.753	-10.13	10.18	13.04
32	16.0	17.0	83	0.0228					
33	17.0	18.0	94	0.0261	31.68	2.740	-10.31	9.89	13.49
34	18.0	19.0	106	0.0360					
35	19.0	20.0	119	0.0299	31.38	2.646	-10.26	9.80	13.84
36	20.0	21.0	132	0.0249	29.70	2.482	-10.44	9.99	13.96
37	21.0	22.0	146	0.0345	27.94	2.221	-10.46	10.43	14.68
38	22.0	23.0	162	0.0413					
39	23.0	24.0	178	0.0316	29.70	2.500	-10.30	9.96	13.86
40	24.0	25.0	195	0.0366					
41	25.0	26.0	214	0.0431	24.47	1.821	-10.96	8.30	15.68
42	26.0	27.0	233	0.0361					
43	27.0	28.0	254	0.0601	22.41	1.677	-11.33	8.18	15.60
44	28.0	29.0	275	0.0614					

Table continued on next page

Table D.11 – Continued

#	top depth (cm)[a]	bottom depth (cm)[a]	Median age (cal. y BP)	Dry density (g/cm^3)	C_{org} (wt. %)	N_{total} (wt. %)	$\delta^{13}C_{org}$ (‰ VPDB)	$\delta^{15}N_{total}$ (‰ AIR)	C/N (atomic)
45	29.0	30.0	297	0.0438	23.47	1.745	-11.70	7.42	15.69
46	30.0	31.0	320	0.0427					
47	31.0	32.0	343	0.0440	22.12	1.630	-11.82	7.47	15.82
48	32.0	33.0	367	0.0582					
49	33.0	34.0	391	0.0527	21.87	1.658	-11.94	7.39	15.56
50	34.0	35.0	416	0.0582					
51	35.0	36.0	440	0.0531	21.61	1.667	-11.97	7.95	15.12
52	36.0	37.0	464	0.0559					
53	37.0	38.0	489	0.0428	22.07	1.845	-11.76	7.13	13.96
54	38.0	39.0	513	0.0538					
55	39.0	40.0	536	0.0497	23.63	2.191	-12.00	6.68	12.59
56	40.0	41.0	560	0.0589					
57	41.0	42.0	583	0.0543	21.73	1.898	-11.77	7.19	13.36
58	42.0	43.0	607	0.0591					
59	43.0	44.0	630	0.0589	22.26	1.878	-11.71	7.03	13.83
60	44.0	45.0	654	0.0500					
61	45.0	46.0	684	0.0522	23.48	1.943	-11.76	6.17	14.10
62	46.0	47.0	727	0.0465					
63	47.0	48.0	771	0.0466	24.73	1.983	-11.72	4.91	14.55
64	48.0	49.0	814	0.0472					
65	49.0	50.0	857	0.0543	25.69	2.044	-11.66	5.10	14.66
66	50.0	51.0	901	0.0532					
67	51.0	52.0	944	0.0539	23.44	1.915	-11.60	5.64	14.28
68	52.0	53.0	987	0.0526					
69	53.0	54.0	1031	0.0574	23.45	1.891	-11.48	6.11	14.47
70	54.0	55.0	1074	0.0524					
71	55.0	56.0	1117	0.0574	22.32	1.846	-11.73	5.98	14.11
72	56.0	57.0	1161	0.0587					
73	57.0	58.0	1204	0.0640	21.67	1.834	-11.71	5.89	13.94
74	58.0	59.0	1247	0.0632					
75	59.0	60.0	1291	0.0650	21.99	1.855	-11.93	5.01	13.83
76	60.0	61.0	1334	0.0632					
77	61.0	62.0	1377	0.0636	23.38	1.879	-11.40	5.59	14.52

(a) Core and composite depths are identical for this core

Table D.12 – Sediment geochemistry of L. Blanca square-rod core 99A.

Drive #	Drive Depth	Composite depth (cm)[a]	Median age (cal. y BP)	Dry density (g/cm^3)	Organic matter (wt. %)[b]
1	5	5.0	-37	0.4134	21.5
1	10	10.0	-25	0.4535	24.9
1	15	15.0	-13	0.5437	22.7
1	20	20.0	-2	0.5055	25.8
1	25	25.0	10	0.5380	26.9
1	30	30.0	22	0.4945	34.8
1	35	35.0	34	0.5041	33.1
1	40	40.0	46	0.4513	24.6
1	45	45.0	58	0.6187	17.1
1	50	50.0	70	0.4275	29.5
1	55	55.0	81	0.5493	20.3
1	60	60.0	93	0.5495	19.1
1	65	65.0	110	0.5184	22.6
1	70	70.0	171	0.6819	16.1
1	75	75.0	231	0.7377	13.3
1	80	80.0	292	0.8080	11.5
1	85	85.0	353	0.7179	14.1
1	90	90.0	414	0.6473	16.4
1	95	95.0	474	0.7080	13.7
2	5	95.0	474	0.7566	14.0
2	10	100.0	535	0.8097	14.3
2	15	105.0	604	0.4515	39.2
2	20	110.0	691	0.3790	43.3
2	25	115.0	778	0.4544	42.4
2	30	120.0	865	0.4160	42.5
2	35	125.0	953	0.3726	49.4
2	40	130.0	1045	0.2029	69.0
2	45	135.0	1136	0.3786	64.8
2	50	140.0	1227	0.3710	68.0
2	55	145.0	1319	0.3566	72.1
2	60	150.0	1410	0.4083	62.8
2	65	155.0	1502	0.4421	55.8
2	70	160.0	1593	0.4172	57.4
2	75	165.0	1684	0.4368	58.6
2	80	170.0	1776	0.4159	52.3
2	85	175.0	1867	0.4358	59.6
3	7	184.4	2038	0.4553	21.1
3	10	187.5	2096	0.0764	95.1
3	15	192.8	2200	0.1004	89.7
3	20	198.1	2306	0.1259	63.8
3	25	203.3	2413	0.0801	98.2
3	30	208.6	2519	0.1037	81.6
3	35	213.8	2625	0.1322	76.1
3	40	219.1	2732	0.1280	42.4

Table continued on next page

Table D.12 – Continued

Drive #	Drive Depth	Composite depth (cm)[a]	Median age (cal. y BP)	Dry density (g/cm^3)	Organic matter (wt. %)[b]
3	45	224.4	2838	0.0633	98.9
3	50	229.6	2944	0.1429	69.3
3	54	233.8	3029	0.3245	26.8
3	60	240.2	3157	0.0664	96.0
3	65	245.4	3263	0.0939	86.4
3	70	250.7	3370	0.1334	90.0
3	75	255.9	3476	0.1203	45.1
3	80	261.2	3582	0.6097	16.4
3	85	266.5	3689	0.1082	84.2
3	90	271.7	3795	0.0612	82.3
4	7	282.6	4082	0.0892	85.5
4	13	294.2	4389	0.0997	84.3
4	17.5	302.9	4620	0.1163	74.5
4	23	313.6	4940	0.2682	31.4
4	30	327.2	5478	0.1129	82.8
4	35	336.9	5862	0.1330	72.4
4	40	346.6	6247	0.0957	78.7
4	46	358.2	6708	0.0900	87.3
5	5	370.0	7175	0.1348	85.7
5	13	379.6	7555	0.1021	93.3
5	17	384.4	7745	0.3375	40.9
5	20	388.0	7888	0.1166	70.8
5	25	394.0	7950	0.1207	88.3
5	30	400.0	8002	0.2117	58.9
5	35	406.0	8054	0.1100	84.0
5	40	412.0	8106	0.1107	75.4
6	5.5	413.4	8119	0.1189	86.4
6	10	417.9	8158	0.1107	88.1
6	15	422.9	8226	0.1767	77.9
6	17	424.8	8260	0.8343	16.0
6	21	428.8	8328	0.4160	36.8
6	25	432.8	8395	0.4929	32.6
7	30	437.7	9156	0.9018	14.7
7	36	443.6	9392	0.8513	15.3
7	40	447.6	9548	1.0553	11.0
7	45	452.6	9745	1.1095	10.4

(a) Depth below sed. water interface, corrected for overlap between drives and stretching/compression during coring

(b) Determined by loss-on-ignition at 550 °C

Table D.13 – Sediment geochemistry of L. Mucubají percussion core 99A.

Core depth (cm)	Composite depth (cm)[a]	Median age (cal. y BP)	Dry density (g/cm^3)	C_{org} (wt. %)	N_{total} (wt. %)	$\delta^{13}C_{org}$ (‰ VPDB)	$\delta^{15}N_{total}$ (‰ AIR)	C/N (atomic)
3	26.5	202	0.2760	9.29	0.653	-25.12	3.70	16.60
5	27.6	215	0.3230	8.33	0.604	-25.00	3.77	16.10
7	28.7	228	0.2495	7.09	0.499	-24.94	3.50	16.62
9	29.8	241	0.2691	10.58	0.744	-25.07	3.23	16.58
11	30.9	255	0.2732	10.25	0.742	-24.96	3.73	16.10
13	31.9	268	0.2817	8.83	0.641	-24.88	3.32	16.06
15	33.0	281	0.2737	9.67	0.681	-25.20	3.23	16.56
17	34.5	298	0.3365	6.99	0.502	-25.09	3.77	16.24
19	36.0	317	0.4551	5.72	0.403	-25.13	4.09	16.58
21	37.5	336	0.5020	4.17	0.292	-25.07	3.57	16.62
23	39.4	358	0.4068	7.65	0.532	-24.88	3.60	16.73
25	41.3	384	0.3528	8.39	0.580	-25.16	3.03	16.87
27	42.8	424	0.4056	7.03	0.503	-25.27	3.46	16.28
30	45.0	484	0.3819	7.80	0.564	-24.76	3.63	16.14
31.5	46.1	514	0.3331	9.34	0.649	-25.02	3.53	16.79
33	47.2	543	0.2211	10.56	0.798	-24.54	3.33	15.45
35	48.6	584	0.1765	13.22	0.983	-25.14	3.13	15.69
37	50.1	642	0.2883	6.41	0.517	-24.53	3.44	14.47
38.5	51.2	684	0.2214	11.18	0.849	-24.30	3.06	15.36
40	52.3	727	0.2158	10.96	0.828	-24.19	3.00	15.46
43	54.7	822	0.2262	10.85	0.831	-24.64	2.91	15.24
46	57.8	946	0.2441	10.88	0.804	-24.60	2.91	15.78
49	61.0	1070	0.2206	11.29	0.819	-24.75	2.81	16.09
52	64.2	1152	0.1372	12.22	0.909	-25.16	3.11	15.68
55	67.3	1231	0.2098	11.21	0.784	-25.84	3.30	16.94
58	70.5	1318	0.1756	11.59	0.952	-24.55	3.02	14.21
61	73.6	1424	0.2391	10.26	0.822	-24.29	2.74	14.56
65	77.8	1566	0.2539					
68	81.0	1672	0.2148					
71	84.2	1779	0.2214					
74	87.3	1885	0.2214					
77	90.5	1992	0.2308					
80	93.6	2105	0.2188					
83	96.8	2257	0.2337					
86	99.9	2408	0.2395					
89	103.0	2554	0.2418					
92	105.7	2684	0.4863					
95	108.4	2903	0.5934					
96.5	109.8	3075	0.2741					
98.25	111.2	3255	0.3081					
100	112.4	3356	0.2545					
103	114.5	3417	0.2839					
106	116.6	3477	0.3376					

Table continued on next page

Table D.13 – Continued

Core depth (cm)	Composite depth (cm)[a]	Median age (cal. y BP)	Dry density (g/cm^3)	C_{org} (wt. %)	N_{total} (wt. %)	$\delta^{13}C_{org}$ (‰ VPDB)	$\delta^{15}N_{total}$ (‰ AIR)	C/N (atomic)
109	118.7	3538	0.3307					
112	120.8	3598	0.3619					
114.5	122.6	3649	0.3143					
117.5	126.1	3752	0.3103					
120	129.5	3849	0.4340					
123	133.5	3966	0.2849					
126	137.2	4206	0.2988					
128	138.1	4274	0.3128					
130	139.0	4341	0.3458					
132	140.1	4420	0.3970					
135	142.3	4565	0.4480					
137	143.7	4617	0.6008					
140	147.0	4738	0.3338					
142	149.4	4826	0.4472					
144	151.8	4915	0.3553					
146	155.7	5057	0.3316					
147.5	158.7	5169	0.3789					
149	159.7	5207	0.2942					
151.5	161.8	5284	0.3838					
153.5	163.5	5347	0.2729					
157	168.5	5516	0.3270					
160	171.5	5614	0.3519					
163	174.0	5729	0.3105					
165	175.7	5808	0.3401					
167	177.3	5883	0.4630					
169	178.9	5958	0.5646					
171	180.5	6033	0.7083					
173	182.4	6121	0.5421					
176	185.6	6270	0.5084					
179	188.9	6413	0.4826					
182	192.1	6556	0.3529					
184	193.9	6635	0.4137					
186	195.5	6705	0.6358					
188	197.0	6775	0.6857					
190.5	199.0	6862	0.6027					
192	200.2	6914	0.4965					
194	201.8	6984	0.4271					
196	203.4	7054	0.5556					
199	205.7	7158	0.4097					
202	208.4	7275	0.3234					
204	212.1	7442	0.3779					
206	215.8	7571	0.4506					
209	221.2	7691	0.5027					

Table continued on next page

Table D.13 – Continued

Core depth (cm)	Composite depth (cm)[a]	Median age (cal. y BP)	Dry density (g/cm^3)	C_{org} (wt. %)	N_{total} (wt. %)	$\delta^{13}C_{org}$ (‰ VPDB)	$\delta^{15}N_{total}$ (‰ AIR)	C/N (atomic)
212	226.3	7805	0.6594					
215	229.0	7865	0.5474					
218	231.6	7923	0.4569					
220	232.8	7948	0.4652					
222	233.9	7973	0.4517					
224	235.0	7998	0.5358					
226	236.1	8023	0.6645					

(a) Depth below sed. water interface corrected for stretching/compression during coring and for overlap between all L. Mucubají cores

Table D.14 – Sediment geochemistry of L. Mucubají square-rod core 99C.

Drive #	Drive depth (cm)	Composite depth (cm)[a]	Median age (cal. y BP)	Dry density (g/cm^3)	C_{org} (wt. %)	N_{total} (wt. %)	$\delta^{13}C_{org}$ (‰ VPDB)	$\delta^{15}N_{total}$ (‰ AIR)	C/N (atomic)	biog. SiO_2 (wt. %)[b]
1	2	19.0	109	0.2921	11.80	0.810	-26.33	3.80	17.00	8.8
1	6	23.0	159	0.2694	12.80	0.890	-24.83	3.34	16.78	4.4
1	10	27.1	208	0.3095	11.70	0.810	-25.33	3.55	16.85	9.4
1	15	32.1	270	0.2627	12.50	0.870	-25.62	3.04	16.76	5.8
1	18	35.5	312	0.3204	12.1[c]					
1	20	37.9	340	0.4221	7.00	0.470	-25.90	3.54	17.38	3.0
1	23	41.1	380	0.2885	10.40	0.700	-25.82	3.77	17.33	6.9
1	27	45.6	501	0.3282	10.00	0.670	-25.82	3.43	17.41	7.4
1	32	50.5	658	0.2719	10.50	0.720	-26.69	2.68	17.01	5.1
1	35	53.5	775	0.0809	16.50	1.300		2.69	14.81	18.5
1	40	57.7	941	0.1851	18.70	1.090	-26.24	2.76	20.02	16.8
1	45	61.5	1086	0.1770	18.00	1.180	-26.36	2.82	17.80	15.8
1	50	65.2	1178	0.1330	19.10	1.290	-26.82	2.50	17.27	15.8
1	55	71.1	1339	0.1345	17.80	1.210	-26.70	2.34	17.16	8.8
1	60	81.0	1671	0.1814	21.00	1.180		2.53	20.76	8.0
1	63.5	85.2	1815	0.2320	21.0[c]					
1	67	89.2	1950	0.2630	12.30	0.820	-25.90	2.66	17.50	24.3
1	72	93.8	2113	0.1718	15.60	0.980	-26.65	2.64	18.57	13.7
1	76	97.2	2279	0.1941	21.80	1.320		2.82	19.27	17.3
1	80	101.2	2468	0.2410	16.20	0.980	-27.33	2.40	19.29	12.4
1	85	104.7	2634	0.2064	16.50	1.000	-26.18	2.70	19.25	9.6
1	90	107.9	2831	0.1994	20.10	1.090		3.06	21.51	11.1
1	94	112.3	3351	0.2742	13.90	0.950	-26.10	2.60	17.07	16.9
2	3	97.9	2310	0.2095	18.30	1.110	-27.51	2.83	19.23	9.7
2	6	100.9	2455	0.2279	20.9[c]					
2	8	102.3	2521	0.1784	18.10	1.060	-25.83	2.71	19.92	14.4
2	11	104.5	2626	0.2362	13.50	0.930	-25.90	2.88	16.94	22.3
2	17	108.3	2892	0.4223	6.70	0.420	-25.41	3.20	18.61	3.0
2	20	111.9	3342	0.3037	10.50	0.640	-26.89	2.54	19.14	5.5
2	22.5	114.5	3417	0.3048						
2	25	116.6	3477	0.2296	11.90	0.730	-26.46	3.03	19.02	9.8
2	30	120.8	3597	0.2657	13.80	0.910	-24.88	2.87	17.69	12.3
2	35	126.4	3759	0.2773	12.90	0.880	-25.41	2.60	17.10	10.2
2	39	131.8	3916	0.3481	12.60	0.780	-25.83	3.28	18.85	4.0
2	41.5	134.3	3986	0.2279	12.40	0.830	-26.30	2.65	17.43	3.5
2	45	137.8	4249	0.2595						5.6
2	47.5	140.5	4455	0.3141	13.9[c]					
2	50	143.3	4600	0.4079	15.00	0.960	-25.37	2.86	18.23	3.4
2	55	148.0	4773	0.2400	8.10	0.490	-25.65	3.15	19.29	5.5
2	60	153.3	4969	0.2364	15.30	1.020	-25.76	2.76	17.50	19.3
2	65	159.4	5194	0.2927	14.50	0.870	-26.75	3.16	19.44	5.0
2	70	164.5	5384	0.2456	12.70	0.770	-26.49	2.94	19.24	14.3
2	75	170.0	5564	0.2832	14.32	0.960	-24.96	3.06	17.40	16.3

Table continued on next page

Table D.14 – Continued

Drive #	Drive depth (cm)	Composite depth (cm)[a]	Median age (cal. y BP)	Dry density (g/cm^3)	C_{org} (wt. %)	N_{total} (wt. %)	$\delta^{13}C_{org}$ (‰ VPDB)	$\delta^{15}N_{total}$ (‰ AIR)	C/N (atomic)	biog. SiO_2 (wt. %)[b]
2	76.5	171.5	5615	0.2686	14.8[c]					
2	80	174.7	5759	0.2733	15.65	1.040	-25.87	2.84	17.56	6.5
2	85	180.4	6029	0.5311	6.98	0.460	-25.10	3.07	17.70	2.2
2	90	187.1	6336	0.5234	7.67	0.470	-25.33	3.12	19.04	5.5
2	94	192.2	6559	0.4596	9.56	0.560	-26.27	2.77	19.92	7.9
3	2.5	182.6	6131	0.4521	8.42	0.550	-24.83	2.81	17.86	6.0
3	6.5	188.8	6409	0.3955	5.94	0.370	-25.80	2.88	18.73	7.6
3	9.5	192.2	6559	0.3478	13.66	0.930		2.96	17.14	7.9
3	12.5	195.0	6686	0.5943	5.77	0.350	-25.58	3.00	19.23	2.9
3	15.5	198.2	6825	0.3822	10.32	0.680	-25.36	2.74	17.71	4.5
3	19.5	202.8	7027	0.4214	10.41	0.680	-25.38	2.73	17.86	4.8
3	21.5	205.0	7128	0.3487	13.24	0.890	-25.57	2.73	17.36	11.8
3	24.5	209.3	7316	0.3850	11.96	0.790	-25.54	2.85	17.66	5.1
3	27	215.7	7568	0.3014	14.12	0.910	-25.34	2.77	18.10	13.4
3	29.5	219.7	7657	0.4185	11.22	0.730	-25.68	2.77	17.93	9.6
3	32.5	224.5	7764	0.5304	5.85	0.360	-25.72	2.98	18.96	5.9
3	35.5	229.0	7864	0.4768	9.1[c]					
3	38.5	233.4	7961	0.4795	9.64	0.610	-25.36	2.86	18.44	8.3

(a) Depth below sed. water interface corrected for stretching/compression during coring and for overlap between all L. Mucubaji cores

(b) determined by time-dissolution experiments and measured by ICP-AES

(c) Calculated as 0.728 x loss-on-ignition at 550° C

Table D.15 – Sediment geochemistry of L. Mucubají square-rod core 02F.

Drive #	Drive Depth	Composite depth (cm)[a]	Median age (cal. y BP)[b]	Dry density (g/cm^3)	Organic matter (wt. %)[c]
3	2	186.4	6304	0.4233	15.3
3	5	189.4	6437	0.4206	16.3
3	8	192.4	6569	0.2793	23.5
3	10	194.4	6658	0.3847	14.9
3	12	196.4	6746	0.6376	9.7
3	16	200.4	6923	0.3623	18.6
3	19	203.4	7055	0.4231	15.6
3	22	206.4	7188	0.3527	18.6
3	25	209.4	7320	0.2935	23.1
3	27	211.4	7409	0.3275	20.4
3	29	213.4	7497	0.3622	17.2
3	31	215.4	7562	0.3238	21.4
3	35	219.4	7651	0.3813	17.8
3	39	223.4	7740	0.4410	14.8
3	42	226.4	7807	0.5808	10.5
3	45	229.4	7873	0.4393	14.6
3	49	233.4	7962	0.3914	19.0
3	51	235.4	8007	0.4396	16.2
3	53	237.4	8052	0.4948	14.1
3	54	238.4	8074	0.5605	11.3
3	56	240.4	8118	0.3623	8.1
3	58	242.4	8163	0.3870	18.2
3	61	245.4		0.3945	17.0
3	64	248.4		0.3423	20.8
3	67	251.4		0.3487	20.5
3	70	254.4		0.3241	22.6
3	73	257.4		0.3427	20.7
3	76	260.4		0.3689	21.1
3	79	263.4		0.3716	20.6
3	82	266.4		0.4114	19.7
3	85	269.4		0.4874	18.6
3	88	272.4		0.3693	15.2
3	91	275.4		0.4084	19.0
3	94	278.4		0.3503	21.9
3	97	281.4		0.3962	18.0
3	99	283.4		0.4050	16.8
4	2	286.8		0.4048	20.5
4	5	289.8		0.4318	16.6
4	8	292.8		0.5218	14.5
4	11	295.8		0.4220	17.0
4	14	298.8		0.3073	17.3
4	16	300.8		0.4453	14.3
4	18	302.8		0.4488	15.9

Table continued on next page

Table D.15 – Continued

Drive #	Drive Depth	Composite depth (cm)[a]	Median age (cal. y BP)[b]	Dry density (g/cm^3)	Organic matter (wt. %)[c]
4	20	304.8		0.4911	14.4
4	21.5	306.3		0.5655	11.0
4	24	308.8		0.4753	14.6
4	27	311.8		0.5502	11.8
4	30	314.8		0.5603	11.9
4	32.5	317.3		0.6059	10.3
4	35	319.8		0.5444	13.1
4	38	322.8		0.4292	18.3
4	41	325.8		0.4972	14.0
4	44	328.8		0.6815	9.0
4	47	331.8		0.7725	7.4
4	50	334.8		0.6039	10.8
4	53	337.8		0.5096	14.0
4	56	340.8		0.4173	19.5
4	59	343.8		0.5692	13.0
4	62	346.8		0.6982	9.6
4	65	349.8		0.6911	9.5
4	68	352.8		0.5548	11.9
4	71	355.8		0.7095	9.9
4	74	358.8		0.5792	12.4
4	77	361.8		0.7024	9.2
4	80	364.8		0.5949	10.5
4	83	367.8		0.5405	11.2
4	86	370.8		0.6296	12.5
4	89	373.8		0.5708	11.4
4	92	376.8		0.7449	9.3
4	95	379.8		0.5636	13.4
4	98	382.8		0.6309	10.8
5	7	392.6		0.6932	9.1
5	10	395.6		0.6281	9.2
5	12.5	398.1		0.4574	11.5
5	14	399.6		0.6338	8.8
5	16	401.6		0.9742	4.7
5	18	403.6		0.9764	5.0
5	21	406.6		0.9591	5.2
5	24	409.6		1.1192	4.6
5	27	412.6		1.0363	4.2
5	30	415.6		1.1832	3.07
5	33	418.6		0.9173	4.14
5	36	421.6		0.8022	6.60
5	39	424.6		0.9700	4.64
5	41	426.6		0.9876	4.32
5	43	428.6		0.6900	9.91

Table continued on next page

Table D.15 – Continued

Drive #	Drive Depth	Composite depth (cm)[a]	Median age (cal. y BP)[b]	Dry density (g/cm^3)	Organic matter (wt. %)[c]
5	46	431.6		0.6104	10.23
5	48	433.6		0.9632	4.18
5	51	436.6		1.1039	3.38
5	54	439.6		0.9317	4.66
5	57	442.6		1.1215	3.13
5	60	445.6		0.9837	4.46
5	63	448.6		0.8902	5.28
5	66	451.6		0.9116	4.81
5	69	454.6		0.9025	4.81
5	72	457.6		0.7625	6.38
5	75	460.6		0.7812	6.10
5	78	463.6		1.0961	3.43
5	81	466.6		1.1967	2.70
5	84	469.6		1.2661	2.50
5	87	472.6		1.1326	2.20
5	90	475.6		1.0008	3.70
5	92	477.6		1.1171	2.99
5	94	479.6		0.8485	5.27
5	96	481.6		0.7584	6.16
5	98	483.6		0.9754	4.07
6	1.5	488.0		1.1226	3.20
6	3	489.5		1.1698	3.01
6	6	492.5		1.0451	3.33
6	7.5	494.0		0.8283	5.01
6	10	496.5		0.7537	5.91
6	12	498.5		0.7032	6.62
6	14	500.5		0.6844	4.82
6	16	502.5		0.7524	2.93
6	19	505.5		1.2651	2.07
6	22	508.5		1.3100	1.66
6	26	512.5		1.3204	1.91
6	30	516.5		1.2248	2.03
6	35	521.5		1.1113	0.55
6	40	526.5		1.0231	3.26
6	45	531.5		1.1685	2.77
6	50	536.5		1.1394	2.72
6	55	541.5		0.9871	4.20
6	60	546.5		0.9089	4.71
6	65	551.5		0.8917	5.25
6	70	556.5		0.9373	5.04
6	75	561.5		0.9483	5.81
6	80	566.5		1.3286	2.05
6	85	571.5		1.0757	3.33

Table continued on next page

Table D.15 – Continued

Drive #	Drive Depth	Composite depth (cm)[a]	Median age (cal. y BP)[b]	Dry density (g/cm^3)	Organic matter (wt. %)[c]
6	89	575.5		1.2865	2.47

(a) Depth below sed. water interface corrected for stretching/compression during coring and for overlap between all L. Mucubají cores

(c) Missing ages are deeper than the oldest radiocarbon age in age model

(b) Determined by loss-on-ignition at 550 °C

Table D.16 – Sediment geochemistry of L. Verdes Alta core 99A.

Drive #	Drive depth (cm)	Composite depth (cm)[a]	Median age (cal. y BP)	Dry density (g/cm^3)	C_{org} (wt. %)	N_{total} (wt. %)	$\delta^{13}C_{org}$ (‰ VPDB)	$\delta^{15}N_{total}$ (‰ AIR)	C/N (atomic)
1	5	10.0	-24	0.0504	30.79	2.750	-16.52	3.83	13.06
1	10	15.0	2	0.0435	30.22	2.460	-16.20	2.87	14.33
1	14	19.0	38	0.0481	31.55	2.290	-16.20	2.82	16.07
1	20	25.0	120	0.0488	29.30	2.300	-16.52	3.28	14.86
1	25	30.0	400	0.0520	33.20	2.200	-16.59	2.63	17.61
1	30	35.0	821	0.0530	26.00	1.800	-16.32	3.20	16.85
1	35	40.0	1179	0.0592	39.35	2.220	-14.54	3.15	20.69
1	40	45.0	1536	0.0411	38.88	2.100	-14.76	2.48	21.63
1	45	50.0	1810	0.0630	30.60	2.100	-17.63	2.85	17.00
1	49	54.0	2001	0.0696	29.30	2.300	-16.79	3.35	14.86
1	55	60.0	2288	0.0664	27.00	1.900	-16.83	2.89	16.58
1	60	65.0	2527	0.0642	30.50	2.200	-16.40	3.57	16.17
1	65	70.0	2766	0.0689	27.30	2.100	-16.56	3.26	15.17
1	70	75.0	3005	0.0701	28.10	2.100	-16.09	4.46	15.61
1	75	80.0	3243	0.0732	30.30	2.000	-16.63	3.42	17.68
1	80	85.0	3482	0.0758	29.00	2.100	-16.77	3.78	16.11
1	85	90.0	3721	0.0711	32.30	2.200	-17.04	4.36	17.13
1	90	95.0	3960	0.0752	33.20	2.300	-17.05	4.34	16.84
1	95	100.0	4199	0.0775	30.40	2.100	-17.62	4.06	16.89
2	2	97.0	4056	0.0855	30.80	2.200	-17.24	3.85	16.33
2	5	100.0	4199	0.0987	27.30	2.000	-17.57	4.05	15.93
2	10	105.0	4438	0.0960	29.40	2.000	-17.58	4.17	17.15
2	15	110.0	4677	0.0972	29.90	2.100	-17.53	5.15	16.61
2	19	114.0	4849	0.0927	28.00	1.900	-17.96	5.59	17.19
2	21	116.0	4934	0.0849	29.80	2.000	-17.16	3.56	17.38
2	25	120.0	5104	0.1020	35.30	2.200	-16.92	3.24	18.72
2	31	126.0	5358	0.1194	25.80	1.700	-17.84	3.05	17.71
2	35	130.0	5528	0.0971	32.00	2.100	-16.68	3.60	17.78
2	40	135.0	5740	0.1016	29.10	2.100	-17.05	4.48	16.17
2	45	140.0	5952	0.0990	26.70	2.000	-18.41	3.89	15.58
2	50	145.0	6164	0.0917	29.90	2.100	-18.40	3.71	16.61
2	53	148.0	6292	0.0975	20.90	1.600	-17.91	5.71	15.24
2	56	151.0	6419	0.0979	29.40	2.200	-17.79	6.48	15.59
2	60	155.0	6589	0.0955	25.90	2.100	-17.43	6.59	14.39
2	65	160.0	6801	0.1111	20.80	1.600	-17.74	5.93	15.17
2	70	165.0	7013	0.0970	24.80	1.900	-17.57	5.66	15.23
2	74	169.0	7183	0.1056	25.40	1.900	-17.95	5.63	15.60
2	76	171.0	7268	0.0988	25.90	1.900	-16.53	3.97	15.90
2	80	175.0	7437	0.0992	27.40	2.100	-16.71	4.63	15.22
2	85	180.0	7649	0.0955	31.72	2.390	-17.33	5.53	15.48
2	90	185.0	7862	0.0897	32.33	2.440	-17.64	6.46	15.46
2	95	190.0	8074	0.0853	32.13	2.330	-16.93	6.68	16.09
3	3	188.0	7989	0.0862	32.18	2.470	-17.47	6.68	15.20

Table continued on next page

Table D.16 – Continued

Drive #	Drive depth (cm)	Composite depth (cm)[a]	Median age (cal. y BP)	Dry density (g/cm^3)	C_{org} (wt. %)	N_{total} (wt. %)	$\delta^{13}C_{org}$ (‰ VPDB)	$\delta^{15}N_{total}$ (‰ AIR)	C/N (atomic)
3	7	192.0	8159	0.0935	29.55	2.240	-17.44	6.68	15.39
3	11	196.0	8328	0.0875	33.10	2.580	-16.94	6.48	14.97
3	15	200.0	8498	0.0918	32.43	2.510	-16.80	6.10	15.07
3	20	205.0	8710	0.1168	25.96	1.890	-16.98	4.63	16.03
3	22	207.0	8795	0.1292	20.68	1.620	-17.10	3.59	14.89
3	27	212.0	9007	0.1062	24.57	1.950	-16.99	4.91	14.70
3	30	215.0	9135	0.0971	30.26	2.470	-16.39	5.17	14.29
3	34.5	219.5	9326	0.1083	25.45	2.130	-16.22	6.50	13.94
3	37	222.0	9432	0.0941	28.44	3.790	-16.59	4.72	8.76
3	41	226.0	9601	0.1032	26.22	3.280	-15.42	6.24	9.34
3	45	230.0	9771	0.1059	32.99	4.240	-15.96	5.86	9.08
3	50	235.0	9983	0.1072	26.42	2.320	-14.78	6.37	13.29
3	55	240.0	10195	0.1220	17.82	1.540	-15.14	5.14	13.50
3	60	245.0	10408	0.1750	13.01	1.090	-14.31	5.27	13.93
3	65	250.0	10620	0.1366	20.37	1.710	-13.80	4.00	13.90
3	71	256.0	10874	0.1176	17.11	1.540	-14.20	4.24	12.96
3	73	258.0	10982	0.1635	12.41	1.000	-12.48	3.17	14.55
3	77	262.0	11204	0.1927	10.59	0.850	-12.55	1.88	14.61
3	82	267.0	11483	0.1824	14.03	1.150	-12.14	2.51	14.30
3	88	273.0	11817	0.1762	16.51	1.560	-11.78	2.30	12.31
3	93	278.0	12095	0.1615	18.85	1.740	-11.32	2.13	12.64
3	97	282.0	12318	0.1460	18.56	1.980	-10.50	1.07	10.96
4	11	286.0	12540	0.1798	9.67	0.930	-13.12	1.40	12.13
4	15	290.0	12763	0.2099	11.03	1.140	-12.81	-0.01	11.29
4	20	295.0	13041	0.2001	9.64	0.840	-13.72	-0.32	13.39
4	26	301.0	13375	0.2721	6.53	0.520	-12.85	0.19	14.65
4	31	306.0	13654	0.1822	12.71	1.210	-11.63	-2.16	12.26
4	36	311.0	13932	0.2125	17.65	1.330	-10.06	-1.48	15.46
4	38.5	313.5	14071	0.9654	0.34	0.030	-20.24	2.65	11.93
4	41	316.0	14210	0.5300	1.95	0.140	-19.18	-0.22	16.62
4	45	320.0	14433	0.2532	7.81	0.570	-13.46	-1.40	15.99
4	50	325.0	14711	0.3262	7.22	0.570	-12.13	-1.72	14.78
4	54	329.0	14934	0.3869	7.29	0.440	-14.73	-1.56	19.33
4	60	335.0	15268	1.2077	1.18	0.100	-23.17	1.40	13.26
4	65	340.0	15546	1.1206	0.72	0.03	-30.74	1.01	30.307

(a) Depth below sed. water interface, corrected for overlap between drives and stretching/compression during coring

Table D.17 – Sediment geochemistry of L. Verdes Baja core 99A.

Drive #	Drive depth (cm)	Composite depth (cm)[a]	Median age (cal. y BP)	Dry density (g/cm^3)	Organic matter (wt. %)[b]	C_{org} (wt. %)	N_{total} (wt. %)	$\delta^{13}C_{org}$ (‰ VPDB)	$\delta^{15}N_{total}$ (‰ AIR)	C/N (atomic)
1	7	17.2	91	0.0418	56.4					
1	8	18.2	102			30.06	2.573	-10.94	9.88	13.63
1	10	20.2	128			29.78	2.312	-10.65	9.80	15.04
1	12	22.2	157			27.85	2.104	-11.14	9.33	15.44
1	14	24.2	190			26.82	1.972	-11.25	8.40	15.82
1	15	25.2	208	0.0523	59.5					
1	16	26.2	227			24.90	1.837	-11.97	7.88	15.81
1	18	28.2	269			23.73	1.727	-11.90	7.60	16.02
1	20	30.2	313	0.0637	47.2	23.03	1.675	-12.16	8.02	16.04
1	22	32.2	360			21.26	1.595	-12.15	7.19	15.58
1	25	35.2	433	0.0644	35.3	21.06	1.637	-12.05	7.53	15.01
1	27	37.2	481			21.50	1.689	-12.07	7.21	14.86
1	29	39.2	529			22.74	1.750	-11.97	7.84	15.16
1	30	40.2	553	0.0606	25.0					
1	31	41.2	576			22.58	1.725	-11.95	7.36	15.27
1	34	44.2	647			22.44	1.759	-12.02	6.46	14.99
1	35	45.2	672	0.0654	49.7					
1	37	47.2	758			24.89	1.950	-12.03	4.80	14.89
1	40	50.2	888	0.0637	51.4	24.59	1.956	-11.88	5.09	14.67
1	45	55.2	1104	0.0671	48.2	22.94	1.843	-11.88	6.09	14.53
1	50	60.2	1321	0.0705	48.2	22.46	1.796	-12.13	5.20	14.59
1	55	65.2	1538	0.0710	52.1	24.25	1.904	-11.61	5.42	14.86
1	60	70.2	1754	0.0811	46.3	22.82	1.767	-11.84	4.98	15.07
1	65	75.2	1971	0.0835	48.1	22.85	1.736	-11.86	4.38	15.35
1	70	80.2	2188	0.0819	50.3	24.63	1.886	-11.60	5.25	15.24
1	75	85.2	2404	0.0900	44.7	22.46	1.722	-11.78	5.84	15.22
1	80	90.2	2621	0.0918	43.3	20.40	1.522	-11.96	5.96	15.64
1	85	95.2	2838	0.1047	41.2	19.77	1.405	-11.77	6.56	16.42
1	90	100.2	3054	0.0932	43.7	21.37	1.719	-12.03	6.41	14.50
2	5	110.2	3488	0.1274	40.1	19.82	1.506	-11.47	6.27	15.35
2	10	115.2	3704	0.1019	48.9	20.62	1.652	-11.43	4.53	14.56
2	15	120.2	3921	0.1052	48.9	24.17	1.843	-11.46	3.80	15.31
2	20	125.2	4138	0.1139	44.0	22.06	1.757	-10.93	5.48	14.65
2	25	130.2	4354	0.0985	44.7	22.73	1.813	-10.95	5.14	14.62
2	30	135.2	4571	0.1112	47.9	22.71	1.810	-10.88	5.05	14.63
2	35	140.2	4788	0.1040	47.8	22.84	1.760	-11.37	4.62	15.14
2	39	144.2	4961	0.1158	47.5	23.91	1.787	-10.98	6.37	15.61
2	44	149.2	5178	0.1366	39.7	18.44	1.267	-11.40	6.34	16.98
2	50	155.2	5438	0.1197	48.9	22.47	1.687	-11.27	4.75	15.54
2	55	160.2	5654	0.1135	50.7	22.58	1.645	-11.61	6.40	16.02
2	60	165.2	5871	0.1247	45.8	21.57	1.566	-11.74	6.21	16.08
2	65	170.2	6088	0.1359	45.0	20.82	1.569	-12.05	5.77	15.48
2	70	175.2	6304	0.1220	47.2	22.24	1.659	-11.99	6.78	15.64

Table continued on next page

Table D.17 – Continued

Drive #	Drive depth (cm)	Composite depth (cm)[a]	Median age (cal. y BP)	Dry density (g/cm^3)	Organic matter (wt. %)[b]	C_{org} (wt. %)	N_{total} (wt. %)	$\delta^{13}C_{org}$ (‰ VPDB)	$\delta^{15}N_{total}$ (‰ AIR)	C/N (atomic)
2	75	180.2	6521	0.1418	38.9	18.49	1.287	-12.74	5.01	16.77
2	80	185.2	6738	0.1268	44.3	20.54	1.509	-12.83	4.37	15.87
2	85	190.2	6954	0.1236	46.8	21.37	1.630	-12.32	6.07	15.29
2	90	195.2	7171	0.1144	49.6	23.01	1.698	-11.98	6.42	15.81
3	5	200.2	7388	0.1989	38.8	18.86	1.311	-12.55	4.17	16.78
3	10	205.2	7604	0.1606	44.9	22.21	1.650	-12.24	4.31	15.70
3	15	210.2	7821	0.1483	42.9	20.92	1.618	-12.14	3.97	15.08
3	20	215.2	8038	0.1268	50.9	23.96	1.815	-11.89	3.83	15.40
3	25	220.2	8254	0.1336	45.3	22.75	1.717	-11.97	3.64	15.46
3	30	225.2	8471	0.1421	42.5	21.45	1.607	-12.17	2.73	15.57
3	35	230.2	8688	0.1254	47.4	23.95	1.844	-11.55	4.42	15.15
3	40	235.2	8904	0.1459	40.0	20.12	1.571	-12.02	2.95	14.95
3	45	240.2	9121	0.1246	37.4	19.90	1.560	-12.24	3.29	14.88
3	50	245.2	9338	0.1255	42.0	20.00	1.617	-12.09	2.42	14.43
3	55	250.2	9554	0.1458	43.6	21.22	1.714	-12.45	2.24	14.44
3	60	255.2	9771	0.1514	39.9	21.34	1.751	-11.75	2.23	14.22
3	65	260.2	9983	0.1698	38.9	20.18	1.649	-11.75	2.42	14.28
3	70	265.2	10195	0.1659	34.0	16.75	1.285	-11.16	3.40	15.46
3	75	270.2	10408	0.2647	21.5	11.39	0.880	-11.26	3.03	15.10
3	80	275.2	10980	0.2908	21.8	11.91	0.998	-10.95	2.48	13.69
3	85	280.2	11552	0.2422	25.7	13.21	1.140	-12.03	1.19	13.52
3	90	285.2	12125	0.2276	26.8	12.85	1.127	-12.42	1.13	13.29
4	4	289.2	12583			14.17	1.261	-12.88	0.91	13.10
4	5	290.2	12697	0.2260	26.3					
4	6	291.2	12812			15.60	1.389	-13.41	1.31	13.09
4	10	295.2	13270	0.1894	24.7	12.83	1.129	-12.14	0.72	13.26
4	12	297.2	13499			12.81	1.464	-13.82	-0.51	10.21
4	14	299.2	13728	0.1806	26.8	13.30	1.330	-13.73	-0.14	11.80
4	17	302.2	14071	0.5511	9.5					
4	18	303.2	14252			15.21	1.416	-12.64	-0.39	12.54
4	19	304.2	14433	0.2595	17.5					
4	20	305.2	14484			8.36	0.776	-12.03	-1.23	12.61
4	23	308.2	14639			9.26	0.563	-10.74	-0.39	19.34
4	25	310.2	14742	0.3046	17.1	8.98	0.541	-10.92	-0.68	19.37
4	28	313.2	14897			9.77	0.549	-10.92	-0.90	19.38
4	30	315.2	15000			9.83	0.565	-11.27	-0.78	20.30
4	32	317.2	15103	0.3946	13.9					
4	33	318.2	15133			5.52	0.558	-17.71	-0.18	11.56
4	35	320.2	15149	0.6315	5.9					
4	38	323.2	15172	0.5868	8.9					
4	45	330.2	15228	1.6165	2.2					
4	50	335.2	15268	1.8368	1.8					
4	55	340.2	15308	1.6602	2.0					

Table continued on next page

Table D.17 – Continued

Drive #	Drive depth (cm)	Composite depth (cm)[a]	Median age (cal. y BP)	Dry density (g/cm^3)	Organic matter (wt. %)[b]	C_{org} (wt. %)	N_{total} (wt. %)	$\delta^{13}C_{org}$ (‰ VPDB)	$\delta^{15}N_{total}$ (‰ AIR)	C/N (atomic)
4	60	345.2	15347	1.7051	1.8					
4	65	350.2	15387	1.5534	2.0					
4	70	355.2	15427	1.6548	2.0					
4	75	360.2	15467	1.5436	1.6					
4	80	365.2	15506	1.4486	2.3					
4	85	370.2	15546	1.4782	2.0					

(a) Depth below sed. water interface, corrected for overlap between drives and stretching/compression during coring

(b) Determined by loss-on-ignition at 550 °C

Table D.18 – Diatom $\delta^{18}O$ of L. Verdes Alta core 99A.

Drive #	top drive depth (cm)	bottom drive depth (cm)	Composite depth (cm)[a]	Median age (cal. y BP)	$\delta^{18}O_{diatom}$ (‰ VSMOW)	±1 σ
1	28.0	31.0	34.5	785	28.98	0.09
1	38.0	41.0	44.5	1500	29.18	0.13
1	49.0	52.0	55.5	2073	29.31	0.19
1	59.5	62.5	66	2575	28.15	0.21
1	68.0	71.0	74.5	2981	28.17	0.02
1	77.7	81.0	84.35	3451	28.27	0.10
1	89.0	92.0	95.5	3984	28.68	0.29
2	8.5	11.5	105	4438	28.55	0.23
2	17.0	20.0	113.5	4828	28.30	0.17
2	26.0	29.2	122.6	5214	28.41	0.15
2	36.0	39.0	132.5	5634	28.69	0.10
2	45.0	48.0	141.5	6016	28.61	0.32
2	55.5	58.5	152	6461	28.91	0.18
2	68.0	71.0	164.5	6992	29.44	0.18
2	78.0	81.0	174.5	7416	29.36	0.35
2	88.5	91.5	185	7862	29.28	0.28
3	8.5	11.5	195	8286	29.37	0.08
3	18.0	21.0	204.5	8689	29.58	0.07
3	28.5	31.5	215	9135	29.95	0.15
3	39.5	42.5	226	9601	30.22	0.18
3	52.0	55.0	238.5	10132	30.20	0.02
3	60.5	63.5	247	10492	30.21	0.19

(a) Depth below sed. water interface, corrected for overlap between drives and stretching/compression during coring

Table D.19 – Diatom $\delta^{18}O$ of L. Verdes Baja core 99A.

Drive #	top drive depth (cm)	bottom drive depth (cm)	Composite depth (cm)[a]	Median age (cal. y BP)	$\delta^{18}O_{diatom}$ (‰ VSMOW)	±1 σ	$\Delta\delta^{18}O_{diatom}$ LVB-LVA (‰)[b]
1	7.5	10.5	19.2	115	32.39	0.24	
1	10.5	13.5	22.2	157	31.67	0.04	
1	13.5	16.5	25.2	208	31.92	0.10	
1	16.5	19.5	28.2	269	31.47	0.33	
1	19.5	22.5	31.2	336	31.68	0.46	
1	22.5	25.5	34.2	408	32.48	0.09	
1	28.5	32.0	40.45	559	32.29	0.31	
1	38.0	39.5	47.95	790	33.04	0.13	
1	39.5	41.5	50.7	909	32.97	0.12	
1	43.5	46.5	55.2	1104	31.79	0.03	
1	48.5	51.5	60.2	1321	31.84	0.10	
1	53.5	56.5	65.2	1538	32.22	0.11	
1	58.5	61.5	70.2	1754	32.25	0.05	
1	63.5	66.5	75.2	1971	32.33	0.09	
1	68.5	71.5	80.2	2188	33.28	0.15	5.14
1	73.5	76.5	85.2	2404	32.19	0.06	4.05
1	78.5	81.5	90.2	2621	32.91	0.11	4.76
1	88.5	91.5	100.2	3054	32.28	0.05	4.09
2	3.5	6.5	110.2	3488	33.24	0.07	4.94
2	7.5	10.5	114.2	3661	32.83	0.29	4.39
2	13.5	16.5	120.2	3921	33.32	0.21	4.69
2	18.5	21.5	125.2	4138	32.88	0.11	4.24
2	23.5	26.5	130.2	4354	32.94	0.08	4.36
2	28.5	31.5	135.2	4571	33.44	0.32	4.98
2	33.5	36.5	140.2	4788	32.95	0.06	4.62
2	68.5	71.5	143.7	4939	32.48	0.16	4.15
2	38.5	41.5	145.2	5004	33.33	0.06	4.98
2	78.5	81.5	148.7	5156	33.85	0.03	5.46
2	43.5	46.5	150.2	5221	32.96	0.11	4.55
2	48.5	51.5	155.2	5438	33.04	0.07	4.48
2	53.5	56.5	160.2	5654	32.81	0.03	4.12
2	58.5	61.5	165.2	5871	33.24	0.02	4.60
2	63.5	66.5	170.2	6088	33.28	0.12	4.62
2	73.5	76.5	180.2	6521	33.24	0.11	4.27
2	83.5	86.5	190.2	6954	33.51	0.15	4.11
2	88.5	91.5	195.2	7171	33.39	0.21	3.98
3	3.5	6.5	200.2	7388	33.72	0.15	4.36
3	8.5	11.5	205.2	7604	33.08	0.21	3.76
3	8.5	11.5	205.2	7604	33.41	0.11	4.09
3	13.5	16.5	210.2	7821	33.28	0.08	3.99
3	18.5	21.5	215.2	8038	32.82	0.33	3.50
3	23.5	26.5	220.2	8254	33.55	0.13	4.19

Table continued on next page

Table D.19 – Continued

Drive #	top drive depth (cm)	bottom drive depth (cm)	Composite depth (cm)[a]	Median age (cal. y BP)	$\delta^{18}O_{diatom}$ (‰ VSMOW)	±1 σ	$\Delta\delta^{18}O_{diatom}$ LVB-LVA (‰)[b]
3	28.5	31.5	225.2	8471	33.78	0.17	4.32
3	33.5	36.5	230.2	8688	33.64	0.21	4.06
3	38.5	41.5	235.2	8904	33.38	0.26	3.62
3	43.5	46.5	240.2	9121	34.45	0.13	4.50
3	48.5	51.5	245.2	9338	33.97	0.53	3.90
3	53.5	56.5	250.2	9554	34.83	0.04	4.64
3	58.5	61.5	255.2	9771	33.97	0.17	3.76
3	63.5	66.5	260.2	9983	35.03	0.11	4.83
3	68.5	71.5	265.2	10195	35.39	0.21	5.19
3	78.5	81.5	275.2	10980	34.97	0.01	
3	88.5	91.5	280.2	11552	34.49	0.09	
3	88.5	91.5	285.2	12125	34.38	0.07	
4	3.5	6.5	290.2	12697	34.60	0.34	
4	8.5	11.5	295.2	13270	34.16	0.17	
4	12.5	15	298.95	13699	34.48	0.11	
4	31.5	32.5	317.7	15129	35.51	0.34	

(a) Depth below sed. water interface, corrected for overlap between drives and stretching/compression during coring
(b) Calculated from linearly interpolated LVA $\delta^{18}O_{diatom}$

Figures

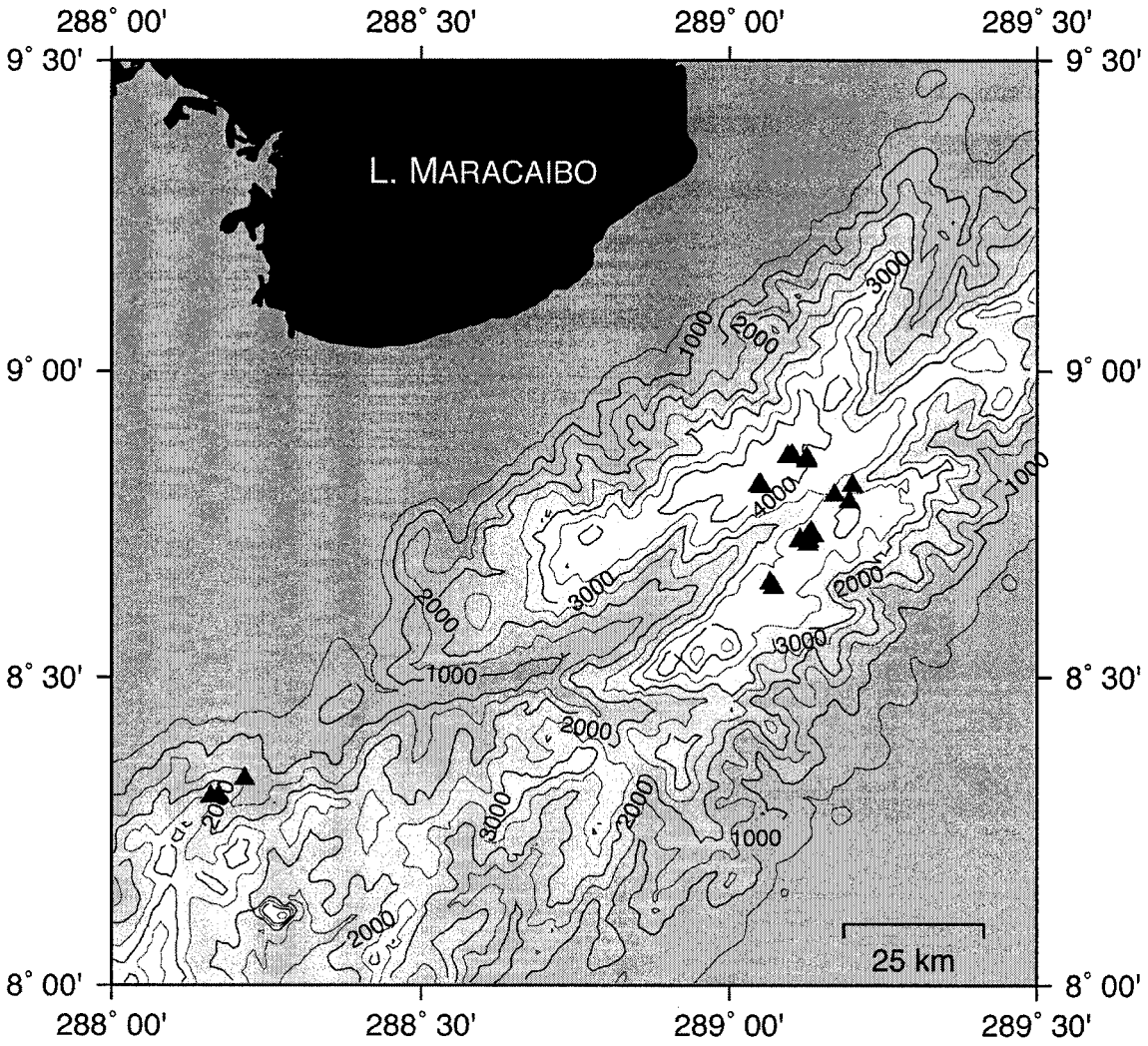

Figure D.1 – Location of modern lake samples.

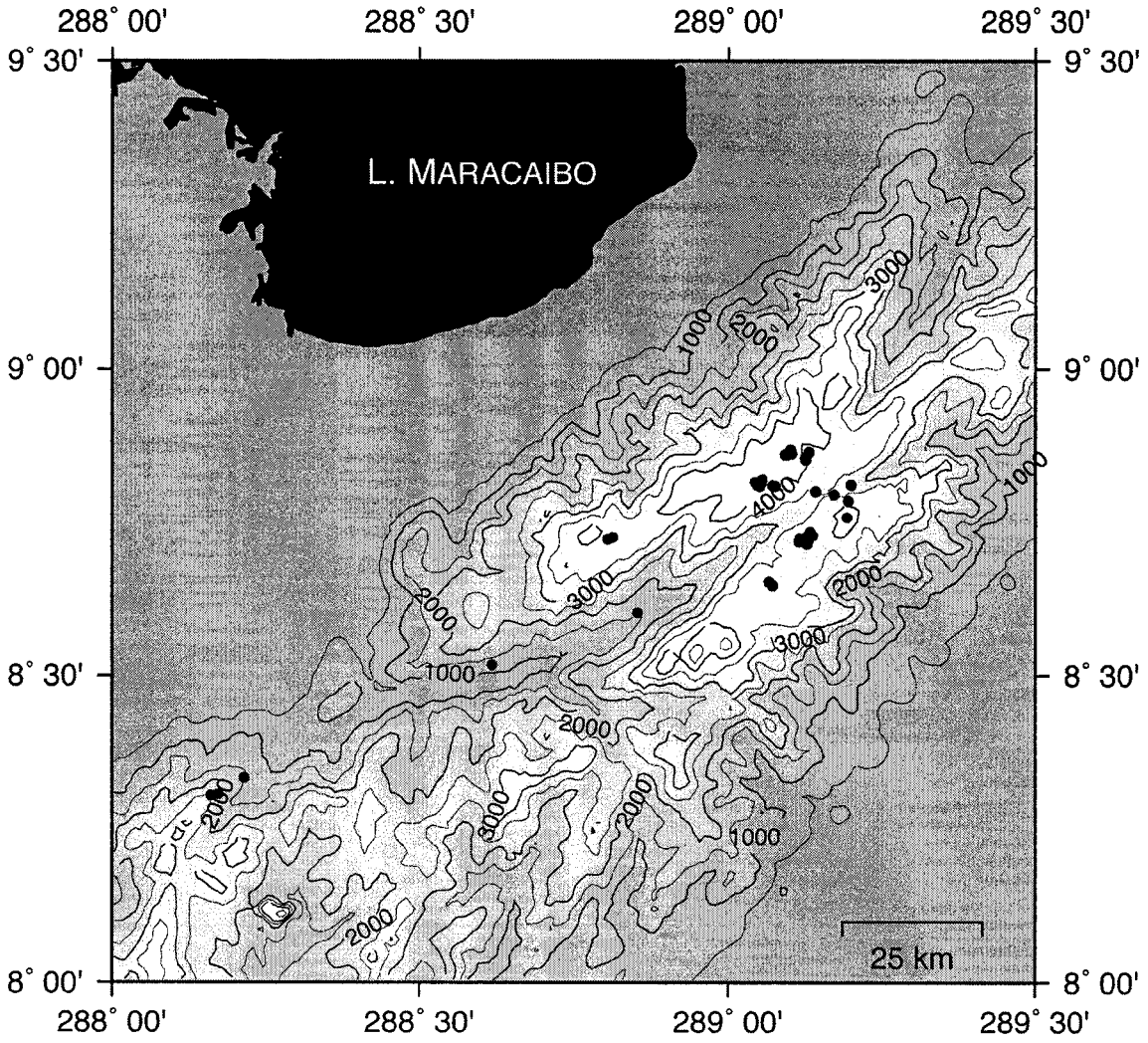

Figure D.2 – Location of surface water and precipitation isotope samples.

REFERENCES

Abbott, M. B., Seltzer, G. O., Kelts, K. R., and Southon, J. (1997). Holocene Paleohydrology of the Tropical Andes from Lake Records. Quaternary Research 47, 70-80.

Abbott, M. B., and Stafford, T. W. (1996). Radiocarbon Geochemistry of Modern and Ancient Arctic Lake Systems, Baffin Island, Canada. Quaternary Research 45, 300-311.

Abbott, M. B., Wolfe, B. B., Wolfe, A. P., Seltzer, G. O., Aravena, R., Mark, B. G., Polissar, P. J., Rodbell, D. T., Rowe, H. D., and Vuille, M. (2003). Holocene paleohydrology and glacial history of the central Andes using multiproxy lake sediment studies. Palaeogeography, Palaeoclimatology, Palaeoecology 194, 123-138.

Aceituno, P. (1988). On the functioning of the southern oscillation in the South American sector. Part I: surface climate. Monthly Weather Review 116, 505-524.

Adkins, J. F., McIntyre, K., and Schrag, D. P. (2002). The salinity, temperature, and $\delta^{18}O$ of the glacial deep ocean. Science 298, 1769-1773.

Andrus, C. F. T., Crowe, D. E., Sandweiss, D. H., Reitz, E. J., and Romanek, C. S. (2002). Otolith $\delta^{18}O$ record of mid-Holocene sea surface temperatures in Peru. Science 295, 1508-1511.

APHA. (1992). "Standard Methods for the Examination of Water and Wastewater." American Public Health Association, Washington D.C.

Appleby, P. G., and Oldfield, F. (1978). The calculation of ^{210}Pb dates assuming a constant rate of supply of unsupported ^{210}Pb in the sediment. Catena 5, 1-8.

Azocar, A., and Monasterio, M. (1980). Caracterización ecológica del clima en El Páramo de Mucubají. In "Estudios Ecologicos en los Páramos Andinos." (M. Monasterio, Ed.), pp. 207-223. Ediciones de la Universidad de Los Andes, Merida, Venezuela.

Baker, P. A., Rigsby, C. A., Seltzer, G. O., Fritz, S. C., Lowenstein, T. K., Bacher, N. P., and Veliz, C. (2001a). Tropical climate changes at millennial and orbital timescales on the Bolivian Altiplano. Nature 409, 698-701.

Baker, P. A., Seltzer, G., Fritz, S., Dunbar, R. B., Grove, M. J., Tapia, P. M., Cross, S. L., Rowe, H. D., and Broda, J. P. (2001b). The history of South American tropical precipitation for the past 25,000 years. Science 291, 640-643.

Bard, E., Arnold, M., Fairbanks, R. G., and Hamelin, B. (1993). ^{230}Th-^{234}U and ^{14}C ages obtained by mass spectrometry on corals. Radiocarbon 35, 191-199.

Bard, E., Hamelin, B., Arnold, M., Montaggioni, L., Cabloch, G., Faure, G., and Rougerie, F. (1996). Deglacial sea-level record from Tahiti corals and the timing of global meltwater discharge. Nature 382, 241-244.

Bard, E., Hamelin, B., and Fairbanks, R. G. (1990a). U-Th ages obtained by mass spectrometry in corals from Barbados: sea level during the past 130,000 years. Nature 346, 456-458.

Bard, E., Hamelin, B., Fairbanks, R. G., and Zindler, A. (1990b). Calibration of the ^{14}C timescale over the past 30,000 years using mass spectrometric U-Th ages from Barbados corals. Nature 345, 405-410.

Bard, E., Hamelin, B., Fairbanks, R. G., Zindler, A., Mathieu, G., and Arnold, M. (1990c). U/Th and ^{14}C ages of corals from Barbados and their use for calibrating the ^{14}C time scale beyond 9000 years B.P. Nuclear Instruments and Methods in Physics Research B52, 461-468.

Bard, E., Raisbeck, G., Yiou, F., and Jouzel, J. (2000). Solar irradiance during the last 1200 years based on cosmogenic nuclides. Tellus 52B, 985-992.

Battarbee, R. W. (1973). A new method for the estimation of absolute microfossil numbers, with reference especially to diatoms. Limnology and Oceanography 18, 647-653.

Behling, H., Keim, G., Irion, G., Junk, W., and de Mello, J. N. (2001). Holocene environmental changes in the Central Amazon Basin inferred from Lago Calado (Brazil). Palaeogeography, Palaeoclimatology, Palaeoecology 173, 87-101.

Berger, A., and Loutre, M. F. (1991). Insolation values for the climate of the last 10 million years. Quaternary Science Review 10, 297-317.

Black, D. E., Peterson, L. C., Overpeck, J. T., Kaplan, A., Evans, M. N., and Kashgarian, M. (1999). Eight Centuries of North Atlantic Ocean Atmosphere Variability. Science 286, 1709-1713.

Bond, G., Kromer, B., Juerg, B., Muscheler, R., Evans, M. N., Showers, W., Hoffman, S., Lotti-Bond, R., Hajdas, I., and Bonani, G. (2001). Persistent Solar Influence on North Atlantic Climate During the Holocene. Science 294, 2130-2136.

Bradbury, J. P. (1989). Late Quaternary lacustrine paleoenvironments in the Cuenca de México. Quaternary Science Reviews 8, 75-1000.

Bradbury, J. P., Leyden, B., Salgado-Labouriau, M., Lewis Jr., W. M., Schubert, C., Binford, M. W., Frey, D. G., Whitehead, D. R., and Weibezahn, F. H. (1981). Late Quaternary environmental history of Lake Valencia, Venezuela. Science 214, 1299-1305.

Bradley, R., Yuretich, R., and Weingarten, B. (1991). Studies of modern climate. In "Late Quaternary climatic fluctuations of the Venezuelan Andes." (R. Yuretich, Ed.), pp. 45-62. Dept. of Geosciences, Univ. of Massachusetts, Amherst, MA.

Bradley, R. S., Keimig, F. T., and Diaz, H. F. (2004). Projected temperature changes along the American cordillera and the planned GCOS network. Geophysical Research Letters 31, doi:10.1029/2004GL020229.

Bradley, R. S., Vuille, M., Hardy, D., and Thompson, L. G. (2003). Low latitude ice cores record Pacific sea surface temperatures. Geophysical Research Letters 30, doi:10.1029/2002GL016546.

Brandriss, M. E., O'Neil, J. R., Edlund, M. B., and Stoermer, E. F. (1998). Oxygen isotope fractionation between diatomaceous silica and water. Geochimica et Cosmochimica Acta 62, 1119-1125.

Bush, A. B. G. (1999). Assessing the impact of Mid-Holocene insolation on the atmosphere-ocean system. Geophysical Research Letters 26, 99-102.

Bush, M. B., Miller, M. C., De Oliveira, P. E., and Colinvaux, P. A. (2002). Orbital forcing signal in sediments of two Amazonian lakes. Journal of Paleolimnology 27, 341-352.

Bush, M. B., Piperno, D. R., Colinvaux, P. A., De Oliveira, P. E., Krissek, L. A., Miller, M. C., and Rowe, W. E. (1992). A 14,300-yr paleoecological profile of a lowland tropical lake in Panama. Ecological Monographs 62, 251-275.

Bush, M. B., and Silman, M. R. (2004). Observations on Late Pleistocene cooling and precipitation in the lowland Neotropics. Journal of Quaternary Science 19, 677-684.

Caballero, M., and Guerrero, B. O. (1998). Lake Levels since about 40,000 Years Ago at Lake Chalco, near Mexico City. Quaternary Research 50, 69-79.

Carré, M., Bentaleb, I., Fontugne, M., and Lavallée, D. (2005). Strong El Niño events during the early Holocene: stable isotope evidence from Peruvian sea shells. The Holocene 15, 42-47.

Carter, S. J., and Colman, S. M. (1994). Biogenic silica in Lake Baikal sediments: Results from 1990-1992 American cores. Journal of Great Lakes Research 20, 751-760.

CIESIN, IFPRI, and WRI. (2000). Gridded population of the world, Version 2. Available at http://sedac.ciesin.columbia.edu/plue/gpw.

Clark, P. U., McCabe, A. M., Mix, A. C., and Weaver, A. J. (2004). Rapid rise of sea level 19,000 years ago and its global implications. Science 304, 1141-1144.

Clayton, T., Pearce, R. B., and Peterson, L. C. (1999). Indirect climatic control of the clay mineral composition of Quaternary sediments from the Cariaco basin, northern Venezuela (ODP Site 1002). Marine Geology 61, 191-206.

Clement, A. C., Seager, R., and Cane, M. A. (2000). Suppression of El Niño during the mid-Holocene by changes in the Earth's orbit. Paleoceanography 15, 731-737.

Colinvaux, P. A., Irion, G., Räsänen, M. E., Bush, M. B., and Nunes de Mello, J. A. S. (2001). A paradigm to be discarded: Geological and paleoecological data falsify the HAFFER & PRANCE refuge hypothesis of Amazonian speciation. Amazoniana XVI, 609-646.

Colinvaux, P. A., Olson, K., and Liu, K.-B. (1988). Late-Glacial and Holocene Pollen Diagrams from Two Endorheic Lakes of the Inter-Andean Plateau of Ecuador. Review of Palaeobotany and Palynology 55, 83-99.

Colinvaux, P. A., and Schofield, E. K. (1976a). Historical ecology in the Galapagos Islands: I. A Holocene pollen record from El Junco lake, Isla San Cristobal. Journal of Ecology 64, 989-1012.

Colinvaux, P. A., and Schofield, E. K. (1976b). Historical ecology in the Galapagos Islands: II. A Holocene spore record from El Junco lake, Isla San Cristobal. Journal of Ecology 64, 1013-1028.

Conley, D. J. (1998). An interlaboratory comparison for the measurement of biogenic silica in sediments. Marine Chemistry 63, 39-48.

Costa, M. H., and Foley, J. A. (1999). Trends in the hydrologic cycle of the Amazon basin. Journal of Geophysical Research-Atmospheres 104, 14189-14198.

Craig, H., and Gordon, L. I. (1965). Deuterium and oxygen-18 variations in the ocean and the marine atmosphere. In "Stable Isotopes in Oceanographic Studies and Paleotemperatures." (E. Tongiorgi, Ed.). Consiglio Nazionale delle Richerche, Laboratorio di Geologica, Pisa.

Cross, S. L., Baker, P. A., Seltzer, G. O., Fritz, S. C., and Dunbar, R. B. (2000). A new estimate of the Holocene lowstand level of Lake Titicaca, and implications for Tropical Paleohydrology. The Holocene 10, 21-32.

Crowley, T. J. (2000). Causes of climate change over the past 1000 years. Science 289, 270-277.

Cruz Jr., F. W., Burns, S. J., Karmann, I., Sharp, W. D., Vuille, M., Cardoso, A. O., Ferrari, J. A., Dias, P. L. S., and Viana Jr., A. (2005). Insolation-driven changes in atmospheric circulation over the past 116,000 years in subtropical Brazil. Nature 434, 63-66.

Curtis, J. H., Brenner, M., and Hodell, D. A. (1999). Climate change in the Lake Valencia Basin, Venezuela, approximately 12,500 yr BP to present. Holocene 9, 609-619.

Curtis, J. H., Hodell, D. A., and Brenner, M. (1996). Climate variability on the Yucatan Peninsula (Mexico) during the past 3500 Years, and implications for Maya cultural evolution. Quaternary Research 46, 37-47.

Curtis, S., and Hastenrath, S. (1999). Trends of upper-air circulation and water vapour over equatorial South America and adjacent oceans. International Journal of Climatology 19, 863-876.

de Freitas, H. A., Pessenda, L. C. R., Aravena, R., Gouveia, S. E. M., Ribeiro, A. d. S., and Boulet, R. (2001). Late Quaternary vegetational dynamics in the southern Amazon basin inferred from carbon isotopes in soil organic matter. Quaternary Research 55, 39-46.

De Oliveira, P. E., Barreto, A. M. F., and Suguio, K. (1999). Late Pleistocene/Holocene climatic and vegetational history of the Brazilian caatinga: the fossil dunes of the middle São Francisco River. Palaeogeography, Palaeoclimatology, Palaeoecology 152, 319-337.

Dean Jr., W. E. (1974). Determination of carbonate and organic matter in calcareous sediments and sedimentary rocks by loss on ignition: comparison with other methods. Journal of Sedimentary Petrology 44, 242-248.

DeMaster, D. J. (1979). "The marine budgets of silica and 32-Si." Unpublished Ph.D. thesis, Yale University.

DeMaster, D. J. (1981). The supply and accumulation of silica in the marine environment. Geochimica et Cosmochimica Acta 45, 1715-1732.

Duplessy, J.-C., Labeyrie, L., and Waelbroeck, C. (2002). Constraints on the ocean oxygen isotopic enrichment between the Last Glacial Maximum and the Holocene: Paleoceanographic implications. Quaternary Science Reviews 221, 315-330.

Edmond, J. M., Palmer, M. R., Measures, C. I., Brown, E. T., and Huh, Y. (1996). Fluvial geochemistry of the eastern slope of the northeastern Andes and its foredeep in the drainage of the Orinoco in Columbia and Venezuela. Geochimica et Cosmochimica Acta 60, 2949-2976.

Edwards, R. L., Beck, J. W., Burr, G. S., Donahue, D. J., Chappell, J. M. A., Bloom, A. L., Druffel, E. R. M., and Taylor, F. W. (1993). A Large Drop in Atmospheric $^{14}C/^{12}C$ and Reduced Melting in the Younger Dryas, Documented with ^{230}Th Ages of Corals. Science 260, 962-968.

Enfield, D. B. (1996). Relationship of inter-American rainfall to tropical Atlantic and Pacific SST variability. Geophysical Research Letters 23, 3305-3308.

Fairbanks, R. G. (1989). A 17,000-year glacio-eustatic sea level record: influence of glacial melting rates on the Younger Dryas event and deep-ocean circulation. Nature 342, 637-642.

Fleming, K., Johnston, P., Zwartz, D., Yokoyama, Y., Lambeck, K., and Chappel, J. (1998). Refining the eustatic sea-level curve since the Last Glacial Maximum using far- and intermediate-field sites. Earth and Planetary Science Letters 163, 327-342.

Garreaud, R. D. (2000). Intraseasonal variability of moisture and rainfall over the South American Altiplano. Monthly Weather Review 128, 3337-3346.

Garreaud, R. D., Vuille, M., and Clement, A. C. (2003). The climate of the Altiplano: observed current conditions and mechanisms of past changes. Palaeogeography, Palaeoclimatology, Palaeoecology 194, 5-22.

Gasse, F. (2000). Hydrologic changes in the African tropics since the Last Glacial Maximum. Quaternary Science Reviews 19, 189-211.

Gat, J. H., and Matsui, E. (1991). Atmospheric water balance in the Amazon Basin: An isotopic evapotranspiration model. Journal of Geophysical Research 96, 13,179-13,188.

Gat, J. R. (1995). Stable Isotopes of Fresh and Saline Lakes. In "The Physics and Chemistry of Lakes." (A. Lerman, D. M. Imboden, and J. R. Gat, Eds.), pp. 139-164. Springer-Verlag, New York.

Gat, J. R. (2000). Atmospheric water balance-the isotopic perspective. Hydrological Processes 14, 1357-1369.

Glasser, N. F., Hambrey, M. J., and Aniya, M. (2002). An advance of Soler Glacier, North Patagonian Icefield, at c. AD 1222-1342. Holocene 12, 113-120.

Gonfiantini, R., Roche, M.-A., Olivry, J.-C., Fontes, J.-C., and Zuppi, G. M. (2001). The altitude effect on the isotopic composition of tropical rains. Chemical Geology 181, 147-167.

González, L. A., and Gómez, R. (2002). High resolution speleothem paleoclimatology of northern Venezuela: a progress report. Boletín de la Sociedad Venezolana Espeleologica 36, 27-29.

Grootes, P. M., and Stuiver, M. (1989). Oxygen isotope changes in tropical ice, Quelccaya, Peru. Journal of Geophysical Research 94, 1187-1194.

Haase-Schramm, A., Böhm, F., Eisenhauuer, A., Dullo, W.-C., Joachimski, M. M., Hansen, B., and Reitner, J. (2003). Sr/Ca ratios and the oxygen isotopes from sclerosponges: Temperature history of the Caribbean mixed layer and thermocline during the Little Ice Age. Paleoceanography 18, 1073-1088.

Haberle, S. G., and Maslin, M. A. (1999). Late Quaternary vegetation and climate change in the Amazon basin based on a 50,000 year pollen record from the Amazon Fan, ODP Site 932. Quaternary Research 51, 27-38.

Hansen, B. C. S., Rodbell, D. T., Seltzer, G., León, B., Young, K. R., and Abbott, M. B. (2003). Late-glacial and Holocene vegetational history from two sites in the western Cordillera of southwestern Ecuador. Palaeogeography, Palaeoclimatology, Palaeoecology 194, 79-108.

Hansen, J., Sato, M., Ruedy, R., Lacis, A., and Oinas, V. (2000). Global warming in the twenty-first century: An alternative scenario. Proceedings of the National Academy of Sciences 97, 9875-9880.

Hardy, D. R., Vuille, M., and Bradley, R. S. (2003). Variability of snow accumulation and isotopic composition on Nevado Sajama, Bolivia. Journal of Geophysical Research 108, doi:10.1029/2003JD003623.

Hastenrath, S. (1984). Interannual variability and the annual cycle: Mechanisms of circulation and climate in the tropical Atlantic sector. Monthly Weather Review 112, 1097-1107.

Hastenrath, S., and Kruss, P. D. (1992). The dramatic retreat of Mount Kenya's glaciers between 1963 and 1987: greenhouse forcing. Annals of Glaciology 16, 127-134.

Hastenrath, S., Polzin, D., and Francou, B. (2004). Circulation variability reflected in ice core and lake records of the southern tropical Andes. Climatic Change 64, 361-375.

Haug, G. H., Hughen, K. A., Sigman, D. M., Peterson, L. C., and Röhl, U. (2001). Southward migration of the intertropical convergence zone through the Holocene. Science 293, 1304-1308.

Heiri, O., Lotter, A. F., and Lemcke, G. (2001). Loss on ignition as a method for estimating organic and carbonate content in sediments: reproducibility and comparability of results. Journal of Paleolimnology 25, 101-110.

Henderson-Sellers, A., McGuffie, K., and Zhang, H. (2002). Stable isotopes as validation tools for global climate model predictions of the impact of Amazonian deforestation. Journal of Climate 15, 2664-2677.

Hodell, D. A., Brenner, M., Curtis, J. H., and Guilderson, T. (2001). Solar Forcing of Drought Frequency in the Maya Lowlands. Science 292, 1367-1370.

Hodell, D. A., Curtis, J. H., and Brenner, M. (1995). Possible role of climate in the collapse of Classic Maya civilization. Nature 375, 391-394.

Hodell, D. A., Curtis, J. H., Jones, G. A., Higuera-Gundy, A., Brenner, M., Binford, M. W., and Dorsey, K. T. (1991). Reconstruction of Caribbean climate change over the past 10,500 years. Nature 352, 790-793.

Hoffmann, G., Ramirez, E., Taupin, J. D., Francou, B., Ribstein, P., Delmas, R., Drr, H., Gallaire, R., Simes, J., Schotterer, U., Stievenard, M., and Werner, M. (2003). Coherent isotope history of Andean ice cores over the last century. Geophysical Research Letters 30, doi:10.1029/2002GL014870.

Horita, J., and Wesolowski, D. J. (1994). Liquid-vapor fractionation of oxygen and hydrogen isotopes of water from the freezing to the critical temperature. Geochimica et Cosmochimica Acta 58, 3425-3437.

Horn, S. P. (1993). Postglacial vegetation and fire history in the Chirripó Páramo of Costa Rica. Quaternary Research 40, 107-116.

Hughen, K. A., Overpeck, J. T., J.Lehman, S., Kashgarian, M., Southon, J., Peterson, L. C., Alley, R., and Sigman, D. M. (1998). Deglacial changes in ocean circulation from an extended radiocarbon calibration. Nature 391, 65-68.

Hughen, K. A., Overpeck, J. T., Peterson, L. C., and Trumbore, S. (1996). Rapid climate changes in the tropical Atlantic region during the last deglaciation. Nature 380, 51-54.

IAEA/WMO. (2001). Global Network of Isotopes in Precipitation. The GNIP Database. Accessible at: http://isohis.iaea.org.

Johnson, D. (1998). MacCount v2.42. www.bgsu.edu/departments/biology/facilities/algae/count/count.html.

Jones, G. A. (1994). Holocene climate and deep ocean circulation changes: Evidence from accelerator mass spectrometer radiocarbon dated Argentine Basin (SW Atlantic) mudwaves. Paleoceanography 9, 1001-1016.

Jones, P. D., and Mann, M. E. (2004). Climate over past millennia. Reviews of Geophysics 42, doi:10.1029/2003RG000143.

Juillet-Leclerc, A., and Labeyrie, L. (1987). Temperature dependence of the oxygen isotopic fractionation between diatom silica and water. Earth and Planetary Science Letters 84, 69-74.

Kalnay, E., Kanamitsu, M., Kistler, R., Collins, W., Deaven, D., Gandin, L., Iredell, M., Saha, S., White, G., Woollen, J., Zhu, Y., Chelliah, M., Ebisuzaki, W., Higgins, W., Janawiak, J., Mo, K. C., Ropelewski, C., Wang, J., Leetmaa, A., Reynolds, R., Jenne, R., and Joseph, D. (1996). The NCEP/NCAR Reanalysis 40-year Project. Bulletin of the American Meteorological Society 77, 437-471.

Kaser, G. (1999). A review of the modern fluctuations of tropical glaciers. Global and Planetary Change 22, 93-103.

Kaser, G. (2001). Glacier-climate interaction at low latitudes. Journal of Glaciology 47, 195-204.

Kaser, G., and Osmaston, H. (2002). "Tropical Glaciers." In "International Hydrology Series." Cambridge Univ. Press, Cambridge, UK.

Kitoh, A., and Murakami, S. (2002). Tropical Pacific climate at the mid-Holocene and the Last Glacial Maximum simulated by a coupled ocean-atmosphere general circulation model. Paleoceanography 17, doi:10.1029/2001PA000724.

Klein, A. G., Seltzer, G. O., and Isacks, B. L. (1999). Modern and last local glacial maximum snowlines in the Central Andes of Peru, Bolivia, and Northern Chile. Quaternary Science Reviews 18, 63-84.

Koutavas, A., and Lynch-Stieglitz, J. (2003). Glacial-interglacial dynamics of the eastern equatorial Pacific cold tongue-Intertropical Convergence Zone system reconstructed from oxygen isotope records. Paleoceanography 18, doi:10.1029/2003PA000894.

Krammer, K., and Lange-Bertalot, H. (1986). "Bacillariophyceae 1 Teil: Naviculaceae." In "Sübwasserflora von Mitteleuropa 2." (H. Ettl, H. Gerloff, H. Heynig, and D. Mollenhauer, Eds.), 876 pp. Gustav Fischer, Stuttgart.

Krammer, K., and Lange-Bertalot, H. (1988). "Bacillariophyceae 2 Teil: Bacillariaceae, Epithemiaceae, Surirellaceae." In "Sübwasserflora von Mitteleuropa 2." (H. Ettl, H. Gerloff, H. Heynig, and D. Mollenhauer, Eds.), 596 pp. Gustav Fischer, Stuttgart.

Krammer, K., and Lange-Bertalot, H. (1991a). "Bacillariophyceae 3 Teil: Centrales, Fragilariaceae, Eunotiaceae." In "Sübwasserflora von Mitteleuropa 2." (H. Ettl, H. Gerloff, H. Heynig, and D. Mollenhauer, Eds.), 576 pp. Gustav Fischer, Stuttgart.

Krammer, K., and Lange-Bertalot, H. (1991b). "Bacillariophyceae 4 Teil: Achnanthaceae, Kritische Ergänzungen zu Navicula (Lineolatae) und Gomphonema Gesamtliteraturverzeichnis." In "Sübwasserflora von Mitteleuropa 2." (H. Ettl, H. Gerloff, H. Heynig, and D. Mollenhauer, Eds.), 437 pp. Gustav Fischer, Stuttgart.

Kuhn, M. (1989). The response of the equilibrium line altitude to climate fluctuations: theory and observations. In "Glacier Fluctuations and Climate Change." (J. Oerlemans, Ed.), pp. 407-417. Kluwer Academic Publishers, The Netherlands.

Lachniet, M. S., Asmerom, Y., Burns, S. J., Patterson, W. P., Polyak, V. J., and Seltzer, G. O. (2004). Tropical response to the 8200 yr B.P. cold event? Speleothem isotopes indicate a weakened early Holocene monsoon in Costa Rica. Geology 32, 957-960.

Lange-Bertalot, H. (1998). "Tropical Diatoms of South America I." In "Iconographia Diatomologica." Vol. 5, 695 pp. Koeltz Scientific Books, Koenigstein, Germany.

Lea, D. W., Pak, D. K., Peterson, L. C., and Hughen, K. A. (2003). Synchroneity of tropical and high-latitude atlantic temperatures over the last glacial termination. Science 301, 1361-1364.

Lea, D. W., Pak, D. K., and Spero, H. J. (2000). Climate impact of late quaternary equatorial Pacific sea surface temperature variations. Science 289, 1719-1724.

Lean, J., Beer, J., and Bradley, R. S. (1995). Reconstruction of solar irradiance since 1610: implications for climate change. Geophysical Research Letters 22, 3195-3198.

Ledru, M.-P., Mourguiart, P., Ceccantini, G., Turcq, B., and Sifeddine, A. (2002). Tropical climates in the game of two hemispheres revealed by abrupt climatic change. Geology 30, 275-278.

Leyden, B. W. (1985). Late Quaternary aridity and Holocene moisture fluctuations in the Lake Valencia basin, Venezuela. Ecology 66, 1279-1295.

Liebmann, B., and Smith, H. J. (1996). Description of a complete (interpolated) outgoing longwave radiation dataset. Bulletin of the American Meteorological Society 77, 1275-1277.

Lin, H.-L., Peterson, L. C., Overpeck, J. T., Trumbore, S. E., and Murray, D. W. (1997). Late Quaternary climate change from $\delta^{18}O$ records of multiple species of planktonic foraminifera: High-resolution records from the anoxic Cariaco Basin, Venezuela. Paleoceanography 12, 415-427.

Liu, Z., Brady, E., and Lynch-Stieglitz, J. (2003). Global ocean response to orbital forcing in the Holocene. Paleoceanography 18, 1041-1081.

Loubere, P., Richaud, M., Liu, Z., and Mekik, F. (2003). Oceanic conditions in the eastern equatorial Pacific during the onset of ENSO in the Holocene. Quaternary Research 60, 142-148.

Lozano-García, M. d. S., and Ortega-Guerrero, B. (1994). Palynological and magnetic susceptibility records of Lake Chalco, central Mexico. Palaeogeography, Palaeoclimatology, Palaeoecology 109, 177-191.

Lyon, B. (2004). The strength of El Niño and the spatial extent of tropical drought. Geophysical Research Letters 31, doi:10.1029/2004GL020901.

Mann, M. E., Bradley, R. S., and Hughes, M. K. (1999). Northern hemisphere temperatures during the past millennium: Inferences, uncertainties, and limitations. Geophysical Research Letters 26, 759-762.

Martinelli, L. A., Victoria, R. L., Sternberg, L. S. L., Ribeiro, A., and Moreira, M. Z. (1996). Using stable isotopes to determine sources of evaporated water to the atmosphere in the Amazon basin. Journal of Hydrology 183, 191-204.

Maslin, M. A., and Burns, S. J. (2000). Reconstruction of the Amazon Basin effective moisture availability over the past 14,000 years. Science 290, 2285-2287.

Matsui, E., Salati, E., Ribeiro, M. N. G., Reis, C. M., Tancredi, A. C. S. N. F., and Gat, J. R. (1983). Precipitation in the central Amazon basin:-The isotopic composition of rain and atmospheric moisture at Belém and Manaus. Acta Amazonica 13, 307-369.

Mayle, F. E., and Beerling, D. J. (2004). Late Quaternary changes in Amazonian ecosystems and their implications for global carbon cycling. Palaeogeography, Palaeoclimatology, Palaeoecology 214, 11-25.

Mayle, F. E., Burbrudge, R., and Killeen, T. J. (2000). Millennial-Scale Dynamics of Southern Amazonian rain forests. Science 290, 2291-2294.

Meirding, T. C. (1982). Late Pleistocene glacial equilibrium-line altitudes in the Colorado Front Range: A comparison of methods. Quaternary Research 18, 289-310.

Milne, G. A., Mitrovica, J. X., and Schrag, D. P. (2002). Estimating past continental ice volume from sea-level data. Quaternary Science Reviews 21, 361-376.

Moreira, M. Z., Sternberg, L. S. L., Martinelli, L. A., Victoria, R. L., Barbosa, E. M., Bonates, L. C., and Nepstad, D. C. (1997). Contribution of transpiration to forest ambient vapour based upon isotopic measurements. Global Change Biology 3, 439-450.

Moschen, R., Lücke, A., and Schleser, G. H. (2005). Sensitivity of biogenic silica oxygen isotopes to changes in surface water temperature and paleoclimatology. Geophysical Research Letters 32, doi: 10.1029/2004GL022167.

Moy, C. M., Seltzer, G., Rodbell, D. T., and Anderson, D. (2002). Variability of El Niño/Southern Oscillation activity at millennial timescales during the Holocene epoch. Nature 420, 162-165.

NODC. (1998). NODC (Levitus) World Ocean Atlas. NOAA-CIRES Climate Diagnostic Center, Boulder, Colorado, USA.

Nyberg, J., Malmgren, B. A., Kuijpers, A., and Winter, A. (2002). A centennial-scale variability of tropical North Atlantic surface hydrography during the late Holocene. Palaeogeography, Palaeoclimatology, Palaeoecology 183, 25-41.

Paterson, W. S. B. (1981). "The Physics of Glaciers." 380 pp. Pergamon Press Inc., New York.

Patrick, R., and Reimer, C. W. (1966). "The Diatoms of the United States exclusive of Alaska and Hawaii." Vol. 1, 688 pp. Academy of Natural Sciences of Philadelphia Monograph 13.

Patrick, R., and Reimer, C. W. (1975). "The Diatoms of the United States exclusive of Alaska and Hawaii." Vol. 2 Part 1, 213 pp. Academy of Natural Sciences of Philadelphia Monograph 13.

Peltier, W. R. (2002). On eustatic sea level history: Last Glacial Maximum to Holocene. Quaternary Science Reviews 21, 377-396.

Pessenda, L. C. R., Gomes, B. M., Aravena, R., Ribeiro, A. d. S., Boulet, R., and Gouveia, S. E. M. (1998). The carbon isotope record in soils along a forest-cerrado ecosystem transect: implications for the vegetation changes in the Rondonia state, southwestern Brazilian Amazon region. The Holocene 8, 599-603.

Pessenda, L. C. R., Ribeiro, A. d. S., Gouveia, S. E. M., Aravena, R., Boulet, R., and Bendassolli, J. A. (2004). Vegetation dynamics during the late Pleistocene in the Barreirinhas region, Maranhão State, northeastern Brazil, based on carbon isotopes in soil organic matter. Quaternary Research 62, 183-193.

Peterson, L. C., Haug, G. H., Hughen, K. A., and Röhl, U. (2000). Rapid Changes in the Hydrologic Cycle of the Tropical Atlantic During the Last Glacial. Science 290, 1947-1951.

Pfister, C. (1992). Monthly temperature and precipitation in central Europe 1525-1979: Quantifying documentary evidence on weather and its effects. In "Climate Since AD 1500." (R. S. Bradley, and P. D. Jones, Eds.), pp. 118-142. Routledge, London.

Pierrehumbert, R. T. (1999). Huascaran $\delta^{18}O$ as an indicator of tropical climate during the Last Glacial Maximum. Geophysical Research Letters 26, 1345-1348.

Piper, D. Z., and Dean Jr., W. E. (2002). Trace-element deposition in the Cariaco Basin, Venezuela Shelf, under sulfate-reducing conditions--a history of the local hydrography and global climate, 20 ka to the Present., pp. 1-45. U.S. Geological Survey, Denver, CO U.S.A.

Placzek, C., Quade, J., and Betancourt, J. L. (2001). Holocene lake-level fluctuations of Lake Aricota, Southern Peru. Quaternary Research 56, 181-190.

Poore, R. Z., Dowsett, H. J., Verardo, S., and Quinn, T. M. (2003). Millennial- to century-scale variability in Gulf of Mexico Holocene climate records. Paleoceanography 18, 1048-1059.

Poore, R. Z., Pavich, M. J., and Grissino-Mayer, H. D. (2005). Record of the North American southwest monsoon from Gulf of Mexico sediment cores. Geology 33, 209-212.

Potapova, M., and Charles, D. F. (2003). Distribution of benthic diatoms in U.S. rivers in relation to conductivity and ionic composition. Freshwater Biology in press.

Poveda, G., and Mesa, O. J. (1997). Feedbacks between hydrological processes in tropical South America and large-scale ocean-atmospheric phenomena. Journal of Climate 10, 2690-2702.

Pulwarty, R. S., Barry, R. G., Hurst, C. M., Sellinger, K., and Mogollon, L. F. (1998). Precipitation in the Venezuelan Andes in the context of regional climate. Meteorology and Atmospheric Physics 67, 217-237.

Pulwarty, R. S., Barry, R. G., and Riehl, H. (1992). Annual and seasonal patterns of rainfall variability over Venezeula. Erdkunde 46, 273-289.

Ramirez, E., Francou, B., Ribstein, P., Descloitres, M., Guerin, R., Mendoza, J., Gallaire, R., Pouyaud, B., and Jordan, E. (2001). Small glaciers disappearing in the tropical Andes: a case-study in Bolivia: Glacier Chacaltaya (16 degrees S). Journal of Glaciology 47, 187-194.

Ramirez, E., Hoffman, G., Taupin, J. D., Francou, B., Ribstein, P., Caillon, N., Ferron, F. A., Landais, A., Petit, J. R., Pouyaud, Schotterer, U., Simmoes, J. C., and Stievenard, M. (2003). A new Andean deep ice core from Nevado Illimani (6350 m), Bolivia. Earth and Planetary Science Letters 212, 337.

Riedinger, M. A., Steinitz-Kannan, M., Last, W. M., and Brenner, M. (2002). A ~6100 ^{14}C yr record of El Niño activity from the Galápagos Islands. Journal of Paleolimnology 27, 1-7.

Ropelewski, C. F., and Halpert, M. S. (1987). Global and regional scale precipitation patterns associated with the El Niño/Southern Oscillation. Monthly Weather Review 115, 1606-?

Rosqvist, G. (1995). Proglacial Lacustrine sediments from El Altar, Ecuador - Evidence for Late-Holocene climatic change. Holocene 5, 111-117.

Rowe, H. D., Guilderson, T., Dunbar, R. B., Southon, J., Seltzer, G., Mucciarone, D. A., Fritz, S., and Baker, P. A. (2003). Late Quaternary lake-level changes constrained by radiocarbon and stable isotope studies on sediment cores from Lake Titicaca, South America. Global and Planetary Change 38, 273-290.

Rowley, D. B., Pierrehumbert, R. T., and Currie, B. S. (2001). A new approach to stable isotope-based paleoaltimetry: implications for paleoaltimetry and paleohypsometry of the High Himalaya since the Late Miocene. Earth and Planetary Science Letters 188, 253-268.

Rull, V., Abbott, M. B., Polissar, P. J., Wolfe, A. P., Bezada, M., and Bradley, R. S. (2005). High altitude vegetation change during the last 15,000 years in the tropical Andes: the pollen record of Laguna Verde Alta, Venezuela. in press (Quaternary Research).

Rull, V., Salgado-Labouriau, M. L., Schubert, C., and Valastro Jr., S. (1987). Late Holocene temperature depression in the Venezuelan Andes: Palynological Evidence. Palaeogeography, Palaeoclimatology, Palaeoecology 60, 109-121.

Rull, V., and Vegas-Vilarrúbia, T. (1993). Palaeolimnological studies in Venezuela. Verh. Internat., Verein. Limnol. 25, 1122-1127.

Ruter, A., Arzt, J., Vavrus, S., Bryson, R. A., and Kutzbach, J. E. (2004). Climate and environment of the subtropical and tropical Americas (NH) in the mid-Holocene: comparison of observations with climate model simulations. Quaternary Science Reviews 23, 663-679.

Rühlemann, C., Mulitza, S., Müller, P. J., Wefer, G., and Zahn, R. (1999). Warming of the tropical Atlantic Ocean and slowdown of the thermohaline circulation during the last deglaciation. Nature 402, 511-514.

Salati, E. (1985). The climatology and hydrology of Amazonia. In "Amazonia." (G. T. Prance, and T. E. Lovejoy, Eds.), pp. 18-48. Pergamon Press, New York.

Salati, E., Dall'Olio, A., Matsui, E., and Gat, J. R. (1979). Recycling of water in the Amazon Basin: an isotopic study. Water Resources Research 15, 1250-1258.

Salgado-Labouriau, M. L., Bradley, R. S., Yuretich, R., and Weingarten, B. (1992). Paleoecological analysis of the sediments of Lake Mucubají, Venezuelan Andes. Journal of Biogeography 19, 317-327.

Salgado-Labouriau, M. L., Schubert, M. L., and Valastro, S. J. (1977). Paleoecologic analysis of a Late Quaternary terrace from Mucubají, Venezuelan Andes. Journal of Biogeography 4, 313-325.

Sandweiss, D. H., Maasch, K. A., Burger, R. L., Richardson III, J. B., Rollins, H. B., and Clement, A. (2001). Variation in Holocene El Niño frequencies: Climate records and cultural consequences in ancient Peru. Geology 29, 603-606.

Schmidt, G. A., Bigg, G. R., and Rohling, E. J. (1999). Global seawater oxygen-18 database. NASA/GISS, http://www.giss.nasa.gov/data/o18data/.

Schmidt, M., Spero, H. J., and Lea, D. W. (2004). Links between salinity variation in the Caribbean and North Atlantic thermohaline circulation. Nature 428, 160-163.

Schrag, D. P., Adkins, J. F., McIntyre, K., Alexander, J. L., Hodell, D. A., Charles, C. D., and McManus, J. F. (2002). The oxygen isotopic composition of seawater during the Last Glacial Maximum. Quaternary Science Reviews 21, 331-342.

Schubert, C. (1972). Geomorphology and glacier retreat in the Pico Bolivar area, Sierra Nevada de Merida, Venezuela. Zeitschrift für Gletscherkunde und Glazialgeologie VIII, 189-202.

Schubert, C. (1984). The Pleistocene and recent extent of the glaciers of the Sierra Nevada de Merida, Venezuela. Erdwissenschaftliche Forschung 18, 269-278.

Schubert, C. (1992). The glaciers of the Sierra Nevada de Merida (Venezuela): A photographic comparison of recent deglaciation. Erdkunde 46, 58-64.

Schubert, C., and Fritz, P. (1985). Radiocarbon ages of peat, Guayana highlands (Venezuela). Naturwissenschaften 72, 427-429.

Seiler, K.-P. (2000). Man's impact on the groundwater systems. In "Man's Impact on the Groundwater System." (W. G. Mook, Ed.), pp. 106. Environmental Isotopes in the Hydrologic Cycle: Principles and Applications. IAEA, Vienna, Germany.

Seltzer, G., Rodbell, D. T., and Burns, S. (2000). Isotopic evidence for late Quaternary climatic change in tropical South America. Geology 28, 35-38.

Seltzer, G. O. (1990). Recent glacial history and paleoclimate of the Peruvian-Bolivian Andes. Quaternary Science Reviews 9, 137-152.

Seltzer, G. O. (1992). Late Quaternary glaciation of the Cordillera Real, Bolivia. Journal of Quaternary Science 7, 87-98.

Seltzer, G. O., Rodbell, D. T., Baker, P. A., Fritz, S. C., Tapia, P. M., Rowe, H. D., and Dunbar, R. B. (2002). Early Warming of Tropical South America at the Last Glacial-Interglacial Transition. Science 296, 1685-1686.

Shemesh, A., Burckle, L. H., and Hays, J. D. (1995). Late Pleistocene oxygen isotope records of biogenic silica from the Atlantic sector of the Southern Ocean. Paleoceanography 10, 179-196.

Shemesh, A., Charles, C. D., and Fairbanks, R. G. (1992). Oxygen isotopes in biogenic silica: global changes in ocean temperature and isotopic composition. Science 256, 1434-1436.

Shemesh, A., and Peteet, D. (1998). Oxygen isotopes in fresh water biogenic opal-Northeastern US Alleröd-Younger Dryas temperature shift. Geophysical Research Letters 25, 1935-1938.

Solanki, S. K., Usoskin, I. G., Kromer, B., Schüssler, M., and Beer, J. (2004). Unusual activity of the Sun during recent decades compared to the previous 11,000 years. Nature 431, 1084-1087.

Stager, J. C., and Mayewski, P. A. (1997). Abrupt Early to Mid-Holocene climatic transition registered at the equator and the poles. Science 276, 1834-1836.

Stansell, N. (2005). "Last Glacial Maximum equilibrium-line altitude reconstructions, paleo-temperature estimates and deglacial chronology of the Mérida Andes, Venezuela." Unpublished M.Sc. thesis, University of Pittsburgh.

Stuiver, M., Reimer, P. J., Bard, E., Beck, J. W., Burr, G. S., Hughen, K. A., Kromer, B., McCormac, F. G., v.d. Plicht, J., and Spurk, M. (1998a). INTCAL98 Radiocarbon age calibration 24,000 - 0 cal BP. Radiocarbon 40, 1041-1083.

Stuiver, M., Reimer, P. J., and Braziunas, T. F. (1998b). High-precision radiocarbon age calibration for terrestrial and marine samples. Radiocarbon 40, 1127-1151.

Ter Braak, C. J. F., and Prentice, I. C. (1988). A Theory of Gradient Analysis. Advances in Ecological Research 18, 271-317.

Thompson, L. G. (2001). Huascaran Ice Core Data. IGBP PAGES/World Data Center A for Paleoclimatology, Data Contribution Series #2001-008, NOAA/NGDC Paleoclimatology Program, Boulder CO, USA.

Thompson, L. G., Davis, M. E., Mosley-Thompson, E., Sowers, T. A., Henderson, K. A., Zagorodnov, V. S., Lin, P.-N., Mikhalenko, V. N., Campen, R. K., Bolzan, J. F., Cole-Dai, J., and Francou, B. (1998). A 25,000-year tropical climate history from Bolivian ice cores. Science 282, 1858-1864.

Thompson, L. G., Mosley-Thompson, E., Bolzan, J. F., and Koci, B. R. (1985). A 1500-year record of tropical precipitation in ice cores from the Quelccaya ice cap, Peru. Science 229, 971-973.

Thompson, L. G., Mosley-Thompson, E., Davis, M. E., Lin, P.-N., Henderson, K. A., Cole-Dai, J., Bolzan, J. F., and Liu, K.-b. (1995). Late Glacial Stage and Holocene tropical ice core records from Huascarán, Peru. Science 269, 46-50.

Thompson, L. G., Mosley-Thompson, E., and Henderson, K. A. (2000). Ice-core palaeoclimate records in tropical South America since the Last Glacial Maximum. Journal of Quaternary Science 15, 377-394.

Trenberth, K. E. (1999). Atmospheric moisture recycling: role of advection and local evaporation. Journal of Climate 12, 1368-1381.

Tudhope, A. W., Chilcott, C. P., McCulloch, M. T., Cook, E. R., Chappel, J., Ellam, R. M., Lea, D. W., Lough, J. M., and Shimmield, G. B. (2001). Variability in the El Niño-Southern Oscillation through a glacial-interglacial cycle. Science 291, 1511-1517.

Valdes, P. J. (2000). South American palaeoclimate model simulations: how reliable are the models? Journal of Quaternary Science 15, 357-+.

Victoria, R. L., Martinelli, L. A., Mortatti, J., and Richey, J. (1991). Mechanisms of water recycling in the Amazon Basin: isotopic insights. Ambio 20, 384-387.

Vink, A., Rühlemann, C., Zonneveld, K. A. F., Mulitza, S., Hüls, M., and Willems, H. (2001). Shifts in the position of the North Equatorial Current and rapid productivity changes in the western Tropical Atlantic during the last glacial. Paleoceanography 16, 479-490.

Vuille, M. (1999). Atmospheric circulation over the Bolivian Altiplano during dry and wet periods and extreme phases of the Southern Oscillation. International Journal of Climatology 19, 1579-1600.

Vuille, M., Bradley, R. S., Healy, R., Werner, M., Hardy, D., Thompson, L. G., and Keimig, F. (2003). Modeling the $\delta^{18}O$ in precipitation over the tropical Americas: 2. Simulation of the stable isotope signal in Andean ice cores. Journal of Geophysical Research 108, doi:10.1029/2001JD002039.

Vuille, M., Bradley, R. S., Werner, M., Healy, R., and Keimig, F. (2001). Modeling $\delta^{18}O$ in precipitation over the tropical Americas: 1. Interannual variability and climatic controls. Journal of Geophysical Research 108, doi:10.1029/2001JD002038.

Vélez, M. I., Hooghiemstra, H., Metcalfe, S., Martínez, I., and Mommersteeg, H. (2003). Pollen- and diatom-based environmental history since the Last Glacial Maximum from the Andean core Fúquene-7, Columbia. Journal of Quaternary Science 18, 17-30.

Watanabe, T., Winter, A., and Oba, T. (2001). Seasonal changes in sea surface temperature and salinity during the Little Ice Age in the Caribbean Sea deduced from Mg/Ca and $^{18}O/^{16}O$ ratios in corals. Marine Geology 173, 21-35.

Watts, W. A., and Hansen, B. C. S. (1994). Pre-Holocene and Holocene pollen records of vegetational history from the Florida peninsula and their climatic implications. Palaeogeography, Palaeoclimatology, Palaeoecology 109, 163-173.

Weingarten, B., Salgado-Labouriau, M. L., Yuretich, R., and Bradley, R. (1991). Late Quaternary environmental history of the Venezuelan Andes. In "Late Quaternary Climatic Fluctuations of the Venezuelan Andes." (R. Yuretich, Ed.), pp. 63-94. University of Massachusetts, Amherst, MA.

Werne, J. P., Hollander, D. J., Lyons, T. W., and Peterson, L. C. (2000). Climate-induced variations in productivity and planktonic ecosystem structure from the Younger Dryas to Holocene in the Cariaco Basin, Venezuela. Paleoceanography 15, 19-29.

Wille, M., Hooghiemstra, H., van Geel, B., Behling, H., de Jong, A., and van der Borg, K. (2003). Submillennium-scale migrations of the rainforest-savanna boundary in Colombia: ^{14}C wiggle-matching and pollen analysis of core Las Margaritas. Palaeogeography, Palaeoclimatology, Palaeoecology 193, 201-223.

Winter, A., Ishioroshi, H., Watanabe, T., Oba, T., and Christy, J. (2000). Caribbean sea surface temperatures: two-to-three degrees cooler than present during the Little Ice Age. Geophysical Research Letters 27, 3365-3368.

Wright, H. E., Mann, D. H., and Glaser, P. H. (1984). Piston corers for peat and lake sediments. Ecology 65, 657-659.

Yokoyama, Y., Lambeck, K., De Deckker, P., Johnston, P., and Fifield, L. K. (2000). Timing of the Last Glacial Maximum from observed sea-level minima. Nature 406, 713-716.

Zhou, J., and Lau, K.-M. (1998). Does a Monsoon Climate Exist over South America? Journal of Climate 11, 1020-1040.